

AD-A242 603



ESL-TR-89-41



# UNITED STATES AIR FORCE 1987 RESEARCH INITIATION PROGRAM

PERRY SULLIVAN

UNIVERSAL ENERGY SYSTEM, INC.  
4401 DAYTON-XENIA ROAD  
DAYTON OH 45432-1894

APRIL 1989

FINAL REPORT

OCTOBER 1987 — DECEMBER 1988

APPROVED FOR PUBLIC RELEASE: DISTRIBUTION UNLIMITED

91-15634



AIR FORCE ENGINEERING & SERVICES CENTER  
ENGINEERING & SERVICES LABORATORY  
TYNDALL AIR FORCE BASE, FLORIDA 32403

NOTICE

PLEASE DO NOT REQUEST COPIES OF THIS REPORT FROM  
HQ AFESC/RD (ENGINEERING AND SERVICES LABORATORY).  
ADDITIONAL COPIES MAY BE PURCHASED FROM:

NATIONAL TECHNICAL INFORMATION SERVICE  
5285 PORT ROYAL ROAD  
SPRINGFIELD, VIRGINIA 22161

FEDERAL GOVERNMENT AGENCIES AND THEIR CONTRACTORS  
REGISTERED WITH DEFENSE TECHNICAL INFORMATION CENTER  
SHOULD DIRECT REQUESTS FOR COPIES OF THIS REPORT TO:

DEFENSE TECHNICAL INFORMATION CENTER  
CAMERON STATION  
ALEXANDRIA, VIRGINIA 22314

REPORT DOCUMENTATION PAGE				Form Approved OMB No. 0704-0188	
1a. REPORT SECURITY CLASSIFICATION <b>UNCLASSIFIED</b>			1b. RESTRICTIVE MARKINGS		
2a. SECURITY CLASSIFICATION AUTHORITY			3. DISTRIBUTION / AVAILABILITY OF REPORT Approved for Public Release. Distribution unlimited.		
2b. DECLASSIFICATION / DOWNGRADING SCHEDULE			4. PERFORMING ORGANIZATION REPORT NUMBER(S)		
5. MONITORING ORGANIZATION REPORT NUMBER(S)  ESL-TR-89-41			6a. NAME OF PERFORMING ORGANIZATION  Universal Energy Systems, Inc.		
6b. OFFICE SYMBOL (if applicable)			7a. NAME OF MONITORING ORGANIZATION  HQ Air Force Engineering & Services Center		
6c. ADDRESS (City, State, and ZIP Code)  4401 Dayton-Xenia Road Dayton Ohio 45432-1894			7b. ADDRESS (City, State, and ZIP Code)  Air Force Engineering and Services Laborator Tyndall Air Force Base, Fl 32403-6001		
8a. NAME OF FUNDING / SPONSORING ORGANIZATION Air Force Office of Scientific Research			8b. OFFICE SYMBOL (if applicable)		
8c. ADDRESS (City, State, and ZIP Code)  Bolling Air Force Base Washington DC			9. PROCUREMENT INSTRUMENT IDENTIFICATION NUMBER  F49620-85-C-0013		
10. SOURCE OF FUNDING NUMBERS			11. TITLE (Include Security Classification)  United States Air Force 1987 Research Initiation Program		
PROGRAM ELEMENT NO.			PROJECT NO.		
TASK NO.			WORK UNIT ACCESSION NO		
12. PERSONAL AUTHOR(S) Perry Sullivan (Project Officer)					
13a. TYPE OF REPORT FINAL		13b. TIME COVERED FROM 10/87 TO 12/88		14. DATE OF REPORT (Year, Month, Day) April 1989	
15. PAGE COUNT 367					
16. SUPPLEMENTARY NOTATION  Availability of this report is specified on reverse of front cover.					
17. COSATI CODES			18. SUBJECT TERMS (Continue on reverse if necessary and identify by block number)		
FIELD	GROUP	SUB-GROUP			
19. ABSTRACT (Continue on reverse if necessary and identify by block number)  This report contains research efforts from participants of the Summer Faculty Research Program.					
20. DISTRIBUTION / AVAILABILITY OF ABSTRACT <input type="checkbox"/> UNCLASSIFIED/UNLIMITED <input checked="" type="checkbox"/> SAME AS RPT <input type="checkbox"/> DTIC USERS			21. ABSTRACT SECURITY CLASSIFICATION		
22a. NAME OF RESPONSIBLE INDIVIDUAL H. Perry Sullivan			22b. TELEPHONE (Include Area Code) (904) 283-6278		22c. OFFICE SYMBOL HQ AFESC/RDXT

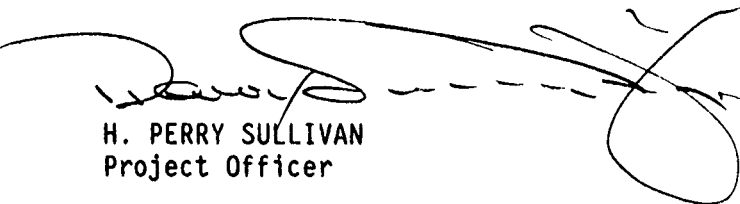
## PREFACE

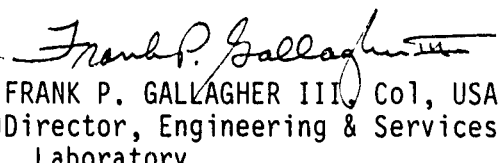
This report was originally prepared by Universal Energy Systems, Inc., under Contract number F49620-85-C-0013 for the Air Force Office of Scientific Research, Bolling Air Force Base, Washington D.C. It contains results of summer faculty research sponsored by the Air Force Engineering and Services Center, Engineering and Services Laboratory, Tyndall Air Force Base, Florida 32403-6001.

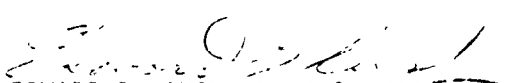
This report covers research performed between October 1987 and December 1988. The report is being reprinted and submitted to Defense Technical Information center because of its widespread interest to the DOD Engineering and Services community. The AFESC/RD Project Officer was H. Perry Sullivan.

The report has been reviewed by the Public Affairs Office (PA) and is releasable to the general public, including foreign nationals.

This report has been reviewed and is approved for public release.

  
H. PERRY SULLIVAN  
Project Officer

  
FRANK P. GALLAGHER III, Col, USAF  
Director, Engineering & Services  
Laboratory

  
EDWARD B. CUSH, Lt Col, USAF  
Chief, Programs and Plans Division

Accession For	
General	<input checked="checked" type="checkbox"/>
Special	<input type="checkbox"/>
Unpublished	<input type="checkbox"/>
Publication	<input type="checkbox"/>
or	
Distribution	
Availability Codes	
Avail and/or	
Unavail	
A-1	

## TABLE OF CONTENTS

<u>SECTION</u>	<u>PAGE</u>
INTRODUCTION . . . . .	vii
STATISTICS . . . . .	ix
PARTICIPANT LABORATORY ASSIGNMENT . . . . .	xv
RESEARCH REPORTS . . . . .	xxv

## INTRODUCTION

### Research Initiation Program - 1987

AFOSR has provided funding for follow-on research efforts for the participants in the Summer Faculty Research Program. Initially this program was conducted by AFOSR and popularly known as the Mini-Grant Program. Since 1983 the program has been conducted by the Summer Faculty Research Program (SFRP) contractor and is now called the Research Initiation Program (RIP). Funding is provided to establish RIP awards to about half the number of participants in the SFRP.

Participants in the 1987 SFRP competed for funding under the 1987 RIP. Participants submitted cost and technical proposals to the contractor by 1 November 1987, following their participation in the 1987 SFRP.

Evaluation of these proposals was made by the contractor. Evaluation criteria consisted of:

1. Technical Excellence of the proposal
2. Continuation of the SFRP effort
3. Cost sharing by the University

The list of proposals selected for award was forwarded to AFOSR for approval of funding. Those approved by AFOSR were funded for research efforts to be completed by 31 December 1988.

The following summarizes the events for the evaluation of proposals and award of funding under the RIP.

- A. Rip proposals were submitted to the contractor by 1 November 1987. The proposals were limited to \$20,000 plus cost sharing by the universities. The universities were encouraged to cost share since this is an effort to establish a long term effort between the Air Force and the university.
- B. Proposals were evaluated on the criteria listed above and the final award approval was given by AFOSR after consultation with the Air Force Laboratories.
- C. Subcontracts were negotiated with the universities. The period of performance of the subcontract was between October 1987 and December 1988.

Copies of the Final Reports are presented in Volumes I through III of the 1987 Research Initiation Program Report. There were a total of 83 RIP awards made under the 1987 program.

## STATISTICS

Total SFRP Participants	159
Total RIP Proposals submitted by SFRP	117
Total RIP Proposals submitted by GSRP	7
Total RIP Proposals submitted	124

Total RIP's funded to SFRP	81
Total RIP's funded to GSRP	2
Total RIP's funded	83

Total RIP's Proposals submitted by HBCU's	11
Total RIP's Proposals funded to HBCU's	7

<u>Laboratory</u>	<u>SFRP Participants</u>	<u>RIP's Submitted</u>	<u>RIP's Funded</u>
AAMRL	13	12 (2 GSRP)	6
AFWAL/APL	8	6	4
ATL	9	8 (1 GSRP)	6
AEDC	6	4	3
AFWAL/AL	9	9 (1 GSRP)	5
LC	1	1	1
ESMC	1	0	0
ESD	1	1	0
ESC	8	8	6
AFWAL/FDL	9	8 (1 GSRP)	6 (1 GSRP)
FJSRL	9	5	5
AFGL	13	10 (1 GSRP)	7
HRL/OT	2	2	1
HRL/LR	3	3	2
HRL/MO	3	2	2
HRL/ID	0	0	0
LMC	3	1	0
AFWAL/ML	13	11 (1 GSRP)	6 (1 GSRP)
OEHL	5	3	3
AL	7	4	3
RADC	11	10	7
SAM	16	8	6
DEOMI	2	2	0
WL	7	6	4
Total	159	124	83

# LIST OF UNIVERSITY THAT PARTICIPATED

Adelphi University	- 1	Meharry Medical College	- 1
Alabama, University of	- 1	Memphis State University	- 1
Alaska-Fairbanks, Univ. of	- 1	Metropolitan State College	- 1
Alfred University	- 1	Michigan State University	- 1
Arizona State University	- 1	Mississippi State University	- 4
Arkansas State University	- 1	Mississippi, University of	- 1
Arkansas, University of	- 1	Missouri-Kansas City, Univ.	- 1
Auburn University	- 1	Missouri-Rolla, Univ. of	- 3
Bishop College	- 1	Montana, University of	- 1
Capital University	- 1	Montclair State College	- 1
Catholic Univ. of America	- 1	Morehouse College	- 1
Cedarville College	- 1	Nazareth College	- 1
Central State University	- 1	Nebraska-Lincoln, Univ. of	- 2
Cincinnati, University of	- 5	New Mexico State University	- 1
Colorado, University of	- 2	New York State, Univ. of	- 3
Dayton, University of	- 7	N. Carolina A&T State Univ.	- 1
Dillard University	- 1	N. Carolina-Greensboro, Univ	- 1
Drury College	- 1	Northwestern University	- 1
Eastern Illinois University	- 1	Ohio State University	- 5
Eastern Kentucky University	- 1	Ohio University	- 2
Eastern New Mexico University	- 2	Oklahoma State University	- 1
Fairfield University	- 1	Oregon Institute of Tech.	- 1
Florida A&M University	- 1	Oregon State University	- 1
Florida, University of	- 2	Ouachita Baptist University	- 1
Fort Lewis College	- 1	Pace University	- 1
Gonzaga University	- 1	Pennsylvania State Univ.	- 1
Grambling State University	- 1	Point Loma College	- 1
Hampton University	- 1	Puerto Rico-Mayaguez, Univ.	- 1
Houston, University of	- 2	Purdue University	- 1
Howard University	- 1	Rochester Inst. of Tech.	- 1
Idaho, University of	- 1	Rose-Hulman Inst. of Tech.	- 2
Illinois-Chicago, Univ. of	- 2	Saint Paul's College	- 1
Indiana University	- 1	San Francisco State Univ.	- 1
Indiana Univ. of Pennsylvania	- 1	South Dakota State Univ.	- 1
Iowa, University of	- 1	South Florida, University of	- 2
Jackson State University	- 1	Southeastern Mass. Univ.	- 2
Jarvis Christian College	- 1	Southern Illinois University	- 2
Jesm Baromedical Res. Inst.	- 1	Southern Mississippi, Univ.	- 1
John Hopkins Evening College	- 1	Southern University	- 2
Kansas State University	- 1	St. Louis University	- 1
Kansas, University of	- 1	St. Mary's University	- 1
Kentucky, University of	- 1	Talladega College	- 1

Continued

LIST OF UNIVERSITY THAT PARTICIPATED  
Continued

Lock Haven Univ. of Pennsylv.	- 1	Taylor University	- 1
Long Island University	- 1	Temple University	- 1
Louisiana State University	- 1	Tennessee Technical Univ.	- 1
Louisiana Tech. University	- 1	Tennessee, University of	- 1
Lowell, University of	- 4	Texas A&M University	- 2
Texas Southern University	- 3	Wichita State University	- 2
Texas Technical University	- 2	Wilberforce University	- 1
Texas-Austin, University of	- 1	Wisconsin-Eau Claire Univ.	- 2
Tuskegee University	- 1	Wisconsin-Madison, Univ. of	- 1
Utah State University	- 1	Wisconsin-Whitewater, Univ.	- 1
Walla Walla College	- 1	Wittenberg University	- 1
Washington State University	- 1	Worcester Polytech. Inst.	- 2
West Florida, University of	- 1	Wright State University	- 3
Western Michigan University	- 3	Xavier University	- 1

## PARTICIPANTS LABORATORY ASSIGNMENT

PARTICIPANT LABORATORY ASSIGNMENT (Page 1)

AERO PROPULSION LABORATORY

(Wright-Patterson Air Force Base)

Dr. Suresh K. Aggarwal  
Univ. of Illinois at Chicago  
Specialty: Aerospace Engineering

Dr. Richard Tankin  
Northwestern University  
Specialty: Mechanical Engineering

Dr. Bryan R. Becker  
Rose-Hulman Institute  
Specialty: Engineering Science

Dr. Cheng-Hsiao Wu  
Univ. of Missouri  
Specialty: Solid State Physics

ARMAMENT LABORATORY

(Eglin Air Force Base)

Dr. Charles Bell  
Arkansas State University  
Specialty: Mechanical Engineering

Dr. Elmer C. Hansen  
University of Florida  
Specialty: Mechanical Engineering

Dr. Robert W. Courter  
Louisiana State University  
Specialty: Aerospace Engineering

Dr. James Hoffmaster  
Gonzaga University  
Specialty: Physics

Dr. Joseph J. Feeley  
University of Idaho  
Specialty: Electrical Engineering

Dr. James Nail  
Mississippi State Univ.  
Specialty: Electrical Engineering

Ms. Jennifer L. Davidson (1986), (GSRP)  
University of Florida  
Specialty: Mathematics

Dr. Meckinley Scott (1986)  
University of Alabama  
Specialty: Statistics

Dr. Mo Samimy (1986)  
Ohio State University  
Specialty: Mechanical Engineering

Mr. Jim S. Sirkis (1986), (GSRP)  
University of Florida  
Specialty: Engineering Mechanics

HARRY G. ARMSTRONG AEROSPACE MEDICAL RESEARCH LABORATORY

(Wright-Patterson Air Force Base)

Dr. Praphulla K. Bajpai  
University of Dayton  
Specialty: Immunology

Dr. Thomas Nygren  
Ohio State University  
Specialty: Psychology

Dr. Gwendolyn Howze  
Texas Southern University  
Specialty: Physics

Dr. Donald Robertson  
Indiana University of PA  
Specialty: Psychology

PARTICIPANT LABORATORY ASSIGNMENT (Page 2)

HARRY G. ARMSTRONG AEROSPACE MEDICAL RESEARCH LABORATORY /  
(Wright-Patterson Air Force Base)  
(continued)

Dr. Noel Nussbaum  
Wright State University  
Specialty: Biology

Dr. John Westerkamp  
University of Dayton  
Specialty: Electrical Engineering

Dr. Jacqueline Paver (1986)  
Duke University  
Specialty: Biomechanical Engineering

ARNOLD ENGINEERING DEVELOPMENT CENTER  
(Arnold Air Force Systems)

Dr. Suhrit K. Dey  
Eastern Illinois University  
Specialty: Aerospace Engineering

Dr. Surgounda Patil  
Tennessee Technical University  
Specialty: Math Statistics

Dr. William M. Grissom  
Morehouse College  
Specialty: Mechanical Engineering

ASTRONAUTICS LABORATORY  
(Edwards Air Force Base)

Dr. Gurbux S. Alag  
Western Michigan University  
Specialty: Systems Engineering

Dr. Lawrence Schovanec  
Texas Tech University  
Specialty: Mathematics

Dr. John Kenney  
Eastern New Mexico University  
Specialty: Physical Chemistry

AVIONICS LABORATORY  
(Wright-Patterson Air Force Base)

Dr. Vernon L. Bakke  
University of Arkansas  
Specialty: Mathematics

Dr. Narayan C. Halder  
University of South Florida  
Specialty: Physics

PARTICIPANT LABORATORY ASSIGNMENT (Page 3)

AVIONICS LABORATORY

(Wright-Patterson Air Force Base)  
(continued)

Prof. William K. Curry  
Rose-Hulman Inst. of Technology  
Specialty: Computer Science

Dr. Alastair McAulay  
Wright State University  
Specialty: Electrical Engineering

Dr. Verlynda S. Dobbs  
Wright State University  
Specialty: Computer Science

Dr. John Y. Cheung (1986)  
University of Oklahoma  
Specialty: Electrical Engineering

Dr. George W. Zobrist (1986)  
University of Missouri-Rolla  
Specialty: Electrical Engineering

ENGINEERING AND SERVICES CENTER  
(Tyndall Air Force Base)

Dr. William W. Bannister  
University of Lowell  
Specialty: Organic Chemistry

Dr. William Schulz  
Eastern Kentucky University  
Specialty: Chemistry

Dr. William M. Bass  
The University of Tennessee  
Specialty: Physical Anthropology

Dr. Joseph Tedesco  
Auburn University  
Specialty: Civil Engineering

Dr. Peter Jeffers  
S.U.N.Y.  
Specialty: Chemistry

Dr. Dennis Truax  
Mississippi State University  
Specialty: Civil Engineering

Dr. William T. Cooper (1986)  
Florida State University  
Specialty: Chemistry

Dr. Yong S. Kim (1986)  
The Catholic Univ. of America  
Specialty: Civil Engineering

FLIGHT DYNAMICS LABORATORY

(Wright-Patterson Air Force Base)

Mr. Thomas Enneking (GSRP)  
University of Notre Dame  
Specialty: Civil Engineering

Dr. Gary Slater  
University of Cincinnati  
Specialty: Aerospace Engineering

PARTICIPANT LABORATORY ASSIGNMENT (Page 4)

FLIGHT DYNAMICS LABORATORY

(Wright-Patterson Air Force Base)  
(continued)

Dr. Oliver McGee  
Ohio State University  
Specialty: Engineering Mechanics

Dr. Forrest Thomas  
University of Montana  
Specialty: Chemistry

Dr. Shiva Singh  
Univ. of Kentucky  
Specialty: Mathematics

Dr. William Wolfe  
Ohio State University  
Specialty: Engineering

Dr. George R. Doyle (1986)  
University of Dayton  
Specialty: Mechanical Engineering

Dr. V. Dakshina Murty (1986)  
University of Portland  
Specialty: Engineering Mechanics

Dr. Tsun-wai G. Yip (1986)  
Ohio State University  
Specialty: Aeronautics-Astronautics Engineering

FRANK J. SEILER RESEARCH RESEARCH LABORATORY

(United State Air Force Academy)

Dr. Charles M. Bump  
Hampton University  
Specialty: Organic Chemistry

Dr. Howard Thompson  
Purdue University  
Specialty: Mechanical Engineering

Dr. Stephen J. Gold  
South Dakota State University  
Specialty: Electrical Engineering

Dr. Melvin Zandler  
Wichita State Univ.  
Specialty: Physical Chemistry

Dr. Henry Kurtz  
Memphis State Univ.  
Specialty: Chemistry

GEOPHYSICS LABORATORY

(Hanscom Air Force Base)

Dr. Lee A. Flippin  
San Francisco State Univ.  
Specialty: Organic Chemistry

Dr. Gandikota Rao  
St. Louis University  
Specialty: Meteorology

PARTICIPANT LABORATORY ASSIGNMENT (Page 5)

GEOPHYSICS LABORATORY

(Hanscom Air Force Base)  
(continued)

Dr. Mayer Humi  
WPI  
Specialty: Applied Mathematics

Dr. Steven Leon  
Southeastern Massachusetts  
Specialty: Mathematics

Dr. Henry Nebel  
Alfred University  
Specialty: Physics

Dr. Timothy Su  
Southeastern Massachusetts Univ.  
Specialty: Physical Chemistry

Dr. Keith Walker  
Point Loma College  
Specialty: Physics

HUMAN RESOURCES LABORATORY

(Brooks, Williams and Wright-Patterson Air Force Base)

Dr. Patricia A. Carlson  
Rose-Hulman Inst. of Technology  
Specialty: Literature/Language

Dr. Ronna E. Dillon  
Southern Illinois University  
Specialty: Educational Psychology

Dr. Michael Matthews  
Drury College  
Specialty: Psychology

Dr. Stephen Loy (1986)  
Iowa State University  
Specialty: Management Information Sys.

Dr. Doris Walker-Dalhouse (1986)  
Jackson State University  
Specialty: Reading Education

Dr. John Uhlarik  
Kansas State University  
Specialty: Psychology

Dr. Charles Wells  
University of Dayton  
Specialty: Management Science

Dr. Charles Lance (1986)  
University of Georgia  
Specialty: Psychology

Dr. Jorge Mendoza  
Texas A&M University  
Specialty: Psychology

Dr. Billy Wooten (1986)  
Brown University  
Specialty: Philosophy, Psychology

PARTICIPANT LABORATORY ASSIGNMENT (Page 6)

LOGISTICS COMMAND

(Wright-Patterson Air Force Base)

Dr. Howard Weiss

Specialty: Industrial Engineering  
Temple University

MATERIALS LABORATORY

(Wright-Patterson Air Force Base)

Dr. Bruce A. DeVantier  
S. Illinois University  
Specialty: Civil Engineering

Dr. John W. Gilmer  
Penn State University  
Specialty: Physical Chemistry

Dr. Ravinder Diwan  
Southern University  
Specialty: Metallurgy

Dr. Gordon Johnson  
Walla Walla College  
Specialty: Electrical Engineering

Dr. Bruce A. Craver  
University of Dayton  
Specialty: Physics

Mr. John Usher (GSRP)  
Louisiana State University  
Specialty: Chemical Engineering

Dr. Robert Patsiga (1986)  
Indiana Univ. of Pennsylvania  
Specialty: Organic Polymer Chemistry

Dr. Nisar Shaikh (1986)  
University of Nebraska-Lincoln  
Specialty: Applied Mathematics

Dr. Gopal M. Mehrotra (1986)  
Wright State University  
Specialty: Metallurgy

OCCUPATIONAL AND ENVIRONMENT HEALTH LABORATORY

(Brooks Air Force Base)

Dr. Richard H. Brown  
Ouachita Baptist University  
Specialty: Physiology

Dr. Kiah Edwards  
Texas Southern University  
Specialty: Molecular Biology

Dr. Elvis E. Deal  
University of Houston  
Specialty: Industrial Engineering

Dr. Ralph J. Rascati (1986)  
Kennesaw College  
Specialty: Biochemistry

PARTICIPANT LABORATORY ASSIGNMENT (Page 7)

ROME AIR DEVELOPMENT CENTER  
(Griffis Air Force Base)

Prof. Beryl L. Barber  
Oregon Institute of Technology  
Specialty: Electrical Engineering

Dr. Kevin Bowyer  
University of South Florida  
Specialty: Computer Science

Dr. Ronald V. Canfield  
Utah State University  
Specialty: Statistics

Dr. Lionel R. Friedman  
Worcester Polytechnic Inst.  
Specialty: Physics

Dr. John M. Jobe (1986)  
Miami University of Ohio  
Specialty: Statistics

Dr. Louis Johnson  
Oklahoma State Univ.  
Specialty: Electrical Engineering

Dr. Panapkkam Ramamoorthy  
University of Cincinnati  
Specialty: Electrical Engineering

Dr. David Sumberg  
Rochester Institute of Tech.  
Specialty: Physics

Dr. Donald Hanson (1986)  
University of Mississippi  
Specialty: Electrical Engineering

Dr. Stephen T. Welstead (1986)  
University of Alabama in Hunts.  
Specialty: Applied Mathematics

SCHOOL OF AEROSPACE MEDICINE  
(Brooks Air Force Base)

Prof. Phillip A. Bishop  
University of Alabama  
Specialty: Exercise Physiology

Dr. Mohammed Maleque  
Meharry Medical College  
Specialty: Pharmacology

Dr. Kurt Oughstun  
University of Wisconsin  
Specialty: Optical Sciences

Dr. Hoffman H. Chen (1986)  
Grambling State University  
Specialty: Mechanical Engineering

Dr. Ralph Peters  
Wichita State University  
Specialty: Zoology

Dr. Stephen Pruett  
Mississippi State University  
Specialty: Immunology

Dr. Wesley Tanaka  
University of Wisconsin  
Specialty: Biochemistry

Dr. Vito DelVecchio (1986)  
University of Scranton  
Specialty: Biochemistry, Genetics

PARTICIPANT LABORATORY ASSIGNMENT (Page 8)

WEAPONS LABORATORY

(Kirtland Air Force Base)

Dr. Jerome Knopp  
University of Missouri  
Specialty: Electrical Engineering

Dr. Barry McConnell  
Florida A&M University  
Specialty: Computer Science

Dr. Martin A. Shadday, Jr. (1986)  
University of South Carolina  
Specialty: Mechanical Engineering

Dr. Randall Peters  
Texas Tech University  
Specialty: Physics

Dr. William Wheless  
New Mexico State University  
Specialty: Electrical Engineering

## RESEARCH REPORTS

# MINI-GRANT RESEARCH REPORTS

→ The reports are in 1987 RESEARCH INITIATION PROGRAM  
*Following of 1987*

Technical Report Number	Title and Mini-Grant No.	Professor
Volume I Armament Laboratory		
1	Report Not Available at this Time 760-7MG-025	Dr. Charles Bell
2	> Effects of Bending Flexibility on the Aerodynamic Characteristics of Slender Cylinders Determined from Free-Flight Ballistic Data 760-7MG-018	Dr. Robert W. Courter
3	> Image Complexity Measures and Edge Detection 760-6MG-024	Ms. Jennifer L. Davidson (1986 GSRP)
4	Report Not Available at this Time 760-7MG-070	Dr. Joesph J. Feeley
5	> Advanced Gun Gas Diversion 760-7MG-012	Dr. Elmer Hansen
6	. A Physical and Numerical Study of Pressure Attenuation in Solids 760-7MG-002	Dr. James Hoffmaster
7	Pyroelectric Sensing for Potential Multi-Mode Use 760-7MG-026	Dr. James Nail
8	Gaseous Fuel Injection and Mixing in a Supersonic Combustor 760-6MG-059	Dr. Mo Samimy (1986)
9	Systems Effectiveness for Targets with Repair or Replacement Facilities of Damaged Components 760-6MG-025	Dr. Meckinley Scott (1986)
10	A Pattern Recognition Application in Elastic-Plastic Boundary Element, Hybrid Stress Analysis 760-6MG-142	Mr. Jim S. Sirkis (1986 GSRP)

Arnold Engineering Development Center

- 11 Vectorized Perturbed Functional  
Iterative Scheme (VPFIS): A Large-  
Scale Nonlinear System Solver  
760-7MG-037

Dr. Suhrit K. Dey

- 12 Liquid Film Cooling in Rocket  
Engines  
760-7MG-022

Dr. William M. Grissom

- 13 Estimation of Autocorrelation and  
Power Spectral Density for Randomly  
Sampled Systems  
760-7MG-085

Dr. Surgounda Patil

Astronautics Laboratory

- 14 Report Not Available at this Time  
760-7MG-042

Dr. Gurbux S. Alag

- 15 Report Not Available at this Time  
760-7MG-019

Dr. John Kenney

- 16 Fracture in Solid Propellant:  
Damage Effects upon Crack  
Propagation  
760-7MG-065

Dr. Lawrence Schovanec

- 17 Novel Conversion of Organometallics to  
Energetic Nitro Compounds  
760-6MG-130

Dr. Nicholas E. Takach  
(1986)

Engineering and Services Center

- 18 Correlations of Spontaneous  
Ignition Temperatures with Molecular  
Structures of Flammable Compounds  
760-7MG-101

Dr. William W. Bannister

- 19 The Estimation of Stature from  
Fragments of the Femur: A  
Revision of the Steele Method  
760-7MG-014

Dr. William M. Bass

- 20 Effects of Water Solubility and  
Functional Group Content on the  
Interactions of Organic Solutes  
with Soil Organic Matter  
760-6MG-081

Dr. William T. Cooper  
(1986)

- 21 Report Not Available at this Time  
760-7MG-038

Dr. Peter Jeffers

- |    |   |                        |
|----|---|------------------------|
| 22 | A Study of Semihardened Concrete Arch Structure Response Under Protective Layers<br>760-6MG-004 | Dr. Yong S. Kim (1986) |
| 23 | Report Not Available at this Time<br>760-7MG-079  | Dr. William Schulz     |
| 24 | Stress Wave Propagation in Layered Media<br>760-7MG-034   | Dr. Joseph Tedesco     |
| 25 | Report Not Available at this Time<br>760-7MG-105  | Dr. Dennis Truax       |

Volume II

Frank J. Seiler Research Laboratory

- |    |   |                     |
|----|---|---------------------|
| 26 | Report Not Available at this Time<br>760-7MG-076                            | Dr. Charles M. Bump |
| 27 | The Omnidirectional Torquer - Experimental Prototype Model I<br>760-7MG-123 | Dr. Stephen J. Gold |
| 28 | Calculation of Nonlinear Optical Properties<br>760-7MG-030                  | Dr. Henry Kurtz     |
| 29 | Report Not Available at this Time<br>760-7MG-071                            | Dr. Howard Thompson |
| 30 | Report Not Available at this Time<br>760-7MG-092                            | Dr. Melvin Zandler  |

Geophysics Laboratory

- |    |   |                    |
|----|---|--------------------|
| 31 | Report Not Available at this Time<br>760-7MG-056  | Dr. Lee A. Flippin |
| 32 | Modelling and Prediction in a Nonlocal Turbulence Model<br>760-7MG-028  | Dr. Mayer Humi     |
| 33 | Report Not Available at this Time<br>760-7MG-036  | Dr. Steven Leon    |
| 34 | CO <sub>2</sub> (001) Vibrational Temperatures and Limb-View Infrared Radiances Under Terminator Conditions in the 60-100 Altitude Range<br>760-7MG-035 | Dr. Henry Nebel    |

35      Comparison of SSM/I Rainrates and  
         Surface Winds with the Corresponding  
         Conventional Data in the North West  
         Pacific Typhoons  
         760-7MG-072      Dr. Gandikota Rao

36      Report Not Available at this Time      Dr. Timothy Su  
         760-7MG-040

37      Development of a System for the  
         Measurement of Electron Excitation  
         Cross Sections of Atoms and Molecules  
         in the Near Infrared  
         760-7MG-074      Dr. Keith Walker

Rome Air Development Center

38      Superconductor Testing      Prof. Beryl L. Barber  
         760-7MG-103

39      A Form and Function Knowledge  
         Representation for Reasoning about  
         Classes and Instances of Objects  
         760-7MG-003      Dr. Kevin Bowyer

40      Development and Evaluation of a  
         Bayesian Test for System Testability  
         760-7MG-032      Dr. Ronald V. Canfield

41      Crystalline Silicon Electro-Optic  
         Waveguides  
         760-7MG-040      Dr. Lionel R. Friedman

42      Measurements of a Slot Antenna Fed  
         by Coplanar Waveguide and Solution  
         of an Infinite Phased Array of Slots  
         Fed by Coplanar Waveguide Over a  
         Dielectric Half-Space  
         760-6MG-092      Dr. Donald Hanson (1986)

43      A New Measure of Maintainability/  
         Reliability and Its Estimation  
         760-6MG-019      Dr. John M. Jobe (1986)

44      Report Not Available at this Time      Dr. Louis Johnson  
         760-7MG-050

45      Signed-Digit Number System for  
         Optical Adaptive Processing  
         760-7MG-015      Dr. Panapkkam Ramamoorthy

46	Report Not Available at this Time 760-7MG-113	Dr. David Sumberg
47	Implementation of Iterative Algorithms for an Optical Signal Processor 760-6MG-063	Dr. Stephen T. Welstead (1986)
Weapons Laboratory		
48	Experimental Evaluation of Imaging Correlography 760-7MG-109	Dr. Jerome Knopp
49	Report Not Available at this Time 760-7MG-047	Dr. Barry McConnell
50	Interaction of Lasers with Superconductors 760-7MG-008	Dr. Randall Peters
51	Three Dimensional Thermal Conduction Effects in High Power CW Laser Target Plates 760-6MG-089	Dr. Martin A. Shadday (1986)
52	Report Not Available at this Time 760-7MG-068	Dr. William Wheless
Volume III		
Air Force Wright Aeronautical Laboratories		
Aero Propulsion Laboratory		
53	Report Not Available at this Time 760-7MG-061	Dr. Suresh K. Aggerwal
54	A Numerical Study of the Flow Field and Heat Transfer in a Rectangular Passage with a Turbulator 760-7MG-066	Dr. Bryan R. Becker
55	Report Not Available at this Time 760-7MG-051	Dr. Richard Tankin
56	Report Not Available at this Time 760-7MG-093	Sr. Cheng-Hsiao Wu
Avionics Laboratory		
57	Analysis of an Algorithm for Multiple Frequency Resolution 760-7MG-090	Dr. Vernon L. Bakke

- |    |  |                           |
|----|--|---------------------------|
| 58 | Signal Processing in EW Environment<br>760-6MG-135   | Dr. John Y. Cheung (1986) |
| 59 | Report Not Available at this Time<br>760-7MG-081   | Prof. William K. Curry    |
| 60 | Implementation of Blackboard Systems<br>in Ada<br>760-7MG-010  | Dr. Verlynda S. Dobbs     |
| 61 | Surface States and Electron Trans-<br>port Properties in Semi-Insulating<br>Gallium Arsenide<br>760-7MG-049                  | Dr. Narayan C. Halder     |
| 62 | Investigate Feasibility of Implemen-<br>ting Associative Memories Using<br>Luminescent Rebroadcasting Devices<br>760-7MG-029 | Dr. Alastair McAulay      |
| 63 | Automated Translation of Digital Logic<br>Equations into Optimized VHDL Code<br>760-6MG-055                                  | Dr. George Zobrist (1986) |

Flight Dynamics Laboratory

- |    |  |                                 |
|----|--|---------------------------------|
| 64 | Analytical Model and Computer Program<br>of F-16 Nose Gear and F-16 ALGS<br>760-6MG-006                                  | Dr. George Doyle (1986)         |
| 65 | Report Not Available at this Time<br>760-7MG-124   | Mr. Thomas Enneking<br>(GSRP)   |
| 66 | Report Not Available at this Time<br>760-7MG-115   | Dr. Oliver McGee                |
| 67 | Development of a Technique for Pre-<br>diction of Internal Heat Transfer in<br>Actively Cooled Structures<br>760-6MG-079 | Dr. V. Dakshina Murty<br>(1986) |
| 68 | Radiation Hypersonic Aerodynamics<br>760-7MG-121   | Dr. Shiva Singh                 |
| 69 | Report Not Available at this Time<br>760-7MG-088   | Dr. Gary Slater                 |
| 70 | Report Not Available at this Time<br>760-7MG-080   | Dr. Forrest Thomas              |

71	Report Not Available at this Time 760-7MG-102	Dr. William Wolfe
72	A Chemical Kinetics Model for Mach 5 - 14 Hypersonic Flow 760-6MG-109	Dr. Tsun-wai G. Yip (1986)
Logistics Command		
73	Development of a Microcomputer Lateral Resupply Simulation System 760-7MG-116	Dr. Howard Weiss
Materials Laboratory		
74	Development of Expert System Control of a Carbon Fiber Production Process 760-7MG-027	Dr. Bruce A. DeVantier
75	Influence of Microstructural Variations on the Thermomechanical Processing in Dynamic Material Modeling of Titanium Aluminides 760-7MG-077	Dr. Ravinder Diwan
76	Report Not Available at this Time 760-7MG-097	Dr. Bruce A. Craver
77	Report Not Available at this Time 760-7MG-013	Dr. John W. Gilmer
78	Report Not Available at this Time 760-7MG-075	Dr. Gordon Johnson
79	Studies on the Compatibility of Potential Matrix and Reinforcement Materials in Ceramic Composites for High-Temperature, Aerospace Applications 760-6MG-121	Dr. Gopal Mehrotra (1986)
80	Synthesis of Compounds Capable of Intramolecular Cyclization - Aromat- ization Reactions 760-6MG-065	Dr. Robert Patsiga (1986)
81	Leaky Rayleigh and Lamb Waves on Composites 760-6MG-007	Dr. Nisar Shaikh (1986)
82	Performance Improvement in Know- ledge-Based Process Control Systems 760-7MG-044	Mr. John Usher (GSRP)

Volume IV

Human Systems Division Laboratories

Harry G. Armstrong Aerospace Medical Research Laboratory

- |    |  |                               |
|----|--|-------------------------------|
| 83 | Development of Implantable Devices<br>for Sustained Delivery of Volatile<br>Hydrocarbons in Rats<br>760-7MG-098      | Dr. Praphulla K. Bajpai       |
| 84 | In Situ Detection of Osteoprogenitor<br>Cells in an Actively Growing Bone<br>System<br>760-7MG-112                   | Dr. Gwendolyn Howze           |
| 85 | Trauma-Activated Periosteum Derived<br>Osteogenic Cells: Response to Selected<br>Growth Factors<br>760-7MG-089       | Dr. Noel Nussbaum             |
| 86 | Assessing the Attributes of Expert<br>Judgment: Measuring Bias in Subjective<br>Uncertainty Estimates<br>760-7MG-052 | Dr. Thomas Nygren             |
| 87 | Mathematical Modeling<br>760-6MG-020   | Dr. Jaqueline Paver<br>(1986) |
| 88 | Report Not Available at this Time<br>760-7MG-094   | Dr. Donald Robertson          |
| 89 | Learning Behavior of Adaptive<br>Filters for Evoked Brain Potentials<br>760-7MG-039                                  | Dr. John Westerkamp           |

Human Resources Laboratory

- |    |  |                          |
|----|--|--------------------------|
| 90 | The Rhetoric of Hypertext: An Exam-<br>ination of Document Database Concepts<br>and the Integrated Maintenance Infor-<br>mation System (IMIS)<br>760-7MG-021 | Dr. Patricia A. Carlson  |
| 91 | Report Not Available at this Time<br>760-7MG-100   | Dr. Ronna E. Dillon      |
| 92 | Structural Representations of Multi-<br>Dimensional Criterion Construct Space<br>760-6MG-031   | Dr. Charles Lance (1986) |
| 93 | Report Not Publishable at this Time<br>760-6MG-134   | Dr. Stephen Loy (1986)   |

94	Comparison of Supervisor's and Incumbent's Estimates of SDy 760-7MG-009	Dr. Michael Matthews
95	Report Not Available at this Time 760-6MG-136	Dr. Jorge Mendoza (1986)
96	The Role of Fourier Descriptions for Shape in Visual Form Perception 760-7MG-082	Dr. John Uhlarik
97	Comprehensibility of Technical Text 760-6MG-080	Dr. Doris Walker-Dalhouse (1986)
98	Report Not Available at this Time 760-7MG-046	Dr. Charles Wells
99	Mechanisms of Contrast and Lightness Constancy 760-6MG-051	Dr. Billy Wooten (1986)
Occupational and Environment Health Laboratory		
100	Phytotoxicity of Soil Residues of JP-4 Aviation Fuel 760-7MG-059	Dr. Richard H. Brown
101	An Impact Study for the Contracting Out of In-House Analytical Services at the USAF Occupational & Environmental Health Laboratory - Brooks AFB, San Antonio, Texas 760-7MG-096	Dr. Elvis E. Deal
102	Effects of Metal Mutagens on the Synthesis and Accumulation of Macromolecules 760-7MG-001	Dr. Kiah Edwards
103	Development of a Rapid and Sensitive Assay Procedure for the Detection of the Protozoan Parasite Giardia Lamblia in Drinking Water Supplies 760-6MG-062	Dr. Ralph J. Rascati (1986)
School of Aerospace Medicine		
104	Limitations to Heavy Work of Personnel Wearing at 21°C: U.S. Military Chemical Defense Ensemble 760-7MG-067	Prof. Phillip A. Bishop

105	Report Not Available at this Time 760-6MG-118	Dr. Hoffman Chen (1986)
106	Nucleic Acid Hybridization - Dot Blot Test for the Presence of Ureaplasma Urealyticum and Mycoplasma Hominis 760-6MG-076	Dr. Vito DelVecchio (1986)
107	Report Not Available at this Time 760-7MG-078	Dr. Mohammed Maleque
108	The Asymptotic Description of Precursor Fields in a Causally Dispersive Medium 760-7MG-033	Dr. Kurt Oughstun
109	Report Not Publishable at this Time 760-7MG-091	Dr. Ralph Peters
110	Model Systems for Assessing the Effects of Microwave Radiation on the Immune System 760-7MG-060	Dr. Stephen Pruett
111	Report Not Available at this Time 760-7MG-043	Dr. Wesley Tanaka

AUTOIGNITION. II. CORRELATIONS OF SPONTANEOUS IGNITION TEMPERATURES  
WITH MOLECULAR STRUCTURES OF FLAMMABLE COMPOUNDS

AIR FORCE OFFICE OF SCIENTIFIC RESEARCH RESEARCH INITIATION PROGRAM

FINAL REPORT TO UNIVERSAL ENERGY SYSTEMS, INC., DAYTON, OHIO

William W. Bannister,\* Stuart B. Clough and Sukant Tripathy  
Department of Chemistry, University of Lowell, Lowell, MA 01854

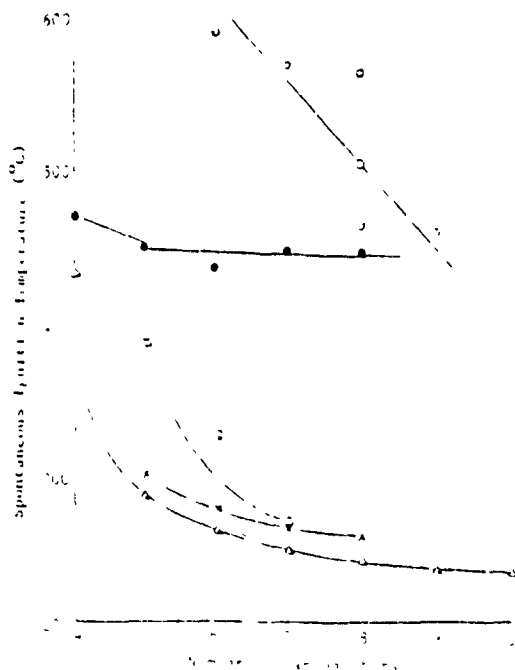
ABSTRACT

As noted in the previous paper of this series, a reversed relationship exists between molecular weight and spontaneous ignition temperature (IT), occasioned by contact with hot surfaces: up to a point, less volatile higher molecular weight fuels have lower IT's and are more easily ignited. For higher members of the alkane family this trend may reverse, resulting in minimum IT's for the C<sub>5</sub> - C<sub>9</sub> alkanes. Branched chain alkanes, arenes and olefins also have higher IT's than analogous straight chain alkanes. Important parameters in governing IT's of fuel components include: (1) the effect of molecular weight on the velocity of the fuel molecule near the hot surface; (2) the effect of rigidity of the fuel molecule on its ability to recoil from the hot surface; and (3) the effect of specific heat of the molecule with regard to ability for dissipation of heat energy within the molecule. Molecular modelling considerations will be discussed to explain anomalous trends.

As can be seen in Figures 1 and 2, there is a decrease in IT values for alkanes with increasing molecular weight, for the range of alkanes from methane (C<sub>1</sub>) through octane (C<sub>8</sub>).

Figure 1. Spontaneous Ignition  
Temperatures for  
Typical Hydrocarbons  
(References 1 and 2)

- Branched Alkanes
- ▲ Paraffins
- Aromatic Hydrocarbons
- Cycloalkanes
- x Olefins

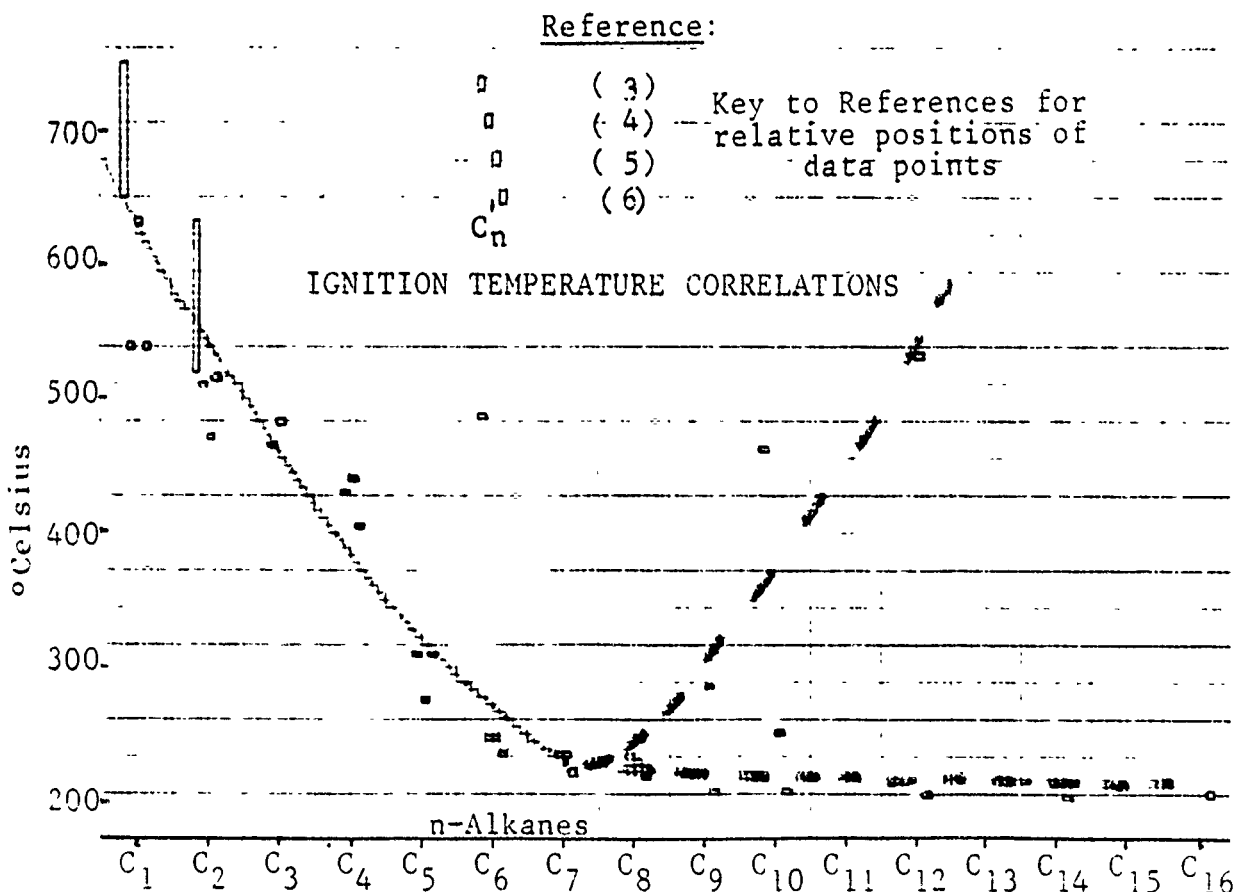


\*Principal Investigator

(The reverse of this page is blank.)

Precise data is not available for higher alkanes. As shown in Fig. 2, in the lower projected track of IT values, one possibility lies in an asymptotic sweep along a 200° isotherm for alkanes beyond C<sub>8</sub>. (Thermal cracking may occur at this temperature, if the hydrocarbons are permitted to linger at the heated surface in accordance with current ASTM procedures.<sup>7,8</sup> Thus, larger alkanes could conceivably have higher ignition temperatures; but by undergoing slow pyrolysis at 200°, some alkanes in the minimum IT region characteristic of C<sub>5</sub> - C<sub>9</sub> would form, with these igniting at this spuriously low temperature.

Figure 2. Correlations of Ignition Temperatures for n-Alkanes



Frank observed increased IT values for C<sub>14</sub> through C<sub>20</sub> alkanes, attributing this to decreasing volatilities,<sup>9</sup> and several other anomalously high IT values have been observed for decane and higher alkanes. Thus, a minimum zone of IT's may exist for C<sub>5</sub> - C<sub>9</sub> alkanes. This is shown in Figure 2 as the upper projected track for the alkanes beyond C<sub>9</sub>. Obviously, either track could actually pertain; currently available data is insufficient and good values are probably poorly available with existing equipment and technique.

Fuel component characteristics which have been identified as having possible impact on the ignition temperatures are discussed on page 3 and illustrated on page 4 of this paper.

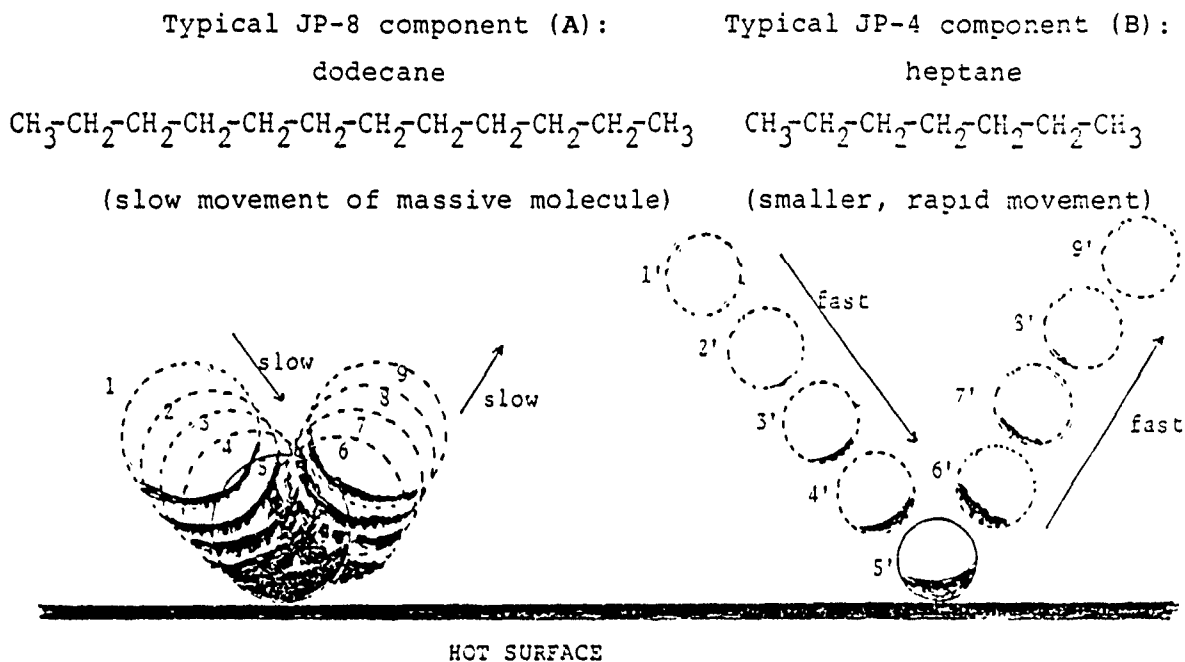
1. Molecular weight effects on speed and inertia for heavier molecules. These effects increase residence time in the vicinity of a hot surface, with increased time for energy transfer.
2. Molecular rigidity. Rigid molecules have reduced rotational degrees of freedom within the molecular structures. This would significantly decrease "floppiness" of the molecule in its impact with a hot surface, allowing the more rigid structure to rebound readily and rapidly with correspondingly reduced residence times in the vicinity of the hot surface, and considerably reduced energy transfer from the surface to the fuel molecule.
3. Specific molecular heat. For smaller molecules relative speed and relative rigidity are important. For the lower alkanes, each addition of a methylene unit imparts a significant increase in molecular weight and in internal degrees of rotational freedom. In going from ethane to propane, for example, there is a 17% decrease in speed at 500°C, whereas decane is only 5% slower than nonane at this temperature. Internal rotational degrees of freedom are even more considerably enhanced for propane, which is very flexible compared with the very rigid ethane; but decane and nonane have very little difference in "mushiness" due to this effect. Thus, decreased speed and rigidity arising from increased molecular weight are much less important for the higher alkanes.

Moreover, higher alkanes begin to enjoy the benefit of increased "molecular specific heat". When lower alkanes such as propane are energized by radiational heat, all atoms of the small molecule are fairly equally irradiated. For larger molecules, some atoms will be in the shadow of others. The hotter surface atoms can then transfer some of their increased energies to the cooler internal atoms. Thus, a higher ignition temperature will be required to attain decomposition energies for a molecule large enough to provide shadowing by some of its atoms to other neighboring atoms.

#### REFERENCES

1. Jackson, J. L. Ind. Eng. Chem. **1961**, 43, 2869.
2. Miller, R. G. Symp. #6, Major Aircraft Fires (Proc.), Fire Research Station, Boreham Wood, Herts, England, Dec. 1966, pp. 54-65.
3. Lange, N. A. "Handbook of Chemistry", 9th ed., Handbook Publishing Co., Sandusky, OH, 1956, p. 824.
4. McCracken, D. J. "Hydrocarbon Combustion and Physical Properties", BRL-1496; Ballistic Res. Lab, Aberdeen Proving Ground, MD (1970).
5. Perry, R. H. "Chemical Engineering Handbook", 3rd ed., McGraw-Hill Book Co., New York, 1950, pp. 1584-1585.
6. "Fire Hazard Properties of Flammable Liquids, Gases and Volatile Solids", National Fire Protection Association, Boston, MA, 1960.
7. "Autoignition Temperature of Liquid Chemicals", ASTM Designation E 659 - 78 (Reapproved 1984).
8. Affens, W. A.; Johnson, J. E.; Carhart, H. E. J. Chem. Eng. Data **1961**, 6, 613-619 (and references cited therein).
9. Frank, C. E.; Blackham, A. U. Ind. Eng. Chem., **1952**, 44, 862-867.

Figure 3. Molecular Characteristics Affecting Ignition Temperatures.



[(1), (2), (3) ... (8), (9) above indicate positions of molecules A and B at same time intervals, relative to hot surface area.]

Molecular velocity at temperature ( $T$ ,  $^{\circ}\text{K}$ ) is inversely proportional to the molecular weight ( $M$ ); smaller molecules have greater speed.

$$\text{Average velocity} = 14,600(T/M)^{\frac{1}{2}} \text{ cm/sec}$$

The slow moving heavy molecule A (above) is therefore near the hot surface longer than the lighter and faster B, and A has more time available to absorb energy from the hot radiating surface.

The larger molecule A has more mobile C-C bonds and therefore more rotational degrees of freedom than the smaller B. Thus, A will tend to be "mushier" with less elastic recoil on impact with the hot surface than the smaller, more rigid B which can bounce away more readily. Again, molecule A will have more time to energize than B.

To offset this, and although the larger molecule has greater surface area enabling it to absorb more heat than the smaller molecule, the large molecule's volume is increased even more than is the surface area (by comparison with the smaller molecule). Absorbed heat is then dissipated more through the large molecule, which accordingly is cooler than the small molecule. This effect is more pronounced with increased molecular weights (and volumes). In this case A (dodecane) needs more heat (with a higher ignition temperature) to energize it to its decomposition point than does B (heptane). For smaller molecules (e.g., comparing hexane [ $\text{C}_6$ ] and propane [ $\text{C}_3$ ]), this offsetting factor of increased molecular specific heats is not as important as the molecular speed and rigidity effects: in such cases the heavier molecule has the lower ignition temperature.

## ACKNOWLEDGMENTS

This research was sponsored and supported by the US Air Force Systems Command and the Air Force Office of Scientific Research. Support was also extended by the College of Pure and Applied Science of the University of Lowell (Massachusetts). Grateful acknowledgement is extended to Universal Energy Systems, Inc. for administration of work under the aegis of the Air Force Summer Faculty Research Program. We are also grateful for valuable information, advice and suggestions provided by Mr. James Sartain and Mr. Andrew Poulis of the Air Force Engineering and Services Center at Tyndall Air Force Base; Dr. Robert Levine, Dr. Kermit Smyth and Dr. J. Houston Miller of the National Institute of Standards and Technology; Mr. William Westfield, Mr. Eugene Klueg and Dr. George Geyer of the Federal Aviation Administration's Engine/Fuel Safety Branch and Services Center at Atlantic City, NJ; Dr. Joseph Leonard and Dr. Homer Carhart of the Naval Research Laboratory; Mr. Michael Beltran of Beltran, Inc.; and Achal Thakkar and Robert Zsofka, and Professors Albert Kowalak and James Pierce of the University of Lowell.

## REFERENCES

1. Jackson, J. L. Ind. Eng. Chem. 1961, 43, 2869.
2. Miller, R. G. Symp. #6, Major Aircraft Fires (Proc.), Fire Research Station, Boreham Wood, Herts, England, Dec. 1966, pp. 54-65.
3. Lange, N. A. "Handbook of Chemistry", 9th ed., Handbook Publishing Co., Sandusky, OH, 1956, p. 824.
4. McCracken, D.J. "Hydrocarbon Combustion and Physical Properties", BRL-1496; Ballistic Res. Lab, Aberdeen Proving Ground, MD (1970).
5. Perry, R. H. "Chemical Engineering Handbook", 3rd ed., McGraw-Hill Book Co., New York, 1950, pp. 1584-1585.
6. "Fire Hazard Properties of Flammable Liquids, Gases and Volatile Solids", National Fire Protection Association, Boston, MA, 1960.
7. "Autoignition Temperature of Liquid Chemicals", ASTM Designation E 659 - 78 (Reapproved 1984).
8. Affens, W. A.; Johnson, J. E.; Carhart, H. E. J. Chem. Eng. Data 1961, 6, 613-619 (and references cited therein).
9. Frank, C. E.; Blackham, A. U. Ind. Eng. Chem., 1952, 44, 862-867.
10. Brooks, B.; Bruccoleri, R.; Olafson, B.; States, D.; Swaminathan, S.; and Karplus, M. J. Comp. Chem. 1983, 4, 187.
11. Allen, M.; Tildesley, D. "Computer Simulation of Liquids", Oxford Science Publications (Clarendon Press, Oxford), 1987.

**THE ESTIMATION OF STATURE FROM FRAGMENTS OF THE FEMUR:  
A Revision of the Steele Method**

**Final Report submitted to  
Universal Energy Systems  
Sept. 23, 1988**

**by**

**William M. Bass**

**Richard L. Jantz**

**Tal Simmons**

**Department of Anthropology  
University of Tennessee  
Knoxville, TN 37996-0720**

## INTRODUCTION

The estimation of stature from various skeletal elements has been an area of critical interest to physical anthropologists for many years. Past studies concerning stature estimation have included those by Manouvrier (1892), Stevenson (1929), Allbrook (1961), Genoves (1967), Lundy (1983) and Lundy and Feldesman (1987). These papers presented data and statistical formulae for the estimation of stature for geographic and racial groups as diverse as the Chinese and the South African Black. The formulae most often employed in the United States are those provided by Trotter and Gleser (1951a; 1951b; 1952; 1958) and Trotter (1970). All of these studies have shown a high correlation between the length of any whole, long limb bone and stature, with the highest single correlation being the femur.

Forensic anthropologists are often confronted with fragmentary remains while the estimation of stature by conventional formulae is dependent upon whole limb bones. The estimation of living stature from long bones is based upon the principle that the various long limb bones correlate positively with stature. Since this is true, the parts of each individual long bone should also be related to stature even though they may not correlate as highly as the length of the whole bone. Stature estimation from fragmentary long bones has been attempted by Muller (1935), Steele and McKern (1969), and Steele (1970). In practice, these methods are difficult to apply because of difficulty in identifying the exact location of necessary anatomical landmarks. Steele (1970:87) himself recognized this problem when he stated:

Another landmark not used in the present study, but used previously by the author and Dr. McKern, involves the humerus alone. The landmark in question is the point of greatest narrowing at the middle of the diaphysis. Although this narrowing can be related to a point, posterolaterally in the radial groove where the lateral supracondylar ridge becomes indistinct (on a level with the distal termination of the surface for m. deltoideus), in practice the point proved impossible to locate with sufficient constancy to give useful results.

Most practicing physical anthropologists have also experienced difficulties in locating many of the other anatomical landmarks used to predict stature from fragmentary long bones. Indeed many do not use either the Steele and McKern (1969) or the Steele (1970) formulae, and hence do not attempt to estimate stature when no whole long limb bones are present because of this very difficulty. However, since skeletal remains are often fragmentary, it would be useful to devise a more reliable technique for stature estimation from smaller segments of long bones.

#### OBJECTIVE

The objective of this study is to assess the feasibility of stature estimation using small fragments of the femur. As described above, the Steele and McKern (1969) and Steele (1970) methods are plagued by the difficulty of identifying the anatomical landmarks which define the various segments of the limb bones from which estimations are calculated. The present approach seeks to avoid this pitfall by using standard, clearly defined measurements taken on the distal, proximal, and midshaft regions of the bone. Many of these measurements are already familiar to physical anthropologists, who regularly use them for

comparative population studies or in some cases, the estimation of gender. It is also hoped that, by presenting data and providing equations for the estimation of stature from small segments of all areas of the bone, any recovered section might be used to estimate stature. It will normally be the case that smaller segments of bone will exhibit weaker relationships to stature than larger segments. Because the emphasis of this study is on smaller segments, the equations generated are therefore expected to offer less accuracy for both maximum femur length and stature. However, when small segments alone are available, this approach will offer the best opportunity for estimation of stature. The relationship of these dimensions to maximum femur length and stature has never been systematically examined.

The femur was selected as the initial skeletal element to be analysed because in addition to its high correlation with stature, it is (along with the feet) one of the bones most frequently recovered from Air Force crash sites. It is a large, durable bone protected by both large amounts of soft tissue and the seat and harness mechanisms of the aircraft.

#### METHODOLOGY

The sample measured was obtained from the Terry anatomical collection housed at the Smithsonian Institution's National Museum of Natural History in Washington, D. C.. The skeletons in the Terry collection are from cadavers dissected at the Washington University School of Medicine, St. Louis, Mo. Accurate data for age, sex, race, and cadaver stature are

available. A sample of approximately 200 males and 200 females from Blacks and Whites, yielding a total sample of 800 individuals was obtained. To be included in the sample an individual must have race and sex recorded on the morgue record. Only femora exhibiting no gross pathological changes of the distal, proximal, or midshaft regions were included in the study. Left femora were measured whenever possible, though right femora were substituted if breakage or pathological conditions precluded the use of the left. Preference for inclusion in the sample was given to individuals for whom age and cadaver stature were also recorded. With few exceptions, photographs of the cadavers were examined in order to be certain that the stature was recorded when the body was placed vertically with the feet in natural plantar position.

The measurements employed are defined in Table 1 and illustrated in Figure 1. All seven measurements are standard and defined in Martin (1957). The definition of number 7 was modified from a midshaft diameter to a minimum transverse shaft diameter in order to avoid the necessity of locating a midpoint on a fragment. All the measurements can be recorded with ease. Maximum femur length was measured on an osteometric board; all other measurements were obtained with sliding calipers. All measurements were taken by Tal Simmons, a Ph.D. student in physical anthropology at the University of Tennessee.

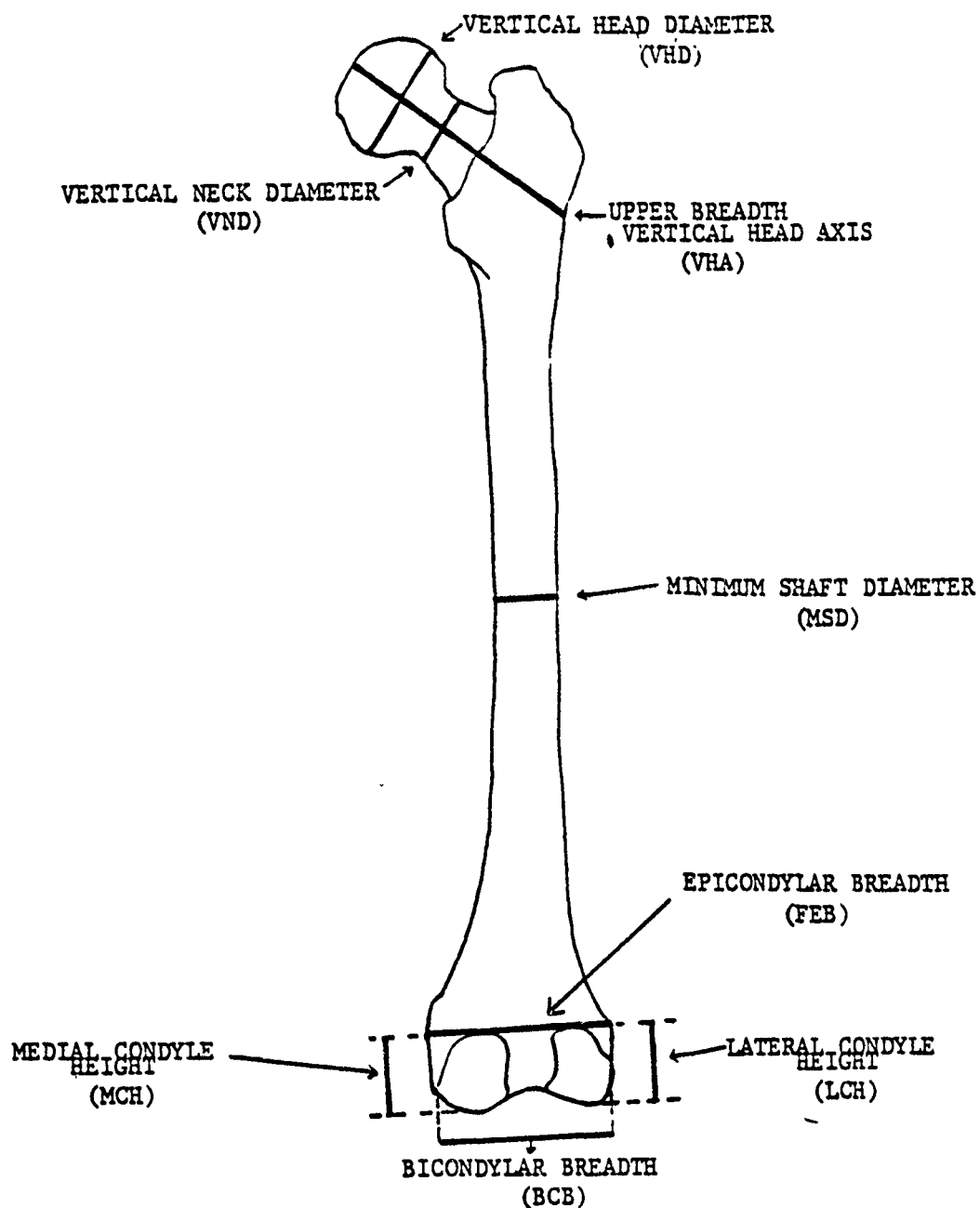


FIG.1 STANDARD MEASUREMENTS OF THE FEMUR USED IN THE REGRESSION EQUATIONS AGAINST MAXIMUM FEMUR LENGTH (FML) .

Table 1 : Measurements (abbreviations in parentheses) used in estimating stature from femoral fragments.

<u>Martin No.</u>	<u>Measurement</u>
1	Maximum Femoral Length (FML)
18	Vertical diameter of the femoral head (VHD)
15	Vertical diameter of the femoral neck (VND)
13	Proximal Breadth of the Femur (VHA)
7	Transverse diameter of midshaft (minimum) (WSD)
-	Bicondylar Breadth (BCB)
21	Epicondylar Breadth (FDL)
25	Lateral Condyle Height (LCH)
26	Medial Condyle Height (MCH)

Data were entered on an IBM compatible PC using dBase III-plus. Analysis of the data was carried out using the SAS package on the University of Tennessee's Vax cluster. Equations for the prediction of stature were generated in two ways. First, stature estimation was performed by the usual method of regressing stature onto bone measurements. Second, because the Terry collection records do not always list the cadaver stature of the individual, maximum femur length was also regressed onto bone measurements. By determining the maximum femur length of an individual from a fragment, the stature may then be estimated also, though the standard error of the estimate will be increased.

## RESULTS

### Age, Stature, and Maximum Femoral Length

Stature, femur length and age of the present sample is compared to other samples which have been used in stature estimation in Table 2. The means and standard deviations for age, stature, and maximum femur length are quite close to those presented by Trotter and Gleser (1952) for the Terry Collection.

They differ, however, from those presented by Steele (1970) presumably because of that author's small sample size and his elimination of older individuals (those over age 70) from his study. Jantz and Moore-Jansen (1988) have shown that the Terry Collection differs from the contemporary White and Black population, present day populations exhibiting significantly longer femora. Table 2 also shows that Terry Collection heights are considerably below Trotter and Gleser's (1958) Korean war dead and Modern Forensic cases. Consequently, regression formulae developed from the Terry collection and applied to modern people may underestimate stature.

#### Summary of Fragment Measurements

Table 3 presents the means and standard deviations for each of the segments measured. Correlations for these measurements with femur length and cadaver stature are given in Table 4. The correlations show the strength of association between the segment measurements, stature and femur length. At the outset we had expected that VHA (proximal femur breadth) would be the best predictor and that is borne out by the correlations in males, but in females several other measurements are more highly correlated. In general, correlations rarely exceed 0.65.

#### Comparison with Steele's Results

Our goal at the outset was to attempt stature estimation from fragments which would equal or exceed Steele's in accuracy but would use standard measurements. We can examine this question by comparing our segment correlation with those from Steele that are more or less comparable. Steele's segment 1 is measured from

Table 2. Means and standard deviations of age(yrs), stature\*(cm.) and femur length(cm.) of various samples compared to present sample.

White Males

Terry(1)	200	58.73	13.88	167.75	7.59	45.64	2.68
Terry(2)	255	61.66	12.55	167.89	7.34	45.66	2.45
Terry(3)	61	52.97	4.98	168.44	4.98	46.24	3.06
War dead(4)	545	23.14	4.31	173.90	6.63	47.29	2.36
War dead(5)	1265	--	--	174.39	6.55	47.17	2.30
Modern(6)	113	37.26	17.08	176.07	8.06	47.18	2.54

Black Males

Terry(1)	203	47.33	16.77	170.18	7.97	47.47	2.93
Terry(2)	360	49.46	15.51	170.23	7.81	47.42	2.97
Terry(3)	42	43.25	13.21	172.02	7.84	47.92	3.28
War dead(4)	54	25.07	4.98	172.11	6.14	48.34	2.26
War dead(5)	191	--	--	173.86	6.65	48.41	2.48
Modern(6)	29	37.45	21.52	179.15	6.68	48.24	2.81

White Females

Terry(1)	201	63.19	15.59	157.07	7.76	42.71	2.36
Terry(2)	63	63.93	16.07	158.18	7.51	42.96	2.53
Terry(3)	52	63.35	17.02	157.62	7.96	42.69	2.71
Modern(6)	89	37.14	21.52	165.54	5.94	43.72	2.02

Black Females

Terry(1)	199	48.11	18.44	159.04	6.63	43.99	2.41
Terry(2)	177	47.21	17.65	158.39	6.53	43.71	2.39
Terry(3)	57	39.58	15.52	159.88	6.22	43.96	2.30
Modern(6)	24	34.37	19.73	165.00	10.80	45.52	3.23

\*Terry collection stature=cadaver stature-2.5cm. All others are stature obtained during life.

1. Present study
2. Trotter and Gleser (1952)
3. Steele (1970)
4. Trotter and Gleser (1952)
5. Trotter and Gleser (1958)
6. Jantz and Moore-Jansen (1988)

the proximal point on the head of the femur to the midpoint of the greater trochanter. It is comparable to our VHA (proximal femur breadth) in the size and location of the fragment.

Table 3. Means and standard deviations (mm.) of the Terry collection segments, by race and sex.

Variable	W Males		B Males		W Females		B Females	
	X	SD	X	SD	X	SD	X	SD
VHA	99.10	5.87	98.99	5.77	88.24	5.18	88.98	5.24
VHD	48.27	3.17	47.65	2.69	42.54	2.50	41.95	2.35
VND	33.09	3.05	31.16	2.60	29.27	2.62	27.17	2.48
WSD	28.26	2.16	28.05	2.21	25.10	2.13	25.18	2.03
LCH	41.35	2.91	42.33	3.00	36.30	2.53	37.05	2.34
MCH	40.92	3.01	41.94	3.22	37.22	2.90	37.75	2.70
BCB	77.81	4.30	77.71	4.57	68.44	3.75	67.74	3.94
FDL	83.42	4.47	83.00	4.22	74.57	3.54	73.94	3.95

Table 5 shows the correlations of our VHA (proximal femur breadth) and Steele's segment 1 with stature and maximum femur length. For stature, our correlations exceed Steele's in three of the four groups; only in White males is it slightly lower. For femur length, Steele's correlations are higher in three of the four groups. All 16 of the correlation coefficients are similar, indicating approximately equal predictive efficiency.

Steele's segment 4 is comparable to our MCH (medial condyle height). His correlations with height and femur length exceed ours in four cases while ours exceed his in four cases. However, our LCH (lateral condyle height) yields consistently higher correlations than MCH in our data (see table 4). Comparing LCH to Steele's segment 4 shows our correlations to exceed his in 7 of 8 comparisons. It is evident that lateral condyle height has the higher correlation with stature and femur length and is to be

preferred as the predictor variable when both condyles are present.

Table 4. Correlations of femur segments with maximum femur length and stature by race and sex.

Var.	W Males		B Males		W Females		B Females	
	Ht	FML	Ht	FML	Ht	FML	HT	FML
VHA	0.587	0.606	0.564	0.592	0.526	0.632	0.432	0.513
VHD	0.462	0.526	0.499	0.454	0.406	0.596	0.540	0.585
VND	0.312	0.384	0.393	0.315	0.409	0.409	0.461	0.422
WSD	0.386	0.281	0.251	0.276	0.428	0.295	0.367	0.277
LCH	0.557	0.571	0.503	0.452	0.677	0.665	0.571	0.585
MCH	0.417	0.459	0.391	0.404	0.595	0.518	0.470	0.403
BCB	0.512	0.541	0.509	0.440	0.294	0.445	0.220	0.345
FDL	0.493	0.521	0.560	0.465	0.428	0.537	0.329	0.415

Table 5. Correlations of upper femur breadth (VHA) and Steele's segment 1 with height and femur length

	Steele's Segment 1		VHA (Proximal Breadth	
	Height	Femur lgth	Height	Femur lgth
White males	0.602	0.651	0.588	0.607
White females	0.498	0.623	0.526	0.632
Black males	0.472	0.606	0.564	0.593
Black females	0.431	0.543	0.432	0.514

### Formulae for the Estimation of Stature and Maximum Femur Length

In this section we present the statistical constants for estimating height and femur length from various fragments. We will present only those equations which offer the best predictive capability and seem useful in forensic work.

Table 6 presents the slopes, intercepts and standard errors of estimates for each race/sex group for stature and femur length using the variable VHA (proximal femur breadth) VHD (femur head diameter) LCH (lateral condyle height) MCH (medial condyle height) as predictor variables. While not presented as an equation, these constants are used in the same manner as traditional regression equations. Thus to estimate stature for a white male, using VHA one takes the slope times VHA and adds the intercept. The standard error of estimate then provides an indication of the range within which the true stature is likely to fall. For example, suppose femur fragments from a White male yield the following measurements: VHA=95mm.; LCH=40mm.; VHD=45mm. These measurements would be used to estimate stature as follows:

$$\text{Stature} = 0.78 \times 95\text{mm.} + 89.64 = 163.74\text{cm.} \pm 6.10\text{cm.}$$

$$\text{Stature} = 1.47 \times 40\text{mm.} + 107.09 = 165.89\text{cm.} \pm 6.24\text{cm.}$$

$$\text{Stature} = 1.11 \times 45\text{mm.} + 113.89 = 163.84\text{cm.} \pm 6.77\text{cm.}$$

The average ages for all groups in this study are similar to those presented by Trotter and Gleser (1952) in their work with the Terry Collection. In addition to concern regarding the secular trend in stature increase discussed above, Trotter and Gleser (1951a) addressed the issue of the effects of aging on stature. The correction of stature for age related effects is

Table 6. Regression constants for estimating stature\* and femur length\*\* from VHA, LCH and VHD. These are the three best predictor variables. See text for instructions.

	Height			Femur length		
	slope	intercept	S.E.	slope	intercept	S.E.
-----						
Predictor variable: VHA (proximal femur breadth)						
-----						
White males	0.78	89.64	6.10	0.29	14.81	2.10
White females	0.73	91.54	6.67	0.21	21.50	2.10
Black males	0.79	91.70	6.60	0.32	13.64	2.30
Black females	0.59	107.10	6.00	0.25	21.90	2.04
-----						
Predictor variable: LCH (lateral condyle height)						
-----						
White males	1.47	107.09	6.24	0.54	20.86	2.18
Black males	1.34	113.23	6.91	0.46	25.44	2.59
White females	1.94	86.10	5.77	0.42	24.96	2.09
Black females	1.59	100.07	5.47	0.56	20.80	2.03
-----						
Predictor variable: VHD (femur head diameter)						
-----						
White males	1.11	113.89	6.77	0.43	23.57	2.32
Black Males	1.51	97.82	6.92	0.54	19.45	2.56
White females	1.35	99.22	7.16	0.47	20.22	2.06
Black females	1.59	92.43	5.59	0.58	17.12	1.99
-----						
* Stature= predictor variable x slope + Intercept + S.E.						
** Femur length= predictor variable x slope + Intercept + S.E.						

given by Trotter and Gleser (1952); they suggest that this formula be applied to all individuals over the age of 35 for whom stature is to be estimated.

## DISCUSSION

The method of femur length and stature estimation presented here has several advantages over previous attempts. First, the anatomical landmarks by which these measurements are defined are standard, well defined, and easy to locate. Many of them are already in standard usage for the estimation of sex or are standard measurements taken for comparative purposes on post cranial material. Second, the standard errors of estimates were equal to or lower than those presented by Steele (1970) for his smaller segments. And third, the sample size used in this study is approximately four times that used by Steele (1970), and thus the regression equations are more accurately estimated.

Perhaps the most significant comparison of the technique presented in this study with that of Steele (1970) concerns the standard errors of estimate. For comparable segments, such as those involving the proximal end (VHA) or the distal end (LCH) our standard errors of estimate are uniformly lower than Steele's. That in turn indicates that our stature estimates are more accurate. To some extent this results from higher standard deviations for femur length and height in Steele's sample. This is apparently a consequence of Steele's smaller sample size.

Our results have demonstrated the feasibility of estimating stature and femur length from small fragments using standard measurements. It is becoming increasingly clear that the Terry collection skeletons were drawn from a population considerably smaller than contemporary Americans. Therefore, our results should be viewed more as indicative of the feasibility of the technique than as providing formula applicable for forensic work

on contemporary people.

#### CONCLUSIONS

The technique for the estimation of stature from fragments of the femur presented in this report represents an improvement over methods which are currently in use. It is desirable to develop formulae using skeletons from contemporary populations, if possible. It is also possible that certain other bones likely to survive air crashes because of protection, such as the bones of the foot, calcaneous and metacarpals in particular, would lend themselves to stature estimation. Future research should be directed along these lines.

#### REFERENCES CITED

- Allbrook, D. (1961). The estimation of stature in British and East African Males. *Journal of Forensic Medicine* 8:15-28.
- Genoves, S. (1967). Proportionality of the long limb bones and their relation to stature among Mesoamericans. *American Journal of Physical Anthropology* 26:67-78.
- Jantz, R. L. and Moore-Jansen, P. H. (1988). A Data Base for Forensic Anthropology. Department of Anthropology Report of Investigations No. 47. Knoxville: The University of Tennessee.
- Lundy, J. (1983). Regression equations for estimating living stature from long limb bones in the South African Negro. *South African Journal of Science* 79:337-338.
- Lundy, J. and Feldesman, M. (1987). Revised equations for estimating living stature from the long bones of the South African Negro. *South African Journal of Science* 83:54-55.
- Manouvrier, L. (1892). Determination de la taille d'apres les grands os les membres. *Revue Mensuelle de l'Ecole d'Anthropologie* 2:227-233.
- Martin, R. (1957). *Lehrbuch der Anthropologie*. Revised Third Edition, Vol. 4. Karl Saller, Editor. Stuttgart: Gustav Fischer Verlag.
- Moore-Jansen, P. H. and Jantz, R. L. (1986). A computerized skeletal data bank for Forensic Anthropology. Knoxville: The University of Tennessee.
- Muller, G. (1935). Zur Bestimmung der Lange beschadigter Extremitatenknochten. *Anthropologischer Anzeiger* 12:70-72.
- Steele, G. (1970). Estimation of stature from fragments of long limb bones. In (T. D. Stewart, Ed.) *Personal Identification*

- in Mass Disasters, pp. 85-97. Washington, D. C.:  
Smithsonian Institution Press.
- Steele, G. and McKern, T. (1969). A method for assessment of  
maximum long bone length and living stature from  
fragmentary long bones. American Journal of Physical  
Anthropology 31:215-227.
- Stevenson, P. (1929). On racial differences in stature long bone  
regression formulae with special reference to stature  
reconstruction formula for the Chinese. Biometrika 21:303-321.
- Trotter, M. (1970). Estimation of stature from intact long limb  
bones. In (Stewart, T. D. Ed.) Personal Identification in  
Mass Disasters, pp. 71-83. Washington, D. C.: Smithsonian  
Institution Press.
- Trotter, M. and Gleser G. (1951a). The effect of aging on  
stature. American Journal of Physical Anthropology 9:311-324.
- Trotter, M. and Gleser, G. (1951b). Trends in stature of American  
Whites and Negroes born between 1840 and 1924. American  
Journal of Physical Anthropology 9:427-440.
- Trotter, M. and Gleser, G. (1952). Estimation of stature from  
long bones of American Whites and Negroes. American  
Journal of Physical Anthropology 10:463-514.
- Trotter, M. and Gleser, G. (1958). A re-evaluation of estimation  
of stature based on measurements of stature taken during life  
and of long bones after death. American Journal of Physical  
Anthropology 16:79-123.

FINAL REPORT

1987-88 Mini-Grant Program

Sponsored by the  
Air Force Office of Scientific Research

Conducted by  
Universal Energy Systems

"EFFECTS OF WATER SOLUBILITY AND FUNCTIONAL GROUP CONTENT ON THE  
INTERACTIONS OF ORGANIC SOLUTES WITH SOIL ORGANIC MATTER"

Prepared by: William T. Cooper, Ph.D.  
Academic Rank: Associate Professor  
Department: Chemistry  
University: Florida State University  
Research Location: Dittmer Laboratory of Chemistry  
Florida State University  
Tallahassee, Florida  
Date: May 19, 1988  
Contract No: F49620-85-C-0013/SB5851-0360  
Purchase Order No: S-760-6MG-081

(The reverse of this page is blank.)

**PART I: CHARACTERIZATION OF POLAR SOLUTE - SOIL ORGANIC MATTER  
INTERACTIONS BY HIGH PERFORMANCE LIQUID CHROMATOGRAPHY**

C.P. Antworth, R.R. Yates and W.T. Cooper\*  
Department of Chemistry  
and  
Center for Biomedical & Toxicological Research  
Florida State University  
Tallahassee, Florida 32306-3006

Presented in the "Symposium on Organic Geochemistry: Techniques  
and Applications"  
Division of Geochemistry  
194th National Meeting of the American Chemical Society  
New Orleans, LA  
September, 1987

Submitted to **ORGANIC GEOCHEMISTRY**  
December, 1987

\* Author to whom correspondence should be addressed

In order to more fully understand the role of soil and sedimentary organic matter (SOM) in the migration and fate of organic pollutants in aquatic systems, a fast and accurate liquid chromatography method has been developed for the determination of sorption isotherms. The method is a modified Frontal Analysis by Characteristic Point (FACP) technique which accounts for hydrodynamic dispersion and which uses conventional HPLC equipment coupled with commercially available chromatography software. We have used this technique to generate sorption isotherms for various fractions of the total SOM. Isotherms are then fit to the Freundlich equation, from which water - organic carbon distribution coefficients ( $K_{oc}$  values) can be calculated. In this presentation we report on our studies of the roles played by various fractions of soil organic matter (lipids, humic/fulvic acids and humin) in the overall sorption process. By using solute probes which interact with solid phases in well-defined ways, we have been able to determine the contributions of acidic, basic and dipolar sites in the various SOM fractions, as well as the contribution of nonspecific hydrophobic partitioning, in the sorption of nonionic, polar organic solutes. It appears that these solutes interact with soil organic matter primarily through specific interactions with active sites in the humin fraction of the organic matrix, although there is some hydrophobic partitioning into the lipid fraction as well.

## INTRODUCTION

It is now generally recognized that the sorption of sparingly soluble organic solutes onto soils and aquifer media is dominated by the natural organic carbon fraction of these materials. Lambert (1965,1968,1978) and Lambert et al. (1965) first demonstrated this principle with studies of neutral organic pesticide uptake onto a variety of soils. Lambert and co-workers (1965) also suggested that soil organic matter might act as an organic solvent in a solvent extraction process, and thus the movement of neutral organics in soils could be considered analogous to a chromatographic process, with dissolved solutes partitioning between a polar aqueous mobile phase and a non-polar stationary phase of soil organic matter coating an inorganic matrix. The partitioning of a neutral organic solute in such a system should then be correlated with the solute's partitioning between water and an immiscible organic solvent, and Briggs (1973) and Chiou et al. (1979) developed empirical equations which related sorption in soil systems to a solute's octanol-water partition coefficient.

The importance of sorption, including adsorption and/or partitioning on/into soil organic matter. in the transport of nonionic organic solutes can be addressed by first considering the relative residence time, or retardation factor,  $(t_r)_i$ , of a solute as it travels from source to observation point in an aquifer. This retardation factor is defined by equation 1:

$$(t_r)_i = \frac{t'_i}{t'_w} \quad (1)$$

where  $t'_i$  and  $t'_w$  represent the average travel times of solute  $i$  and water molecules, respectively. The effect of sorption on this factor can be quantitatively estimated through equation 2:

$$(t_r)_i = 1 + (K_d)_i \frac{\rho_{aq}}{\theta_{aq}} \quad (2)$$

where  $(K_d)_i$  is the distribution coefficient for solute  $i$  between water and the aquifer media and  $\rho_{aq}$  and  $\theta_{aq}$  represent the average bulk density and effective porosity of the media, respectively.

Distribution coefficients for the sorption of nonionic solutes on complex, heterogeneous soils and aquifer materials actually represent the weighted sum of all individual contributions:

$$(K_d)_i = \sum_j f_j (K_d)_{i,j} = f_{inorg} K_{inorg} + f_{org} K_{org} \quad (3)$$

where  $f_j$  represents the fraction of phase  $j$  and  $(K_d)_{i,j}$  the distribution coefficient for solute  $i$  on that phase. However, Karickhoff et al. (1979) evaluated the sorption of many hydrophobic organic solutes on a variety of organic rich (>1% organic matter) natural sediments and found that sorptive effects of the inorganic matrix were negligible. Equation 3 could therefore be written

$$(K_d)_i = f_{oc} (K_{oc})_i \quad (4)$$

where  $(K_{oc})_i$  is the distribution coefficient for the sorption of

i onto the organic fraction alone and  $f_{OC}$  is the mass percentage of this fraction in the mineral assemblage. Karickhoff et al. (1979) also evaluated the relationship between  $K_{OC}$  and a variety of solute properties and found first that, for sorption onto the fine fractions (<50  $\mu m$  particles) of the sediments, a solute tended to have a reasonably constant  $K_{OC}$ , regardless of the origin of the organic matter. These workers also observed, in agreement with previous studies, a highly significant correlation between  $K_{OC}$  and a solute's octanol/water partition coefficient,  $K_{OW}$ .

$$\log K_{OC} = a * \log(K_{OW}) + b \quad (5)$$

Sorption onto the sand fraction (particles >50  $\mu m$ ) could also be described by equation 5, but the fitting coefficients were different than those for the fine fraction.

Substituting equations 4 and 5 into equation 2 yields

$$(t_r)_i = 1 + C * f_{OC} * (K_{OW})_i * \frac{aq}{aq} + C' \quad (6)$$

The relative residence time of organic solutes in aquifers can therefore be predicted from equation 6 if accurate measurements or estimates of  $f_{OC}$ ,  $(K_{OW})_i$ ,  $aq$  and  $aq$  are available.

Numerous studies have confirmed the conclusions of Lambert and co-workers, Briggs, Chiou et al. and Karickhoff et al.

(Hamaker and Thompson, 1972; Schwartzbach and Westall, 1981; Chiou et al., 1983; Chiou et al., 1985; Karickhoff, 1984). These studies invariably involve hydrophobic organic solutes, such as halogenated hydrocarbons, and organic rich soils and sediments. For such systems it is generally accepted that interactions between solutes and soil organic matter result from hydrophobic effects (Tanford, 1980). The driving force for such 'hydrophobic interactions' is the increase in entropy associated with the removal of the structured hydration region that surrounds a solute in water. This hydrophobic model also has been shown to be valid when organic cosolvents are present, and therefore is more generally termed a 'solvophobic' model (Banerjee et al., 1980; Rao et al., 1985; Nkedi-Kizza et al., 1985).

In spite of these advances in understanding the thermodynamic driving forces that control the adsorption and/or partitioning of organic solutes between water and soils, there are still many questions which have not been answered. Even for hydrophobic solutes which should interact only through hydrophobic forces,  $(K_{oc})_i$  values have been observed to vary by as much as factors of 3 to 5 for different mineral/organic assemblages (Curtis et al., 1986). Mingelgrin et al. (1983) found literature values of  $K_{om}$  ( $K_d$  expressed on an organic matter rather than organic carbon basis) that varied by more than an order of magnitude. This is an indication that the fitting coefficients of equation 5 could be a function of the nature of the soil organic matter involved. It is well known in the field of organic geochemistry that the chemical character of organic

matter in sediments depends both on the paleoecological conditions at the time of deposition and the extent of diagenesis within the sediment (Tissot and Welte, 1984). It should not be surprising, therefore, to find that soil and sedimentary organic matter might be highly variable in its ability to interact with organic solutes. Indeed, Lambert et al. (1965) suggested this in their original work. Hartley (1960) argued that the fats-waxes-resins fraction of soil organic matter was actually responsible for the sorption of nonionic organic solutes. In probably the most definitive study to date on this subject, Garbarini and Lion (1986) showed that different components of soil organic matter had widely varying affinities for toluene and trichloroethylene (TCE), both nonionic, hydrophobic organic solutes.

As noted previously, virtually all the studies cited involved nonpolar, hydrophobic organic solutes. If soil organic matter does vary in its affinity for organic solutes, this variability would become more pronounced as the water solubility of the organic solute increases. With increasing water solubility the non-specific hydrophobic effect becomes less important in the sorption process, while specific solute-organic matter interactions correspondingly increase in importance. In such cases it would therefore be necessary to consider the specific adsorptive characteristics of soil and aquifer organic matter.

In this and the following paper we report the results of our initial studies of the sorptive properties and chemical characteristics of several fractions of soil organic matter using the 'Inverse Chromatography' technique. In this approach the

column material itself is characterized by observing the retention behavior of solutes which are chosen because they are known to interact in chemically well-defined ways. The explosive growth in more conventional chromatographic separations that has occurred over the past 15 years has overshadowed the rather unique ability of chromatographic methods to measure meaningful physiochemical parameters.

In order to ensure that the organic matter under investigation is indeed variable in both composition and adsorptive character, we have chosen to study fractions of a single organic matter sample rather than a variety of different samples. An organic rich sediment (peat) was first fractionated into standard organic geochemical classes: lipids, humic and fulvic acids, and non-extractable humin. By comparing the sorption of the chosen solutes on these various organic matter fractions with the sorption observed with the total organic matter, we have been able to define the relative importance of each of these fractions in determining the overall, specific chemical character of soil organic matter.

In this first paper we report on our studies of the interactions of polar organic solutes with soil organic matter fractions using a dispersion corrected High Performance Liquid Chromatography (HPLC)/ Frontal Analysis by Characteristic Point (FACP) technique. We will also present the results of structural and compositional studies carried out primarily by solid state  $^{13}\text{C}$  NMR spectroscopy. This is a powerful technique for studying

insoluble organic material, but a technique which has not yet found significant applications in environmental chemistry. Analyses of the solid state NMR spectra have allowed us to correlate soil organic matter structure with sorption properties.

## EXPERIMENTAL

### Substrate Preparation

Commercially available peat was prepared for fractionation by lyophilizing for 24 hours to obtain what will be termed the total soil organic matter (SOM) fraction. Non-bound lipid material was then removed by repeated methylene chloride-methanol (2:1) extractions, followed by vacuum filtration until a clear organic phase was achieved. The resulting lipid material was rotary-evaporated to dryness. The residue (SOM-Lipid) was split and one-half subjected to a 48 hour saponification in 1N NaOH, followed by repeated washings with 0.01N NaOH until the supernatant became clear. This procedure removed the humic and fulvic acids. The non-extractable residue was subsequently washed with methylene chloride to remove bound lipids freed during the saponification. The remaining residue is termed the Humin fraction. The entire fractionation scheme is summarized in Figure 1.

### Column Preparation

The three insoluble residue fractions were each dried by lyophilization, frozen in liquid nitrogen and ground in a mortar and pestle. The material was then dry-sieved to isolate a 38-53 micron size fraction. To ensure reasonable chromatography retention times an appropriate amount of organic matter was weighed and mechanically mixed with 37-44 micron pellicular

silica gel to yield a 5% w/w organic matter mixture. Lipid material was solublized in methylene chloride and rotary-evaporated onto the silica gel support to yield a 1% w/w coated packing material. The prepared materials were dry packed into stainless steel HPLC analytical columns (4.1 mm I.D.) fitted with 5 micron column frits. Prior to analysis each column was allowed to equilibrate for 4-6 hours under continuous flow of deionized water. After analysis packing material was removed from the columns, dried, and percent organic carbon determined using a Horiba model PIR 2000 General Purpose Infrared Gas Analyzer.

#### Materials and Reagents

Solute probes were purchased from Mallinkrodt (St. Louis, Mo.) and were of analytical reagent grade. Aniline was purified by distillation prior to use. Vydac pellicular silica gel (37-44 micron) was purchased from Alltech Associates Inc. (Deerfield, Ill.). Water used in the analysis was purified by distillation and deionized using a Millipore Milli-Q system.

#### NMR Spectroscopy

$^{13}\text{C}$  CP-MAS NMR spectra were obtained with a Bruker WP-200 SY spectrometer equipped with an IBM solids accessory operating at 50 MHz for carbon. The spectrometer was tuned with t-butyl benzene and the chemical shifts are reported as parts per million downfield from tetramethylsilane. Lyophilized samples were spun at the magic angle at 4 KHz. Use and optimization of this instrument for studying sedimentary organic carbon has been

described previously (Cooper et al., 1985; 1986). Dipolar dephasing delay spectra were obtained using a contact time of 1 millisecond and a 50 microsecond delay period prior to data acquisition during which the proton decoupler is turned off. A  $180^\circ$  refocusing pulse was inserted at the mid-point of this delay period.

### HPLC System

Frontal chromatograms used in the dispersion corrected FACP technique were generated using a conventional HPLC system consisting of a Valco six-port valve outfitted with a 13 mL sample loop, a Waters Model 510 Solvent Delivery System, and a Waters Model 440 Absorbance Detector operating at 254 nm wavelength. All data was collected by and processed using a Hewlett-Packard HP-1000 Lab Automation System.

### Isotherm Generation

Isotherms were calculated from the rear diffuse boundary (i.e. the desorption branch) of a single frontal chromatographic peak. This technique is termed Elution by Characteristic Point (ECP), or Frontal Analysis by Characteristic Point (FACP). It was first introduced by Cremer (1961) and Huber and Kuelemans (1962), and has been thoroughly discussed by Conder and Young (1979). With this technique each point on the isotherm is calculated according to equation 7.

$$q(C) = \frac{1}{m} * \int_0^C (V-V_0) * dC \quad (7)$$

where  $q(C)$  is the uptake, or the concentration of adsorbed solute in equilibrium with the aqueous mobile phase concentration  $C$ ,  $m$  is the mass of organic matter present in the column,  $V$  is the volume eluted at concentration  $C$ , and  $V_0$  is the void volume contribution. Void volumes were determined from frontal chromatograms of non-retained solutes.

The FACP technique, in contrast to the more familiar Frontal Analysis (FA) method, does not take into account dispersional broadening that occurs in the column. In order to refine the FACP technique we have introduced a dispersion correction which employs the diffuse rear boundary of a non-retained solute breakthrough curve. The advantage of this approach is that the entire, dispersion corrected isotherm can be determined from the diffuse rear boundary of a single chromatogram, whereas the FA method requires a separate chromatogram for each isotherm point. Solutes were determined to be non-retained by comparing their retention volumes to those of calcium chloride, as well as column void volumes determined gravimetrically (Jacobson et al., 1984). These comparisons agreed within 3%.

## RESULTS

### Reliability of the HPLC/FACP Method

The dispersion corrected HPLC/FACP method was compared with both a frontal chromatography technique and the more conventional batch isotherm method.  $K_{OC}$  values calculated by the uncorrected FACP method differed from frontal  $K_{OC}$  values by up to 14%, but when the dispersion correction was applied the difference was reduced to within 2%. When compared to  $K_{OC}$ 's obtained by the batch isotherm method, dispersion corrected HPLC/FACP  $K_{OC}$  values differed by as little as 1% to a maximum of 11%. Comparisons of  $K_{OC}$  values generated by these various methods are summarized in Table 1, where the worst cases observed are included.

The dispersion corrected HPLC/FACP method is therefore seen to produce results which are in substantial agreement with those obtained by other, more conventional techniques. It is important to note, however, that an entire isotherm can be generated from a single chromatogram by this method. The frontal chromatography technique requires separate chromatograms for each data point on the isotherm, while the batch method involves an individual experiment for each data point (extraction, analysis, etc.). Once a column has been prepared, the HPLC/FACP method can generate an isotherm approximately every 30 minutes. The speed of this technique thus allows a wide spectrum of solute probes to be investigated in a relatively short time and with a minimum of sample required.

### Soil Constituent Trends

Isotherm data for the four isolated soil organic matter fractions were generated using four solute 'probes'. These solute probes were chosen because they are known to interact with surfaces in well defined ways (Snyder, 1974, 1978). Cresol is a 'soft' acid and interacts strongly with basic sites; aniline a 'soft' base that interacts with acidic sites; nitrobenzene interacts strongly with dipolar sites; and benzene is non-functionalized and therefore interacts via non-specific dispersion forces. While both cresol and aniline are weakly ionizable, at neutral pH their dissociation constants are such that they exist in essentially unionized form ( $pK_a[\text{cresol}] = 10.2$ ,  $pK_b[\text{aniline}] = 9.3$ ).

Sorption data for the four probes and four organic matter fractions are summarized in Figure 2, where experimental  $K_{OC}$  values are plotted vs. calculated  $K_{OW}$ 's. The fitting coefficients (a and b of equation 5) are summarized in Table 2. Interestingly, all fractions exhibit a reasonably linear relationship between  $K_{OC}$  and  $K_{OW}$ , as predicted by equation 5, although in some cases this linear relationship holds for only three of the four solutes. Surprisingly, however, it is only the lipid fraction that exhibits the positive slope observed by others when using nonpolar, hydrophobic solutes. Soil Organic Matter (SOM), SOM-Lipids, and Humin all show a negative relationship between  $K_{OC}$  and  $K_{OW}$ . We interpret these results as indicating that only

sorption onto the lipid fraction of SOM is driven by non-specific hydrophobic (or solvophobic) partitioning. Sorption onto the other fractions appears to result from specific interactions between polar sites in the organic matter and the polar solutes. Since polarity generally increases with increasing water solubility, and therefore decreases with increasing octanol-water partition coefficients, such specific interactions would then be expected to decrease as  $K_{OW}$  values increase. This, of course, is precisely the behavior we have observed with the insoluble soil organic matter fractions.

Consideration of the chemical nature of the solute probes used in these studies gives insight into the observed behavior. Aniline ( $K_{OW} = 0.98$ ), the soft base probe, exhibits the highest  $K_{OC}$  values on all three insoluble SOM fractions, indicating a relatively large population of acidic sites in these fractions. These sites are probably due to carboxyl and phenolic groups, a conclusion which is confirmed by the NMR spectra (Figure 3). Nitrobenzene ( $K_{OW} = 1.85$ ) shows the next highest  $K_{OC}$  values, indicating numerous polar but non acidic sites. Again,  $^{13}C$  NMR is helpful in interpreting the nitrobenzene data, as the spectra show substantial methoxy (carbohydrate) structure. Benzene ( $K_{OW} = 2.13$ ), the non-specific probe, shows the smallest affinity for the insoluble fractions, again suggesting that these materials are highly polar and functionalized. The soft acid probe cresol ( $K_{OW} = 1.94$ ) exhibits erratic behavior which we attribute to either strong hydrogen bonding with the aqueous solvent or exclusion from the largely acidic organic matrix.

It is interesting to note from the data of Table 2 that removal of the lipid material from the intact SOM increases the slope and intercept of the  $\log K_{OC}$  vs.  $\log K_{OW}$  plot. This indicates that binding of polar solutes, when normalized for the fraction of organic carbon comprising the sorbent, increases once the lipid fraction is removed. This increased sorptivity may be a result of the lipid components hindering access to polar sites in the remaining organic matter matrix, or a concentration of polar sites in the residue. A similar effect is observed when the humic and fulvic acids are removed, with the humin fraction exhibiting the largest sorptive capacity for polar solutes per mass of organic carbon than any of the fractions studied. We interpret this trend in increasing sorptivity with removal of extractable organic matter as an indication that the polar, active sites in soil organic matter are concentrated in the non-extractable humin fraction.

#### Relationship Between Sorptive Characteristics and Structure of Soil Organic Matter

With the development of high power decoupling, cross polarization and magic angle spinning techniques (Pines et al., 1973; Schaefer and Stejskal, 1976), it is now possible to obtain  $^{13}C$  NMR spectra of solid, insoluble materials that, in favorable situations, approach the quality of solution spectra. However, the inherent heterogeneity of soil and sedimentary organic matter results in peaks which are sufficiently broad so as to preclude any realistic interpretation of the 'fine structure' that may be

observed. For that reason solid state  $^{13}\text{C}$  NMR spectra of SOM are normally analyzed by comparing relative intensities in four spectral 'windows': 0-50 ppm (aliphatic carbon), 50-100 ppm (methoxy [carbohydrate] carbon), 100-160 ppm (olefinic and aromatic carbon), and 160-190 ppm (carboxyl and amide carbon).

NMR spectra of SOM, SOM-Lipid, and Humin are displayed in Figure 3. One of the most striking features of these spectra is the pronounced relative decrease in the aliphatic peak (ca. 30 ppm) when the lipids are removed (i.e. Figure 3(b) compared to 3(a)). This indicates that non-functionalized, hydrophobic aliphatic carbon is the chief component of the lipid fraction. This explains the sorption results for both the isolated lipid fraction (hydrophobic partitioning), as well as the differences between the SOM and SOM-Lipid fractions. While both of these fractions appear to interact with the polar solute probes through specific interactions at polar sites in the organic matter matrix, the relative number of sites in the SOM-Lipid fraction appears to be greater than the relative number of sites in the unextracted SOM. In other words, the lipid fraction appears to dilute the concentration of active polar sites in the total SOM fraction. The lipid fraction might also physically and/or chemically block some active sites from interacting with the solute probes.

Removal of humic and fulvic acids (Humin, Figure 3(c)) does little to the overall structure of the organic matter, except to reduce the relative intensity of the carboxyl peak (ca. 170-180

ppm). This is an entirely expected result, of course, since humics and fulvics are thought to be primarily polycarboxylate type materials. The important feature of the Humin spectrum is that peaks arising from the important polar carbon functional groups persist after extraction of lipids and humic/fulvic acids, and the relative intensities of these peaks are approximately the same as those observed in the spectrum of unextracted SOM (4(a)). These persistent polar carbon functional groups include methoxy (70-80 ppm), olefinic (100-120 ppm), aromatic (120-140 ppm), substituted aromatic (primarily phenolic, 140-160 ppm), and to a lesser extent carboxyl/amide (170-190 ppm). Also of interest in the Humin spectrum is the intense aliphatic peak at ca. 40 ppm, which is slightly downfield from the aliphatic peaks in the other two spectra. We attribute this peak to  $-CH_2-$  groups adjacent to methoxy carbon, suggesting that a large percentage of aliphatic carbon in the Humin fraction is tied up in polar carbohydrate material, thus reducing the hydrophobic character of this aliphatic carbon. Interpretation of the NMR spectra thus explains nicely the increased polar sorptivity of the Humin fraction relative to SOM and SOM-Lipid.

Figure 3 also includes the 50 usec dipolar dephased spectra of each SOM fraction. Dipolar dephasing (DD) exploits the time dependence of magnetic relaxation to further enhance spectral resolution, and this technique represents what has been termed the 'second generation' of solid state NMR technology (Maciel, 1984). DD-CP-MAS  $^{13}C$  NMR is finding utilization in a variety of studies of organic matter in soils (Wilson et al., 1983), resins

(Wilson et al., 1984), anoxic marine sediments (Cooper et al., 1985; 1986), and peats (Orem and Hatcher, 1987).

To a first approximation, relaxation of  $^{13}\text{C}$  nuclei in the dipolar dephasing experiment is directly related to the number of bonded protons. Thus, intensities arising from  $-\text{CH}_2-$  groups decay faster than those from  $-\text{CH}-$  groups, which will themselves decay faster than quaternary aliphatic carbon. Similarly, unsubstituted aromatic carbon nuclei decay faster than substituted aromatic carbon. The exception to this general trend are  $-\text{CH}_3$  groups, which have long relaxation times due to their rotational mobility. Our previous work (Cooper et al., 1985; 1986) and that of others indicate that spectra obtained with a 50 usec delay show resonances arising only from non-protonated  $^{13}\text{C}$  nuclei, as well as from  $-\text{CH}_3$  groups.

Comparisons of the 50 usec DD spectra of the various SOM fractions support previous conclusions regarding the sorptivity and structure of these materials. Removal of the lipids from the SOM has little effect on the DD spectra (Figure 3(b) compared to Figure 3(a)). Distinct resonances in the DD spectrum of humin (Figure 3(c) are for the most part obscured due to the low signal to noise ratio that results from the lower carbon content of this fraction. However, the broad peak between 100 and 150 ppm, and the carboxyl peak at 175 ppm, indicate substantial non-protonated, functionalized olefinic, aromatic and carboxyl/amide carbon in the humin. The dipolar dephasing NMR experiment thus supports the conclusion that active, polar sorption sites in SOM are located in the non-extractable humin fraction.

## CONCLUSIONS

We have shown that polar, nonionic organic solutes interact with soil organic matter primarily through specific interactions with active sites in the humin fraction of the organic matrix, and not as a result of the hydrophobic forces that are responsible for the sorption of nonpolar organic solutes. It is only sorption onto the lipid component of soil organic matter that appears to be a true hydrophobic phenomenon. Our results therefore substantiate the arguments of Hartley (1960), who described the fats-waxes-resins fraction of soils (i.e. soil lipids) as a solvent for organic pesticides. Our results are also in substantial agreement with those of Garbarini and Lion (1986), who observed wide variations in  $K_{OC}$  values for nonpolar, hydrophobic solutes with different soil organic matter fractions. Interestingly, Garbarini and Lion also observed the highest  $K_{OC}$  values with nonextractable humin.

We believe that these results and the results of others cited have important implications for the modeling of organic solute migration in ground water. For example, with regard to hydrophobic solutes, it may be necessary to recast equation 6 in terms of the weight fraction of lipids in the soil matrix, not the total organic matter fraction. On a broader scale, however, it is probably unreasonable to expect a single empirical parameter (e.g.  $K_{OC}$ ) to adequately predict sorption in soils, sediments and aquifers, given the variations in organic matter composition which are to be expected, as well as our data and

those of others which indicate that the various organic matter fractions differ substantially in their sorptive characteristics. Qualitative interpretation of the conventional and dipolar dephased  $^{13}\text{C}$  NMR spectra indicate that polar sorption sites in the humin fraction arise from aromatic, carboxyl/amide and carbohydrate carbon nuclei, many of which are non-protonated. These qualitative observations are in agreement with the statistical analyses of Garbarini and Lion (1986), who concluded that elemental C,H and O data are necessary parameters for accurately describing solute-soil organic matter interactions.

We also believe that much more work is necessary before accurate, a priori estimates of polar solute sorption can be made. Current efforts underway in our laboratory are directed toward the development of a more general model of sorption of polar solutes based on Snyder's concept of liquid chromatographic selectivity (1974,1978).

## ACKNOWLEDGMENTS

This work was supported by the Air Force Office of Scientific Research through Faculty (Cooper) and Graduate Student (Antworth) Summer Fellowships, as well as by a follow-up Mini Grant that is a part of the Summer Research Program. Much of the work reported here was performed at the Environics Laboratory, Engineering and Services Center, Tyndall Air Force Base, FL. The authors would like to acknowledge the assistance of Dr. Thomas Stauffer of that lab, as well as the helpful discussions with Dr. William MacIntyre of the Virginia Institute of Marine Sciences.

## References

- Banerjee S., Yalkowsky S. H. and Valvani S. C. (1980) Water solubility and octanol/water partition coefficients of organics. Limitations of the solubility-partition coefficient correlation. Env. Sci. Technol. 14, 1227-1229.
- Briggs G. G. (1973) A simple relationship between soil sorption of organic chemicals and their octanol/water partition coefficient. Proc. 7th Bri. Insecticide Fungicide Conf. 11, 475-478.
- Chiou C. T. (1979) A physical concept of soil-water equilibria for nonionic organic compounds. Science 206, 831-832.
- Chiou C. T., Porter P. E. and Schmedding D. W. (1983) Partition equilibria of nonionic Organic compounds between soil organic matter and water. Env. Sci. Technol. 17, 227-231.
- Chiou C. T., Shoup T. D. and Porter P. E. (1985) Mechanistic roles of soil humus and minerals in the sorption of nonionic organic compounds from aqueous and organic solutions. Org. Geochem. 8, 9-14.
- Conder J. R. and Young C. L. (1979) Physicochemical Measurements By Gas Chromatography, 632 pp. J. Wiley and Sons.
- Cooper W. T., Heiman A. S. and Yates R. R. (1985) Early diagenesis of organic carbon in sediments from the Peruvian Upwelling Zone. In Organic Marine Geochemistry (edited by M. Sohn) pp. 158-172. ACS Symp. Series #305.
- Cooper W. T., Heiman A. S. and Yates R. R. (1986) Spectroscopic and chromatographic studies of organic carbon in recent marine sediments from the Peruvian Upwelling Zone. Org. Geochem. 10, 725-732.
- Cooper W. T. and Antworth C. P. (1986) Final Report USAF-UES Summer Faculty Research Program.
- Cremer E. (1961) Mikrobestimmung von adsorptionisothermen durch gas-chromatographie Monatsh. Chem. 92, pp. 112-115.
- Curtis G. P., Reinhard M. and Roberts P. V. (1986) Sorption of hydrophobic organic solutes by sediments. In Geochemical Processes at Mineral Surfaces (edited by J. A. Davis and K. F. Hayes) ACS Symp. Series.
- Franks F. (1985) The hydrophobic Interaction. In Water: A Comprehensive Treatise (edited by F. Franks), Vol. 4, pp. 1-94, Plenum Press.

- Garbarini D. R., Lion L. W.(1986) Influence of the nature of soil organics on the sorption of toluene and trichloroethylene. Env. Sci. Technol. 20, 1263-1269.
- Hamaker J. W. and Thompson J. M. (1972) Adsorption In Organic Chemicals in the Soil Environment (edited by Goring C. A. I. and Hamaker J. W.), Vol. 1, pp. 49-144, Marcel Dekker Inc.
- Hartley G. S.(1960) In Herbicides in the Soil (edited by Woodford E. F. and Sager G. R.), pp. 63-78, Blackwell Scientific.
- Huber J. F. K. and Keulmans A. I. M. (1962) Nonlinear ideal chromatography and the potentialities of linear gas-solid chromatography. In Gas Chromatography 1962 (edited by van Swaay M.), pp. 26-62, Buttersworth.
- Jacobson J., Frenz J. and Horvath C.(1984) Measurement of adsorption isotherms by liquid chromatography. J. Chromatogr. 316, 53-68.
- Karickhoff S. W., Brown D. S. and Scott T. A.(1979) Sorption of hydrophobic pollutants on natural sediments. Water Res. 13, 241-248.
- Karickhoff S. W.(1984) Organic pollutant sorption in aquatic systems. J. of Hydraulic Engineering 110, 707-735.
- Lambert S. M.(1966) The influence of soil moisture content on herbicidal response. Weeds 14, 273-275.
- Lambert S. M.(1967) Functional relationship between sorption in soil and chemical structure. J. Agric. Food Chem. 15, 572-576.
- Lambert S. M.(1968) Omega, a useful index of soil sorption equilibria. J. Agric. Food Chem. 16, 340-343.
- Lambert S. M., Porter P. E. and Schieferstein R. H.(1965) Movement and sorption of chemicals applied to the soil Weeds 13, 185-190.
- Maciel G. E.(1984) High resolution nuclear magnetic resonance of solids. Science 226, 282-287.
- Mingelgrin U. and Gerstl Z.(1983) Reevaluation of partitioning as a mechanism of nonionic chemicals adsorption in soils. J. Environ. Qual. 12, 1-11.
- Nkedi-Kizza P., Rao P. S. C. and Hornsby A. G.(1985) Influence of organic cosolvents on sorption of hydrophobic organic chemicals by soils. Env. Sci. Technol. 19, 975-979.
- Orem W. H. and Hatcher P. G.(1987) Early diagenesis of organic matter in a sawgrass peat from the Everglades, Florida. Int. J. of Coal Geol. 8, 33-54.

- Pines A., Gibby M. G. and Waugh J. S. (1973) Proton Enhanced NMR of dilute spins in solids. J. Chem. Physics. 59, 569-590.
- Rao P. S. C., Hornsby A. G., Kilcrease D. P. and Nkedi-Kizza P. (1985) Sorption and transport of hydrophobic organic chemicals in aqueous and mixed solvent systems. Model development and preliminary evaluation. J. Environ. Qual. 14, 376-383.
- Schaefer J. and Stejskal E. O. (1976) Carbon-13 nuclear magnetic resonance of polymers spinning at the magic angle. J. Am. Chem. Soc. 98, 1031-1033.
- Schwarzenbach R. P. and Westall J. (1981) Transport of nonpolar organic compounds from surface water to groundwater. Laboratory sorption studies. Env. Sci. Technol. 15, 1360-1367.
- Snyder L. R. (1974) Classification of the solvent properties of common liquids. J. Chromatogr. 92, 223-230.
- Snyder L. R. (1978) Classification of the solvent properties of common liquids. J. Chromatogr. Sci. 16, 223-234.
- Tanford C. (1980) The Hydrophobic Effect, 2nd ed., 233 pp. Wiley-Interscience.
- Tissot B. P. and Welte D. H. (1984) Petroleum Formation and Occurrence, 2nd ed., 699 pp. Springer-Verlag.
- Wilson M. A., Pugmire R. J. and Grant D. M. (1983) Nuclear magnetic resonance spectroscopy of soils and related materials. Relaxation of  $^{13}\text{C}$  nuclei in cross polarization nuclear magnetic resonance experiments. Org. Geochem. 5, 121-129.
- Wilson M. A., Collin P. J., Vassallo A. M. and Russell N. J. (1984) The nature of olefins and carboxyl groups in Australian brown coal resin. Org. Geochem. 7, 161-168.

Table 1. Comparison of  $K_D$  Values Obtained by Different Techniques.

<u>Method</u>	<u>System</u>	
	Aniline/Humin	o-Cresol/Humin
Uncorrected HPLC/FACP	----	10.5
Corrected HPLC/Facp	----	9.5
Frontal Analysis	----	9.3
Corrected HPLC/FACP (dynamic)	40	----
Conventional Batch (static)	39	----

Table 2. Linear Fitting Coefficients fro Equation 5.

<u>Surface</u>	<u>a</u>	<u>b</u>	<u>correlation coefficient</u>
Lipid*	0.31	1.24	0.95
SOM	-0.36	1.97	0.80
Som-Lipid	-0.44	2.53	0.92
Humin	-0.61	3.16	0.92

\* o-cresol was excluded

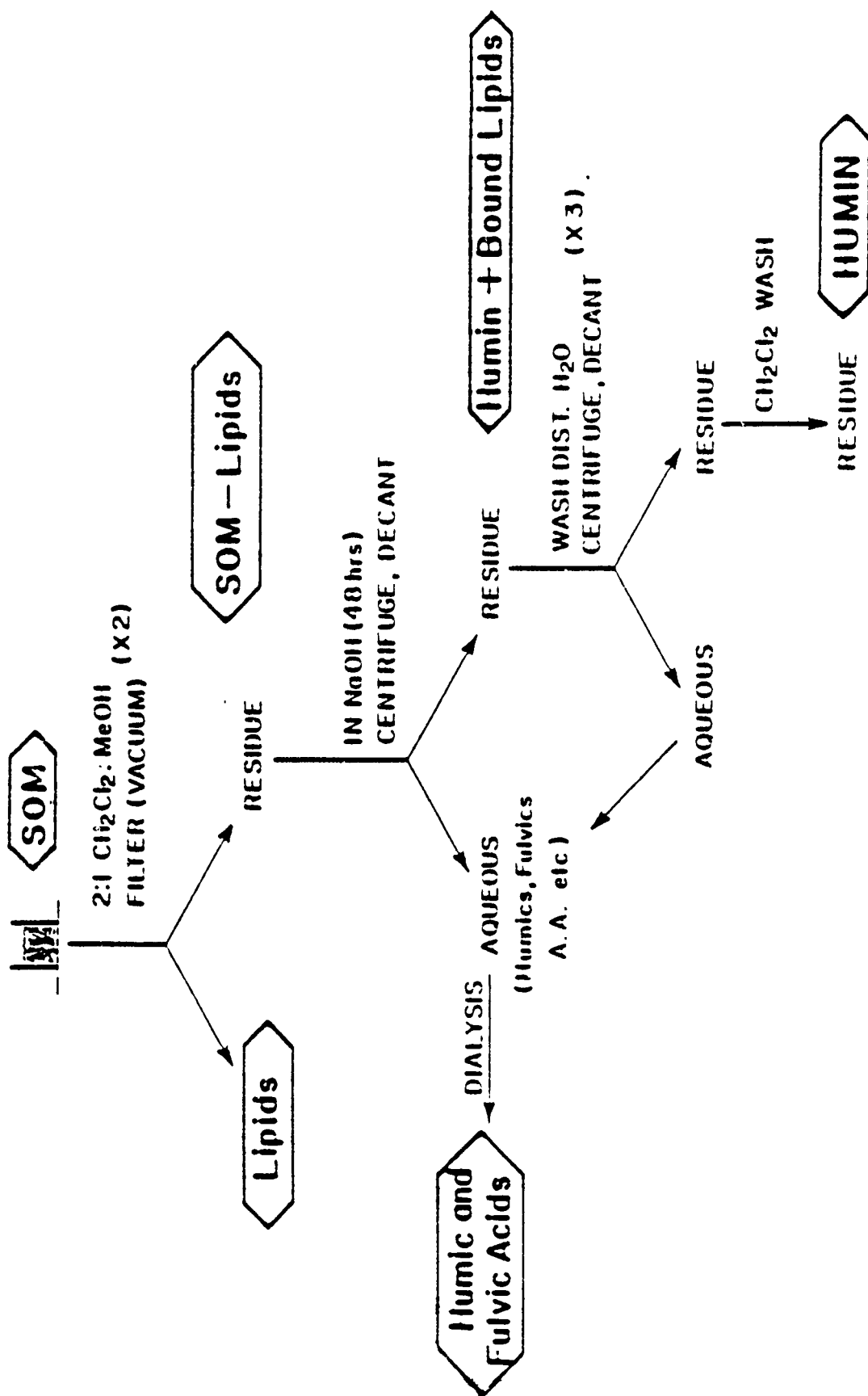
## FIGURE CAPTIONS

Figure 1. Extraction scheme used to isolate soil organic matter fractions.

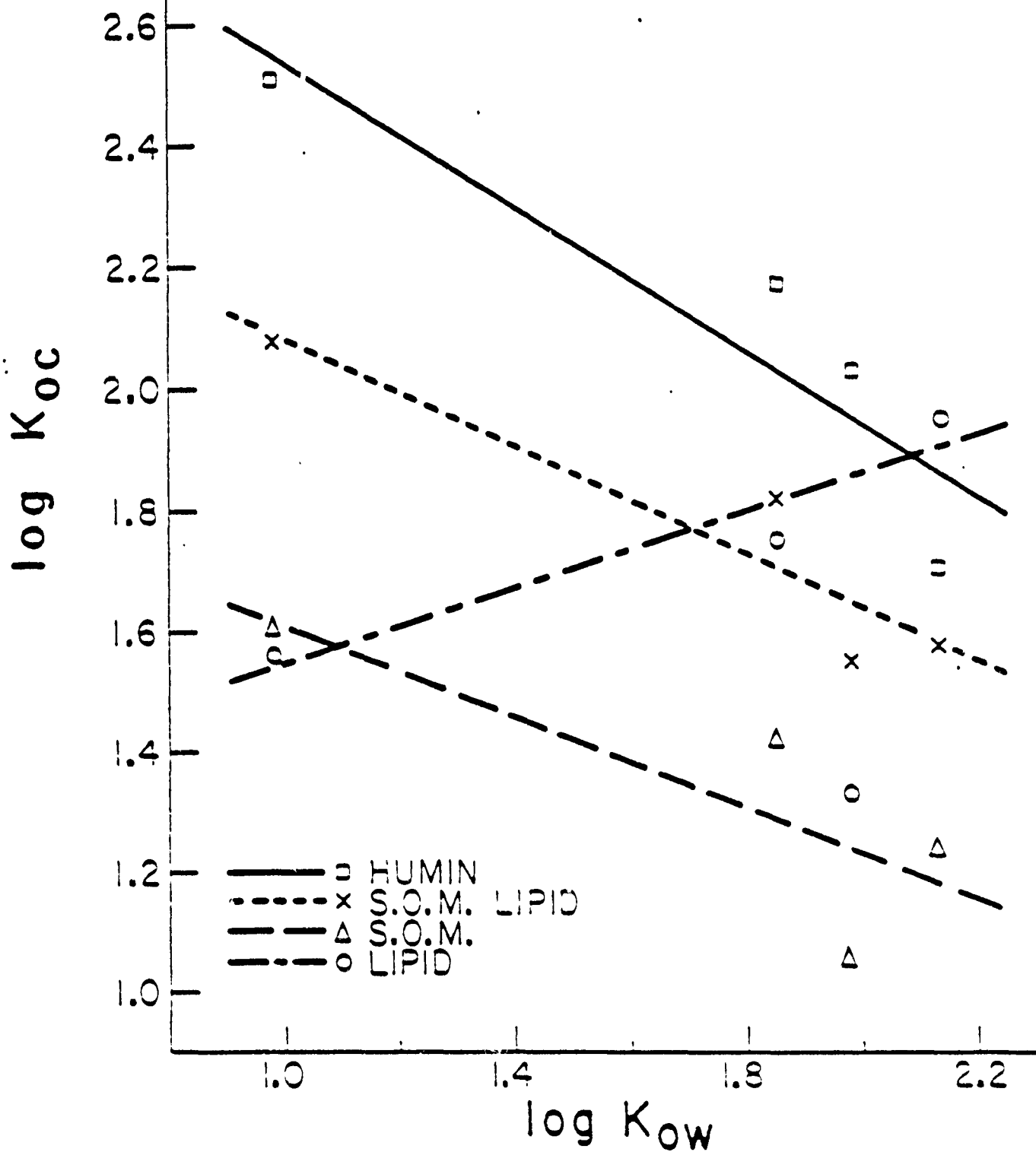
Figure 2. Plot of  $\log K_{OC}$  versus  $\log K_{OW}$  for the isolated organic matter fractions.

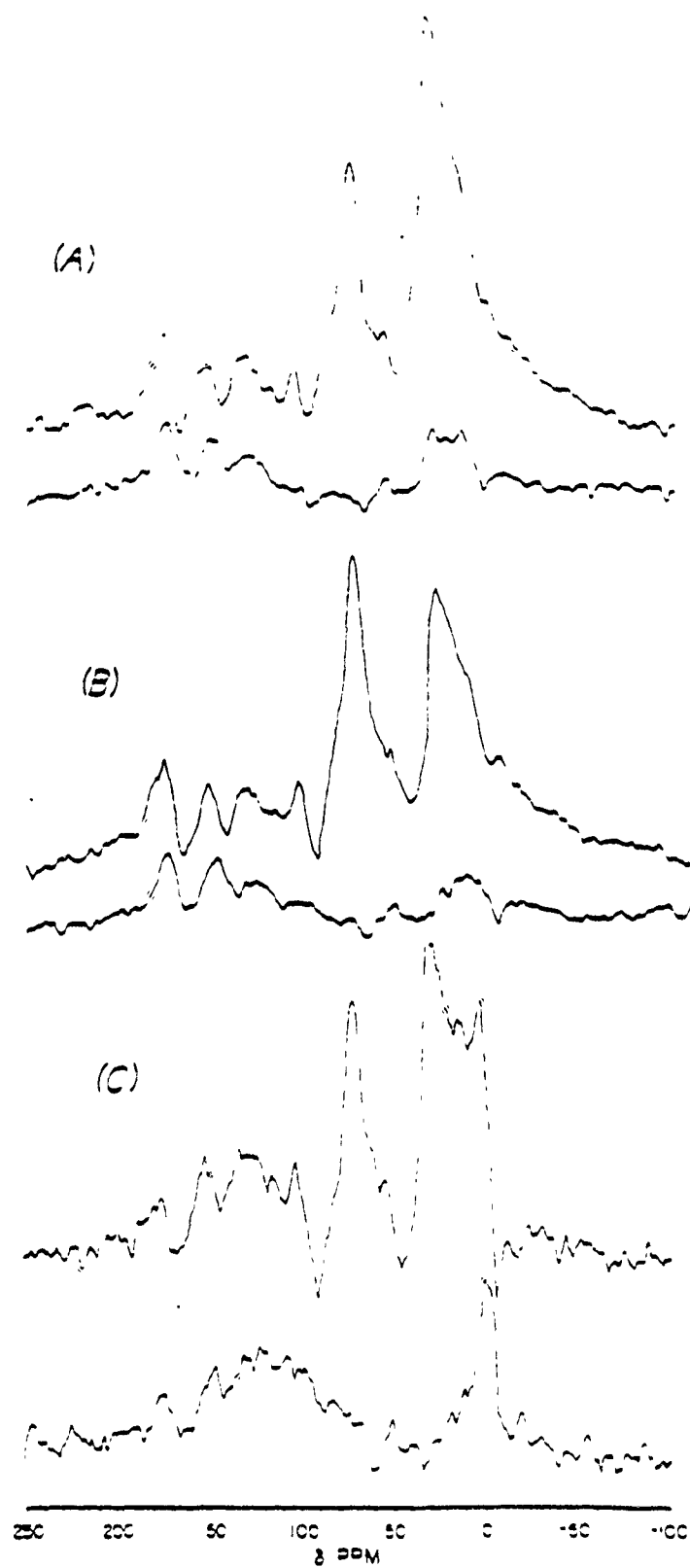
Figure 3. CP-MAS  $^{13}C$  NMR spectra of (a) total soil organic matter (SOM) (b) SOM-Lipids (c) Humin. Top spectra represent 0 usec DD delay, while bottom represent 50 usec delay.

# FRACTIONATION OF SOM



# SOIL CONSTITUENT TRENDS





PART 2: MEASUREMENT OF SOLUTE ACTIVITY COEFFICIENTS IN ORGANIC  
GEOPOLYMERS BY GAS CHROMATOGRAPHY

H. Collazo-Lopez, R.R. Yates and W.T. Cooper\*  
Department of Chemistry  
and  
Center for Biomedical & Toxicological Research  
Florida State University  
Tallahassee, Florida 32306-3006

Presented in the "Symposium on Organic Geochemistry: Techniques  
and Applications"  
Division of Geochemistry  
194th National American Chemical Society Meeting  
New Orleans, LA

September, 1987

Submitted to ORGANIC GEOCHEMISTRY

December, 1987

\*Author to whom correspondence should be addressed

Gas chromatography has been used to measure the molal activity coefficients of a series of nonpolar organic solutes in sedimentary organic matter and its various extractable components. Organic matter from a peat deposit of higher plant origin in the Florida Everglades was isolated at three depths in the peat core. The organic matter was then fractionated into its lipid, humic acid and humin components, and the activity coefficients measured for solutes ranging in electronic polarizability from pentane to dichloroethane. Activity coefficients, which are a thermodynamic measure of the affinity of a solute for a polymeric solution, show a reasonable correlation with electronic polarizability for the total organic matter and its lipid and humin fractions. There is also a marked increase in the lipophilic character of the humin fraction with increasing depth of burial. In spite of this change in humin solution capabilities, however, all of the solutes exhibit decreased affinities for the deeper total organic matter, which we believe is due to its lower lipid content, as well as a somewhat lower affinity for the more mature lipid fraction. Solid state  $^{13}\text{C}$  NMR spectra of the unfractionated organic matter and the humic acid and humin fractions give some insight into the relationship between their structure and sorption characteristics, although the chemical basis for the evolution of the nonpolar, lipophilic humin at depth is not readily apparent.

## INTRODUCTION

In the preceding manuscript (Antworth et al., 1987) we demonstrated that the sorption of polar, nonionic organic solutes onto fractions of soil organic matter depended on the composition of the organic matter fraction. The results presented in that paper suggest that hydrophobic (solvophobic) partitioning of these solutes occurs only with the lipid fraction, and that specific polar interactions between the solutes and active sites in the nonextractable humin fraction actually dominate the sorption of polar solutes. It would thus appear that the empirical relationship between octanol-water partition coefficients and soil and sedimentary organic matter partitioning (Briggs, 1973; Chiou et al., 1979; Karickhoff et al., 1979) cannot be extended to polar organic solutes with water solubilities greater than that of benzene (~1000 ppm). It would also appear that the composition and structure of the organic matter involved must also be considered. Indeed, the work of Garbarini and Lion (1986), who correlated the sorption of toluene and trichloroethylene into a variety of organic matter samples with C and O content of the organic matter, suggest that soil organic matter composition must be considered for accurately predicting sorption of even hydrophobic solutes (solubilities less than ~100 ppm). Garbarini and Lion also observed that, when normalized for organic carbon content, humin showed the highest affinity for hydrophobic solutes of all the organic matter studied. Interestingly, we observed the same phenomenon with polar, more soluble solutes.

Accurate predictions of solute - organic matter partitioning would thus appear to require some knowledge of the organic matter involved. However, for such predictions to be included in realistic models of the movement and behavior of organic solutes in hydrologic systems, they must rely on parameters which can be reasonably acquired in a laboratory. We suggest that the relative proportions of lipids, humic/fulvic acids, and humin comprising soil and sedimentary organic matter, along with the elemental composition (C,H,N,O) of each fraction which was first suggested by Garbarini and Lion, represent a reasonable first approximation of the character of organic matter.

In order to more fully understand the chemical nature of these organic matter fractions, as well as to provide a more thorough scientific rationale for these suggestions, we have embarked on a detailed study of the solution properties of soil lipids, humic/fulvic acids and humin. We have again chosen organic-rich peat as our model soil organic matter since this material, low in inorganic content, can be considered essentially pure organic matter. This greatly simplifies the experimental aspects of the work. We do not mean to imply, however, that all soil and sedimentary organic carbon will behave as does peat. At this point our primary interest is more in understanding the differences in chemical properties of organic matter fractions, rather than the differences between peat and low-carbon soils and sediments. The similarities between the various organic fractions of peat and analogous fractions from other environments will be the subject of future investigations.

We have chosen to characterize these organic matter fractions, which can be considered mixtures of discrete geopolymers, by one form of the Inverse Chromatography Technique. Specifically, we have measured activity coefficients of organic solutes in these polymeric mixtures by gas chromatography. It has been experimentally verified that, under the proper conditions, gas chromatography can provide reliable thermodynamic values which can be used to study the interactions of molecules with different solvents (Conder et al., 1977; Conder et al., 1986). Particularly attractive features of the gas chromatographic approach are its essential simplicity, non-destructive nature, the speed with which large amounts of data can be obtained, and the ability to work at solute concentrations close to what is considered infinite dilution.

In this work we have again used different fractions of total organic matter as stationary phases. Solute are injected in the gaseous state, and their retention volumes then related to molal activity coefficients by equation 1.

$$\ln a_i = \ln \frac{RTW_2}{P_i V_n 10^3} - \frac{P_i^0 (B_{11} - v_i)}{RT} + \frac{P_0 (2B_{12} - v_i) J_3^4}{RT} \quad (1)$$

where  $a_i$  is the activity coefficient,  $T$  the absolute temperature,  $R$  the gas constant,  $W_2$  the weight of stationary phase in the column,  $P_i^0$  the saturation pressure of the pure solute,  $P_0$  the pressure at the column outlet,  $V_n$  the net retention volume, and  $B_{11}$  and  $B_{12}$  the second virial coefficients of the pure solute and

the solute in the carrier gas, respectively. This equation was first derived by Martire (1974) and it has been shown that if the column pressure differential is less than two atmospheres, the carrier gas can be treated as an ideal gas, and the contributions of the last two terms are insignificant. Activity coefficients less than one are interpreted as an indication of high affinity for the stationary phase, while values greater than one indicate low affinity, or unfavorable mixing of the solute with the stationary phase.

The activity coefficient measurements just described have been supported by both conventional (CP-MAS) and dipolar dephased (DD-CP-MAS) Cross Polarization-Magic Angle Spinning  $^{13}\text{C}$  NMR spectroscopy. The dipolar dephasing experiment takes advantage of the faster relaxation of protonated carbons. By allowing protonated carbons to dephase during a dipolar coupling period prior to data acquisition, the resonances of C-H and C-H<sub>2</sub> groups can be suppressed so that the remaining signal corresponds to non-protonated carbons, as well as methyl carbons that couple weakly because of their rapid rotational mobility. By using an optimum delay period (40-50 usec) the protonated carbon signal can be removed from the total signal, leaving resonances primarily from non-protonated carbon atoms.

## EXPERIMENTAL

### Gas Chromatography.

All chromatographic measurements were performed with a Varian 3700 gas chromatograph equipped with a flame ionization detector that was maintained at 200°C. For infinite dilution retention volume measurements the oven was kept at 25°C and the temperature of the column was monitored to  $\pm 0.1^\circ\text{C}$  with a copper-constantan thermocouple. The inlet and outlet pressures were monitored with an amplified pressure transducer (105 series, Omega).

### $^{13}\text{C}$ NMR Spectroscopy

NMR spectra were obtained with a Bruker WP-200 SY spectrometer equipped with an IBM solids control accessory operating at 50 MHz for carbon. The spectrometer was tuned with t-butyl benzene and chemical shift scales are reported as parts per million downfield from tetramethylsilane. Samples were spun at the magic angle at approximately 4.5 KHz. A contact time of 1 msec was used throughout, and for dipolar dephasing experiments a 40 usec delay was inserted prior to data acquisition. This delay consisted of two 20 usec intervals separated by a 10 usec,  $180^\circ$  refocusing pulse. The repetition rate for all NMR experiments was 3 sec. The data was acquired as 2K sets, zero-filled to 8K and exponentially multiplied prior to Fourier transformation.

### Extractions

The sedimentary organic matter used in this study was from a 2 meter peat core obtained from the Everglades National Park (FL)

during March of 1986. The core was taken from a Mahogany Hammock adjacent to the PaHayOkee visitor site. The core was refrigerated and stored in a sealed plastic container under a nitrogen atmosphere in the field, then frozen upon return to the lab until it was ready for use. Three horizons of 8 cm were cut from the core at 12, 35 and 151 cm and labeled as horizons A, B and C, respectively. Each sample horizon was lyophilized, mechanically homogenized and stored in sealed vials before analysis.

The total organic matter (TOM) from each horizon was continuously extracted with a 2:1 mixture of dichloromethane and methanol until a clear supernatant was achieved. The material extracted in this operation was defined as the lipid fraction. The residue left after the lipid extraction was then extracted with 0.5 N NaOH under a nitrogen atmosphere to remove humic and fulvic acids. The insoluble material was separated from the supernatant by centrifugation at 12000 RPM. This operation was repeated until no further material could be extracted from the residue and the supernatant was clear. The remaining residue was then washed with distilled water and lyophilized. This is the humin fraction. The NaOH solution was acidified with HCl to a pH of 1.0 and the humic acids that precipitated were separated by centrifugation at 12000 RPM, resuspended in an aqueous solution of pH 3 to protonate phenolic and carboxylic sites, and then lyophilized. The isolated fulvic acids were not used in this study.

After extraction of the lipids, the residue was dried and re-weighed. Lipid contents in horizons A, B and C were found to be

4.3%, 3.8% and 1.3% by weight, respectively.

#### Activity Coefficient Measurements

Activity coefficients were determined according to the procedures described by Conder and Young (1977) . The carrier gas flow rate was adjusted until the retention volumes of each probe showed no dependence on flow rate. This procedure was done separately for each of the fractions. Columns were made with 1/16 inch ID glass capillary tubes. Lipids were coated onto carefully silanized 100/200 mesh silica gel. Humic acids, humin and TOM were lyophilized and size fractionated to 100/200 mesh, then packed into columns without any additional silica support particles. The probes were injected as head space vapor and the amount injected was adjusted individually for each sample so that the infinite dilution condition was achieved (i.e. no dependence of sample size on retention volume).

## RESULTS AND DISCUSSION

### Activity Coefficients

Activity coefficients for the organic matter fractions from the deeper, more altered horizons B (35-42 cm) and C (151-158 cm) are summarized in Table 1. The solutes used in these studies are arranged from top to bottom in Table 1 according to increasing electronic polarizability. Electronic polarizability determines the contribution of nonspecific interactions to the total interaction energy involved in the chromatographic process (Barrer, 1966), and a correlation between sorption affinity and polarizability is an indication that nonspecific dispersion forces are responsible for the observed sorption, thus implying a partition process.

Solute activity coefficients are lowest for the lipid fractions, as expected, indicating that the probes have the highest affinity for this material. Chromatographic peaks were very symmetrical, and retention volumes showed no dependence on flow rate or concentration. Except for the relatively low coefficient for carbon tetrachloride in the lipids from horizon C, activity coefficients exhibit a negative relationship with polarizability (i.e. increasing sorption with increasing polarizability). Interestingly, all probes except carbon tetrachloride have higher activity coefficients in (lower affinities for) the lipid material from the deeper horizon, suggesting that the qualitative character of lipids in this sediment changes with depth, along with quantitative changes (note that lipids comprise 3.8% of the organic matter in horizon

B, but only 1.3% in horizon C).

The humic acid fractions show very little affinity for the probes, as indicated by the large activity coefficients obtained. We also observed that peaks were less symmetrical than those obtained with the lipids, and the concentrations needed to achieve infinite dilution were significantly lower. These data and observations indicate that the polar and ionic character of humic acids results in very little tendency for nonpolar solutes to partition into them. A weak surface adsorption process is probably responsible for what little sorption is observed. There does not appear to be any significant change in the sorption properties of humic acids with depth.

Humin showed intermediate affinities for the probes, with sorption of the chlorinated probes being particularly strong. Peak shapes were significantly more symmetrical than those for the humic acids, although some asymmetry was still apparent. As with the lipids, increasing affinity correlates with increasing polarizability, again excepting carbon tetrachloride. In contrast to the lipids, however, there is a very significant increase in sorption of the probes by the lower horizon. This data suggest substantive diagenetic alteration of the humin fraction, resulting in a much less polar, more lipophilic material. Other researchers have observed similar phenomena. Shin et al. (1970) observed that DDT adsorption was greater in more humified soil organic matter. Garbarini and Lion (1986) demonstrated a significant correlation between atomic C/O ratios of various

organic matter samples and the affinity of the organic matter for the hydrophobic solutes toluene and trichloroethylene.

Another explanation for this change may be the inclusion of non-solvent extractable lipids into the humin fraction during diagenesis. In contrast to the studies reported in the previous manuscript (Antworth et al., 1988), only solvent extractable lipids were removed from the organic matrix here. 'Bound' lipids must first be freed by saponification, then removed by solvent extraction. Several workers have noted increases in the amount of bound lipids with depth of burial (Mackenzie et al., 1982 and references cited therein,, and it is presumed that diagenetic alteration of sedimentary organic matter results in certain lipids forming ester, amide, ether, etc. linkages with the organic, and possibly inorganic, matrices.

Table 1 also includes activity coefficients for the original, unfractionated organic matter. As with the humin and lipids, sorption increases with increasing solute polarizability. Unlike the humin fraction, however, sorption into the total, unfractionated sedimentary organic matter decreases with increasing horizon depth, in spite of a significantly more lipophilic humin component. This is a reasonable result if we presume that the non-bound, solvent extractable lipid fraction dominates the sorption of nonpolar organic solutes by the intact, unfractionated organic matter, since this lipid fraction comprises only 1.3% of the TOM of horizon C, but 3.8% of the TOM of horizon B.

In order to further illustrate the dominance of the lipid fraction in the sorption process, we have calculated the ratio of the solute activity coefficients of the humic acid, humin and TOM fractions to those in the lipid fractions for the same compound and depth. The results, summarized in Table 2, provide an estimate of the relative affinities of these nonpolar compounds for the various fractions. Again, smaller values in Table 2 reflect affinities more similar to those for the lipid fraction; that is, a more 'lipid-like', or lipophilic, material. The data of Table 2 reinforces the fact that, with increasing depth of burial, the total organic matter contained in the peat sediment becomes slightly less lipophilic, in spite of a substantial increase in the lipophilic character of the humin fraction. This again suggests that the free, solvent-extractable portion of soil and sedimentary lipids dominates the sorption of nonpolar organic solutes.

### <sup>13</sup>C NMR Spectroscopy

The zero-delay CP-MAS <sup>13</sup>C NMR spectra of the total sedimentary organic matter and the humic acid and humin fractions are displayed in Figure 1. Included are spectra from horizon A (12-20 cm) in order to give a broader perspective of the diagenetic processes within this core.

The primary changes observed in the unfractionated organic matter are the relative loss of intensities in resonances arising from alcoholic (54 ppm), carbohydrate (74 ppm) and carboxyl (175 ppm) carbon, with corresponding increases in aliphatic (30 ppm) and aromatic (130,154 ppm) carbon. These changes probably reflect

removal of the more labile carbohydrates, leaving a material enriched in aliphatic and aromatic structures. Orem and Hatcher (1987) observed the same basic trends in whole peats from a sawgrass plain in the Everglades, although that peat appears to contain a significantly greater carbohydrate fraction. Indeed, the spectrum of Orem and Hatcher's whole peat from the 70-90 cm horizon is almost identical to the spectrum we obtained on unfractionated peat from the 151-158 cm horizon.

There appears to be little significant change in the humic acid fraction with depth. Slight decreases in the aliphatic and carboxyl peaks relative to the aromatic peaks are noted, however.

Interpretation of the humin spectra is much less straightforward. First, all of the humin fractions, even that from horizon A, have a significant aliphatic component. These spectra thus resemble those of deeper humin samples (10 cm and below) obtained by Orem and Hatcher. The evolution of our humin, however, appears quite different from that observed by them, where there was a steady loss of carbohydrate, alcoholic and carboxyl carbon in humin from the surface (0-5 cm) through humin in the 55-70 cm horizon. While we observe this same trend in humin evolution on going from the 12-20 cm horizon to the 35-43 cm horizon, both carboxyl and alcoholic peaks reappear in humin from the 151-158 cm horizon. We do not as yet fully understand these observations, but the humin in horizon C may include some incorporated humic acids which are no longer extractable. Alternatively, there may have been some change in the sedimentary

environment which accelerated the production of extractable humic acids in horizon B (or hindered the humic acid evolution in horizon C). These last arguments presume that the hypothesis of Orem and Hatcher that humic acids originate as decomposition products of humin is correct.

As a final word on the NMR spectra of these humin samples, it should be noted that a second set of spectra were obtained in order to ensure that we were not observing some spectral artifact. These spectra were identical to the originals, and we thus believe that we are observing a real phenomenon.

With regard to the present study on the solution properties of organic matter fractions, the most important and consistent difference in humin from horizon B and horizon C appears to be an increase in the relative proportion of aromatic carbon. Furthermore, dipolar dephased NMR spectra (Figure 2) show persistent aromatic resonances after 40 usec, indicating that this aromatic carbon is significantly nonprotonated; that is, highly cross-linked to other carbon moieties. Current efforts are directed at a better understanding of degraded humin structure, and why this structure results in a lipophilic polymeric material when compared to its less altered precursor.

## SUMMARY

The sorption of nonpolar, hydrophobic solutes into sedimentary organic matter, and the lipid and humin fractions of the organic matter, is seen to correlate with electronic polarizability of the solutes, implying a non-specific dispersion, or partition, process. As expected, the lipid fraction shows by far the highest affinity for these solutes. Sorption by the total, unfractionated organic matter seems to be dominated by this extractable, non-bound lipid component, even at depth where humin has acquired a significantly lipophilic character.

The results of this physiochemical investigation of sedimentary organic matter and its various components seem to support previous results of Hartley (1960), who described the fats-waxes-resin fraction (i.e. lipids) as the fraction of soil organic matter into which hydrophobic solutes partition, as well as those of Shin et al. (1970) and Garbarini and Lion (1986), both of whom observed increasing hydrophobic solute sorption with increasing maturation of soil and sedimentary organic matter.

#### ACKNOWLEDGMENTS

This work was supported by the Air Force Office of Scientific Research through a follow-up Mini Grant that is a part of the Faculty and Graduate Student Summer Research Program.

## REFERENCES

- Antworth C.P. Cooper W.T.(1987) Applications of inverse chromatography in organic geochemistry. Part 1: Characterization of polar solute - soil organic matter interactions by high performance liquid chromatography. Org. Geochem., submitted.
- Barrer R.M. (1966) Specificity in physical adsorption. J. Colloid Interface Sci., 21, 415-434.
- Briggs G. G. (1973) A simple relationship between soil sorption of organic chemicals and their octanol/water partition coefficient. Proc. 7th Bri. Insecticide Fungicide Conf. 11, pp. 475-478.
- Chiou C. T. (1979) A physical concept of soil-water equilibria for nonionic organic compounds. Science 206, 831-832.
- Conder J.R. McHale S. Jones M.A. (1987) Evaluation of methods for measuring gas-solid chromatographic retention on skewed peaks. Anal. Chem. 58, 2663-2668.
- Conder J.R., Young C.L.(1977) Physicochemical Measurements by Gas Chromatography, J. Wiley and Sons, New York, pp 155-277.
- Garbarini D. R., Lion L. W.(1986) Influence of the nature of soil organics on the sorption of toluene and trichloroethylene. Env. Sci. Technol. 20, 1263-1269.
- Hartley G. S.(1960) In Herbicides in the Soil (edited by Woodford E. F. and Sager G. R.), Blackwell Scientific, pp 63-78.
- Hatcher P.G., Breger I.A., Dennis L.W., Maciel G.E. (1983) Solid-state  $^{13}\text{C}$  NMR of sedimentary humic substances. In Aquatic and Terrestrial Humic Material (R.F. Christman and E.T.Gjessing, eds.) Ann Harbor Science, pp.37-82.
- Karickhoff S. W., Brown D. S. and Scott T. A.(1979) Sorption of hydrophobic pollutants on natural sediments. Water Res. 13, 241-248.
- Mackenzie A.S., Brassell S.C., Eglinton G., Maxwell J.R. (1982) Chemical fossils: The geological fate of steroids. Science 217, 491-504.
- Martire D.E. (1974) Dependence of the solute retention parameters on stationary phase molecular weight in gas-liquid chromatography. Anal. Chem. 46, 626-633.
- Orem W. H. and Hatcher P. G.(1987) Early diagenesis of organic matter in a sawgrass peat from the Everglades, Florida. Int. J. of Coal Geol. 8, 33-54.

Shin Y.O., Chodan J.J., Wolcott A.R. (1970) Adsorption of DDT by soils, soil fractions, and biological materials. J. Agr. Food Chem. 18, 1129-1133.

Table 1. Molal Activity Coefficients Obtained at 25°C.

Horizon Depth(cm)	Lipids		Humic Acids		Humin		TOM	
	B 35-43	C 150-158	B 35-43	C 150-158	B 35-43	C 150-158	B 35-43	C 150-158
<u>Solute</u>								
C <sub>5</sub> H <sub>12</sub>	0.036	0.043	>10	>10	5.2	1.5	4.5	5.7
C <sub>6</sub> H <sub>14</sub>	0.013	0.015	9.0	>10	1.3	0.54	2.4	2.3
CCl <sub>4</sub>	0.013	0.004	7.9	7.0	1.6	0.60	1.6	2.0
C <sub>2</sub> HCl <sub>3</sub>	0.008	0.009	>10	>10	0.45	0.20	0.49	0.54
C <sub>2</sub> H <sub>4</sub> Cl <sub>2</sub>	0.003	0.009	8.5	9.8	0.36	0.12	0.55	0.66

Table 2. Relative Activity Coefficients, Normalized to Corresponding Activity Coefficient for Lipid Fraction.

Horizon Depth(cm)	Humic Acid		Humin		TOM	
	B 35-43	C 150-158	B 35-43	C 150-158	B 35-43	C 150-158
<u>Solute</u>						
C <sub>5</sub> H <sub>12</sub>	278	232	144	34	125	132
C <sub>6</sub> H <sub>14</sub>	692	666	100	36	184	153
CCl <sub>4</sub>	607	1750	123	150	184	500
C <sub>2</sub> HCl <sub>3</sub>	1250	1111	56	22	61	60
C <sub>2</sub> H <sub>4</sub> Cl <sub>2</sub>	2833	3266	120	40	183	220

# FIGURE CAPTIONS

Figure 1. CP-MAS  $^{13}\text{C}$  NMR spectra of total organic matter, humic acids and humin as a function of depth.

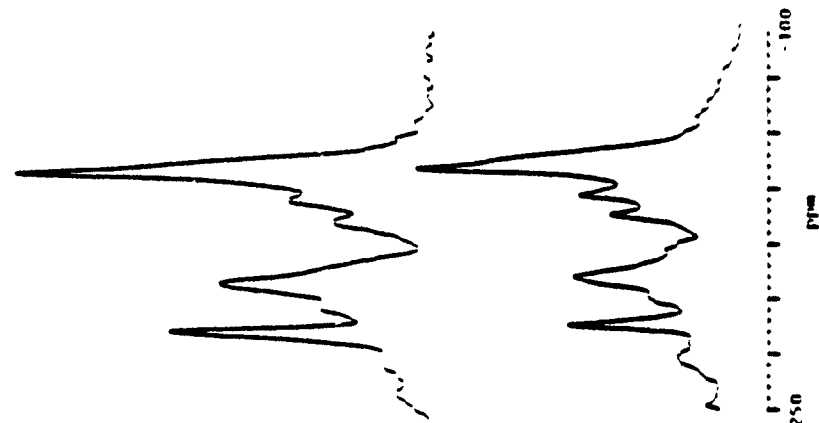
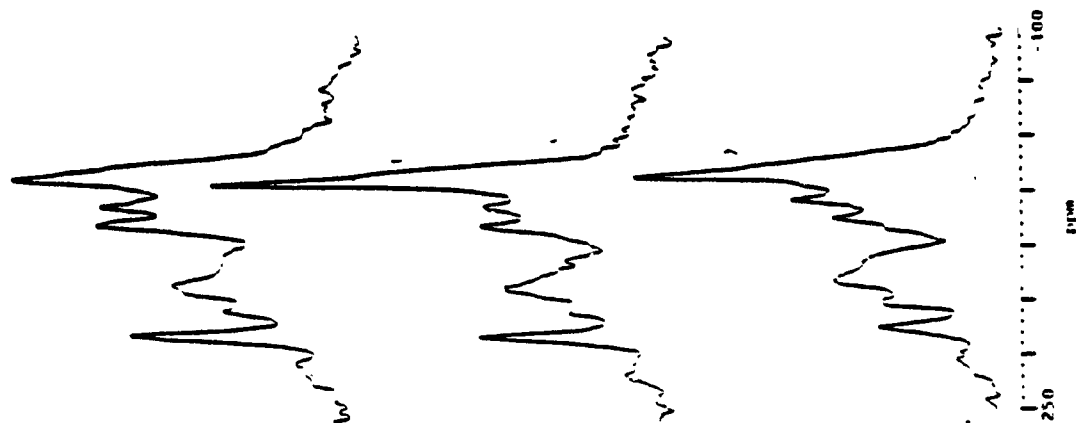
Figure 2. Dipolar dephased CP-MAS  $^{13}\text{C}$  NMR spectra (0-40 usec) of humin from 35-43 and 151-158 cm horizons.

# MAS $^{13}\text{C}$ NMR

TOTAL ORGANIC MATTER

HUMIC ACID

HUMIN



12 CM.

35 CM.

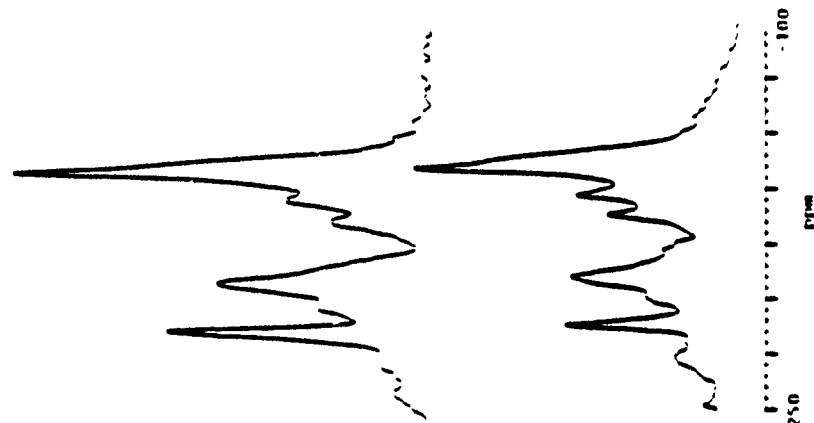
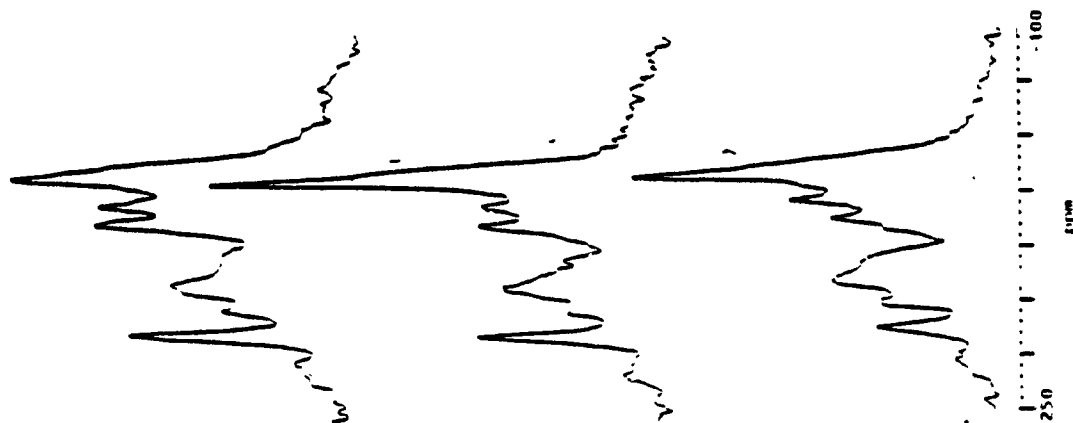
151 CM.

# MAS - $^{13}\text{C}$ NMR

TOTAL ORGANIC MATTER

HUMIC ACID

HUMIN



12 CM.

35 CM.

151 CM.

FINAL REPORT NUMBER 21  
REPORT NOT AVAILABLE AT THIS TIME  
Dr. Peter Jeffers  
760-7MG-038

1986 USAF-UES RESEARCH INITIATION PROGRAM

Sponsored by the

AIR FORCE OFFICE OF SCIENTIFIC RESEARCH

Conducted by the

UNIVERSAL ENERGY SYSTEMS, INC.

FINAL REPORT

A STUDY OF SEMIHARDENED CONCRETE ARCH STRUCTURE

RESPONSE UNDER PROTECTIVE LAYERS

Prepared by:	Y.S. Kim and R.R. Domingo
Department and	Department of Civil Engineering
University:	Catholic University of America
Research Period:	April 1, 1987 - March 31, 1988
Contract No.:	F49620-85-C-0013/SB5851-0360

(The reverse of this page is blank.)

## ACKNOWLEDGEMENT

The authors would like to thank the Air Force Systems Command, the Air Force Office of Scientific Research and the Universal Energy Systems, Inc. for supporting this research project. In particular, they would like to thank the research engineers in the Facility Systems and Analysis Branch at the Tyndall Air Force Base for suggesting this area of research and for their collaboration.

Also, the authors would like to thank Mr. M. Womack and his staff in the Operations Support Branch at the Tyndall Air Force Base for providing them warm hospitality and excellent working conditions during the stay at Tyndall for the centrifuge model tests.

## ABSTRACT

A reinforced concrete arch structure is modeled under a sloping embankment consisting of three different protective layers: compacted soil, concrete slab, and rock cover. The variables taken into account are: bedding condition, embankment slope, embankment soil type, and type of rock cover.

Structural responses are predicted through finite element code, CANDE (Culvert ANalysis and DEsign). The results of CANDE analyses include nonlinear constitutive models for characterizing arch structure and soil, incremental construction and free vertical movement with a symmetric mesh, and allowed the comparison of structural responses for different structural systems modeled.

Also, a preliminary investigation to study the behavior of a buried arch structure using the centrifuge model technique is performed and described in the report.

## SECTION I

### INTRODUCTION

#### A. PURPOSE

During the recent years, several research programs were undertaken by the United States Air Force (References 1,2,3,25) to develop the protective antipenetration system for military facilities (e.g., arch-, circular-, and box-type structures) constructed on the ground surface (Figure 1.1). Protective concepts consisting of rock rubble/boulder and burster slab over soils were introduced, and full-scale models were tested to determine the levels of protection against conventional weapons (Figure 1.2). A parametric study on the thickness of rock rubble/boulder layer, ratio of size of rock rubble/boulder to size of the weapons, thickness of burster slab, and density and thickness of sand layer was performed and qualitative results have been obtained from the field model tests. Based on information observed, the system has proven effective to resist the penetration of conventional weapons and it is now being considered for application over military facilities as a hardening protective structure. However, the designers are facing one critical question before the application of the system (Reference 25): Will these military structures be safe under static loadings due to the weight of embankment soil, rock rubble/boulder layers and/or burster slab? The purpose of the research, therefore, is to study the behavior of the buried arch structures subjected to static loadings by using centrifuge and numerical modeling techniques.

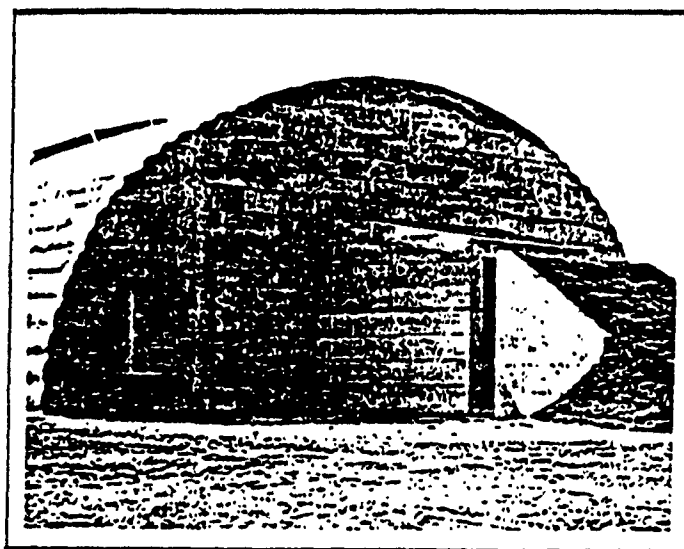
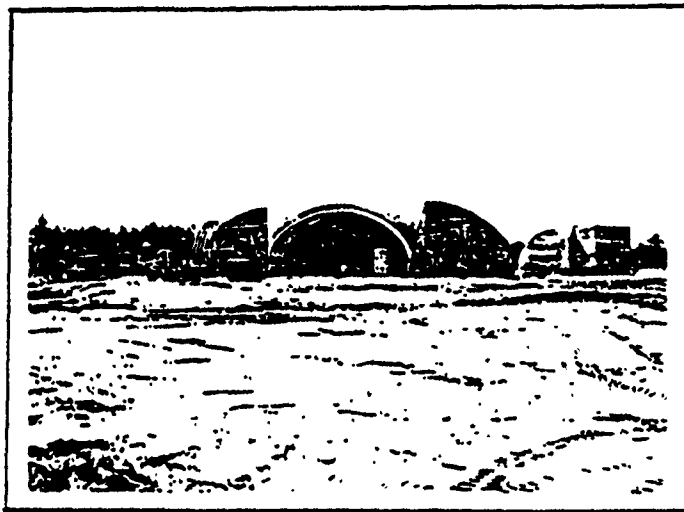
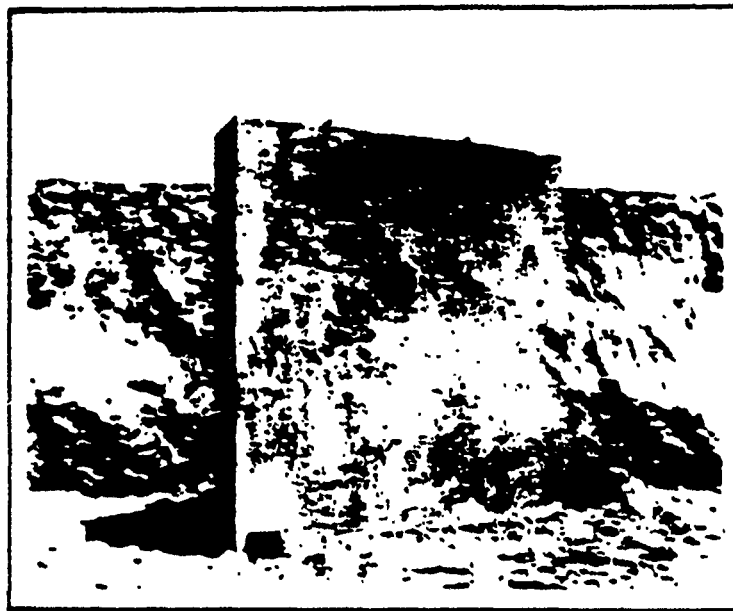
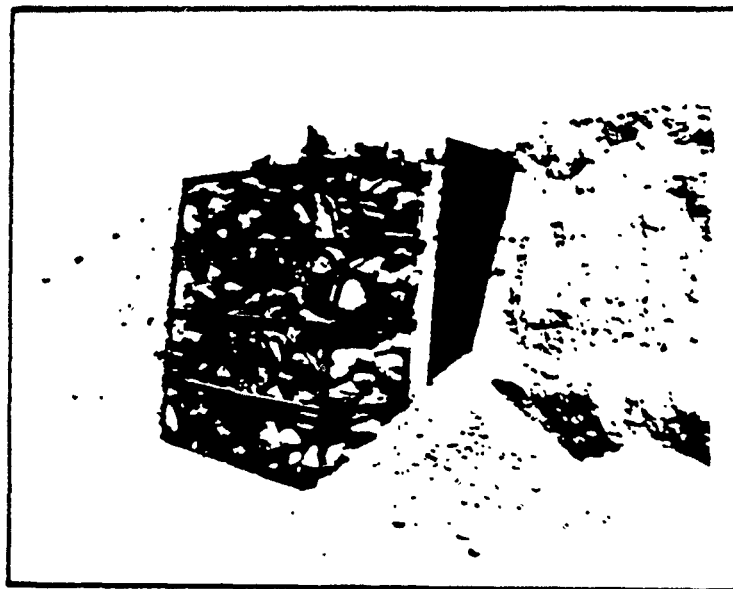


Figure 1.1 Reinforced Concrete Arch Structures



a) Burster Slab



b) Rock/Rubble Protective Layer

Figure 1.2

## B. OBJECTIVE

The primary objective of this study is to investigate the soil-structure interaction problems of a buried concrete arch structure subjected to static loadings. More specifically, the objectives of this study are to:

1. Develop an experimental technique to simulate the behavior of a prototype arch structure in a centrifuge.
2. Conduct a preliminary series of centrifuge model experiments on a small capacity centrifuge.
3. Predict the behavior of the arch using finite element analysis.
4. Gain experience necessary for model studies in a large capacity centrifuge.

## C. SCOPE

With these objectives in mind, the research is reported in the following sections. They contain a description of the centrifuge facility used for model study; design and fabrication of an accompanying testing apparatus; preliminary model test results, and recommendation for further centrifuge model study; and investigation of the influence of soil types for in-situ bedding and backfill, and slope of the embankment using finite element analysis. Finally, some potential topics for future research in this area are mentioned.

## SECTION II

### CENTRIFUGE MODEL STUDY

#### A. FUNDAMENTALS OF CENTRIFUGE MODELING

One of the most ideal approaches for obtaining information on the behavior of prototype structures is full-scale model testing. A full scale model with the necessary instrumentation (i.e., soil stress meters, pore water pressure transducers, settlement gauges and strain gauges, etc.) could give the best results for estimating prototype behavior.

Unfortunately, full-scale model testing has serious major drawbacks: mainly, cost and time of construction and operation. Because of these reasons, small scale model testing is becoming a favorite testing method in geotechnical engineering.

However, use of small scale model tests in the laboratory is severely limited when the gravity body force of the structure itself is the principal load on the system, such as in dams and embankments. This limitation is due to two major factors. One is that soil characteristics are nonlinear and overburden dependent, and the other involves stress magnitudes. The stresses in a small scale model due to its own weight are much smaller in magnitude than those in the corresponding prototype system. To eliminate these deficiencies, the centrifuge modeling technique has been used since 1931. The increase in unit weight is achieved by placing a model in a centrifuge and spinning it to produce an acceleration field that is equivalent to an artificial gravitational field. In this way the state of stress at every point in the model under an artificial

gravitational field is equal to that at the homologous point in the prototype. This technique has been applied to a variety of geotechnical problems (i.e., slope stability, reinforced earth, foundation design, offshore gravity platforms, rockfill dams, tunnels, and buried circular pipes) reported elsewhere (References 5,10,13,14,23,24,28,29 and 30). Table 2.1 summarizes the scaling rules that have been developed for relating the behavior of the centrifuge model and an equivalent full scale geotechnical structure.

## B. THE AFESC CENTRIFUGE FACILITY

### 1. The Centrifuge

The centrifuge installed at Tyndall Air Force Base (AFB) was originally built for testing of electronic and mechanical packages under G-loadings that simulate those experienced in actual flight. It was initially installed at Kirtland AFB, New Mexico. The machine was modified for geotechnical studies in 1981 and moved to the Air Force Engineering and Services Center (AFESC) at Tyndall AFB in 1986. The centrifuge was assembled and housed in a 7-ft. high, 16-ft. diameter, 9-in. thick reinforced concrete retaining structure (Figure 2.1).

The Center's centrifuge is a medium size rotary accelerator designed by Genisco, Inc., of California (Model E-185). The machine is capable of applying controlled centrifugal accelerations up to 100 g's and a limit of 30,000 g-lb. at a nominal radius of 6 ft. The payload of the test package can be as heavy as 500 lb. The machine includes a variable-speed hydraulic drive system, timing belt drive, RPM pick-up, rotating

Table 2.1 Scaling Relations (Reference 29)

Quantity	Full Scale (Prototype)	Centrifugal Model at n g's
Linear Dimension	1	$1/n$
Area	1	$1/n^2$
Volume	1	$1/n^3$
Time		
In Dynamic Terms	1	$1/n$
In Diffusion Cases	1	$1/n^2$
In Viscous Flow Cases	1	1
Velocity (Distance/Time)	1	1
Acceleration (Distance/Time)	1	n
Mass	1	$1/n^3$
Force	1	$1/n^2$
Energy	1	$1/n^3$
Stress (Force/Area)	1	1
Strain (Displacement/Unit Length)	1	1
Density	1	1
Energy Density	1	1
Frequency		
In Dynamic Terms	1	n

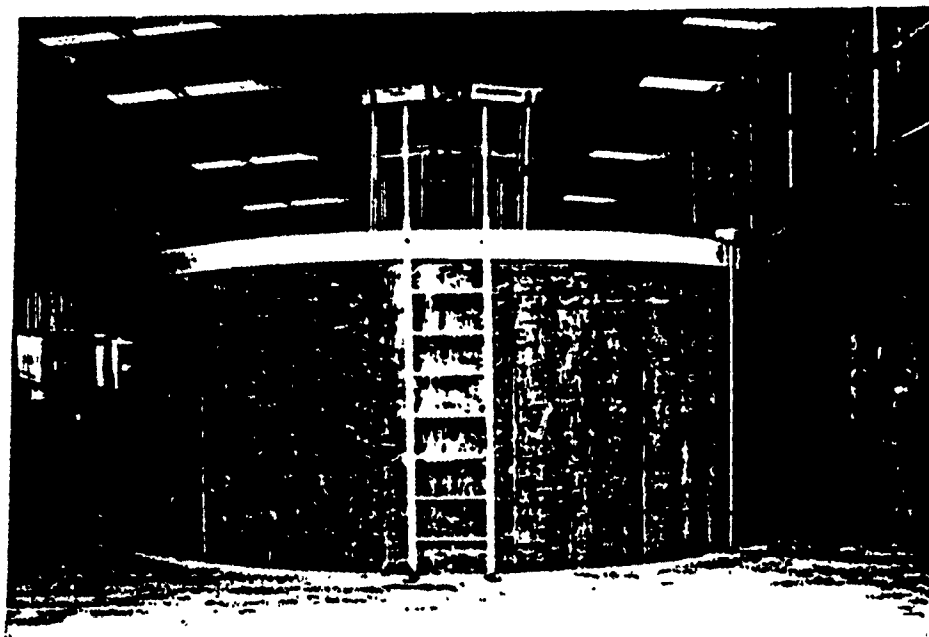


Figure 2.1 A View of the Centrifuge Facility at Tyndall AFB

arm assembly, terminal box for control and test connections.

The hydraulic drive system consists of an electric drive motor coupled to a variable-displacement pump, a constant-displacement fluid motor couple to the rotor drive shaft, and two pressure-relief valves. A 4-way solenoid-operated spring-loaded control valve provides rotational stability, maximum hunting, and constant torque characteristics. The hydraulic power unit is enclosed in the console, and the fluid motor is installed at the bottom of the rotor assembly (Figure 2.2). Maximum pressure of the hydraulic system has been set at approximately 2,200 psi.

The boom consists of two symmetrical cantilever arms, and an adjustable 30-in. square cradle-type mounting platform carried on aircraft-type roller bearings. The platform is held by two arms attached to the spokes by two pivots. It can be locked into horizontal, 45, 90, 135 or 180 degree positions. This permits the soil surface to remain perpendicular to the vector sum of the centrifuge acceleration and the acceleration due to gravity.

One of the unique features of the machine is the automatic dynamic balancing system. Dynamic balance is accomplished automatically by vertical displacement of the two arms of the boom until the center of gravity of the opposing mass lies in the same horizontal plane. It requires approximately 20 seconds for full compensation. If compensation cannot be accomplished within the 12-in. travel limitations, the balance motor is automatically shut down by limit switches. Corrective measures are indicated by the relative attitudes of the mounting

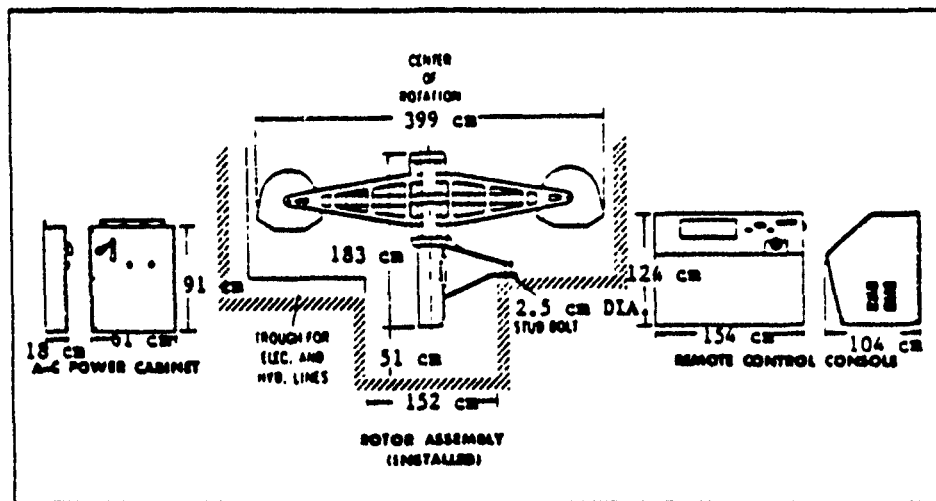


Figure 2.2 Rotary Accelerator (Model E-185) - Outline Drawing

platforms after shut down.

Hydraulic and electrical services are available to the model in flight. The hydraulic lines may be used to conduct compressed air or fluids from the outside control area to the model. Hydraulic services are transmitted through rotary joints. Electrical signals are transmitted to the centrifuge rotor and then to the model in flight through a stack of slip rings. A total of 40 slip rings (electrical channels) are provided in the machine, of which 28 are sending power and receiving signals from transducers which monitor the behavior of the model. These 28 slip rings include 12 instrumentation slip rings (shielded-conductor) designed for 1-amp, low resistance and low noise, and 16 power slip rings (shielded-conductor) of 5-amp current rating. The twelve slip rings not used for test purposes are part of the static and dynamic balancing motor and control circuitry for television. A summary of major specifications is listed in Table 2.2.

Table 2.2 Major Specification

---

Maximum centrifugal capacity	30,000 g-lb
Maximum acceleration	100 g
Maximum payload	500 lb.
Maximum effective radius	72 in.
Maximum number of rotation	220 rpm
Space of swinging platform	30 in. x 30 in.
Electric Slip Rings	40

---

## 2. Video Recording System

Video camera and recording devices are also available as part of the monitoring system. This video camera is mounted near the hub of the centrifuge. This system provides a continuous and instantaneous monitor of the test while in progress, and a permanent, replayable record of model tests.

## 3. Data Acquisition System

Digital oscilloscopes (Nicolet Model 4094) have been used for collecting sensor signals from model structures for centrifuge model study. The Model 4094 digital oscilloscope with multi-channel plugs is capable of performing acquisition with 12 bit resolution at a rate of 2 million sample/sec (16 bits samples). The system allows zero time to be set anywhere in the displaying area and enables two-channel measurements with each channel set at an independent pre- or post-trigger delay. It displays these two functions as well as a combination of them. Also, the system, a combination of them. A HP plotter interfaced with the oscilloscope has been used to create hard copy records.

## C. FABRICATION OF MODEL BOX

A requirement of centrifuge modeling is the fabrication of a model box that contains the small-scale model of the structure together with the soils sample. The dimensions of the model box were made small enough to fit the centrifuge swing bucket platform, and large enough to house the structure model and a sufficient amount of soil sample. The model box has a platform

base of 24 in. x 24 in. and a total height of 17.875 in. It was totally made of 2024-T-35 aluminum plates welded at the sides and the bottom at almost 100% penetration. The model box has a top lid as well a front lid for easy access to the model and cleaning purposes. Both lids are secured by steel screws, the front lid is designed to withstand the internal lateral pressure caused by the soil at increased gravity conditions (100 g's), while the top lid is designed to withstand the pressure generated by the surcharged system (50 psi).

The base of the model box extends 2 in. from every side and has a hole drilled into each corner so as to enable the researchers to bolt down the box onto the centrifuge platform to prevent it from slipping. Although theory states that the box would not slip off the swing bucket while the centrifuge is running, this is merely a safety precaution taken by the researchers. For easy and safe handling of the model box, the top edges of the two opposing sides are extended and holed-out to accomodate crane hooks. A detailed diagram of the model box is illustrated in Figure 2.3

#### D. ARCH STRUCTURE MODEL AND STRAIN GAUGES

The model semi-circular concrete arch structure was made of a microconcrete mix composed of gypsum molding plaster and silica sand, with gypsum:aggregate:water ratio of 1:2:1 by weight. The structure has an inner diameter of 9 in. and a shell thickness of 0.3 in. The total length was 16 in. The structure model was complete with miniature reinforcement set on both circumferential and longitudinal directions. Reinforcement

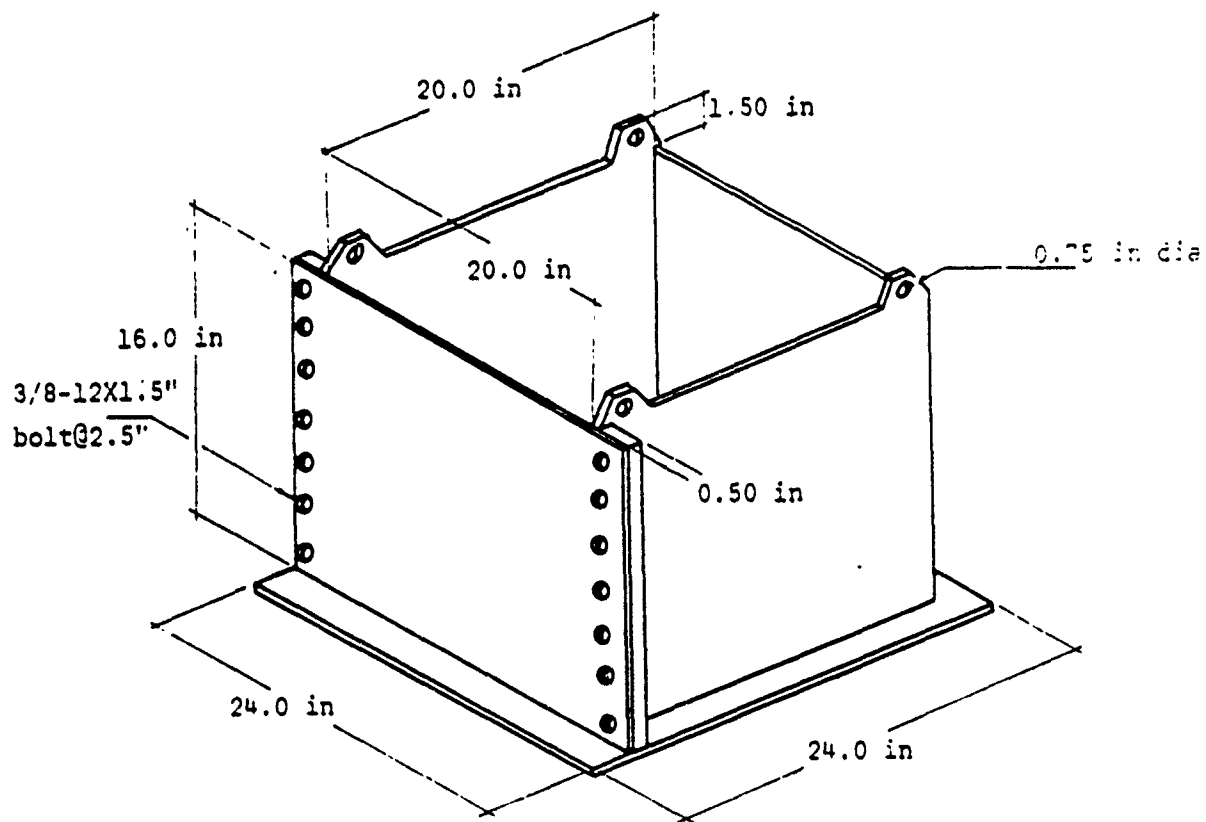


Figure 2.3 The Centrifuge Model Box

bar diameter was 22-gauge. The model arch structure also included a reinforced floor slab made of the same material (see Figure 2.4).

Five pairs of strain gauges (gauge type CEA-13-125UW-120) manufactured by Measurement Group, Inc. were used to measure strain along the circumference of the structure at midspan. Gauges were mounted at 5, 45, 90, 135, 175 degrees and hooked up in a full-bridge fashion. The arch structure with attached strain gauges placed in the model container is shown in Figure 2.5.

#### E. MODEL PREPARATION

##### 1. Miniaturized Concrete Arch Structure

The structures used in the tests are 1/60th size of the prototype structure. It is made of a microconcrete mix composed of gypsum plaster as cement and silica sand as aggregate. Scaling down the prototype to 1/60th size resulted with a model that requires a membrane thickness of 0.3 inch. Due to this, the consistency of the microconcrete mix had to be very slurry for it to go down the mold. The final mix had a gypsum:aggregate:water ratio of 1:2:1.

The mold is made up of two aluminum tubings, one with an outer diameter equal to the desired inner diameter of the model, the other with an inner diameter equal to the desired outer diameter of the model. The frame work is made of plexiglass which also serves to hold the reinforcement cage in place while letting the mix to cure.

The miniaturized reinforcement used was 22-gauge wires in

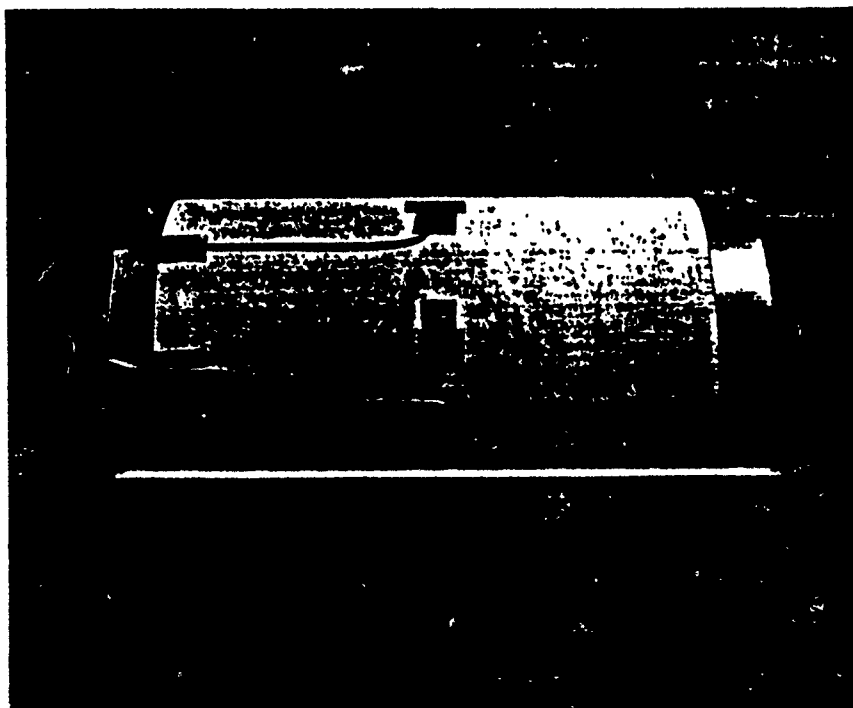
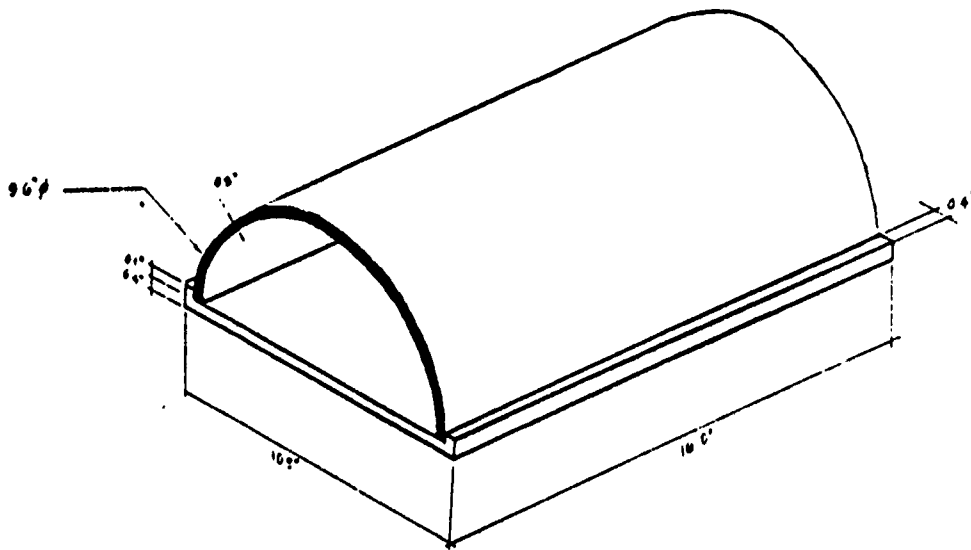


Figure 2.4 The Miniaturized Scale Model with Strain Gauges

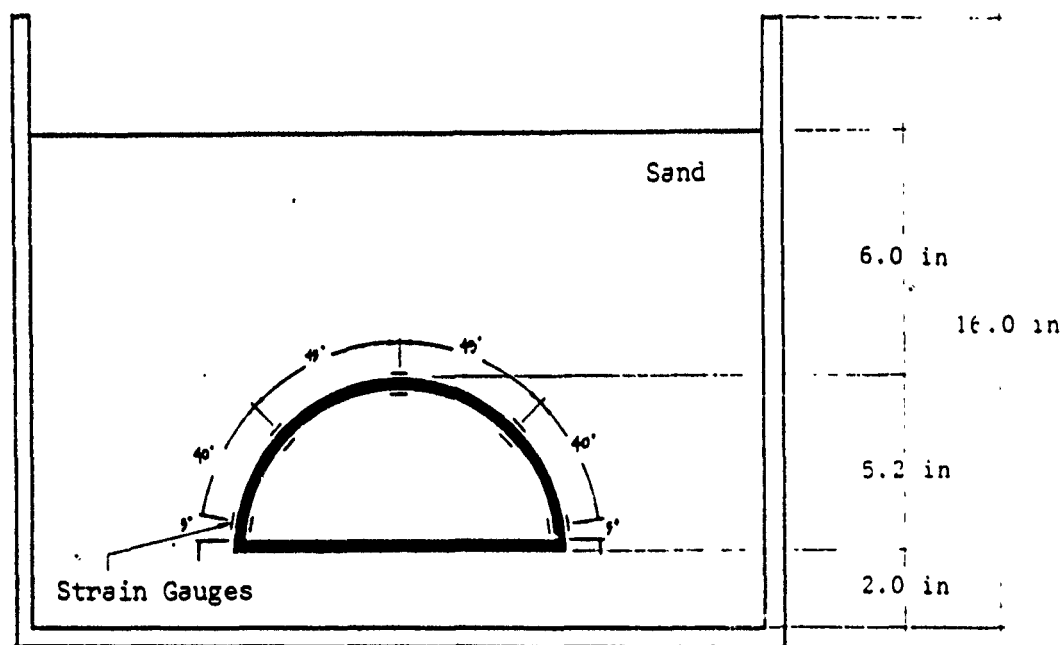


Figure 2.5 The Instrumented Arch Structure in the Model Box

both the longitudinal and circumferential directions. Prior to the installation of the wires, it was necessary to apply a small amount of pretension to remove all bends and coils. Also, it was necessary to roughen up the surface of the wires with very coarse sand paper to assure better bonding to the microconcrete.

The models were left to cure for two days and then were coated with concrete shellac to preserve the water content. Allowing the models to dry for more than the set amount of time produced a very chalky and brittle surface. After application of shellac, the structure was left to cure for at least another two days before testing.

## 2. Soil Pluviator

To attain reliable data from the tests, most of the variables must be held constant for every test. This includes the soil sample properties. Although grain size and sample height of the soil can easily be produced, it is the reproduction of the soil sample density that is important. For this purpose, the researchers use the sand raining method or, pluviation. This method is commonly used due to its simplicity and for the simple reason that it is the best method of reproducing soil samples. The purpose involves forming a sand mass to a homogeneous condition with a specified density, using a process that can be repeated as many times without the variation of the sand properties other than as chosen by the researchers.

A sand pluviator was designed and built at AFESC/RDCO facility at Tyndall Air Force Base (Figure 2.6). It has a total

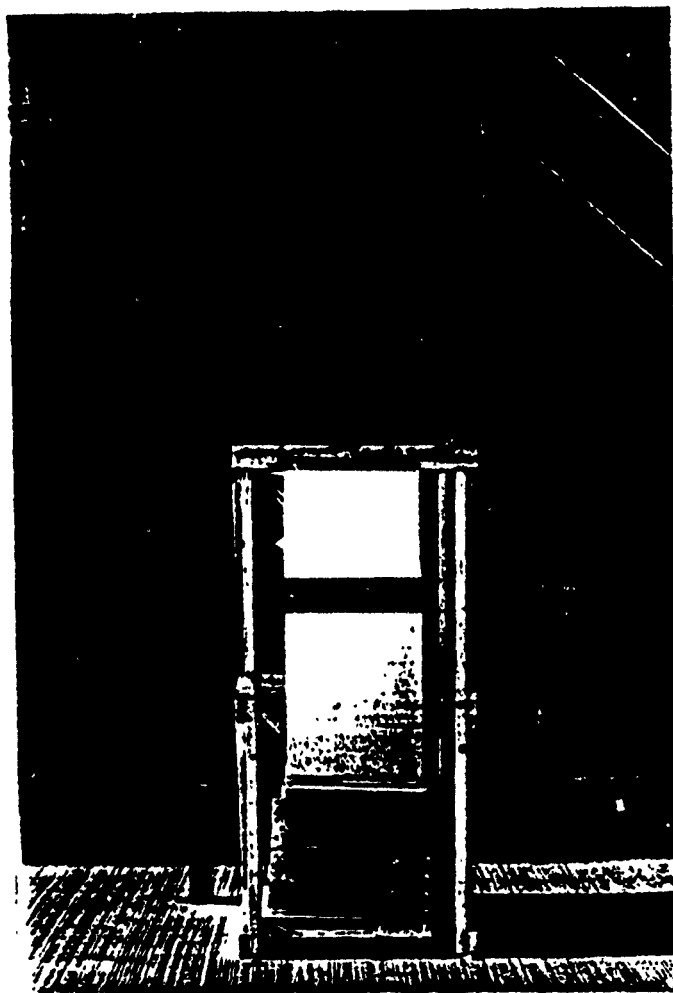


Figure 2.6 The Soil Pluviator

height of approximately 90 inches and covers a minimum area of 12 square feet. The pluviator is capable of producing sand samples of extreme densities. By selecting the proper perforation board, the researcher can control the desired discharge rate resulting to a specific sample density.

The soil strata used as a model consisted of three pluviation steps. The first step was pluviating a shallow sand layer on the bottom of the model box to act as the bedding layer. At the completion of this step, the model box was pulled out from underneath the pluviator and the model was then put in place. The second step was to bury the structure to the desired embankment depth using the same process. Again, the model box is pulled out from underneath the pluviator to set the burster slab model in place. The final layer of sand is then pluviated and the model box is ready to be mounted on the centrifuge swing bucket.

### 3. Loading Model Box

The first step taken before loading the model box onto the centrifuge swing bucket was to weigh the model box complete with the lid with its contents to determine the amount of counterweight to be used. Since the model box was set on the center of the platform, the counterweight needed was equal to box weight itself (+ 5 lbs). As long as the red indicator light remains off after setting the model box and the counterweight, the system is considered balanced. Note that the weight on either side should not exceed 500 lbs. The model box was then secured onto the centrifuge swing bucket by bolting it down on

the platform (Figure 2.7).

As soon as the model box is secured onto the swing bucket, all instrumentation is wired up to the slip rings taking note of all channel designations. At the centrifuge control panel, all wires were hooked up to designated ports on the channel switch and onto the strain indicator.

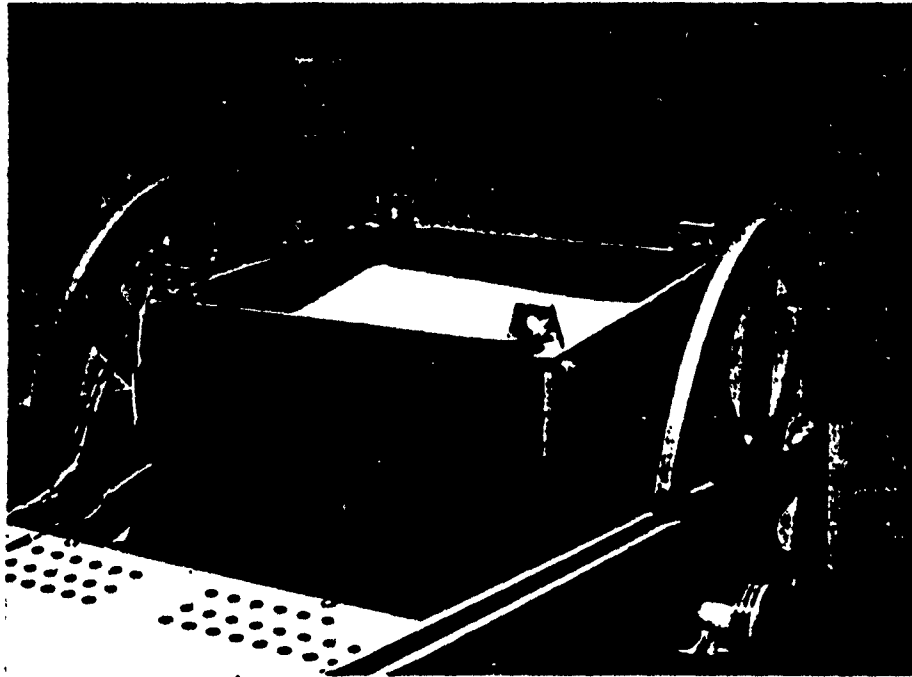


Figure 2.7 The Model Box on the Centrifuge Swing Bucket

## SECTION III

### FINITE ELEMENT ANALYSIS

#### A. DESCRIPTION OF THE COMPUTER CODE

The computer code, CANDE (Culvert Analysis and DEsign), used in this study was developed by Katona et al. (References 11 and 12). The basic assumptions of the program are: plane strain geometry and loading, small displacement theory, and quasistatic response. The following description summarizes salient features of CANDE used in the analysis.

##### 1. Modeling of Structure

The box culvert was modeled as a series of straight line segments with a one-dimensional beam-column bending element comprising each segment. This bending element employs a plane-strain formulation which neglects shearing deformations. Two nodes with three degrees of freedom per node (horizontal and vertical displacement and a rotation) define each element. At each node, cubic and linear displacement approximations were used in calculations of displacements in the transverse and axial directions, respectively. Figure 3.1 shows the coordinate system of the beam element.

##### 2. Modeling of Soil

Nonconforming quadrilateral and triangular elements were used to represent the soil (see Figure 3.2). The quadrilateral,

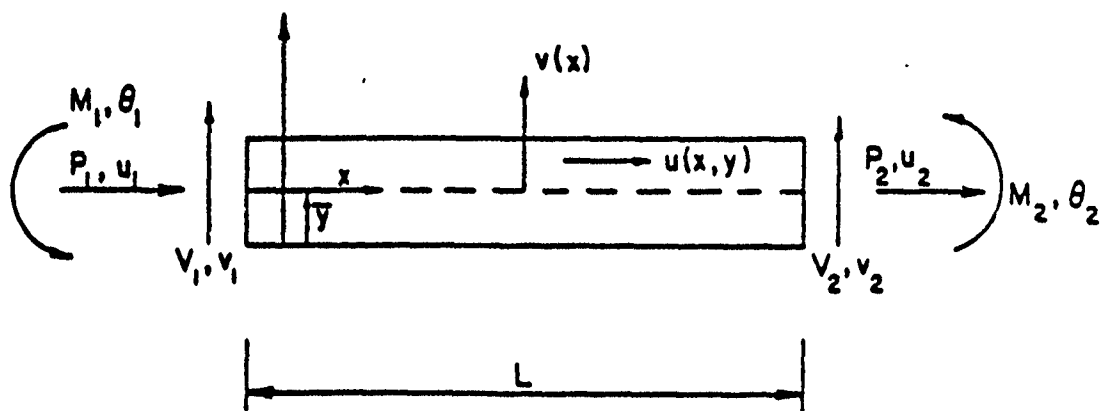


Figure 3.1 The Coordinate System of the Beam Element in CANDE

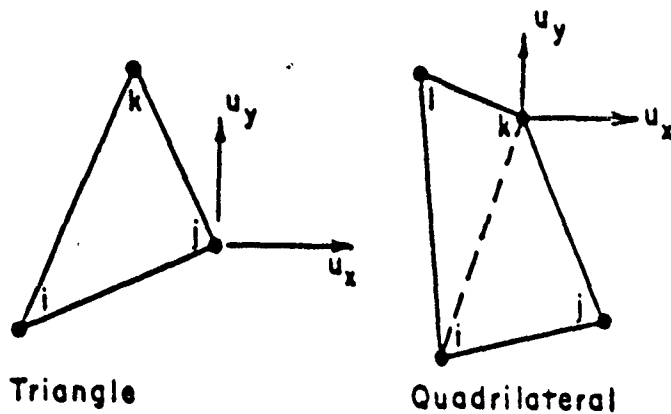


Figure 3.2 The Element Types Used for Soil Model in CANDE

defined by four nodes with two degrees of freedom (horizontal and vertical displacements) per node comprise two triangles with complete, quadratic, interpolation functions specified within each triangle. Application of appropriate constraints and static condensation procedures result in a four-node quadrilateral element (Reference 11).

There are four material characterizations available for the soil properties: linear elastic; incremental elastic (overburden dependent); extended-Hardin; and Duncan's hyperbolic stress-strain relationship, which employs tangent Young's modulus and tangent bulk modulus formulations (References 7, 12, 33).

### 3. Modeling of Slip

A constrained finite element formulation, which is based on a generalized principle of virtual work, was used to model the relative movement of the soil with respect to the pipe at the soil-structure interface, and relative movement of the soil with respect to the soil-soil interface (i.e., trench). An interface element is defined by a set of paired nodes joining two elements as shown in Figure 3.3. The paired nodes which have two degree of freedom per node (vertical and horizontal displacement), initially take the same position in space before any loading, but are assigned to separate elements. Therefore, each node responds individually under any applied loading. In addition, a third node, which is assigned between the paired nodes, provides normal and shear forces existing between the paired nodes. It should be observed that these interface forces arise only from

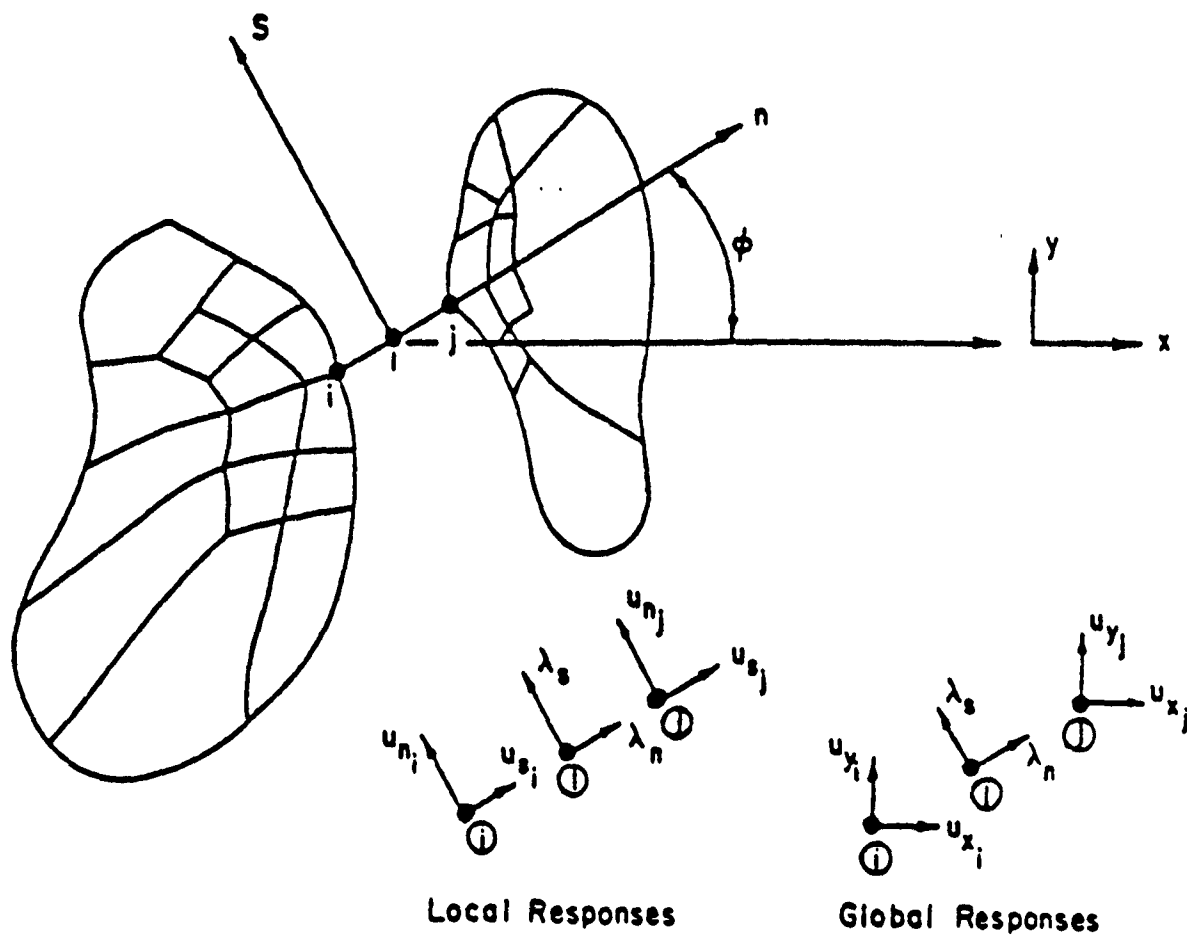


Figure 3.3 Nodes for Constraint Interface Element in CANDE

the adjoining element interaction and applied forces at the paired nodes.

#### 4. Modeling of Incremental Construction

CANDE uses incremental iterative solution techniques to represent the placing of the culvert and embankment in a series of soil layers. The basis of the techniques is superposition of solutions from successive soil layers and a newly added layer. At each increment, iterative calculations determine soil and structure moduli until equilibrium is approximated within an allowable error.

#### B. FINITE ELEMENT PARAMETERS

##### 1. Finite Element Mesh and Boundary Conditions

The finite element grid with boundard conditions used in this study is shown in Figure. 3.4. Since the model and its loading is symmetric, only half of the mode was analyzed. Boundary conditions on the culvert used in the analysis are show in the figure: a fixed movement conditions in the horizontal direction and free movement condition in the vertical direction. The arch structure was represented by 12 beam-column elements.

##### 2. Soil-Culvert Interface and Incremental Solution

###### Procedure

A fixed condition was used at the soil-culvert interface. Although it is possible to represent the slip between the continuum (soil) and beam elements, the fixed condition was used

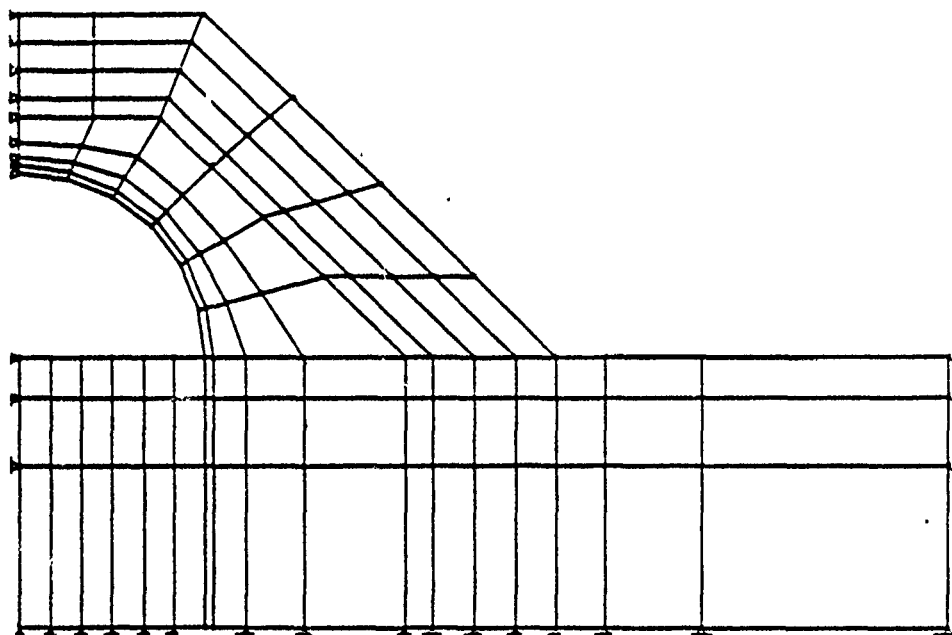


Figure 3.4a Mesh No. 1: 3 Rock Layers, 45 Degree Slope

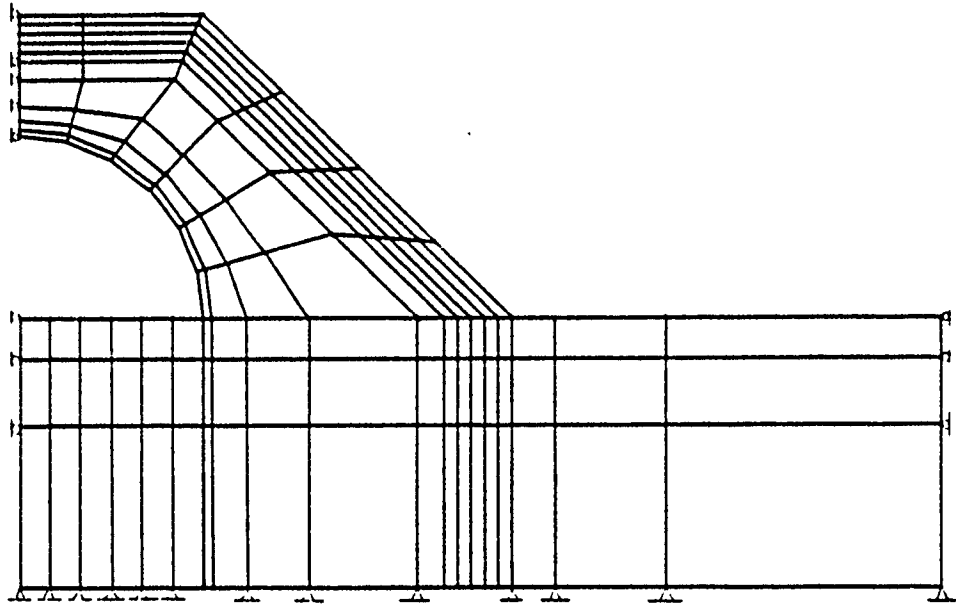


Figure 3.4b Mesh No. 2: 5 Rock Layers, 45 Degree Slope

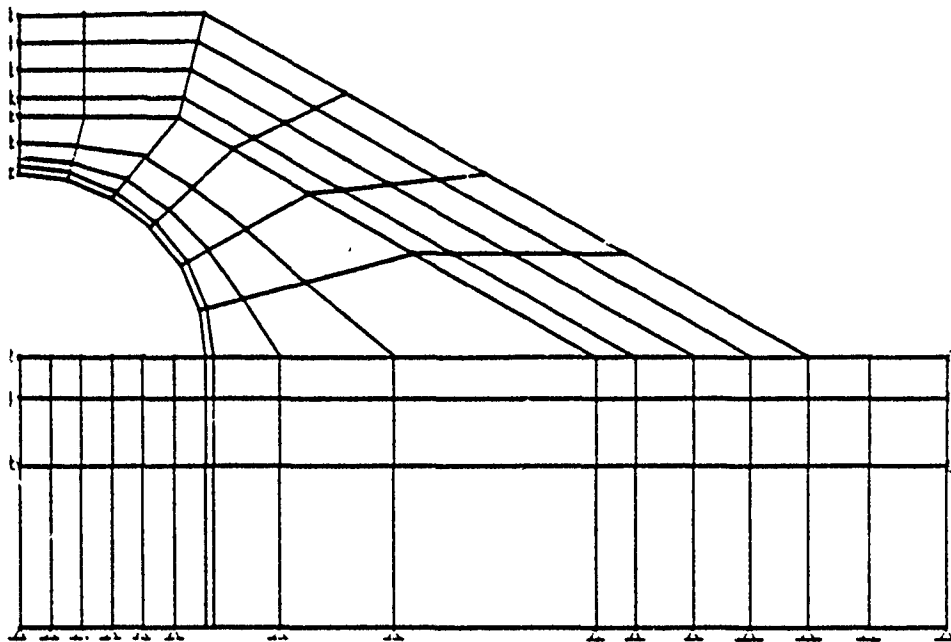


Figure 3.4c Mesh No. 3: 3 Rock Layers, 30 Degree Slope

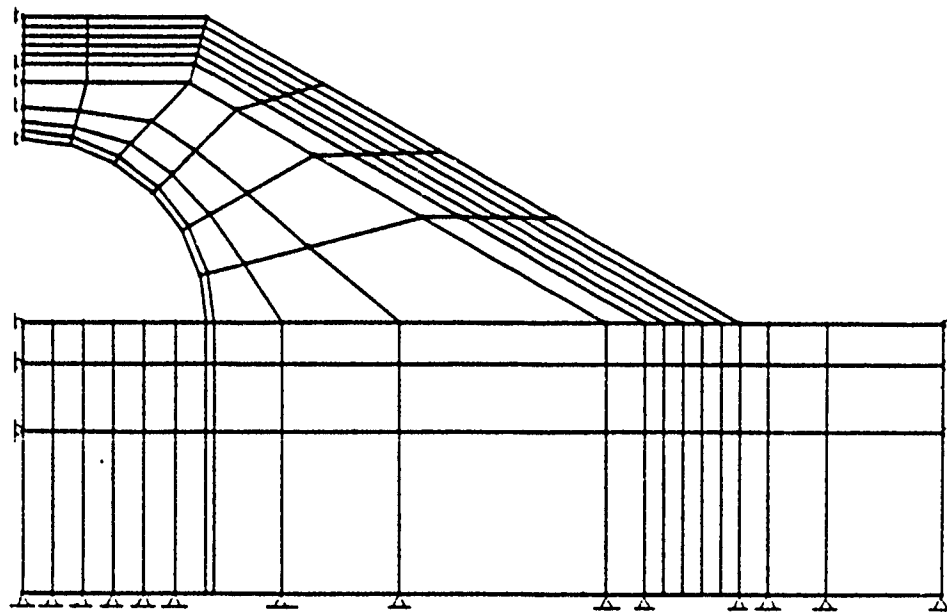


Figure 3.4d Mesh No. 4: 5 Rock Layers, 30 Degree Slope

in this preliminary study due to large amounts of CPU (Central Processing Unit) time, and substantial computational costs when slip was allowed.

The incremental solution procedure for embankment and trench simulated the actual installation process of placing soil layers in a series of lifts. Figure 3.5 shows the construction increment numbers of element groups entering sequentially into a system. The first construction increment included placing all bedding pad, in situ soil, and the arch structural elements. Subsequent increments, numbers 2 through 9, were gravity loaded elements of fill soil.

### 3. Material Properties

The soil model employed in the study is a characterization proposed by Duncan et al. (References 7 and 12) which has had a substantial history of development and application over the last decade. This soil model characterizes soil behavior with a variable tangent Young's modulus and tangent bulk modulus. Eight parameters are needed to define a particular soil in loading:  $K$ ,  $n$ ,  $R_f$ ,  $c$ ,  $\phi$ , and  $\Delta\phi$  for the tangent Young's modulus; and  $K_b$  and  $m$  for the tangent bulk modulus. Table 3.1 shows the material properties used for soil, concrete arch, rock, and burster slab in the analysis.

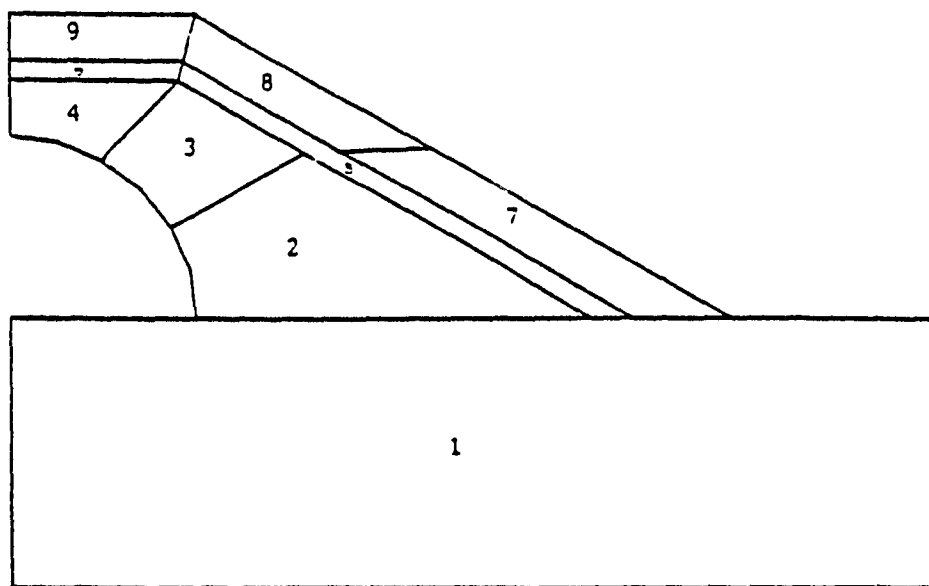


Figure 3.5 Incremental Construction

Unified Soil Classification	RC* Stand. AASHTO	$\gamma_m$ k/ft <sup>3</sup>	$\phi_o$ deg	$\Delta\phi$ deg	c k/ft <sup>2</sup>	K	n	$R_f$	$k_b$	m
GW, GP SW, SP  Coarse Aggregates	105	0.150	42	9	0	600	0.4	0.7	175	0.2
	100	0.145	39	7	0	450	0.4	0.7	125	0.2
	95	0.140	36	5	0	300	0.4	0.7	75	0.2
	90	0.135	33	3	0	200	0.4	0.7	50	0.2
SM  Silty Sand	100	0.135	36	8	0	600	0.25	0.7	450	0.0
	95	0.130	34	6	0	450	0.25	0.7	350	0.0
	90	0.125	32	4	0	300	0.25	0.7	250	0.0
	85	0.120	30	2	0	150	0.25	0.7	150	0.0
SM-SC  Silty-Clayey Sand	100	0.135	33	0	0.5	400	0.6	0.7	200	0.5
	95	0.130	33	0	0.4	200	0.6	0.7	100	0.5
	90	0.125	33	0	0.3	150	0.6	0.7	75	0.5
	85	0.120	33	0	0.2	100	0.6	0.7	50	0.5
CL  Silty Clay	100	0.135	30	0	0.4	150	0.45	0.7	140	0.2
	95	0.130	30	0	0.3	120	0.45	0.7	110	0.2
	90	0.125	30	0	0.2	90	0.45	0.7	80	0.2
	85	0.120	30	0	0.1	60	0.45	0.7	50	0.2

\* RC = relative compaction, in percent

Table 3.1 Duncan's Material Characterization Used for Soil Model

CONCRETE	
Compressive strength, $f'_c$	5,000 psi
Young's modulus in elastic range, E	4,070,000 psi
Poisson's ratio, $\nu$	0.25
Unit weight, $\gamma$	150 pcf
Strain at which tensile cracking occurs	0.0001
Strain at elastic limit in compression	0.0013
Strain at initial compressive strength,	0.0040

REINFORCING STEEL	
Yield stress, $f_y$	60,000 psi
Young's modulus, E	29,000,000 psi
Poisson's ratio, $\nu$	0.3
Spacing of reinforcement	1.5 in.
Area of inner cage reinforcement	0.31 sq. in./in.
Area of outer cage reinforcement	0.31 sq. in./in.
Thickness of concrete cover to center of inner cage	1.25 in.
Thickness of concrete cover to center of outer cage	1.25 in.

Table 3.2 Concrete and Steel Properties Used for Arch Structure

Type	Young's modulus E	Poisson's ratio $\nu$	Unit weight $\gamma$
Rock	1,500,000 psi	0.2	86.94 pcf
Burster slab	4,070,000 psi	0.25	145.0 pcf

Table 3.3 Material Properties used for Rock and Burster Slab

## SECTION IV

### RESULTS AND DISCUSSIONS

#### A. CENTRIFUGE MODEL STUDY

Since the authors are the first time-users of the centrifuge facility at Tyndall Air Force Base with a small-scale structure and instrumentation, a series of centrifuge model tests was first performed as a pilot study to check the proper operations of the centrifuge machine and instruments. During this preliminary test, the instruments faced two major difficult problems: (1) a limited number of slip rings available for data transmission, and (2) brush noise caused by dynamic vibration occurred at the centrifuge slip rings. The voltage fluctuations generated by the noise at the slip rings were found to be much greater than the instrument signals themselves. The major centrifuge model tests, therefore, were not able to be performed during the stay at Tyndall Air Force Base due to the limitation and unavailability of testing equipments. Rather, this section discusses the various computer-based data acquisition systems required to overcome these problems for a future centrifuge model study. The description given below is a brief one; readers interested in more detailed information should refer elsewhere (References 8,9,17-22,26,32).

#### Transmission of Signals:

Direct transmission of signals is used the most in model

studies mainly because of its simplicity and relatively low cost. Also there is no distortion of signals. When used in centrifuge modeling, direct transmission consists of the physical linkage of system components by wire cables. Brush-and-slip ring riggings are a commonly used method of providing a signal path from the centrifuge shaft to the outside. Brush noise is caused by dynamic vibration in the area in which the brush is in contact with the slip ring. This vibration in contact area gives a variation in circuit resistance. An increase in signal level before reaching slip rings, through amplification, can give a desirable increase in the signal-to-noise ratio. Another beneficial technique is to decrease the total brush resistance by providing multiple parallel current paths; noise would be reduced because variations in brush contact for individual brushes would not be as significant when other brushes are in the path. If a large number of slip rings dedicated to signal transmission are available, the direct transmission system should be considered. It has the advantage of simplicity and uninterrupted transmission of signals.

However, for most of the smaller size centrifuges, there are only a limited number of slip rings for data transmission. A multiplexer-demultiplexer unit (indirect method) is therefore used to facilitate the transmission of signals from a relatively large number of sensors. The two most commonly used multiplexer-demultiplexer units are the time division unit and the frequency modulation (FM) frequency division unit. The time

division unit works as a synchronized channel selector as shown in Figure 4.1 where the frequency division unit works as a dedicated frequency carrier along with FM detectors as shown in Figure 4.2. Of the two indirect methods of signal transmission, the time division technique is relatively simple and less costly to install; however, additional control signals are needed to synchronize the functions of the multiplexer and demultiplexer. This additional control and operation time impedes the sampling rate of the system. The frequency division technique, on the other hand, is costly but capable of transmitting signals at much higher rates. Since the FM system is sensitive only to frequency variations and not amplitudes, it is immune to most noises induced along the transmission line.

It should also be mentioned that wireless sensors can be adopted to transmit radio frequency signals thus bypassing the use of connecting wires between sensors and the signal conditioning unit. However, these sensors are very expensive and usually too big in size and too heavy, not readily suitable for geotechnical use. The author does not foresee the need to use wireless sensors in centrifuge modeling in the future.

## B. FINITE ELEMENT ANALYSIS

### 1. The Influence of Installation Type

The first part of this investigation deals with the influence of the type of installation on the relative displacement of the crown of the structure (refer to Figures 4.3 thru 4.6). The comparisons have been made between a system with a 3-layer rock cover versus one with a 5-layer rock cover. All other variables were considered in the comparison to determine

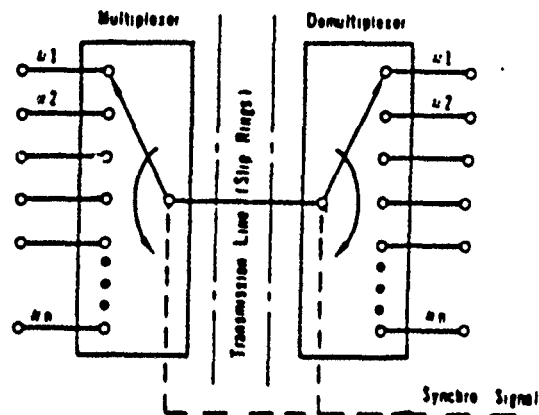


Figure 4.1 A Time Division Multiplexer-Demultiplexer Unit

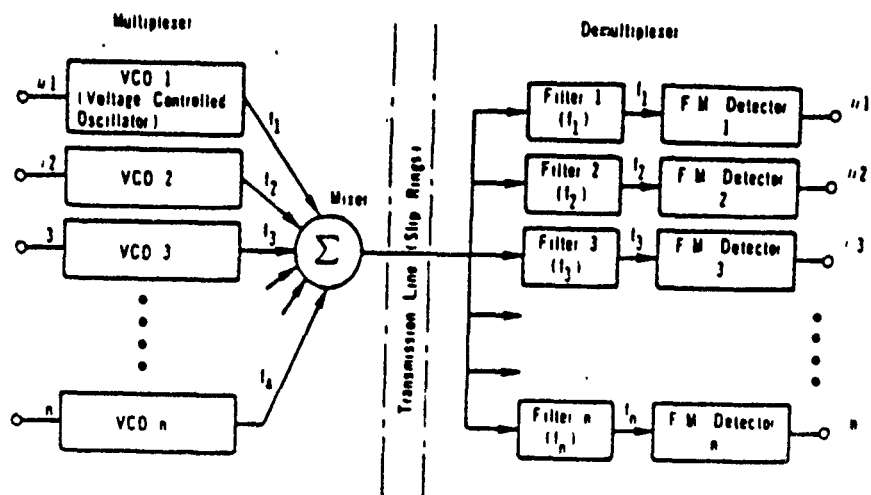


Figure 4.2 A Frequency Division Multiplexer-Demultiplexer Unit

# CL85 BEDDING, 30 DEG SLOPE

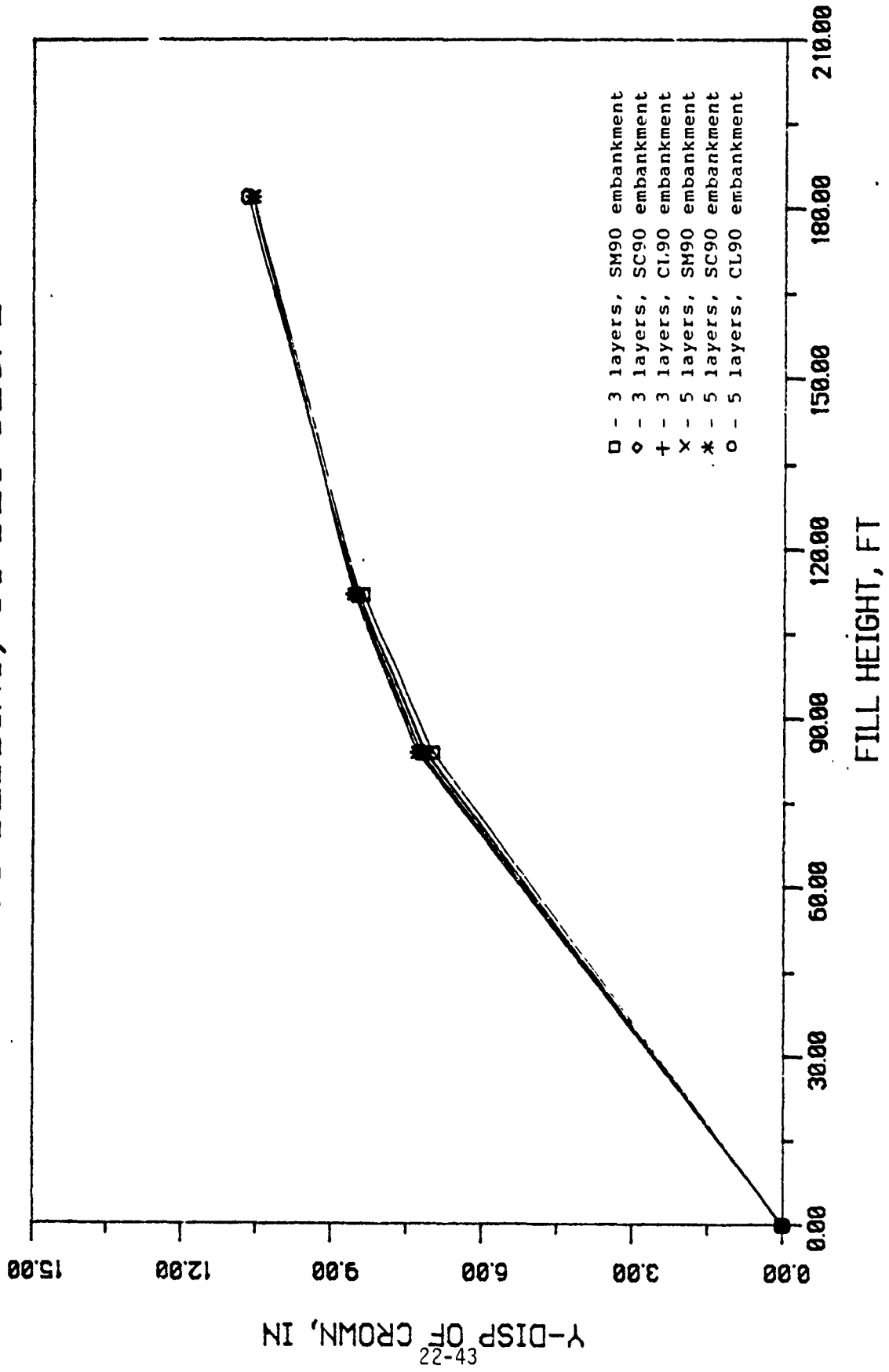


Figure 4.3 Relative Crown Deflection vs. Fill Height for Case 11A

# SM85 BEDDING, 30 DEG SLOPE

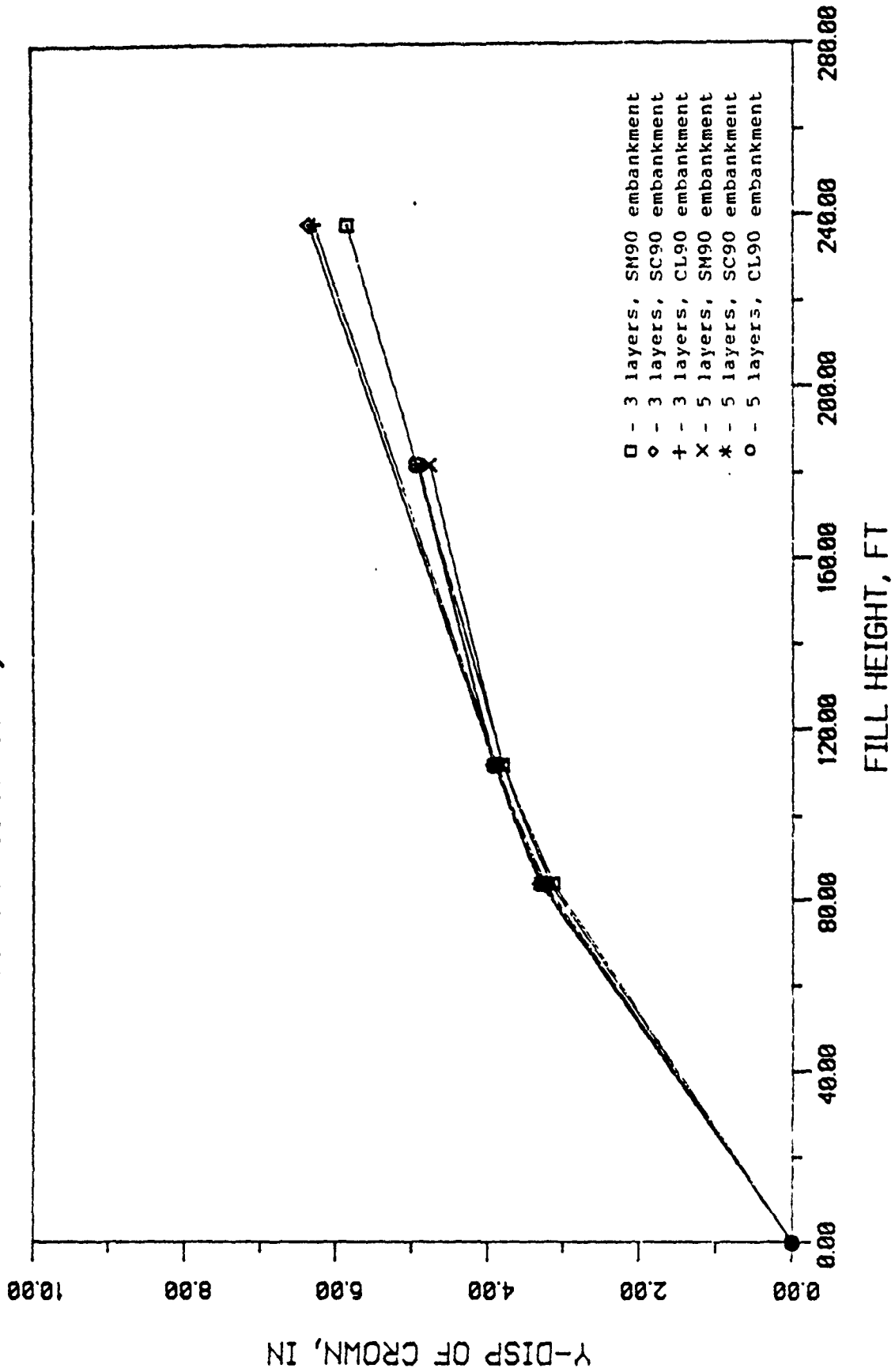


Figure 4.4 Relative Crown Deflection vs. Fill Height for Case 11B

# CL85 BEDDING, 45 DEG SLOPE

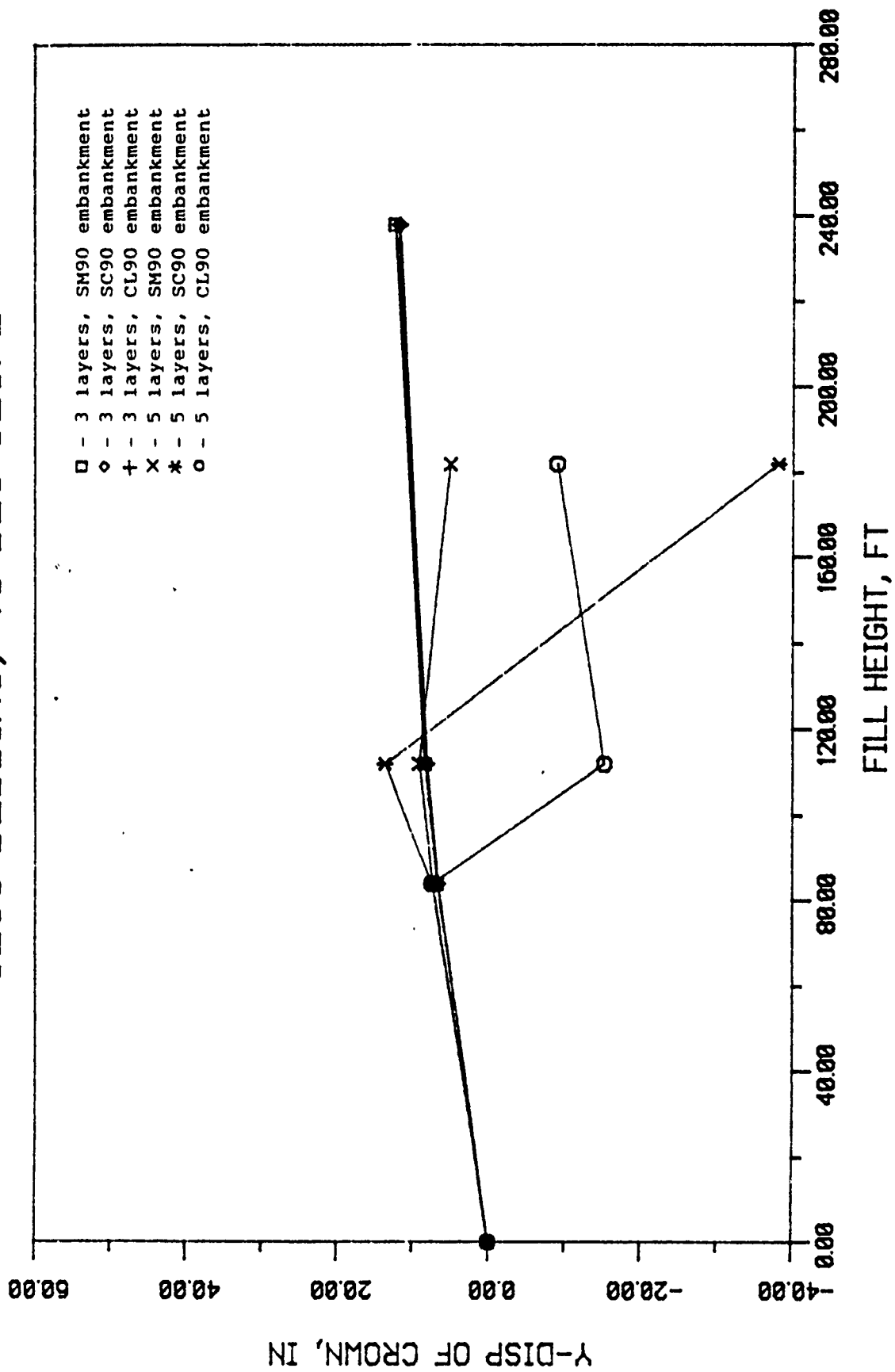


Figure 4.5 Relative Crown Deflection vs. Fill Height for Case 12A

# SM85 BEDDING, 45 DEG SLOPE

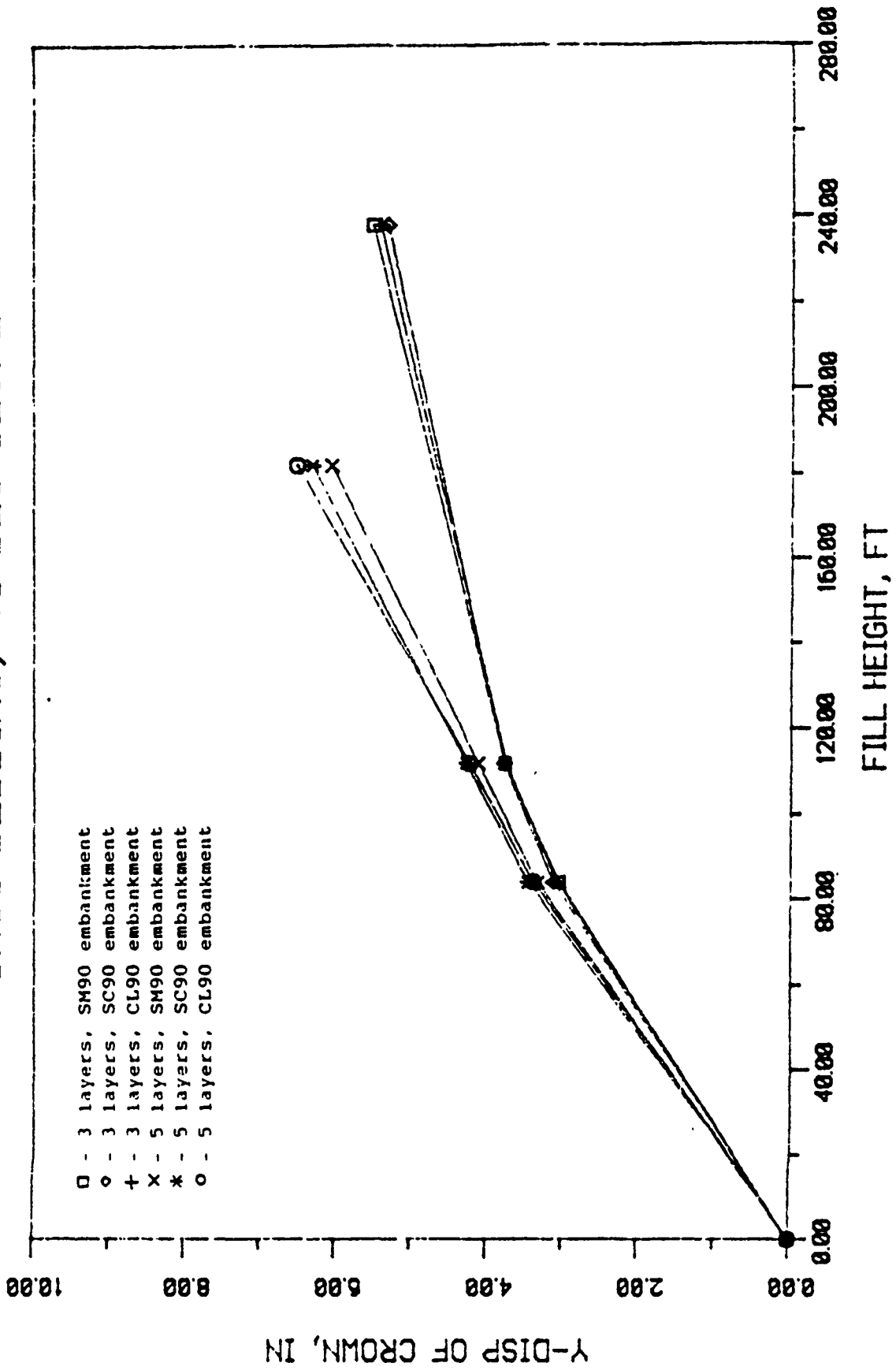


Figure 4.6 Relative Crown Deflection vs. Fill Height for the Case 12B

one with a 5-layer rock cover. All other variables were considered in the comparison to determine the degree of influence of installation type on the displacement of the crown.

For Case I1A where the structure is modeled on CL85 (clay) soil type bedding and 30-degree slope embankment, the finite element analysis predicted a steel safety factor equal to 1.00 at the end of eight construction increments when a 3-layer rock cover is installed, meaning that the steel reinforcement of the structure had failed under these conditions. A 5-layer rock cover proved to be the best alternative in this case.

As for Case I1B where the structure is modeled on SM85 (sand) soil type bedding and 30-degree slope embankment, the influence of the type of rock layer embankment can be seen at fill heights greater than 112 ft. It can clearly be seen that the system under a 5-layer rock embankment caused less crown deflection than the 3-layer type. Minimum relative crown deflection at fill height of 182 ft. is 4.76 inches and occurs when the embankment is of SC90 (sand-clay) type soil.

Case I2A deals with the structure modeled on CL85 soil bedding and 45-degree slope embankment. With the case where the 5-layer rock embankment system was installed, the finite element analysis predicted a steel safety factor and concrete compression safety factor both equal to 1.00 at the end of four construction increments, meaning that the structure had failed under these conditions. In this case, therefore, a 3-layer rock cover would be the best and only solution.

The last installation case examined is Case I2B where the

structure is modeled on SM85 soil type bedding and a 45-degree slope embankment. In this case the influence of the type of rock-layer installed is much more clearly defined. Case I2B shows that the system with a 3-layer rock cover causes less deflection of the crown of the structure. Differences in deflection of the crown is close to the 1.25-inch range. Even at a higher fill height, the system with a 3-layer rock cover causes less deflection than the system with the 5-layer rock cover. Minimum relative crown deflection at a fill height of 182 ft is 5.31 inches and occurs when the embankment soil is of SC90 type and the rock cover is of the 3-layer type.

The second part of the investigation deals with the influence of installation type on the bending moment developed at the crown of the structure depending upon the type of rock cover installed on the system (refer to Figures 4.7 thru 4.10). Similar to the discussion above, the comparison has been made between a system with a 3-layer rock cover versus one with a 5-layer rock cover. In Case I1A, the numerical analysis of the system predicted the failure of the structure under a 3-layer rock cover at the end of eight construction increments. And as for Case I2A, the same situation arised with a structure under a 5-layer rock cover but after the application of only four load increments. Therefore, the comparisons were limited to two cases.

Case I1B showed that at a fill height greater than 182 feet, the system with the 5-layer rock cover produced less bending moment at the crown compared to the one with the 3-layer

# CL85 BEDDING, 30 DEG SLOPE

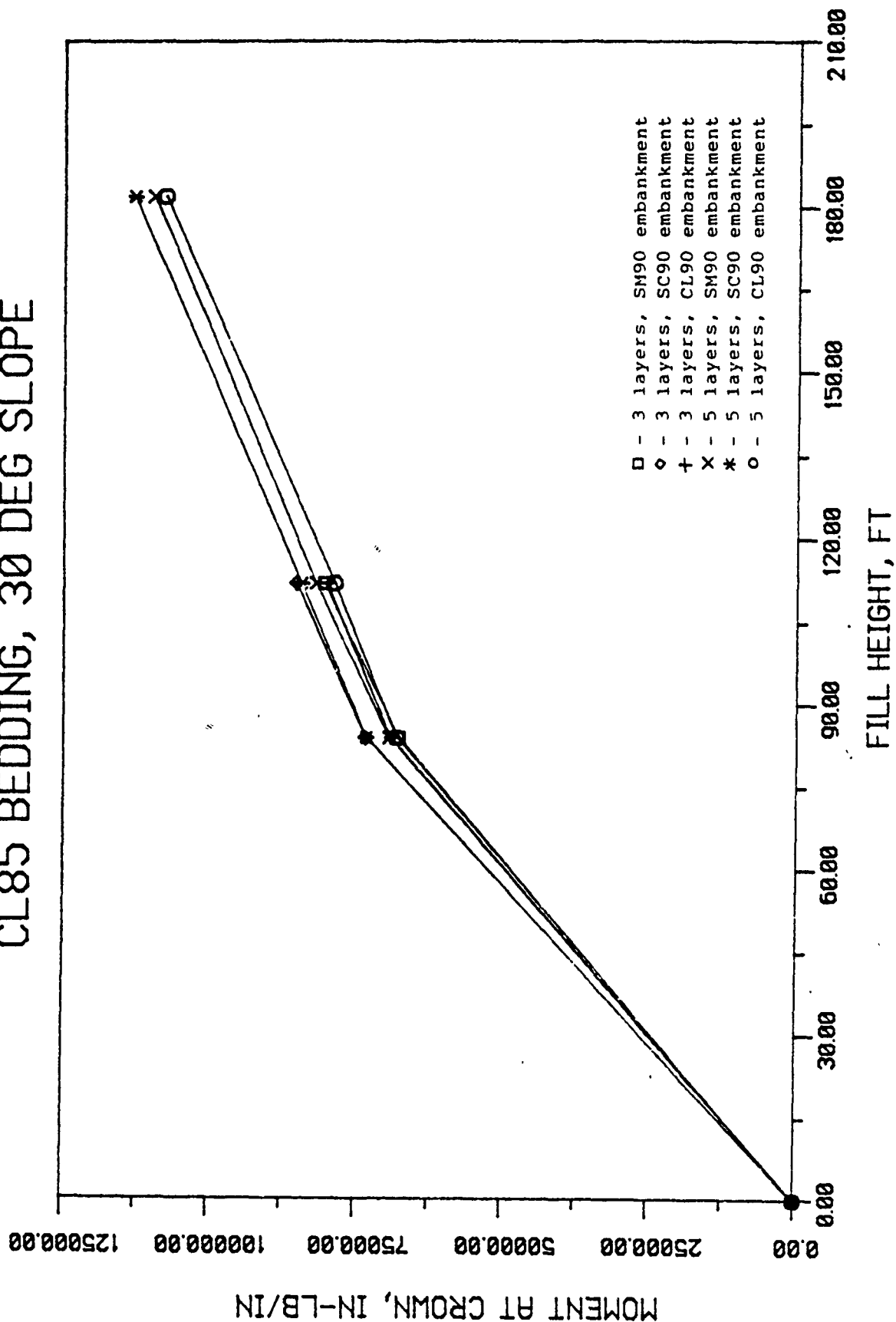


Figure 4.7 Crown Moment vs. Fill Height for Case 11A

# SM85 BEDDING, 30 DEG SLOPE

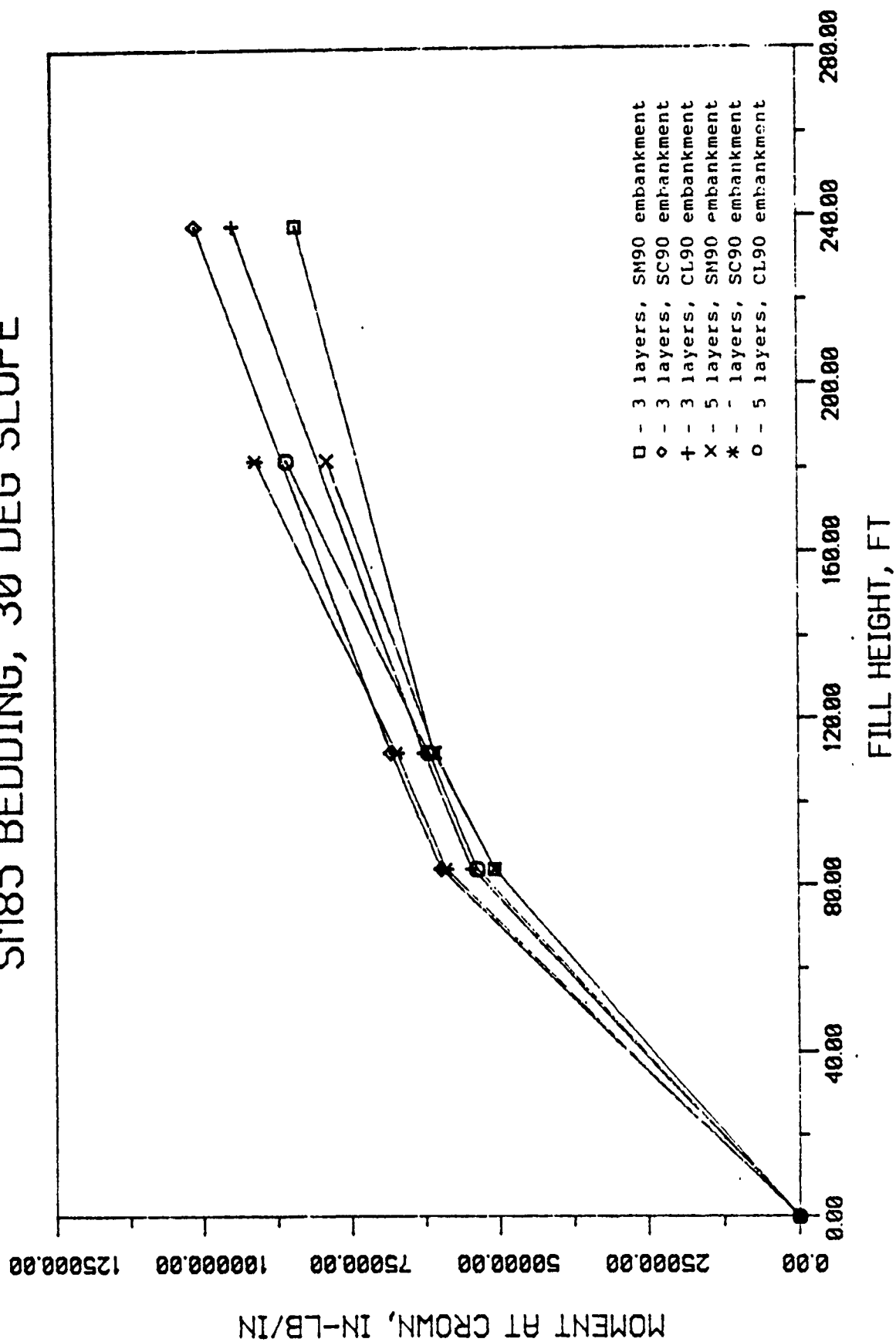


Figure 4.8 Crown Moment vs. Fill Height for Case 11B

# CL85 BEDDING, 45 DEG SLOPE

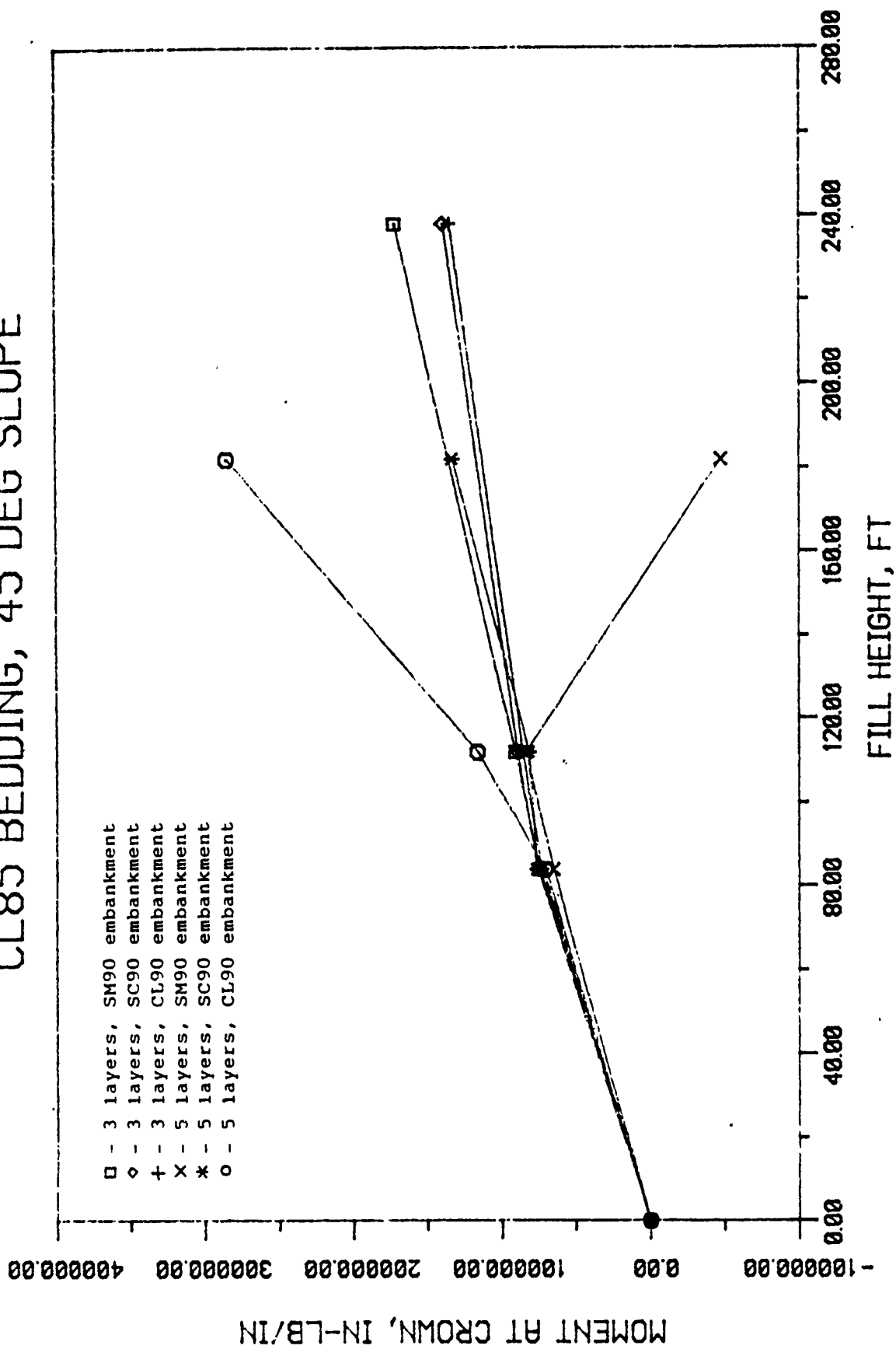


Figure 4.9 Crown Moment vs. Fill Height for Case 12A

# SM85 BEDDING, 45 DEG SLOPE

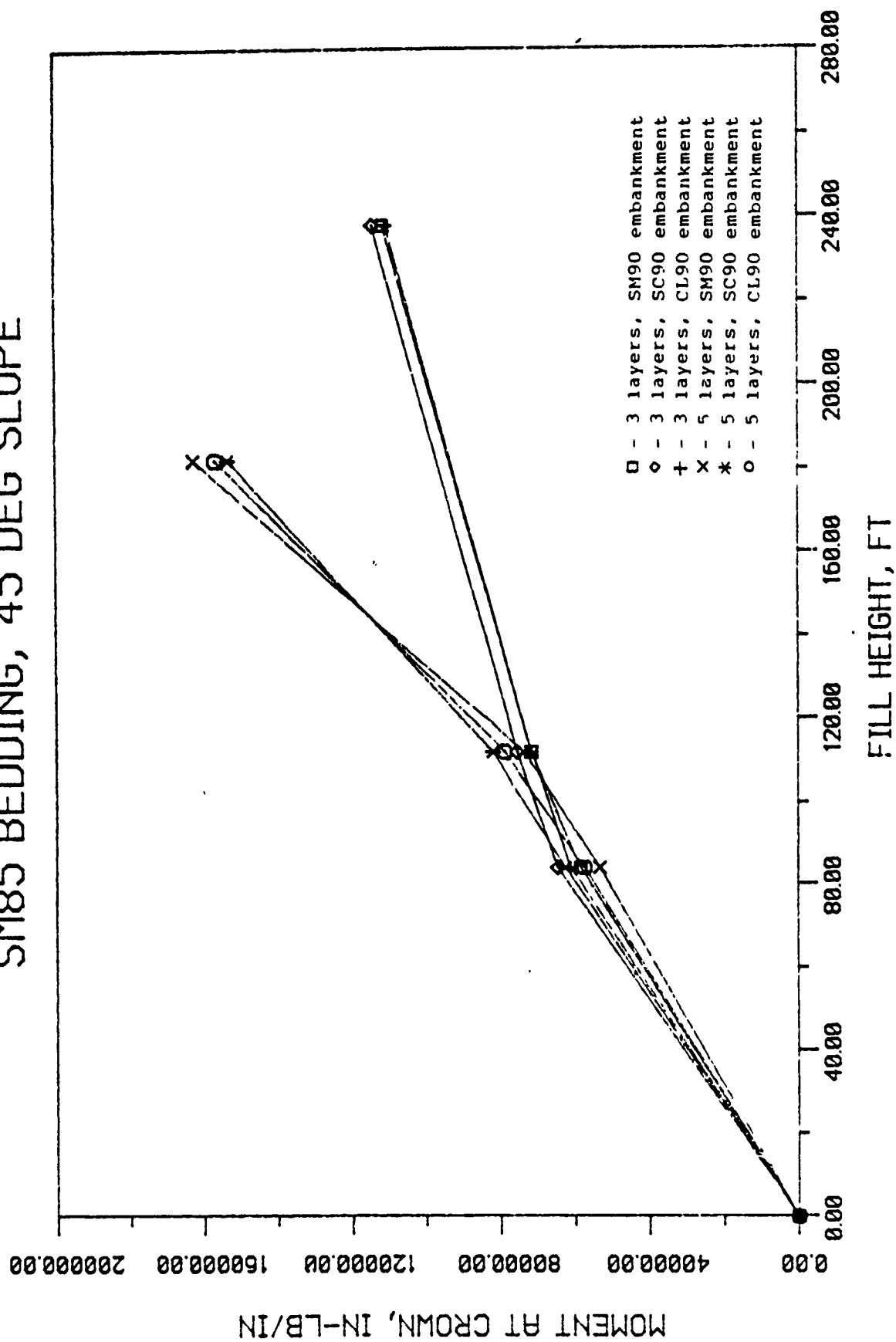


Figure 4.10 Crown Moment vs. Fill Height for Case 12B

rock cover. The difference between the moments occurring at the crown due to the two types of rock cover averaged 7988.667 in-lb/in. Minimum moment developed at the crown of the structure has a magnitude of 78640 in-lb/in and occurs when the embankment is of SM90 type soil.

Case I2B showed that the structure modeled with a 3-layer rock cover produced much less moment at the crown compared to that with a 5-layer rock cover. The average difference of the moment developed at the crown is 45594.0 in-lb/in and minimum moment with a magnitude of 110336.10 in-lb/in. with the use of CL90 soil for the embankment. Although the soil type of the embankment has considerable contribution to this difference, one can still see the dramatic rate of increase in the moment developed at the crown beginning at load increment 7 when the first section of the rock cover is installed. Although the 3-layer type rock cover produces a much higher fill height, the moment developed at the crown of the structure is significantly lower than that generated by the 5-layer type.

Overall, the results discussed in this section are quite consistent. Observing that the moment developed at the structural crown is less when the 3-layer type rock cover is installed at a fill height of 182 ft. But since layer type and embankment height are coupled, the 5-layer type rock cover proves to produce the least amount of bending moment at the crown of the structure at the completion of rock cover installation. The least amount of moment is developed then the 5-layer rock cover is installed in combination with SM90 soil

type for the embankment.

The thrust developed at the crown of the structure is also dependent upon the type of installation that the structure is built under (refer to Figure 4.11 thru 4.14). This section describes thrust in relation to the type of rock cover installed on the system. The comparisons have been made between only two cases wherein the structure withstood the entire loading scheme, these include Case I1B and I2B. The loading scheme for Case I1A with a 3-layer rock embankment and Case I2A caused structural failure after eight and four step load increments, respectively.

Thrust developed at the crown of the structure with a 30-degree slope embankment and SM85 soil type bedding (Case I1B) was minimal with the employment of the 3-layer rock cover. The thrust ranged from 651 lb/in when the embankment is of CL90 type soil to as low as -531 lb/in when the embankment is of SC90 type soil. As for the 5-layer type rock cover, the values of thrust ranged from -1664 lb/in when the embankment is of SC90 type soil to as high as -1810 lb/in when the embankment is of CL90 type soil. Again, even though the fill height generated by the 3-layer rock embankment is much higher than the 5-layer type, it is observed that the final thrust magnitude developed at the crown is less with the 3-layer type rock cover.

Case I2B shows a totally contradicting set of values. At the completion of both types of rock covers, final thrust magnitudes developed at the crown ranged from at least -1413 lb/in when the rock cover type is 5-layer and the embankment is SM90 type soil to as high as 1927 lb/in when the rock cover type

# CL85 BEDDING, 30 DEG SLOPE

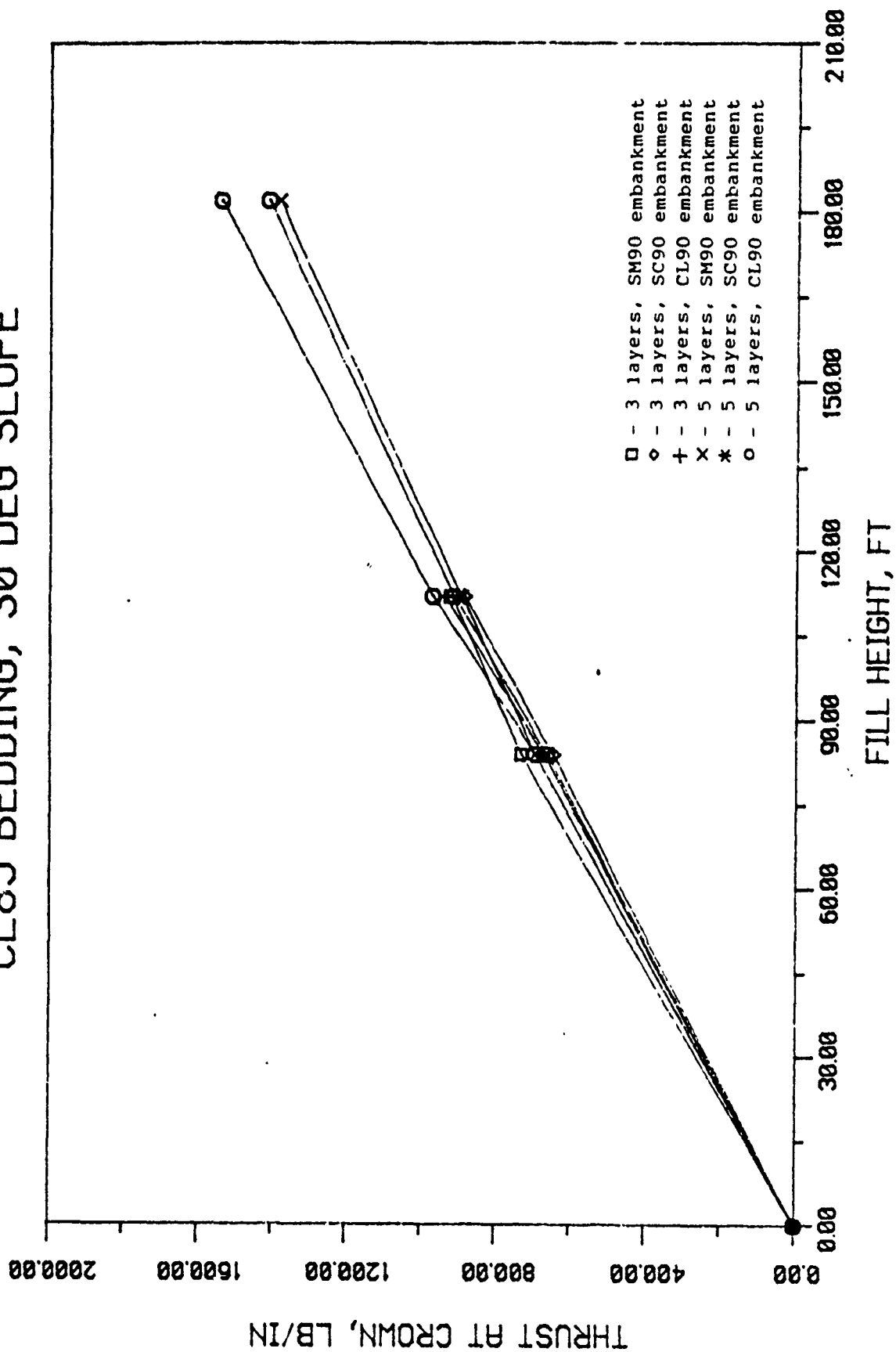


Figure 4.11 Crown Thrust vs. Fill Height for Case 11A

# SM85 BEDDING, 30 DEG SLOPE

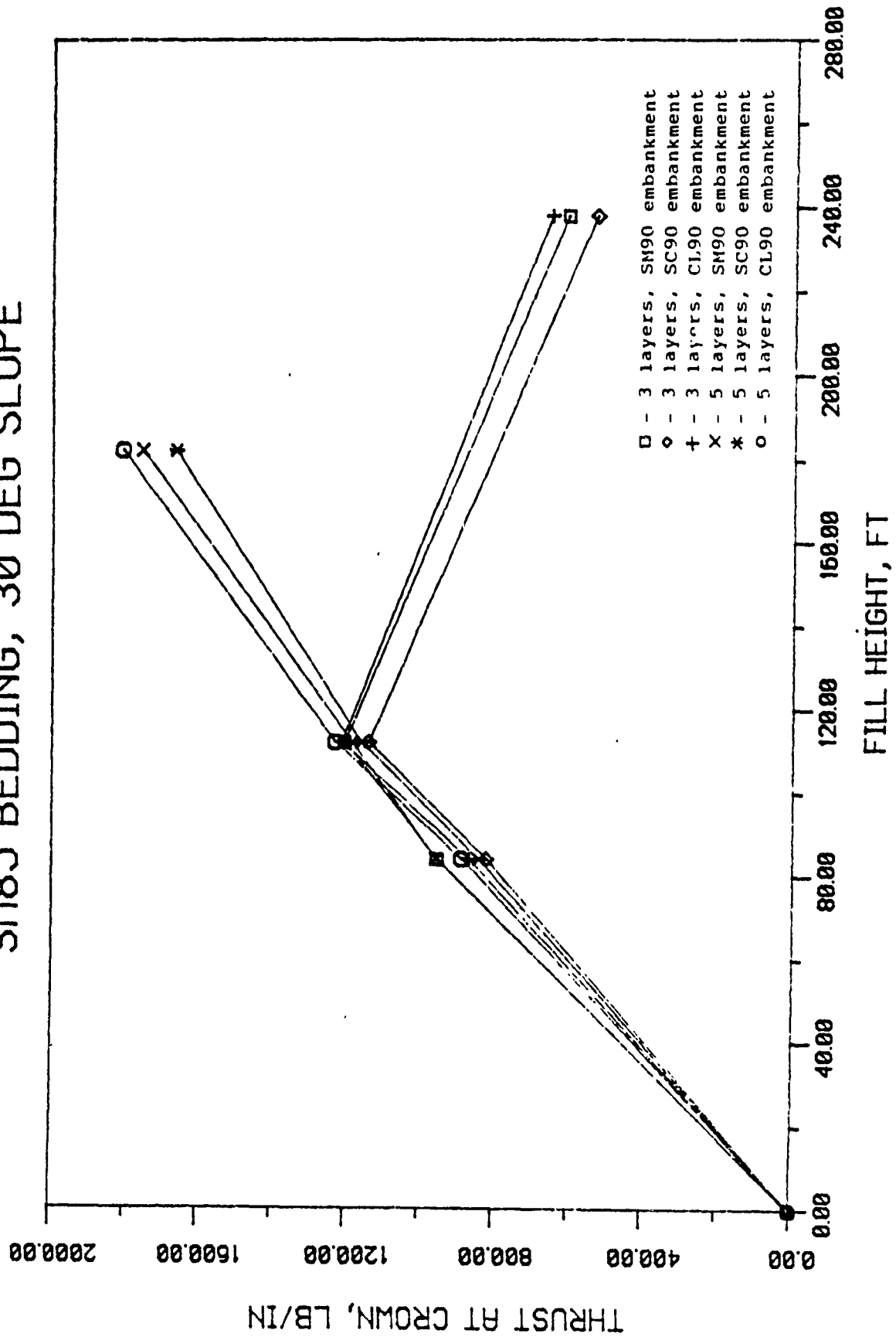


Figure 4.12 Crown Thrust vs. Fill Height for Case 11B

# CL85 BEDDING, 45 DEG SLOPE

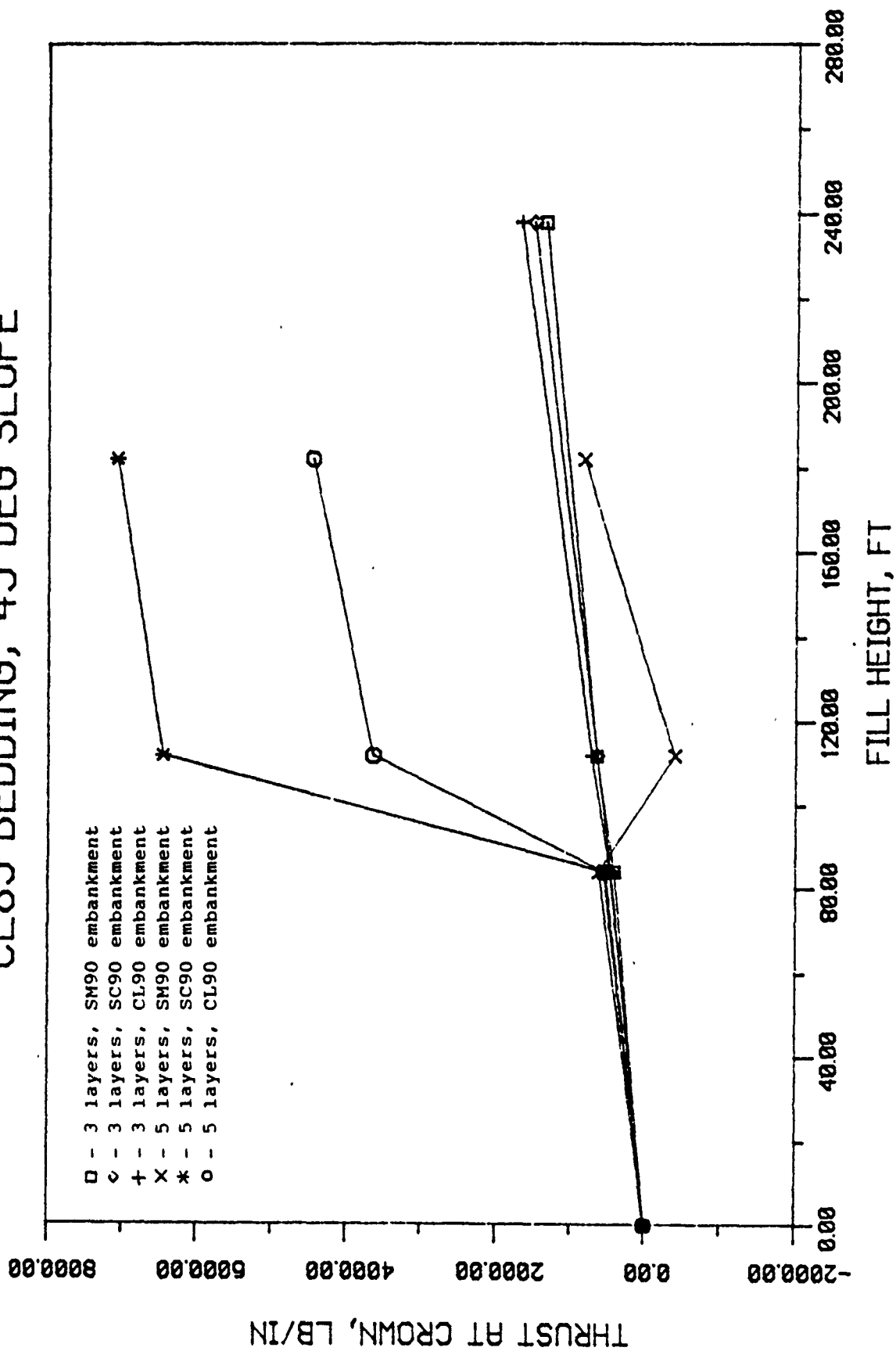


Figure 4.13 Crown Thrust vs. Fill Height for Case I2A

# SM85 BEDDING, 45 DEG SLOPE

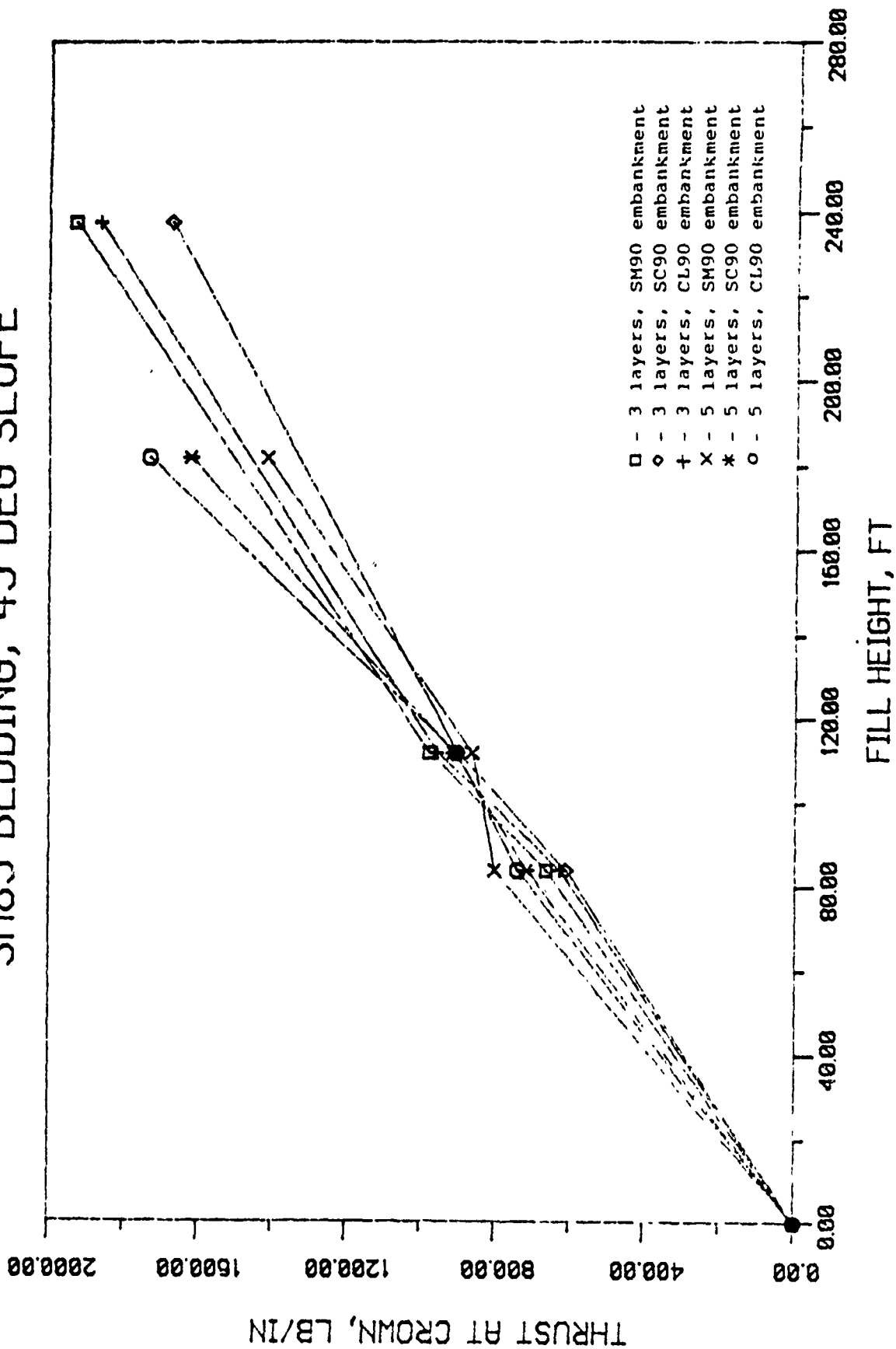


Figure 4.14 Crown Thrust vs. Fill Height for Case I2B

is 3-layer and the embankment is SM90 type soil. The interesting part of this case that when the rock cover is of the 3-layer type, and the embankment is of the SC90 type soil, the final thrust magnitude developed at the crown is 1669 lb/in, the second lowest value for thrust found in this case. It is, therefore, difficult to make any conclusions about the influence of the rock cover type on the thrust for this particular case.

## 2. The Influence of the Slope of Embankment

To determine the effect of the embankment slope on the deflection of the crown of the structure, certain variables had to be held constant to be able to easily focus on the effect of the slope. The main variable that was held constant in all cases of the analysis is the number of layers used for the rock cover, in this case the 3-layer type, is selected. All other variables such as the bedding and soil embankment conditions were used, but values for crown displacement were compared individually for every case.

The first three cases studied in this discussion is a system with CL85 bedding and combination with SM90, SC90, and CL90 soil type embankments designated as Case IIIA (refer to Figure 4.15). Unfortunately, the structural model failed after eight load increments for all cases with a 30-degree slope embankment. Comparison between the effect of the embankment slope was therefore limited to the values of the crown displacement after installation of step load increment 6, the completion of the concrete slab. In the first case, where the

# CL85 BEDDING, 3 LAYERS, SM90 EMBA

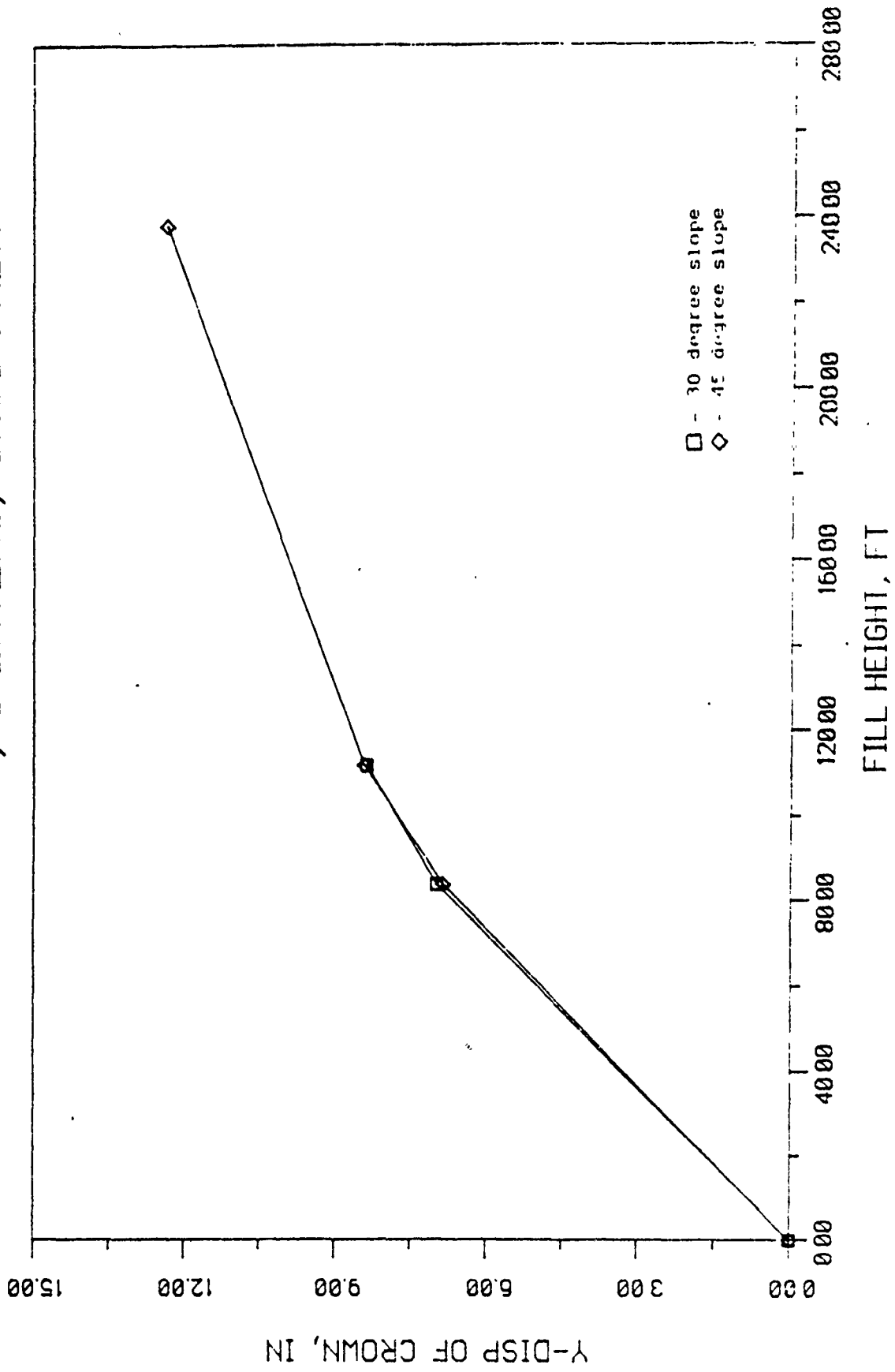


Figure 4.15a Relative Crown Deflection vs. Fill Height for Case IIIA

# CL85 BEDDING, 3 LAYERS, SC90 EMBA

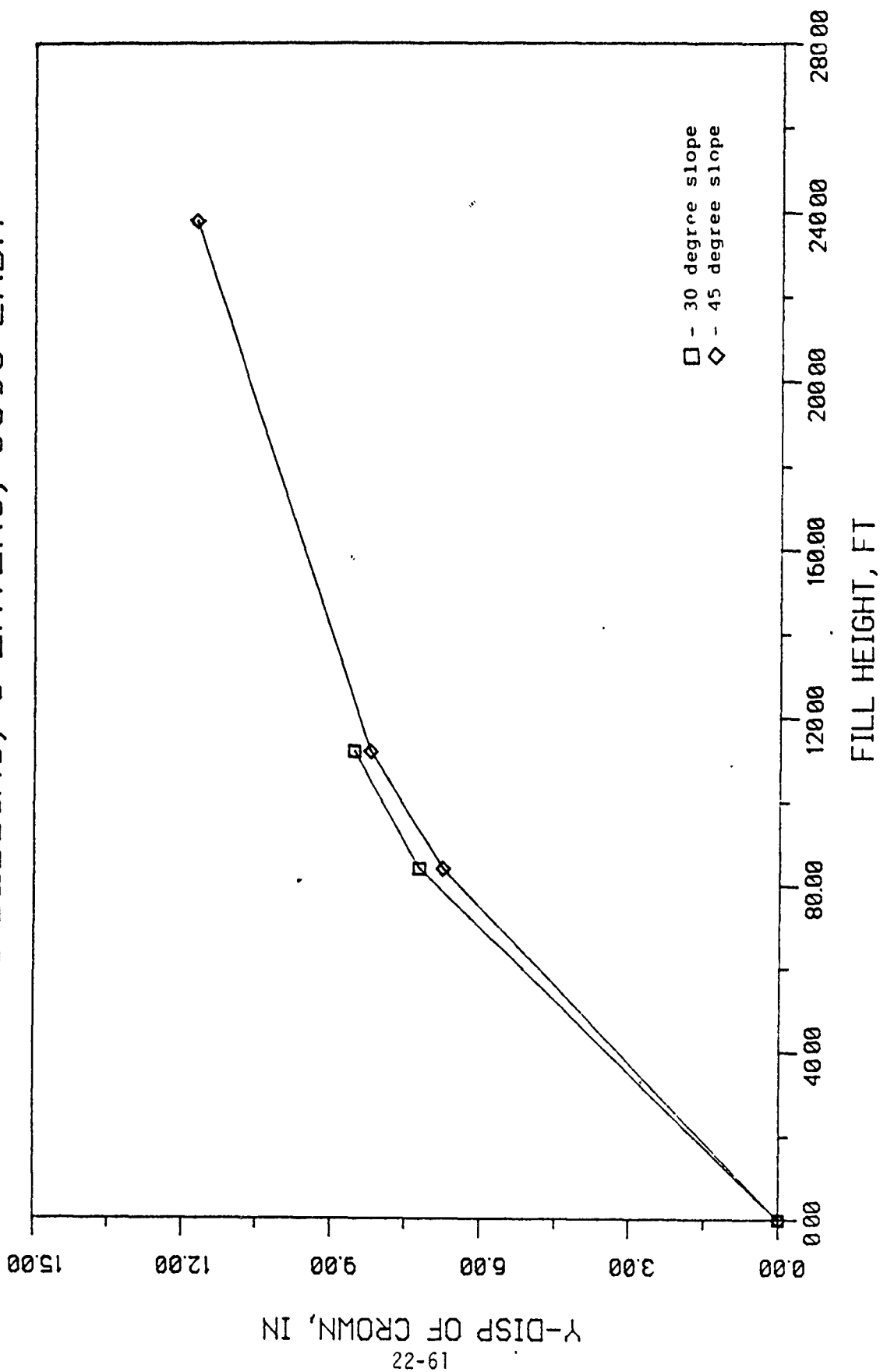


Figure 4.15b Relative Crown Deflection vs. Fill Height for Case IIIA

# CL85 BEDDING, 3 LAYERS, CL90 EMBA

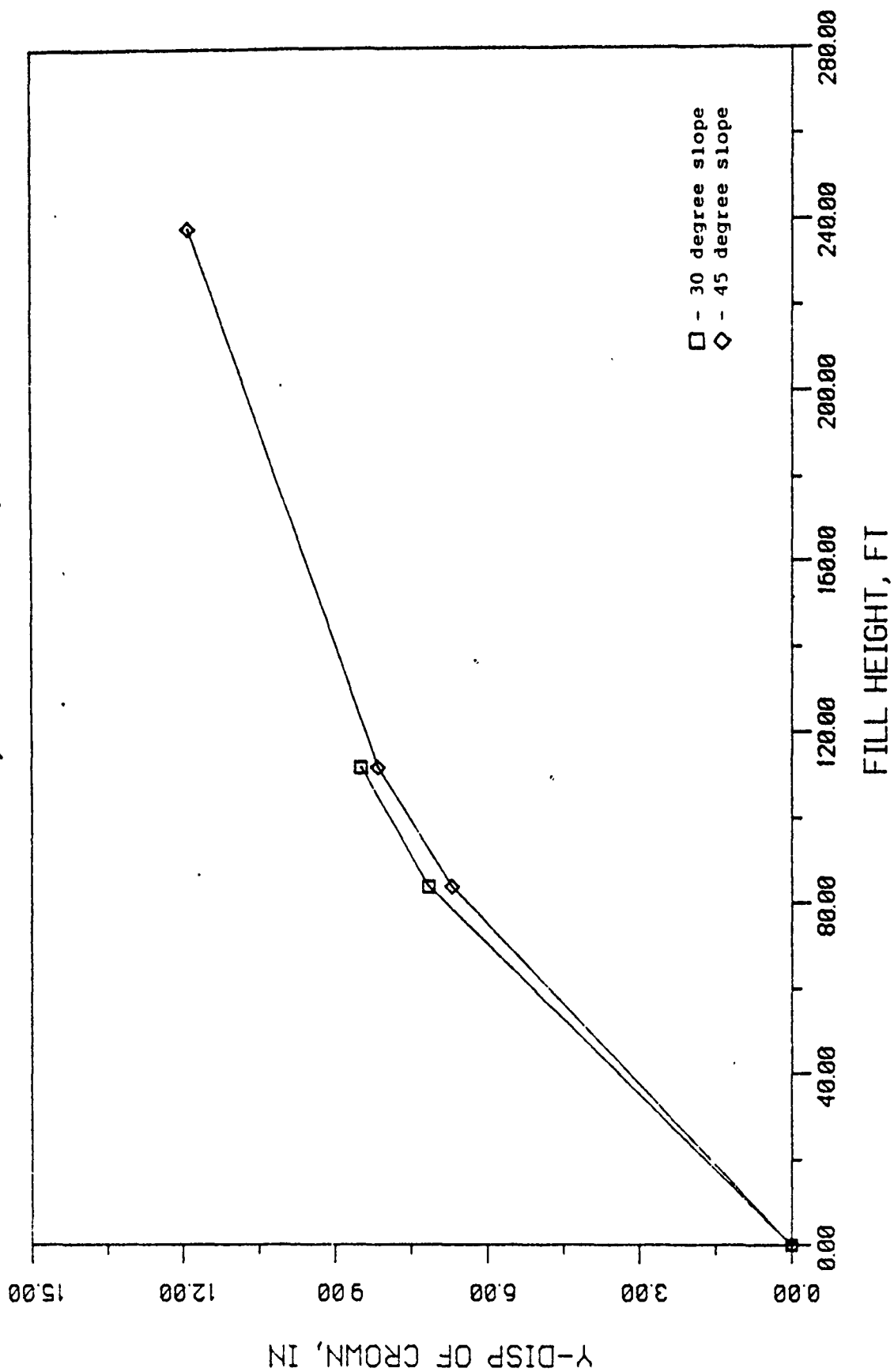


Figure 4.15c Relative Crown Deflection vs. Fill Height for Case IIIA

embankment is made up of SM90 type soil, maximum difference between crown deflection is only 0.13 inch after six load increments. The cases where the embankment is made up of SC90 and CL90 type soil, the influence of the embankment slope is much more apparent. The difference between crown deflection after six load increments was found to be 0.33 inch in both cases.

The next three cases examined in this section is a structure modeled on a bedding condition using SM85 type soil in combination with SM90, SC90, and CL90 type soil for the embankment designated as Case II2B (refer to Figure 4.16). All structural models proved to withstand the entire load scheme for these cases, therefore, producing a complete picture of crown deflection with both the 30 and 45 degree slope embankment. For the model with the SM90 soil embankment, the system with the 30-degree embankment produced greater crown deflection than its counterpart. The difference between the two was 0.33 inch at the end of nine load step increments. For the model with SC90 soil embankment, a better distinction between the crown deflection for both slope conditions. In this case, the 30-degree slope embankment causes a crown deflection of 1.01 inches more than the 45-degree slope embankment at the end of nine step load increments. Finally, for the model with CL90 soil embankment, the embankment slope of 45-degrees produces less crown deflection than the 30-degree embankment slope, the difference being at least 0.86 inch.

# SM85 BEDDING, 3 LAYERS, SM90 EMBA

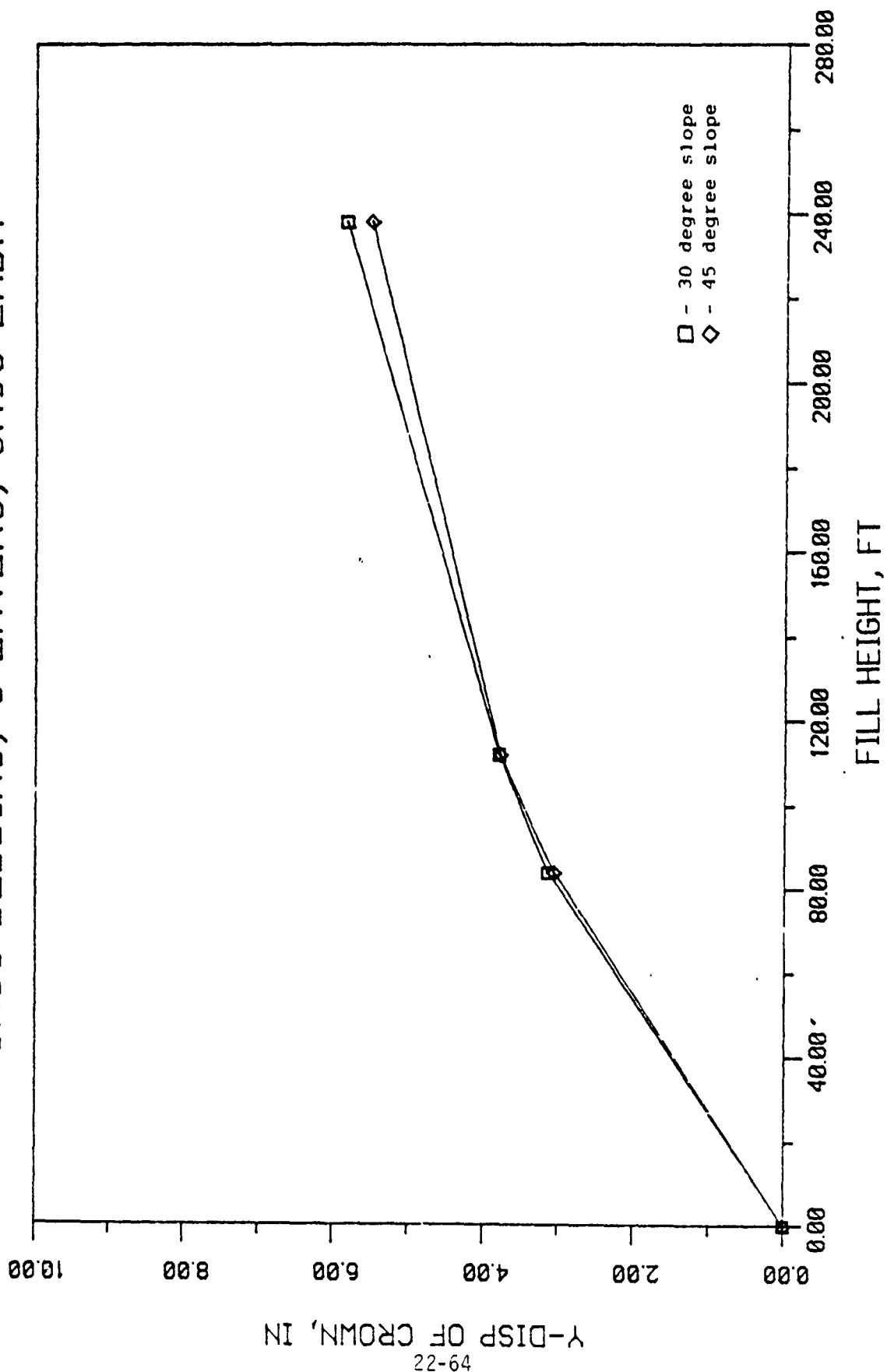


Figure 4.16a Relative Crown Deflection vs. Fill Height for Case 112A

# SM85 BEDDING, 3 LAYERS, SC90 EMBA

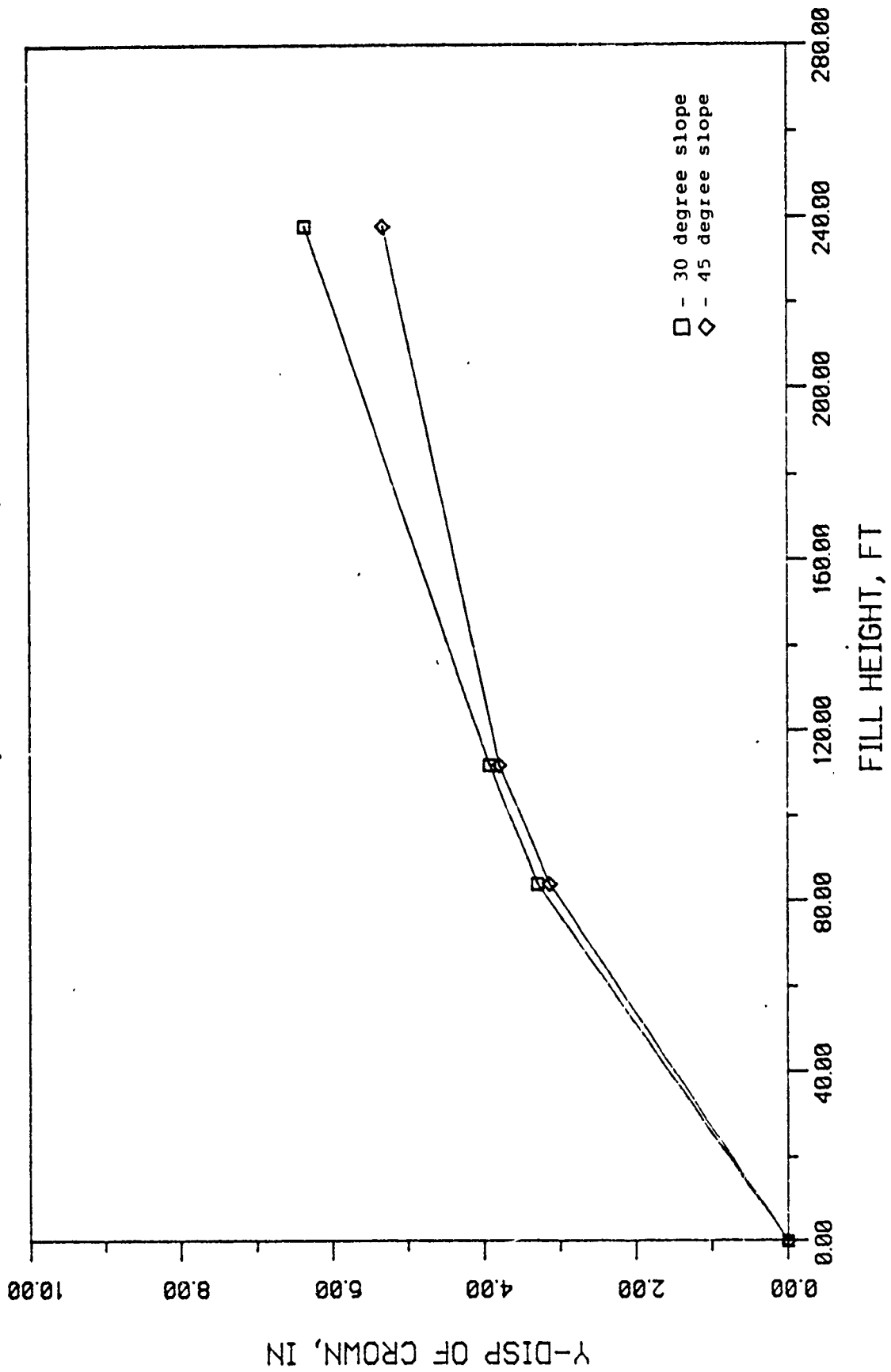


Figure 4.16b Relative Crown Deflection vs. Fill Height for Case II2A

# SM85 BEDDING, 3 LAYERS, CL90 EMBA

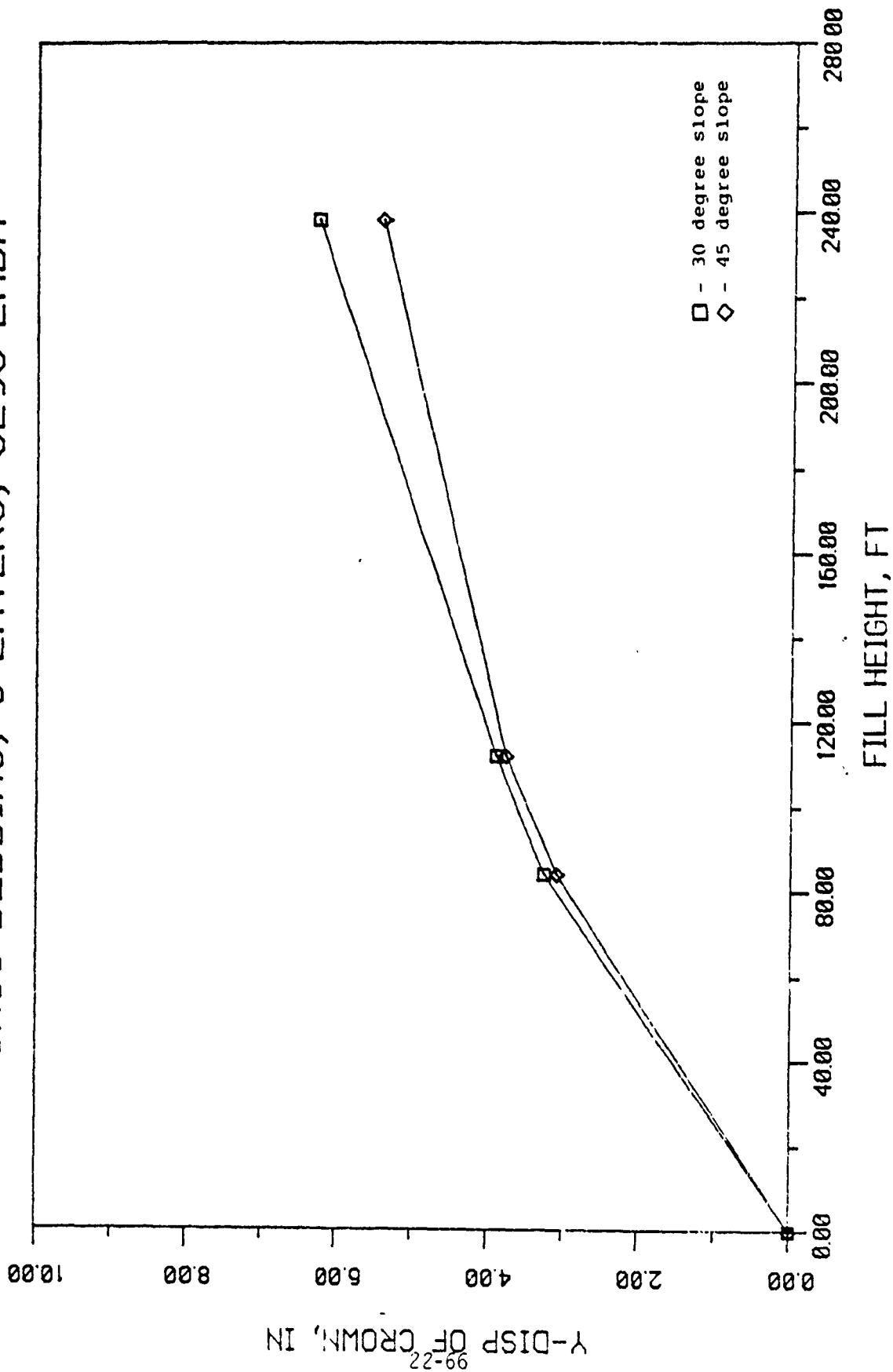


Figure 4.16c Relative Crown Deflection vs. Fill Height for Case 112A

In general, an embankment slope of 45 degrees shall result in less crown deflection for systems with SM85 soil for bedding conditions, and minimal when combined with SC90 soil for the embankment for all cases with a 3-layer rock cover.

A procedure similar to the previous one is used in the analysis of the influence of the embankment slope on the bending moment developed at the crown of the structure. That is, the installation type is held constant, here taken to be the 3-layer type rock cover, to easily focus on the effect of the slope and only the slope on the moment developed at the crown. All other variables are taken into account, though, to assure consistency of the findings. Two bedding conditions, CL85 and SM85, plus three embankment conditions: SM90, SC90, CL90; are included in the analysis.

The first three cases examined is a system with CL85 soil bedding in combination with SM90, SC90, and CL90 soil embankments (refer to Figure 4.17). The structural models failed after the completion eight load increments for all cases with the 30-degree slope embankment. Then again, the comparison between the two slope conditions for the moment developed at the crown is limited to the values of crown moment developed after six load increments. The first case, where the embankment is made up of SM90 type soil, shows that by installing a 30-degree slope embankment, the moment at the crown can be reduced by as much as 10647 in-lb/in, less than that developed with a 45-degree slope embankment at the end of six load increments. The same is true with the next case, where the embankment is

# CL85 BEDDING, 3 LAYERS, SM90 EMBA

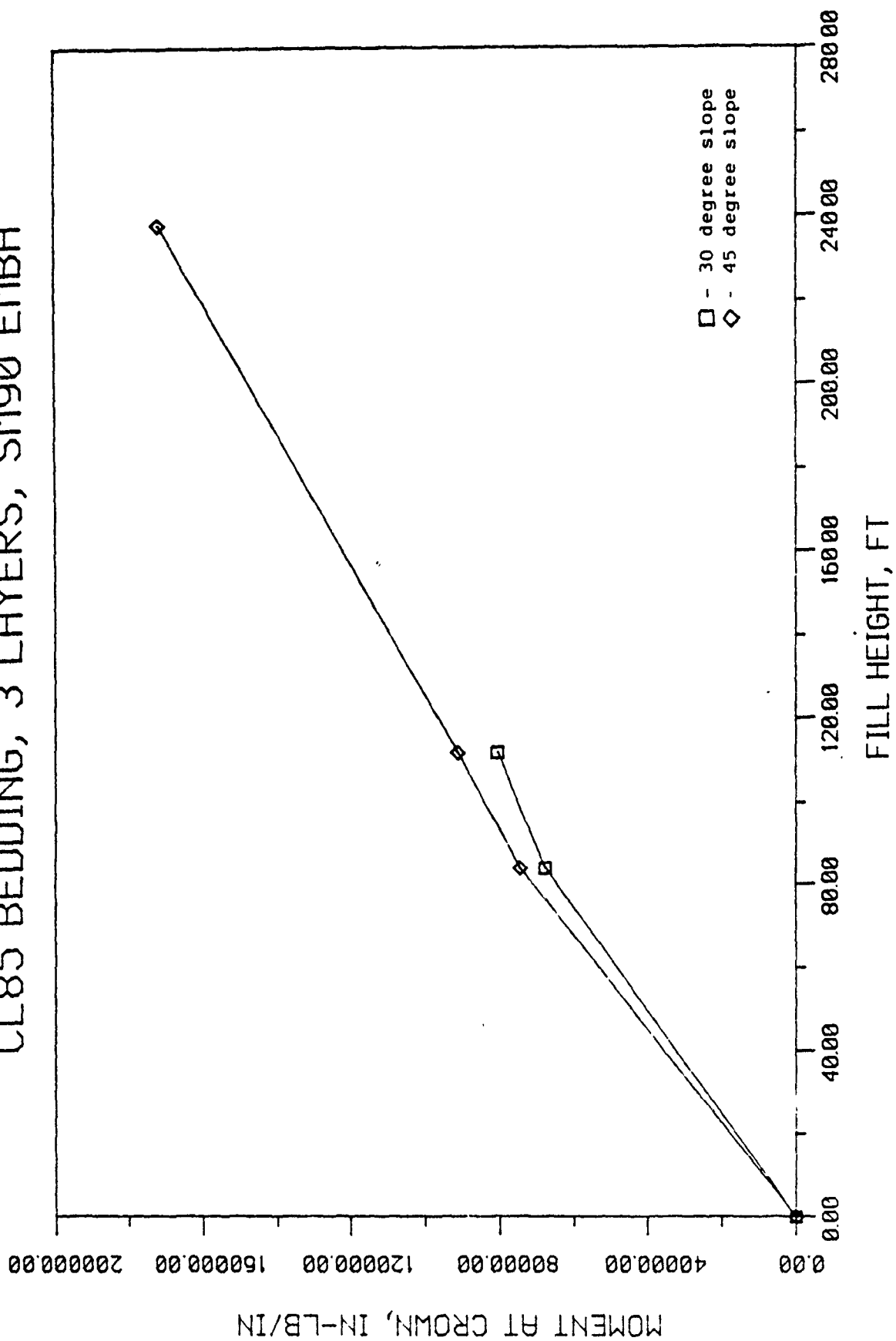


Figure 4.17a Crown Moment vs. Fill Height for Case IIB

# CL85 BEDDING, 3 LAYERS, SC90 EMBA

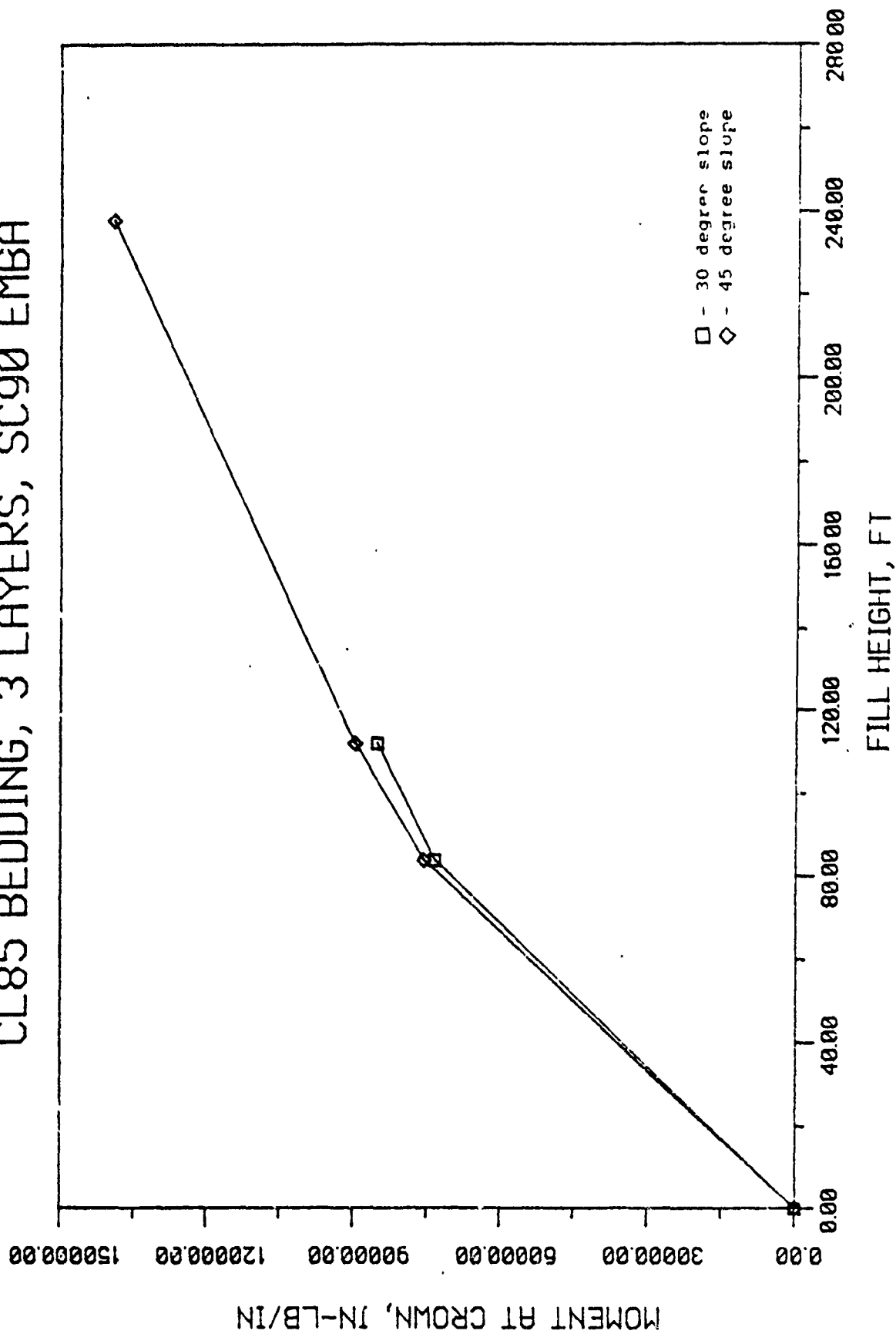


Figure 4.17b Crown Moment vs. Fill Height for Case IIIB

# CL85 BEDDING, 3 LAYERS, CL90 EMBA

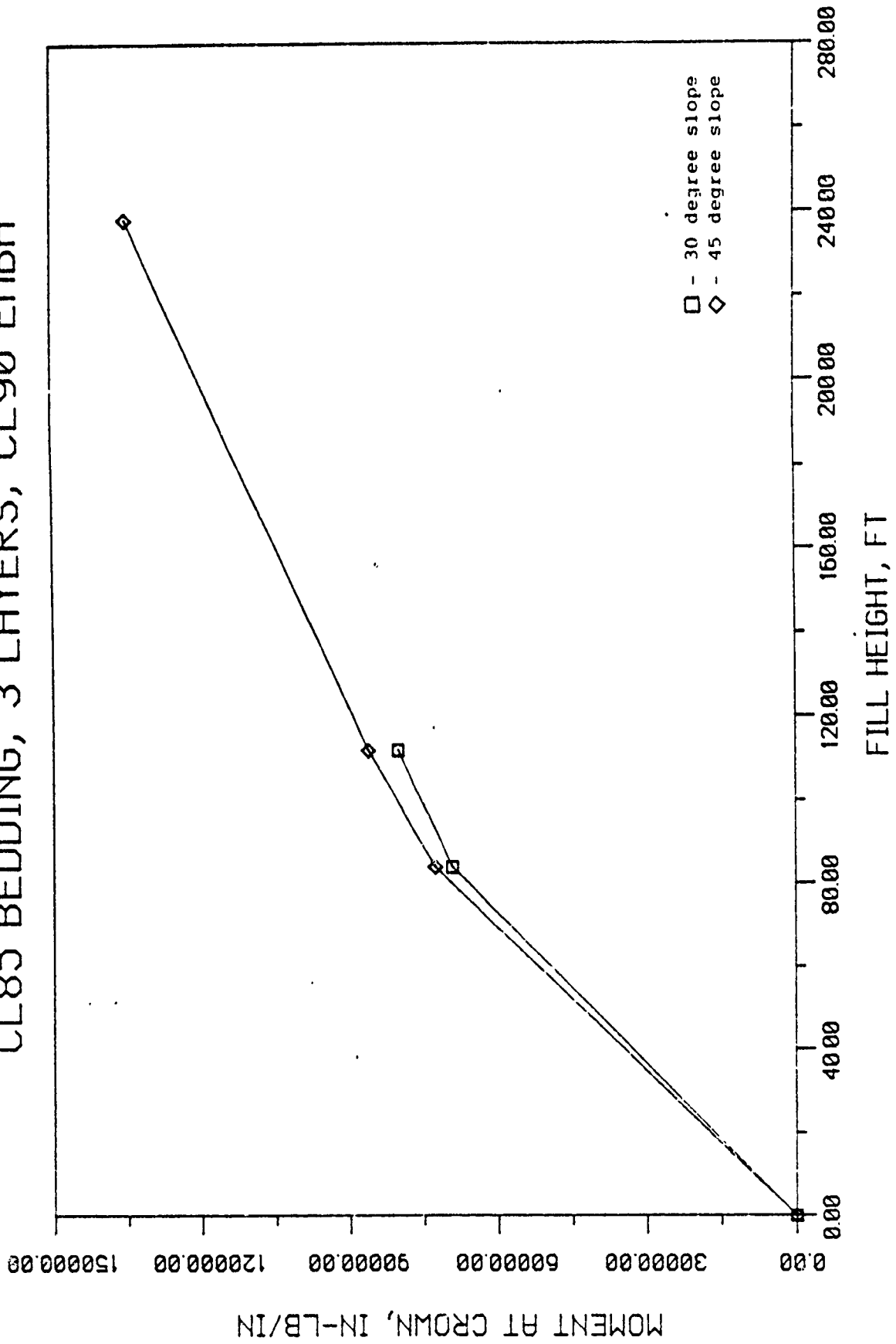


Figure 4.17c Crown Moment vs. Fill Height for Case 111B

made up of SC90 type soil. The moment developed at the crown is 4528 in-lb/in less with a 30-degree slope embankment installed than with a 45-degree slope embankment. Finally with an embankment type soil of CL90 used, a 30-degree slope embankment produces 5939 in-lb/in less moment than a 45-degree slope embankment.

The next three cases examined is a system with SM85 soil bedding in combination with SM90, and CL90 soil embankments (refer to Figure 4.18). For the model with SM90 type soil for the embankment material, the bending moment developed at the crown of the structure was found to be greater when a 45-degree slope embankment is installed. The difference in magnitude being 7705 in-lb/in at the end of four load increments up to 27364 in-lb/in at the completion of nine load increments. Results from the tests using the structure model with SC90 type embankment soil are consistent with the previous one but less the differences in the moment are less dramatic. Results show that again, by using a 30-degree slope embankment, the moment developed at the crown is less than that with a 45-degree embankment. The differences being 4919 in-lb/in at the end of four load increments up to 13344 in-lb/in at the completion of nine load increments. Finally, with the case of the system consisting of an embankment made up of CL90 type soil, it was also found that the embankment with a 30-degree slope produces less moment at the crown. This is the case wherein the influence of the slope on the moment is most apparent. At the end of nine load increments, the crown moment with a 45-degree

# SM85 BEDDING, 3 LAYERS, SM90 EMBA

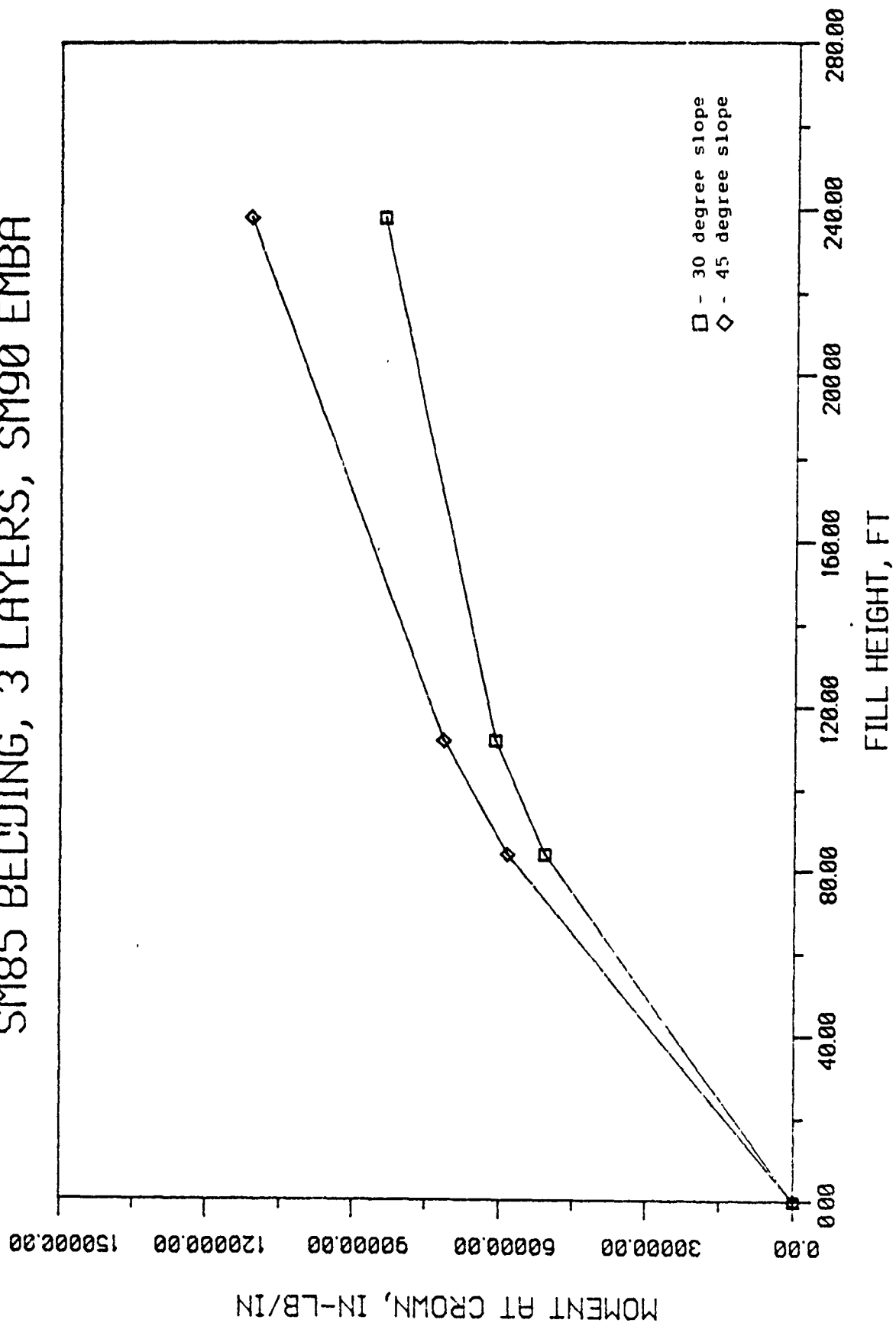


Figure 4.18a Crown Moment vs. Fill Height for Case 112B

# SM85 BEDDING, 3 LAYERS, SC90 EMBA

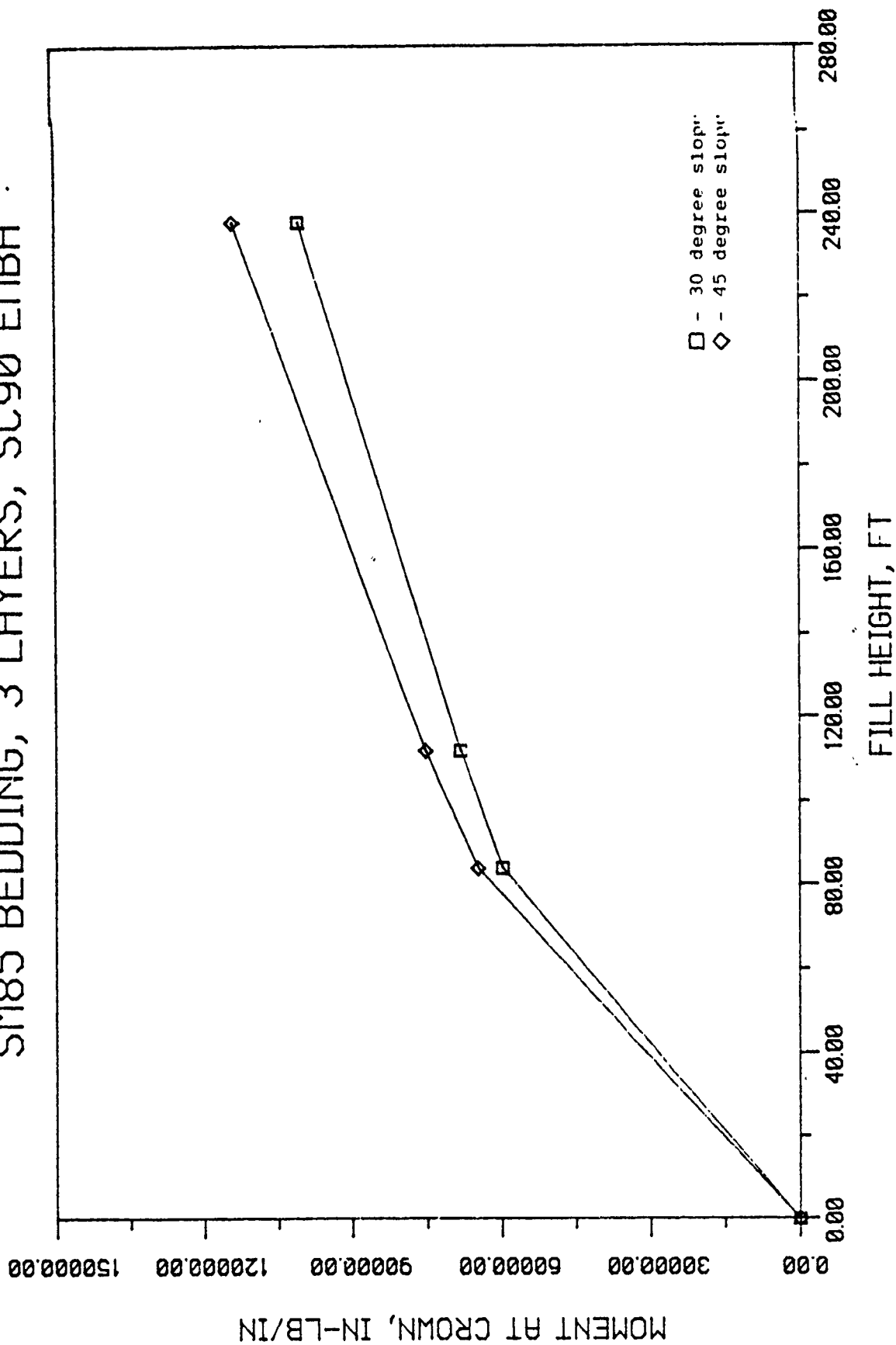


Figure 4.18b Crown Moment vs. Fill Height for Case II2B

# SM85 BEDDING, 3 LAYERS, CL90 EMBA

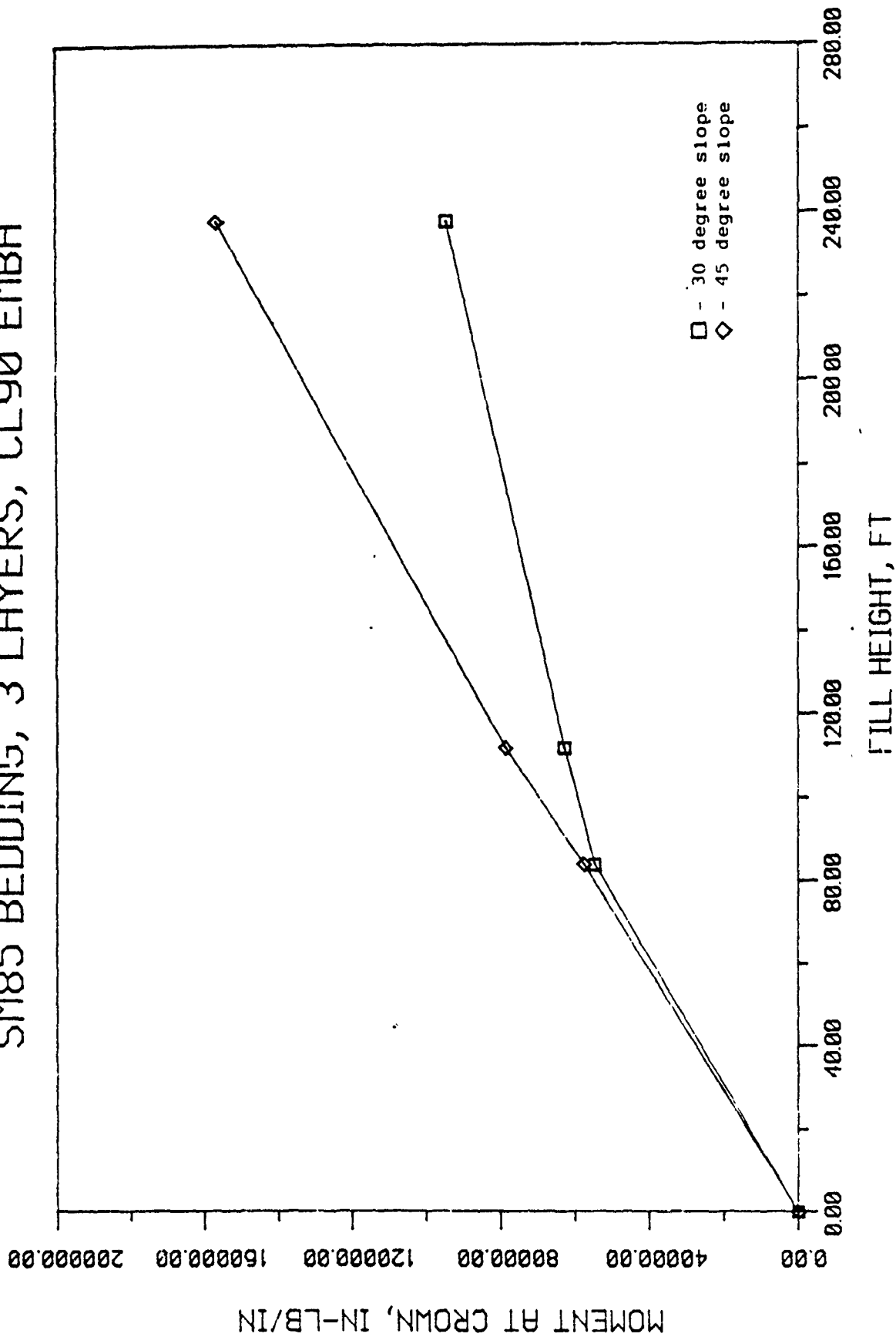


Figure 4.18c Crown Moment vs. Fill Height for Case IIb

slope embankment was found to be 156650 in-lb/in, nearly 665 in-lb/in greater than the moment developed at the crown with a 30-degree slope embankment.

The thrust developed at the crown of the structure is also highly influenced by the slope of the embankment. Again, to make the analysis simpler and to be able to focus on the influence of only the slope, the installation type is held constant for all cases and taken to be the 3-layer type rock cover. The bedding types included in the analysis are SM85 and CL85, and embankment types used are SM90, SC90, and CL90.

The first three cases analyzed are systems in CL85 bedding (refer to Figure 4.19). This condition though, structural models failed after eight load increments for systems with 30-degree slope embankments. Therefore, like the former analyses made in this section the observations will be limited to the crown thrust after six load increments for each case. Even though the 45-degree condition is not feasible in practice, analyses is still performed to determine the consistency of the results. The first case analyzed is the system constructed in a SM90 soil embankment. Here, the results show that an embankment with a 45-degree slope produces less thrust at the crown than an embankment with a 30-degree slope. It was found that at the end of six construction increments, a 45-degree slope produces less thrust at the crown than the 30-degree slope. The difference being 269 lb/in, nearly 42% smaller with a steeper slope. Similarly, the case where the embankment is made of SC90 type soil, the same results occur. An embankment with a 45-degree

# CL85 BEDDING, 3 LAYERS, SM90 EMBA

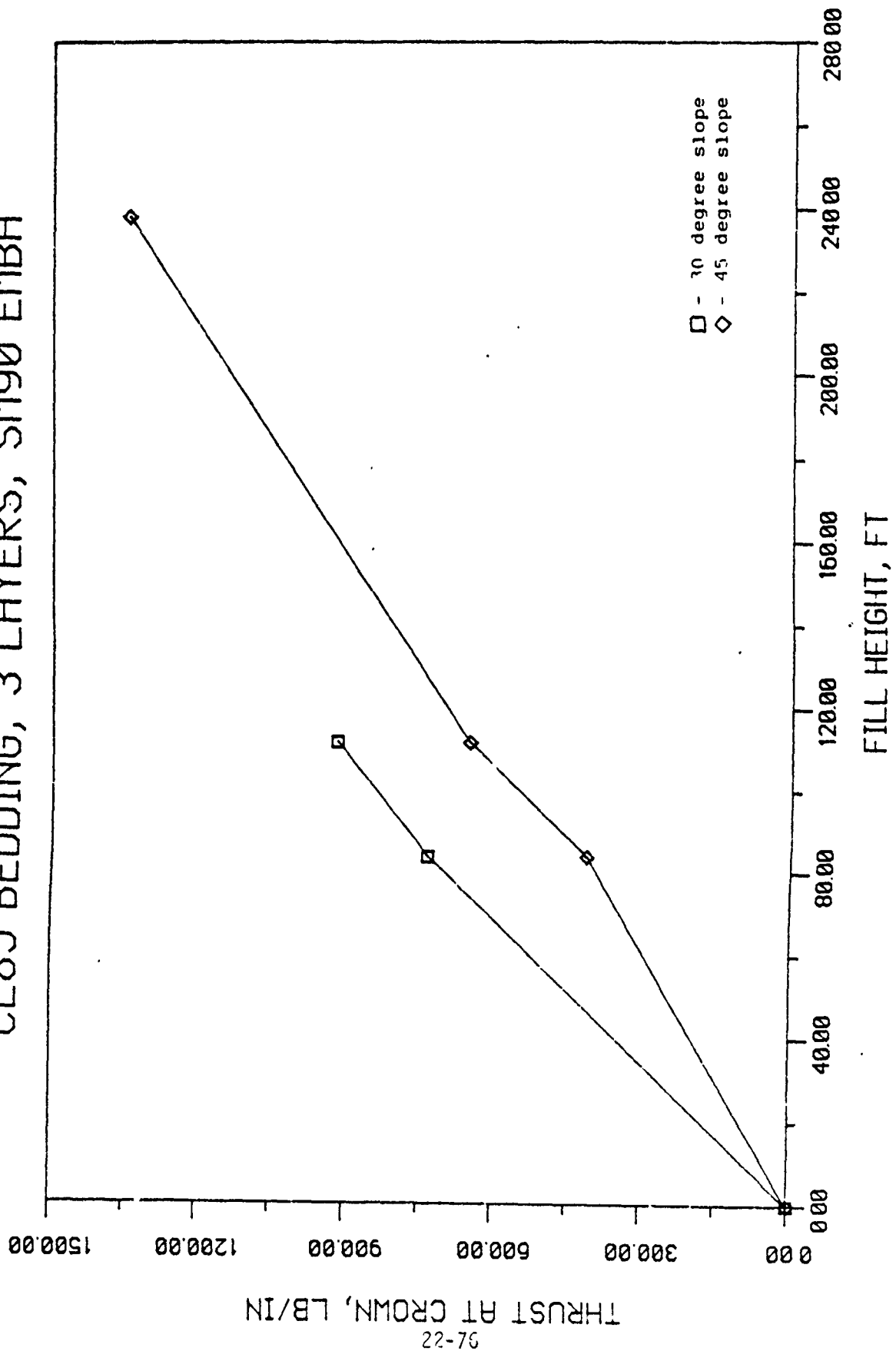


Figure 4.19a Crown Thrust vs. Fill Height for Case 111C

# CL85 BEDDING, 3 LAYERS, SC90 EMBA

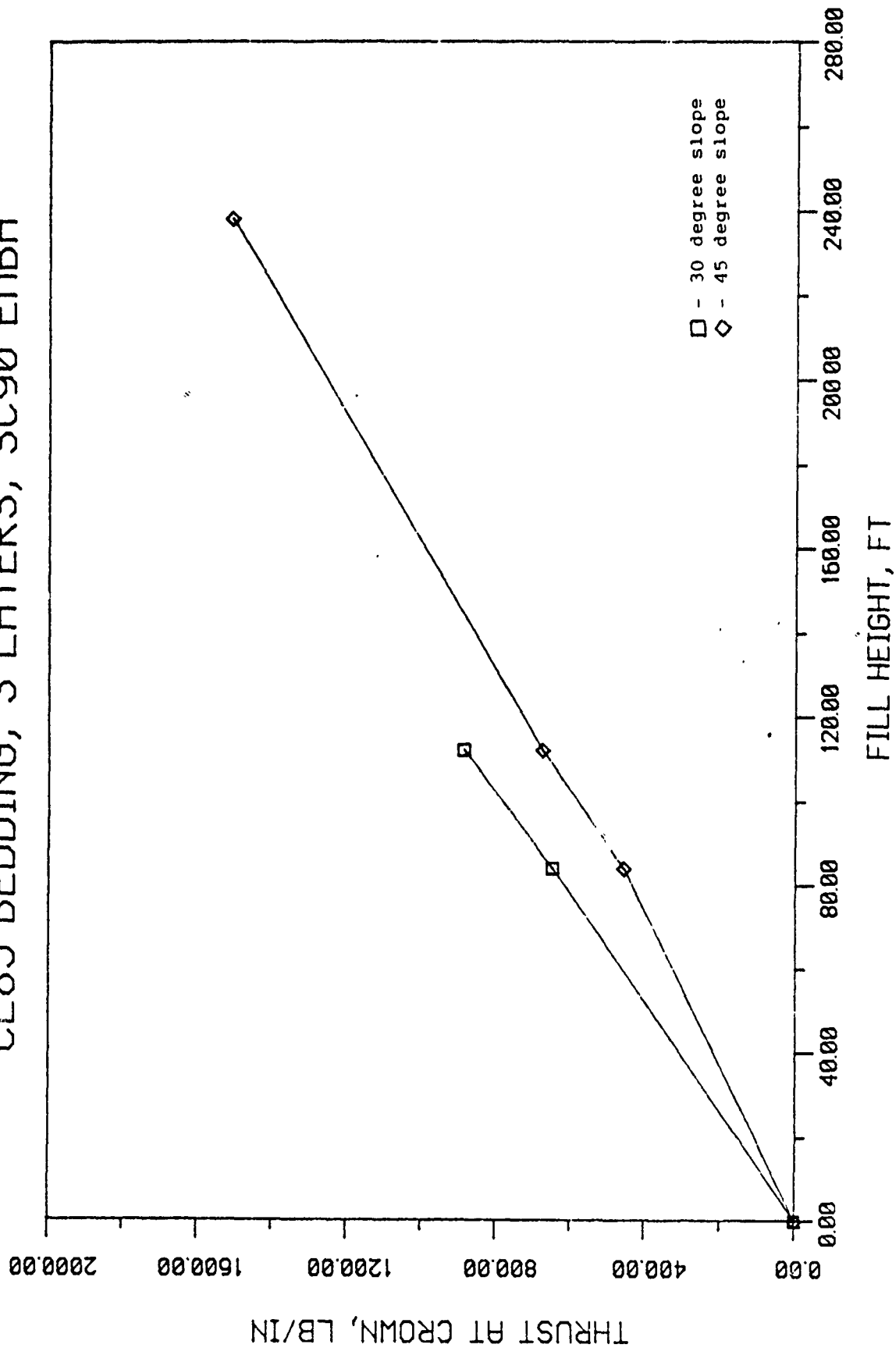


Figure 4.19b Crown Thrust vs. Fill Height for Case IILC

# CL85 BEDDING, 3 LAYERS, CL90 EMBA

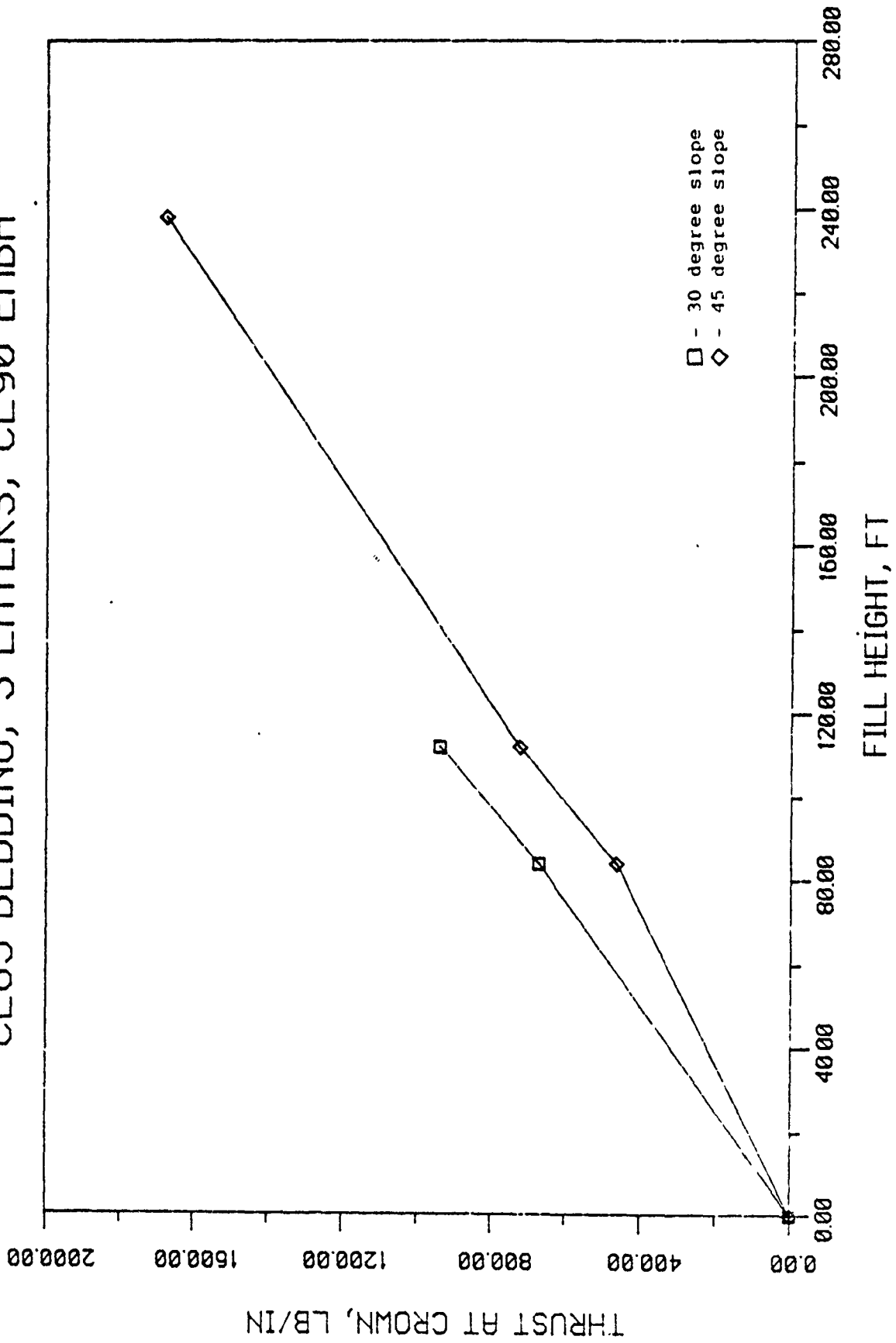


Figure 4.19c Crown Thrust vs. Fill Height for Case IIIc

slope produces nearly 32% less thrust than an embankment with a 30-degree slope. Finally, system with an embankment of CL90 type soil, unsurprisingly yields the same results. An embankment slope of 45-degrees produces nearly 30% less thrust than the embankment with a 30-degree slope. In general, for a system with CL85 soil bedding, an embankment of SM90 type soil installed in a 45-degree slope produces the least thrust at the crown after the completion of all step load increments.

The next three cases examined were systems wherein the structure is modeled on SM85 type soil bedding in combination with SM90, SC90, and CL90 type soil for the embankment (refer to Figure 4.20). In all three cases it was found that at the end of six step load increments, the system with the 30-degree slope embankment produced more thrust at the crown than the 45-degree option, the average difference of the thrust developed at the crown being 242 lb/in. But at the completion of all nine step load increments, it was found that an embankment with a 30-degree slope shall produce a final crown thrust magnitude up to at least 186% to at most 218%. With SM90 soil embankment, the difference of the final thrust magnitude produced at the crown between the 30-degree and 45-degree slope is 1320 lb/in favoring the former. With SC90 soil embankment, the difference was found to be 1212 lb/in. The system producing the least thrust at the end of all step load increments is the one with the SC90 soil for the embankment, with a final crown thrust magnitude of 531 lb/in.

# SM85 BEDDING, 3 LAYERS, SM90 EMBA

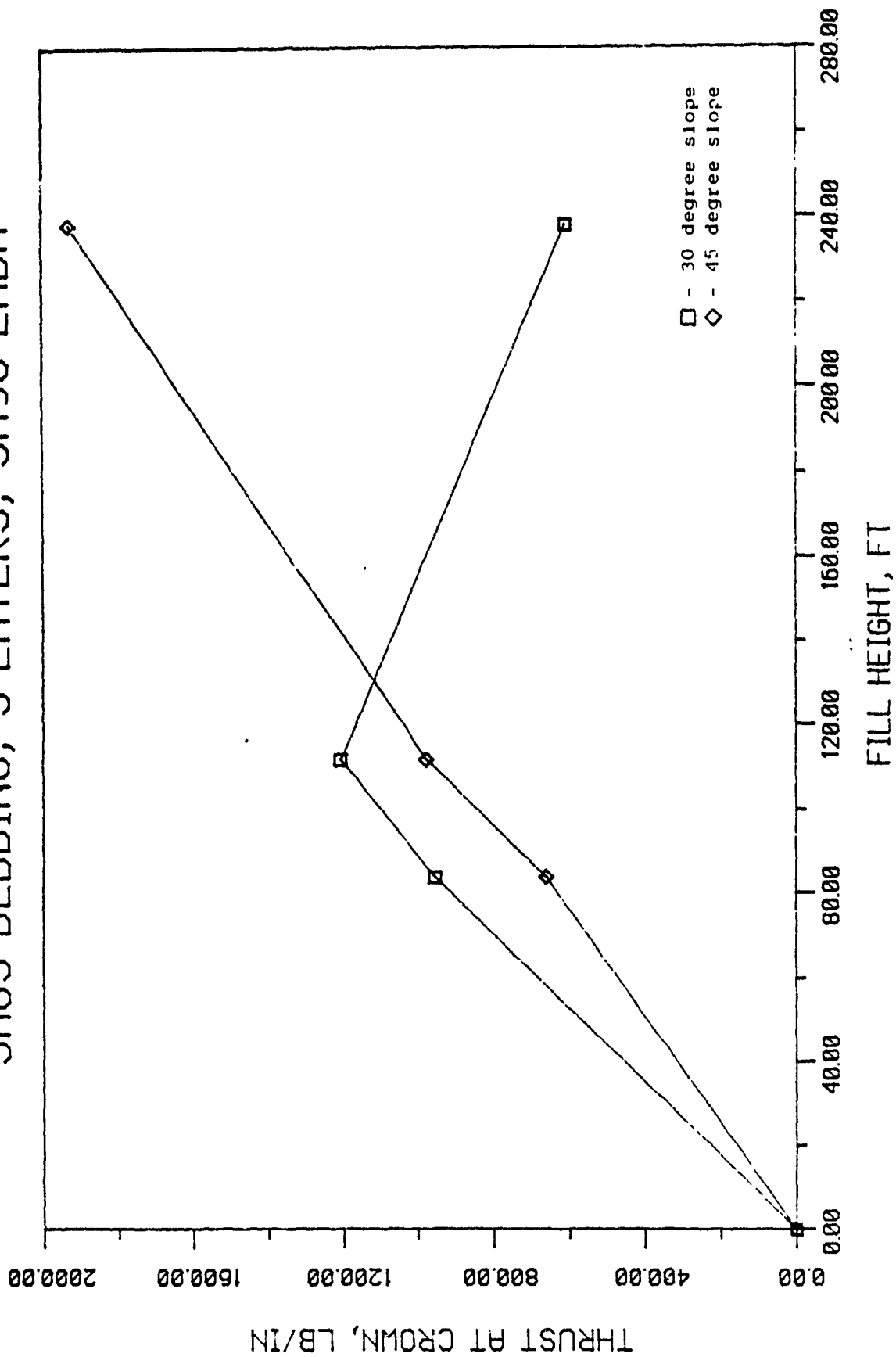


Figure 4.20a Crown Thrust vs. Fill Height for Case 1120

# SM85 BEDDING, 3 LAYERS, SC90 EMBA

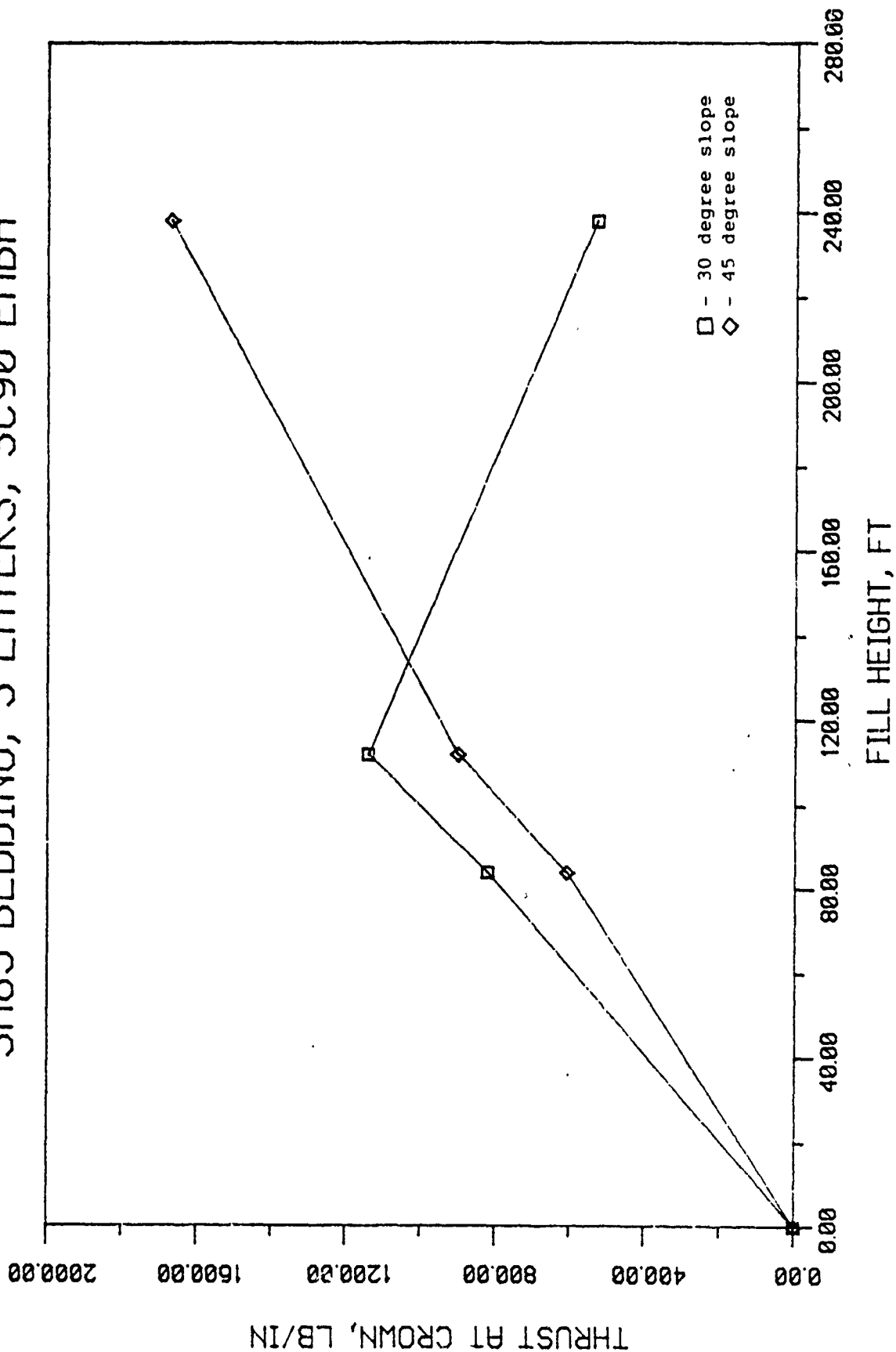


Figure 4.20b Crown Thrust vs. Fill Height for Case I12C

# SM85 BEDDING, 3 LAYERS, CL90 EMBA

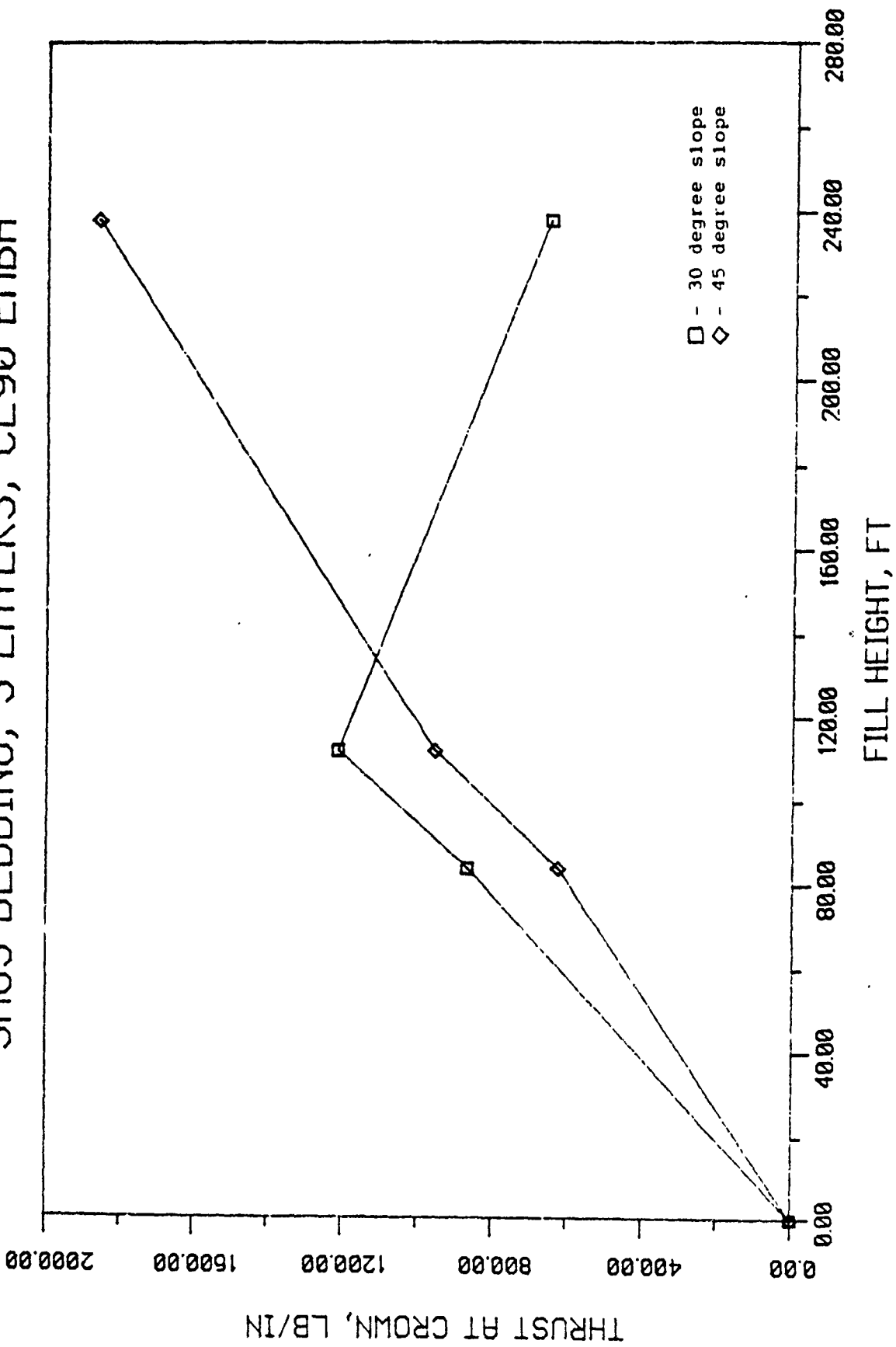


Figure 4.20c Crown Thrust vs. Fill Height for Case 112C

### 3. The Influence of Soil Type of Embankment

Crown deflection is greatly influenced by soil type, meaning that the physical properties of the soil, not only the density, plays an important part in the determination of load transfer from soil to structure. This section discusses the results found on the influence of soil type on the relative deflection of the crown. To minimize the number of cases to be examined and focus the attention on the influence of only the embankment soil on the structure, the system models were set to have a constant embankment slope, taken to be 30 degrees designated as Case IIII. All other variables such as bedding type and the number of layers for the rock cover are taken into account (refer to Figure 4.21).

The first case studied is a system model on CL85 soil bedding with a 3-layer rock cover. Although it was found that at the end of six load increments, crown relative settlement had a standard deviation of 0.07 in. with the minimum of 8.38 in. occurring when the embankment is of SM90 type to maximum of 8.55 in. occurring when the embankment is of SC90 type, the structural models failed. Meaning that these types of embankment soil installed within these conditions is not feasible for practical purposes.

The second case studied is a system similar to the one described above only that this is modeled with a 5-layer rock cover. Relative crown deflection at the completion of all nine load increments had a standard deviation of 0.048 in. with the minimum being 10.58 in. occurring when the embankment is of SM90

# CL85 BEDDING, 3 LAYERS, 30 DEG SLOPE

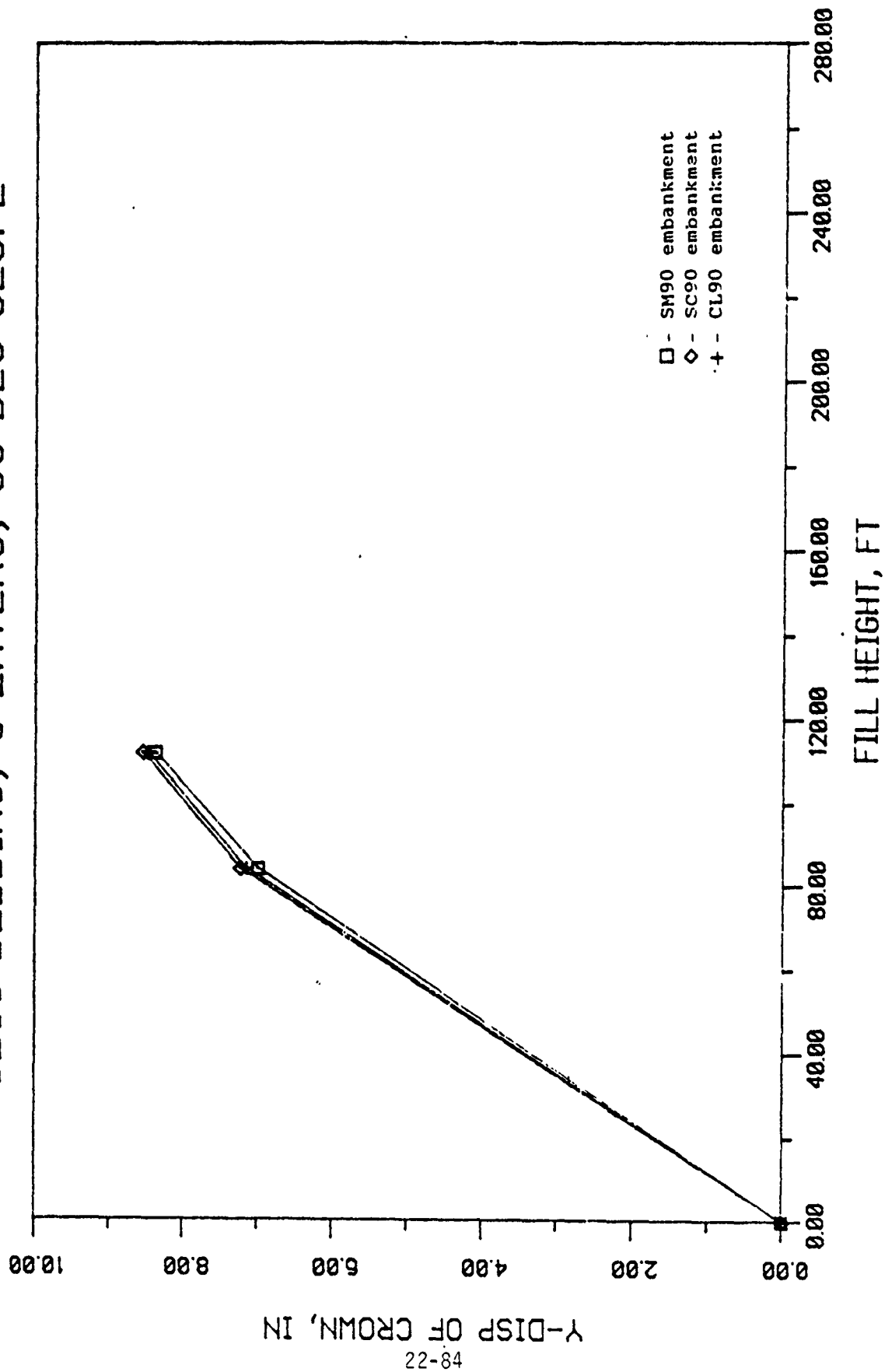


Figure 4.21a Relative Crown Deflection vs. Fill Height for Case III

# CL85 BEDDING, 5 LAYERS, 30 DEG SLOPE

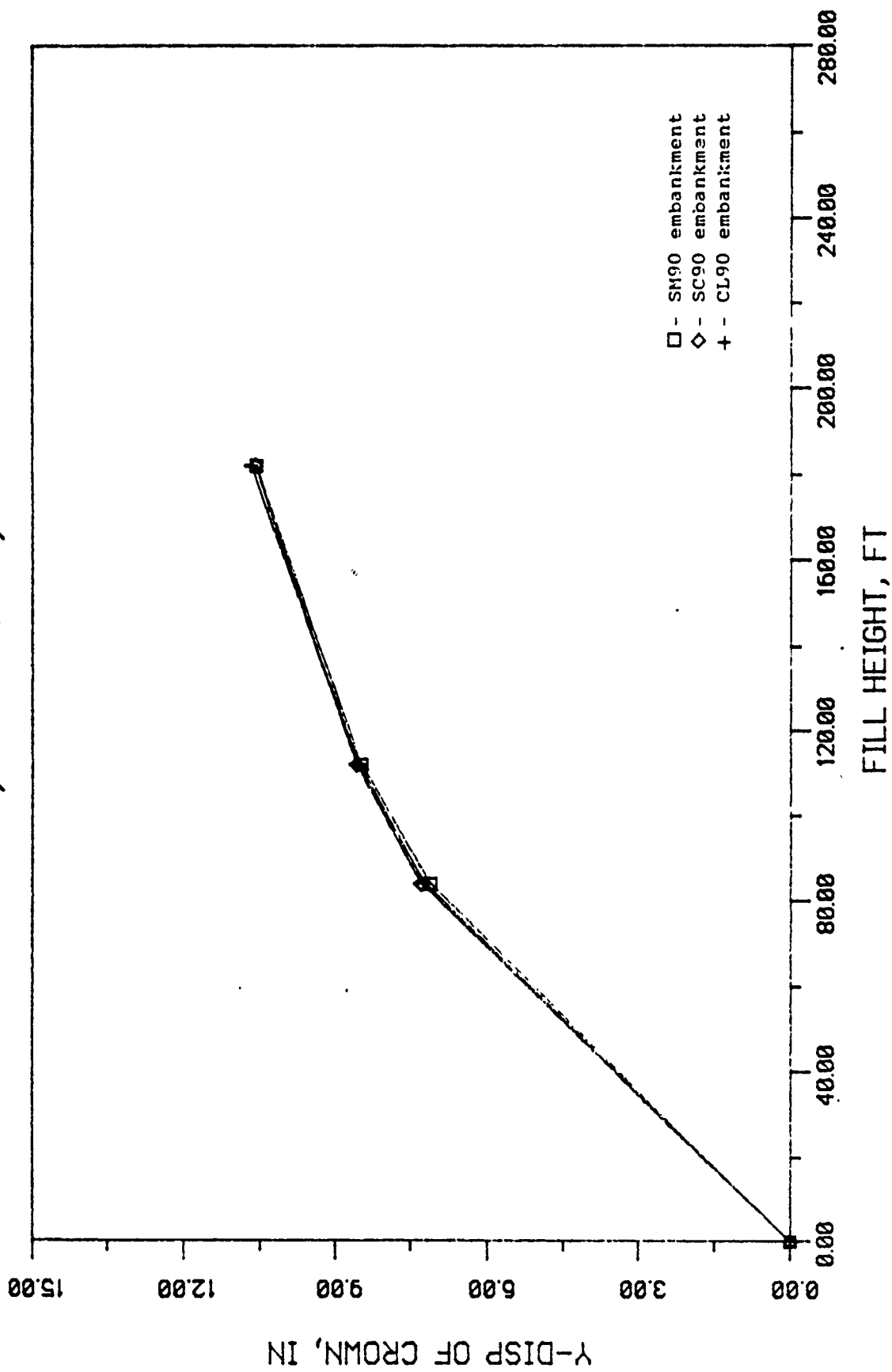


Figure 4.21b Relative Crown Deflection vs. Fill Height for Case III

# SM85 BEDDING, 3 LAYERS, 30 DEG SLOPE

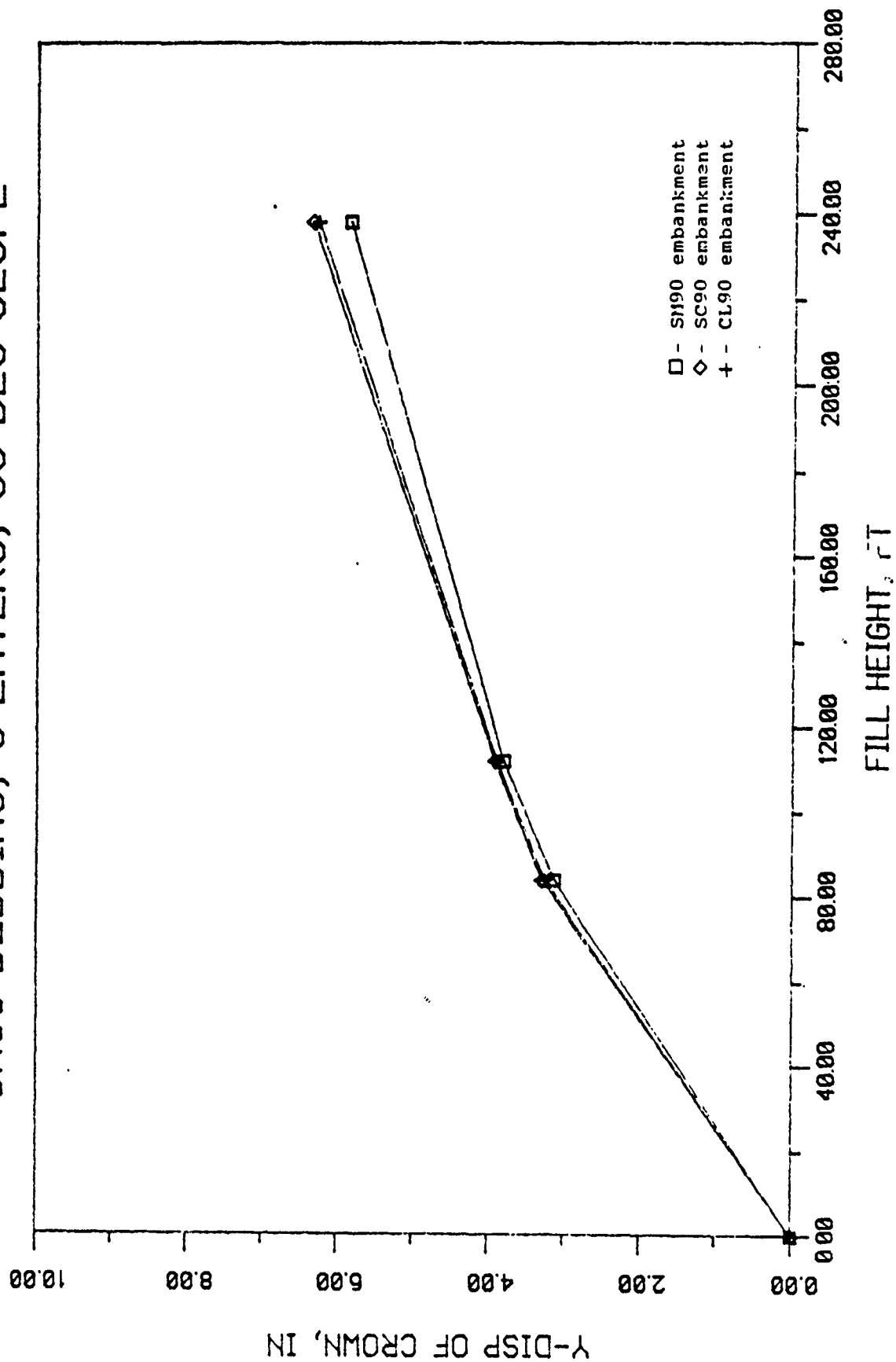


Figure 4.21c Relative Crown Deflection vs. Fill Height for Case III

# SM85 BEDDING, 5 LAYERS, 30 DEG SLOPE

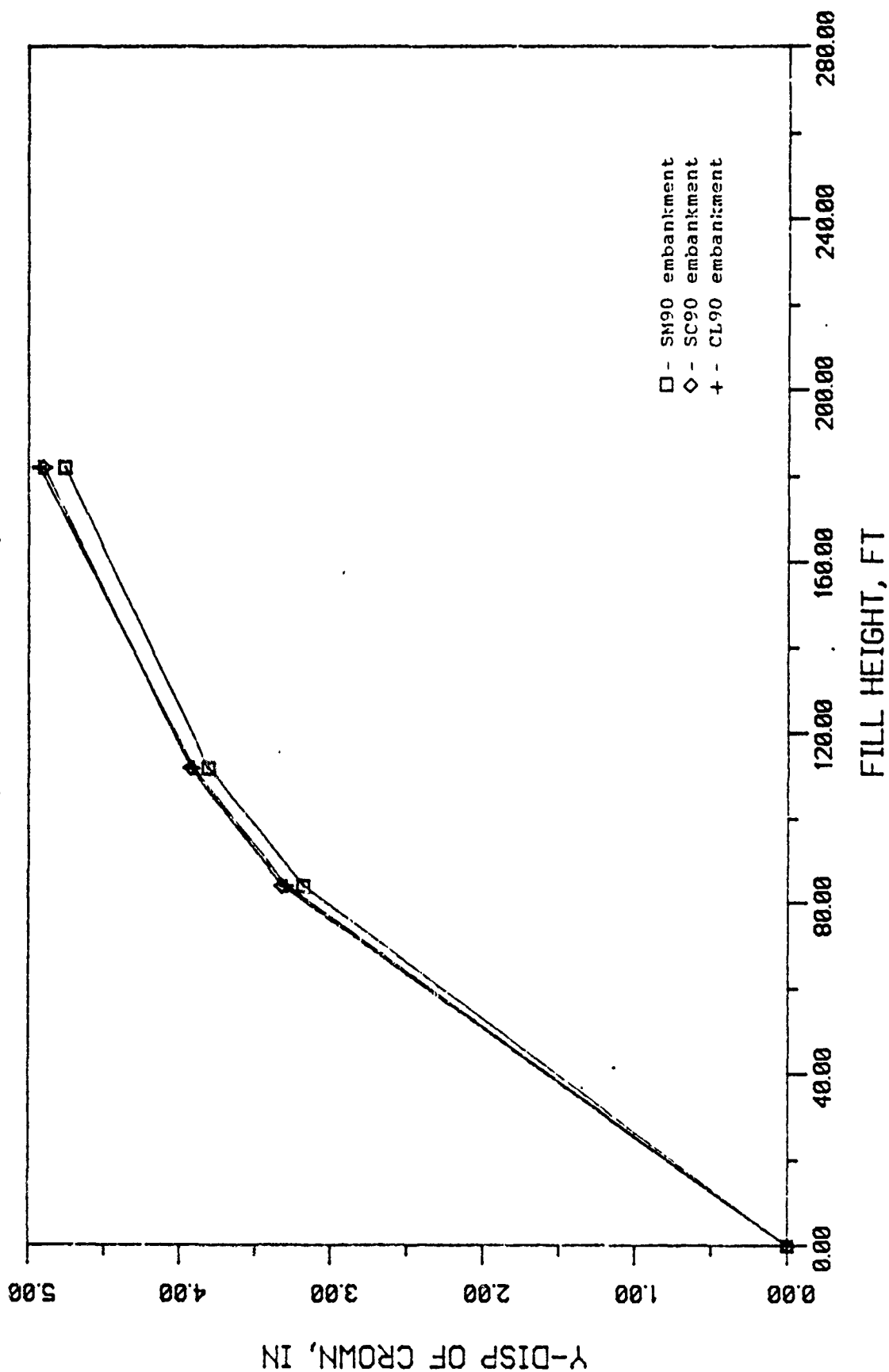


Figure 4.21d Relative Crown Deflection vs. Fill Height for Case III1

type to a maximum of 10.69 in. occurring when the embankment is of CL90 type. In this case, it could be said that the soil type for the embankment does not cause extreme difference in the relative deflection of the crown.

The third case is a system modeled on SM85 soil bedding with a 3-layer rock cover installed. In this case, a system model with the SM90 soil embankment caused the least amount of relative crown deflection, being 5.84 in. The installation of SC90 soil for the embankment causes the crown to deflect by 6.34 in., half-inch more than with the previous condition. In this case overall, an SM90 type soil used for the embankment material shall produce the least crown deflection.

The fourth and final case was found to be the most ideal among all the cases studied. The minimum relative crown deflection was found to be 4.76 in. and attained by installing an SM90 soil type embankment under a 5-layer rock-cover over an SM85 soil bedding. The maximum is found to be 4.93 in. with an SC90 soil embankment.

Overall, by examining all the observations mentioned above, it was found that an SM90 type soil used for the embankment causes the least amount of crown relative deflection.

Moments developed at crown are also highly influenced by the soil type of the embankment. In this discussion, similar to the previous one, the system models were set to have a constant embankment slope of 30 degrees for the same reason as to focus the attention on the influence of the embankment soil only. Also, all other variables such as bedding type and the number of

layers for the rock cover are taken into account to visualize the consistency of the results (refer to Figure 4.22).

Case number III2.a involves a system model on CL85 soil bedding with 3 layers of rock as the cover. The moment at the crown of the structure at the completion of six load increments was governed by the CL90 embankment producing a minimum moment magnitude of 80039 in-lb/in. The maximum being 85160 in-lb/in produced by SC90 embankment. This analysis covers crown moment after six load increments only because a system under these conditions failed after eight load increments.

The next case, Case III2.b involves a system modeled in the same manner as the previous one discussed except that a 5-layer rock cover was installed. The structure models withstood the entire load scheme for all nine load increments providing complete data for analysis. The bending moments occurring at the crown had a standard deviation of 2211 in-lb/in with a maximum of 113096 in-lb/in occurring when the embankment is of SC90 soil and a minimum of 17756 in-lb/in occurring when the embankment is of CL90 soil.

The third case, Case III2.c involves a system modeled on an SM85 bedding with a 3-layer rock cover installed. In this case, the embankment made up of SM90 soil produced the least moment magnitude among all three embankment soil types. At the completion of nine load increments, the SM90 type soil produced a crown moment magnitude of 83773 in-lb/in, a magnitude that is 20% less than that produced by SC90 type soil, which in turn produced the greatest crown moment.

# CL85 BEDDING, 3 LAYERS, 30 DEG SLOPE

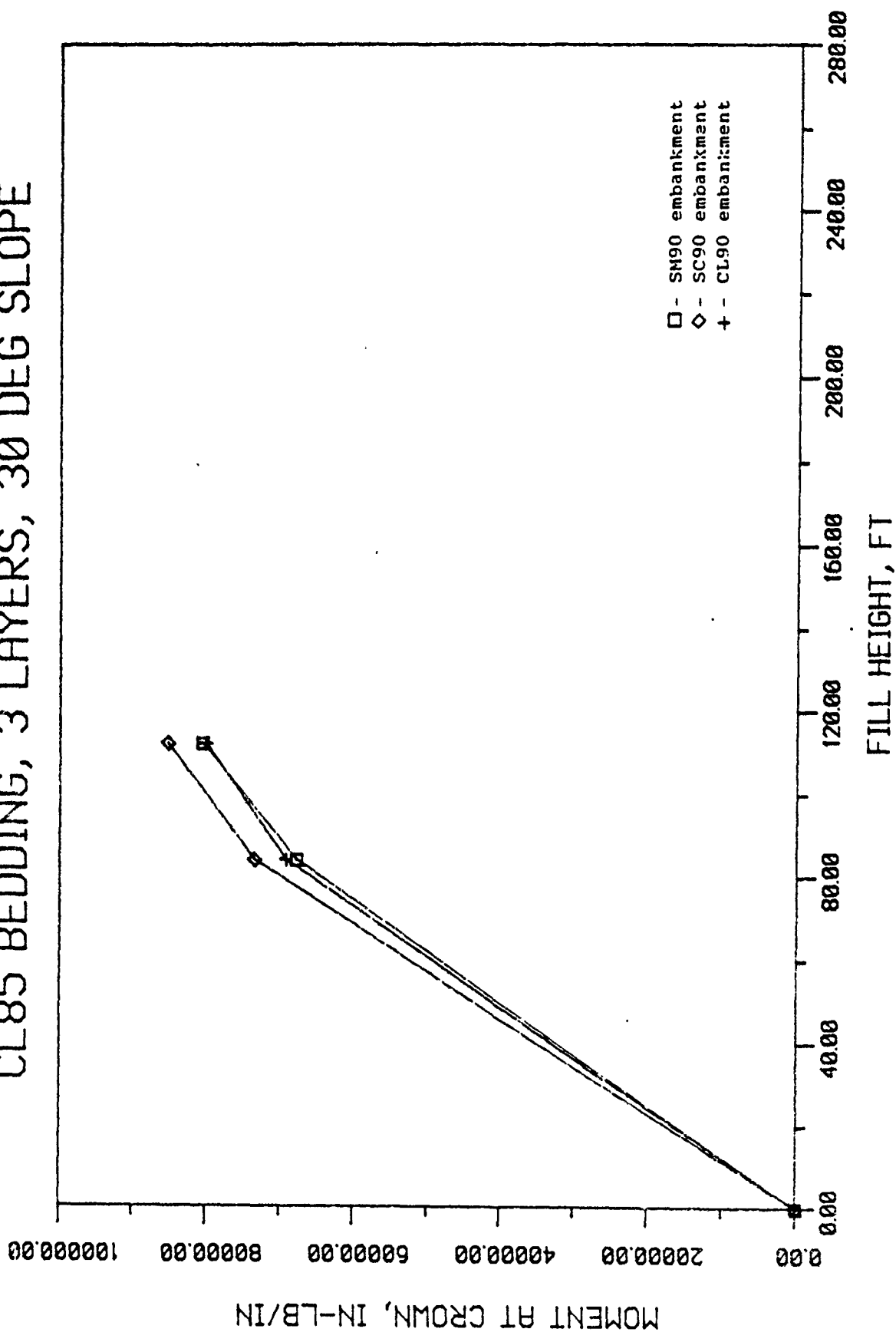


Figure 4.22a Crown Moment vs. Fill Height for Case III2

# CL85 BEDDING, 5 LAYERS, 30 DEG SLOPE

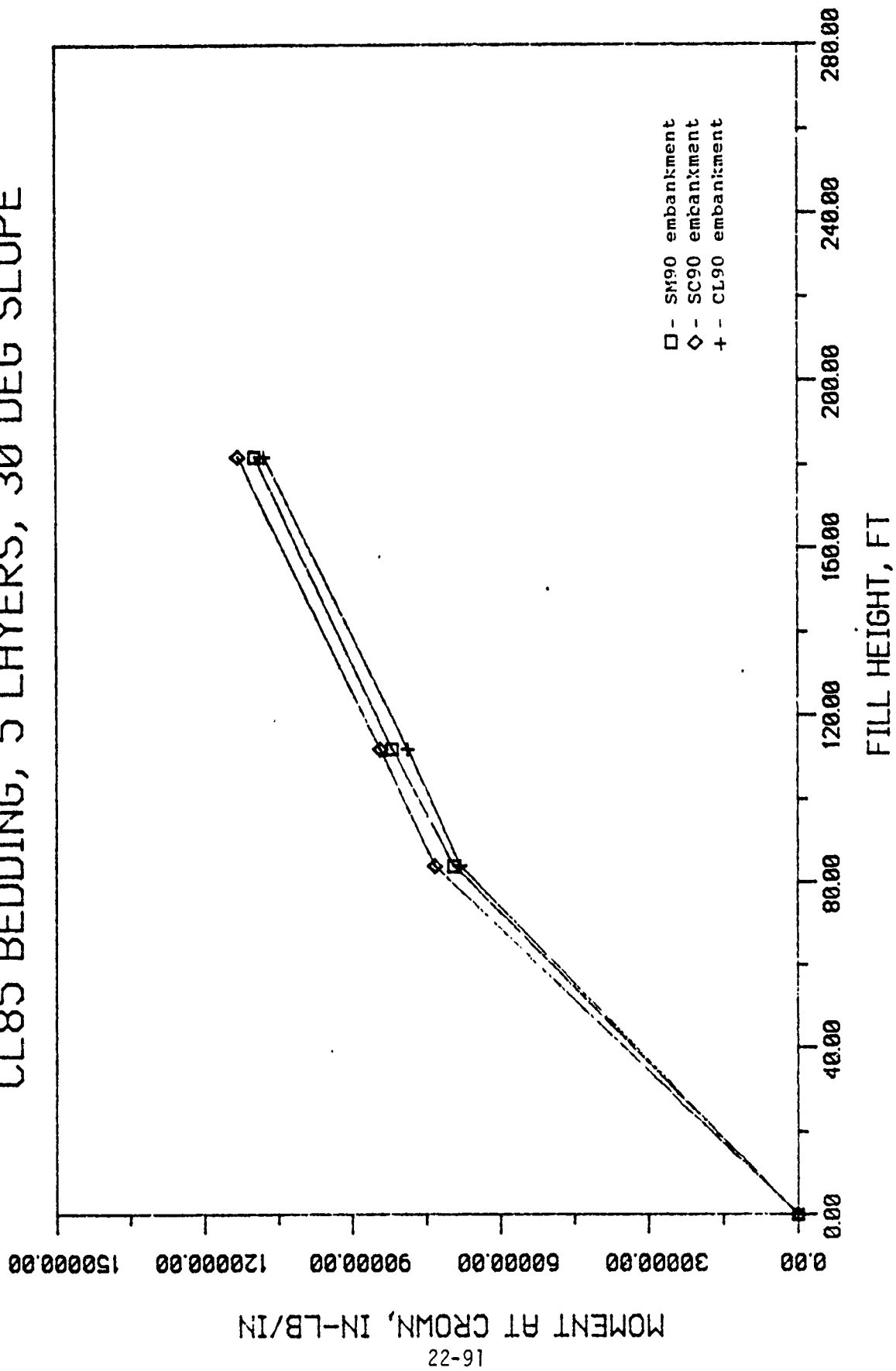


Figure 4.22b Crown Moment vs. Fill Height for Case III2

# SM85 BEDDING, 3 LAYERS, 30 DEG SLOPE

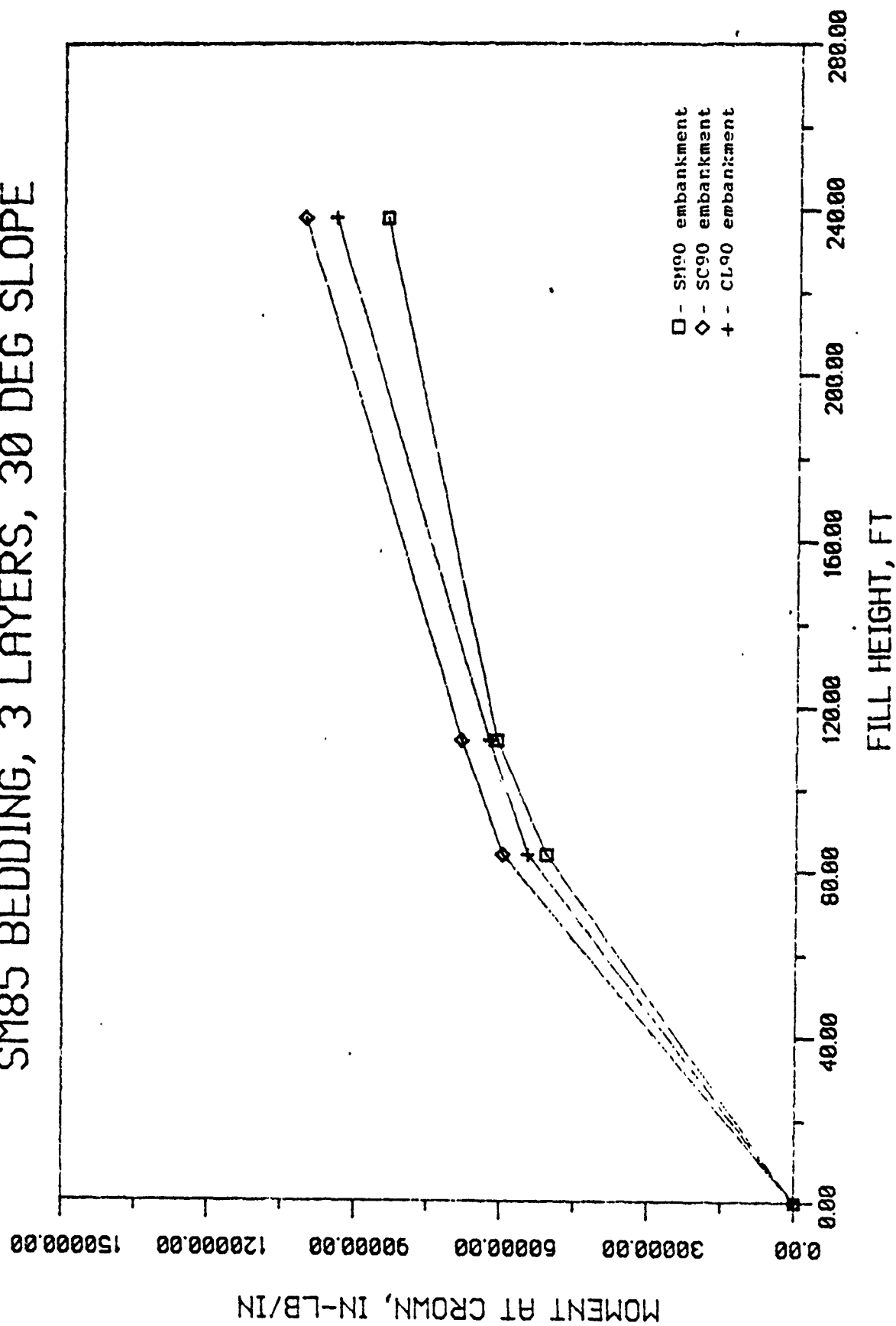


Figure 4.22c Crown Moment vs. Fill Height for Case III2

# SM85 BEDDING, 5 LAYERS, 30 DEG SLOPE

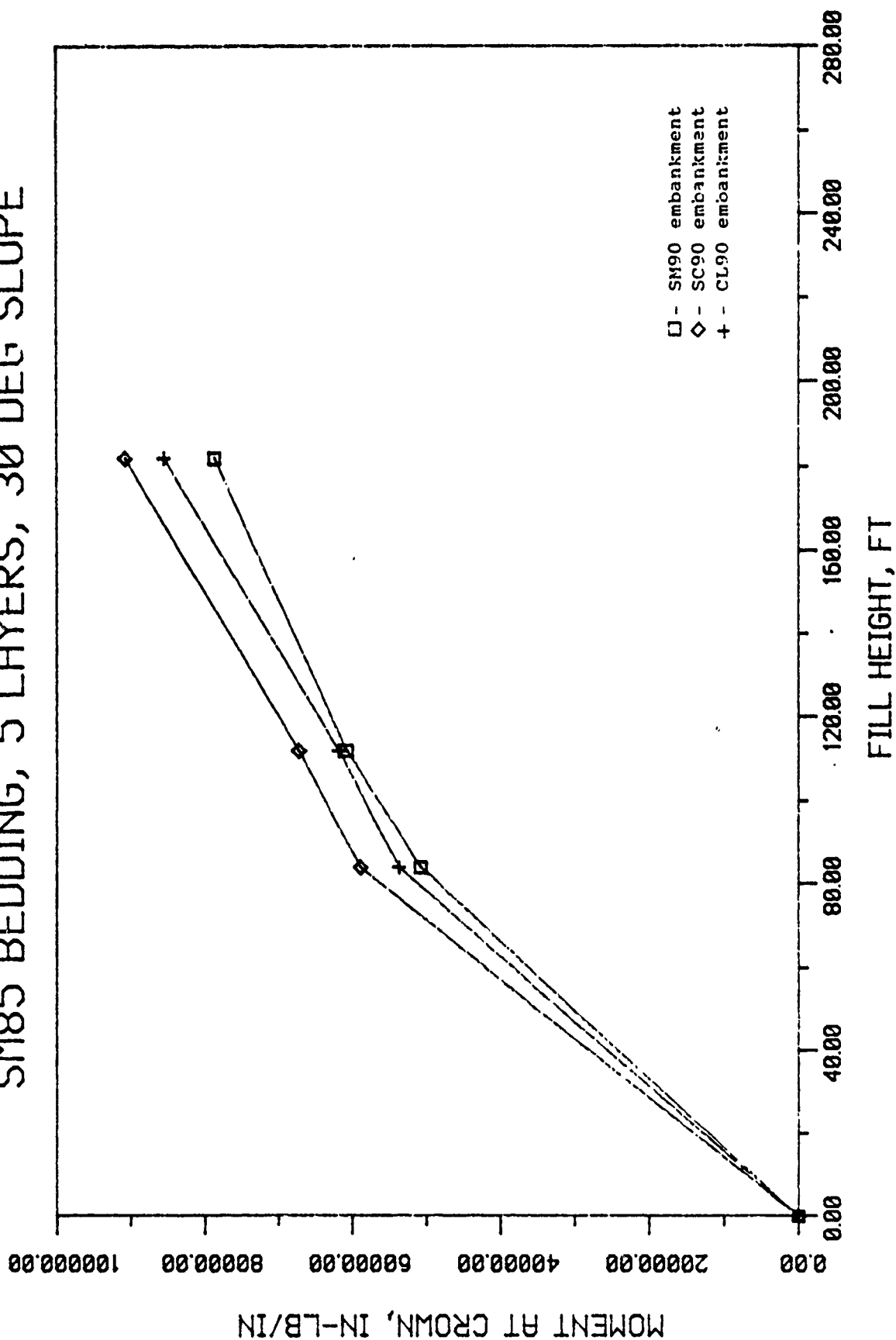


Figure 4.22d Crown Moment vs. Fill Height for Case III2

The fourth and final case, Case III2.d is similar to the previous one except that a 5-layer rock cover is installed. And similarly, the SM90 soil produced the least amount of moment at the completion of nine load increments. A standard deviation of 4958.071 in-lb/in with a maximum of 90750 in-lb/in occurring when the embankment is of SC90 type soil, and a minimum of 78640 in-lb/in when the embankment type is SM90.

Thrust developed at the crown, like the other types of structural reactions are also highly dependent on the kind of soil used for the embankment. This discussion shall also be limited to system models with 30-degree slope embankments, taking into account all the other factors such as bedding conditions and the number of layers for the rock cover, designated as Case III3 (refer to Figure 4.23).

The first case to be analyzed is a structure modeled on CL8 under a 3-layer rock cover. Unfortunately, the structural models for this system failed after eight load increments. Therefore, the analysis is limited to the findings after the completion of six load increments. At the end of the fourth load increment, it was found that the CL90 embankment soil produced less crown thrust magnitude than the SM90 type. But at the completion of six load increments, it was found that the SM90 type soil produced less thrust at the crown than the CL90 type, which in turn produced the highest thrust magnitude between all three types. The SC90 type was consistent throughout the entire scheme in producing the least amount of thrust at the crown, the final thrust magnitude after six load

# CL85 BEDDING, 3 LAYERS, 30 DEG SLOPE

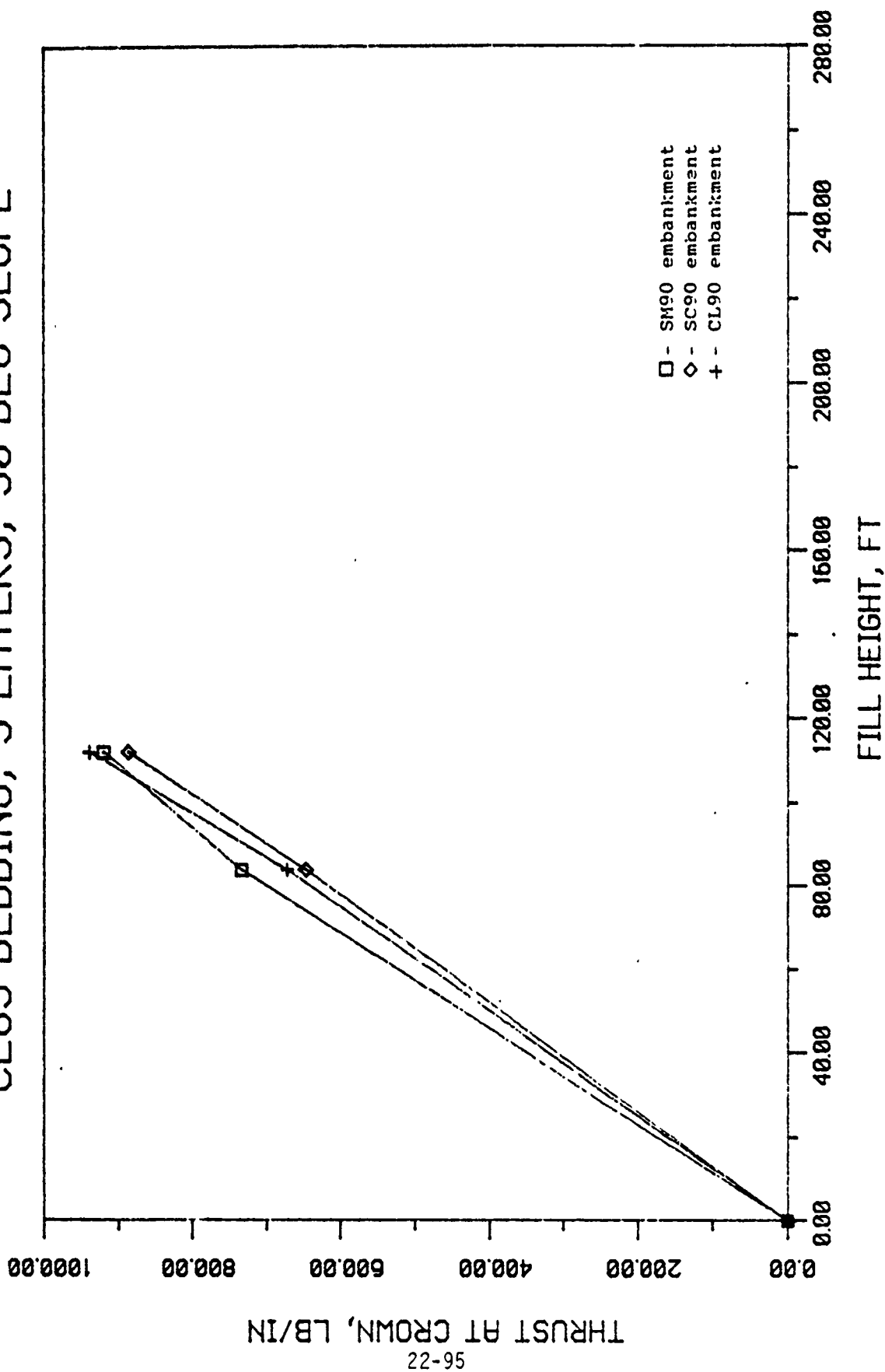


Figure 4.23a Crown Thrust vs. Fill Height for Case III3

# SM85 BEDDING, 5 LAYERS, 30 DEG SLOPE

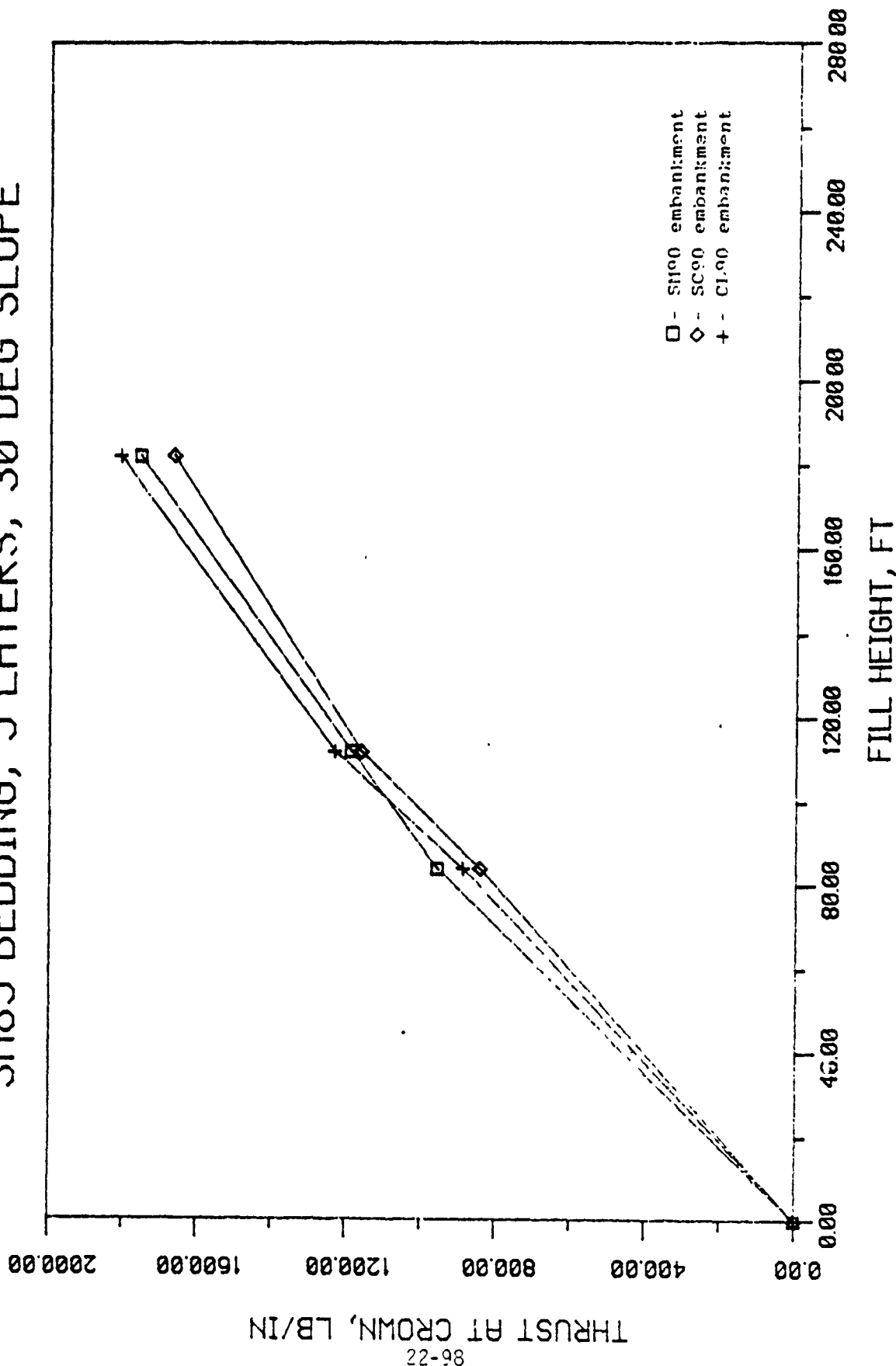


Figure 4.23d Crown Thrust vs. Fill Height for Case III

increments being 887 lb/in.

A different set of results appears when the rock cover of the above case is replaced by the 5-layer type. At the end of four load increments, the SM90 type soil produced greater thrust in magnitude at the crown than the SC90 type. But after six load increments, it was found that the SM90 type soil produced less thrust than the SC90 type. This condition went on until the completion of all nine load increments, making the SM90 type the ideal soil type to use in this case, producing a final crown thrust of 1384 lb/in, 2% less than that produced by the SC90 type. The SC90 type was consistent in producing the largest amount of thrust throughout the entire load increments producing a final crown thrust of 1540 lb/in, 11.3% larger than the minimum.

The most interesting case in this analysis is the case wherein the system is modeled on an SM85 bedding under the 3-layer rock cover. The thrust developed at the crown increased directly proportional to the fill height for all types of embankment soil until the completion of the sixth load increment. The thrust values then decreased even though the fill height continued to increase at the beginning of the seventh load increment. The final thrust developed at the crown per soil type was therefore the least among all the cases studied in this section. The SC90 type produced the least amount of thrust at the crown having a magnitude of 531 lb/in. Followed by embankment soil type SM90 producing a final thrust magnitude of 607 lb/in and then by the CL90 type producing 651

lb./in.

The final case studied in this section is a system modeled on SM85 bedding under a 5-layer rock cover. At the end of fourth load increment, the SM90 soil type produced the greatest amount of thrust at the crown. But after the completion of the sixth load increment, the CL90 soil type produced the highest thrust magnitude among all three embankment types. At the completion of the final load increment, soil type CL90 was found to generate the largest amount of thrust at the crown of the structure, its magnitude being 1810 lb/in. The SC90 type soil was consistent in producing the least amount of thrust on the crown throughout the whole loading scheme, generating a final thrust magnitude after ninth load increment of 1664 lb/in.

## SECTION V

### SUMMARY, CONCLUSIONS AND RECOMMENDATIONS

#### A. SUMMARY AND CONCLUSIONS

This report presents an investigation of the behavior of a reinforced concrete arch structure under various embankment and bedding conditions. A finite element analysis of structural responses was performed on system models with varying bedding, embankment slope, embankment soil type, and rock cover type. The findings and conclusions from this investigation are as follows:

1. The results of the finite element model study showed consistency and reliability in predicting soil and structure responses.
2. The structures that were predicted to fail were the ones systemed in the order of:
  - a. Having a CL85 (clay) soil type bedding, with a 3-layer rock cover, and a 30-degree slope embankment. A structure modeled under these conditions was predicted to fail no matter what type of soil was used for the embankment.
  - b. Having a CL85 (clay) soil type bedding, with a 5-layer rock cover, and a 45-degree slope embankment. A structure modeled under these conditions was predicted to fail no matter what type of soil was used for the embankment.
3. Between the two types of bedding materials used in the

tests, it was found that at a relative compaction of 85%, a silty sand type of soil (type SM85) produced less structural settlement than a clayey type soil (CL85).

4. An embankment constructed with a 45-degree slope caused less moments to develop around the structure than an embankment with a 30-degree slope. In addition the former condition also caused structural reaction to develop more in form of axial forces (thrust) rather than bending moments, which is preferable in shell structures.

5. An embankment constructed with a silty sand type (SM85) of soil produces less moment around the structure and encourages structural reaction to develop through axial forces (thrust).

6. A rock-cover composed of a mean boulder diameter of 14 inches and set in five layers causes less magnitude in structural response at the completion of the embankment than a 3-layer rock cover with a mean boulder diameter of 42 inches.

7. Overall, a structure set on an SM85 sand soil type bedding, with SM90 soil embankment, 5-layer type rock cover, and set on a 30-degree slope proves to be the most effective system. The finite element analysis show that an arch structure constructed in this manner will produce the least amount of bending moment, the load transfer onto the structure being concentrated mainly on axial thrust. Figures 4.24 thru 4.26 show the final soil pressure, moment, and thrust distribution for a structure modelled in this manner.

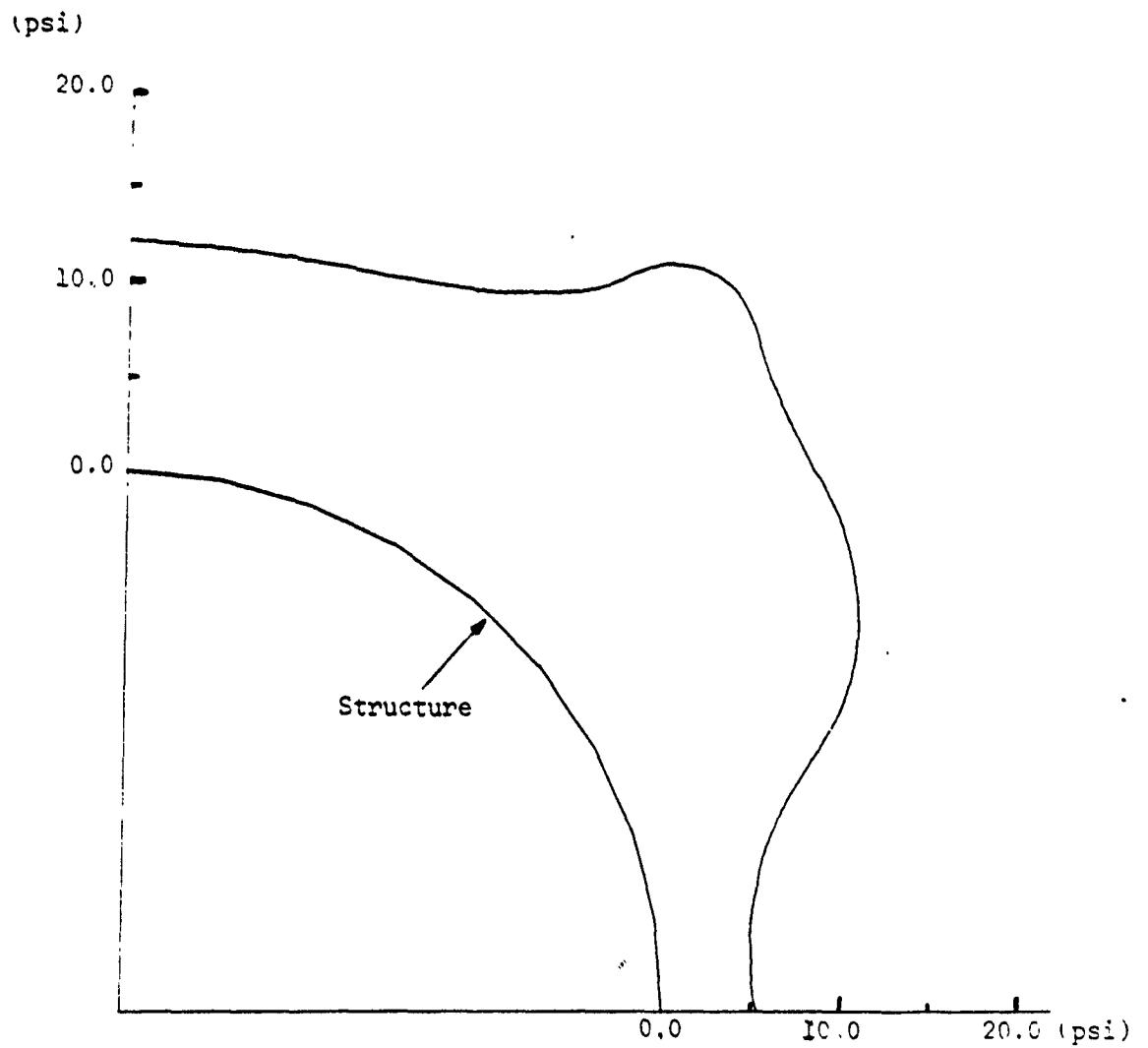


Figure 4.24 Soil Pressure Distribution

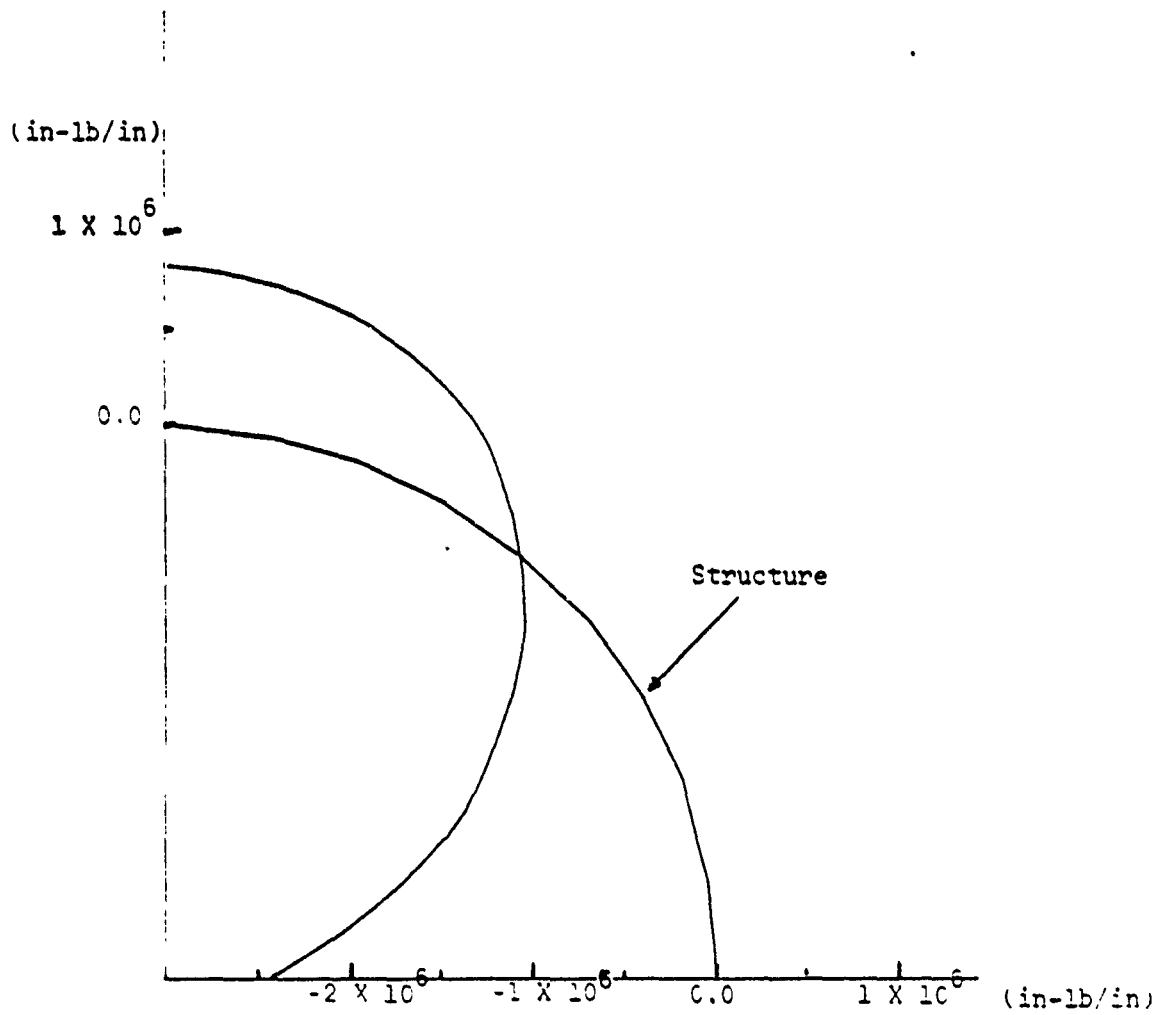


Figure 4.25 Moment Distribution

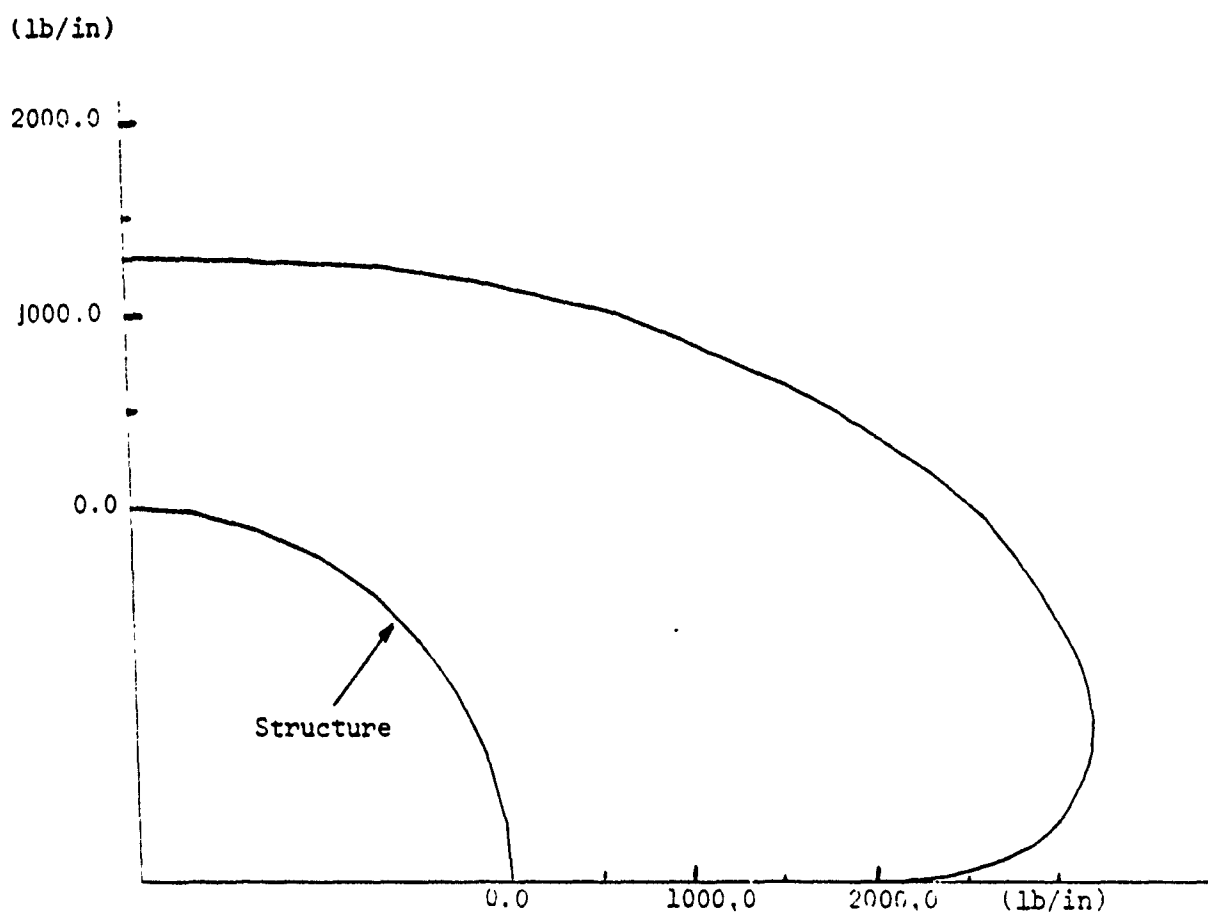


Figure 4.26 Thrust Distribution

## B. RECOMMENDATIONS

Recommendations for research based on this study are as follows:

The results of the finite element model study presented in this report are based on the preliminary investigation for the feasibility study of an arch structure in a centrifuge. A more comprehensive (extensive) research including embankments of other sizes and geometries, structural reinforcement, different soil types, compaction for embankments, and bedding parameters is required in order to gain a better understanding of the relationship of the arch structure and the embankment.

In order to achieve a comprehensive model study using the centrifuge model technique, an on-board data acquisition system is required. Past experience of the researchers prove that this is a necessity for acquiring reliable and qualitative data.

A field study is necessary to verify the results of the centrifuge model study and finite element analysis once reasonable information is obtained.

## REFERENCES

1. Austin, C.F., Halsey, C.C., Clodt, R.L. and Berry, S.L., "Full Scale Penetration into Semiconfined Diorite Boulders by a Semiarmor-Piercing (SAB) Bomb," Report No. ESL-TR-81-47, Air Force Engineering Services Center, Tyndall AFB, Florida, January 1982, UNCLASSIFIED.
2. Austin, C.F., Halsey, C.C., Clodt, R.L., and Berry, S.L., "Protective Antipenetration Systems Development," Report No. ESL-TR-83-39, Air Force Engineering Services Center, Tyndall AFB, Florida, September, 1983, UNCLASSIFIED.
3. Austin, C.F., Halsey, C.C., Berry, S.L., and Anderson, C.R., "Burster Slab Penetration Test," Report No. ESL-TR-84-49, Air Force Engineering Services Center, Tyndall AFB, Florida, July 1985, UNCLASSIFIED.
4. Bucky, P.B., "Use of Models for the Study of Mining Problems," A.I.M.M.E. Technical Publication No. 425, 1931.
5. Coles, C.K., "Centrifuge Models of a Spile-Reinforced Tunnel," M.S. Thesis, University of California, Davis, June, 1982.
6. Cunningham, C.H., Townsend, F.C., and Fagundo, F.E., "The Development of Micro-Concrete for Scale Model Testing of Buried Structures," Report No. ESL-TR-85-49, Air Force Engineering Services Center, Tyndall AFB, Florida, January 1986.
7. Duncan, J.M., et al., "Strength, Stress-Strain and Bulk Modulus Parameters for Finite Element Analyses of Stresses and Movements in Soil Masses," Report No. UCB/GT/78-02, National Science Foundation, April, 1978.
8. Finkel, J., Computer-Aided Experimentation, John Wiley, New York, 1975.
9. Freeman, R.L. Telecommunication Transmission Handbook, Wiley, New York, 1975.
10. James, R.G., and Larsen, H., "Centrifugal Model tests of Buried Rigid Pipes," Proceedings of the Ninth International Conference on Soil Mechanics and Foundation Engineering, Tokyo, Japan, 1977.
11. Katona, M.G., Smith, J.M., Odello, R.J., and Allgood, J.R., "CANDE-A Modern Approach for the Structural Design and Analysis of Buried Culverts," Report No. FHWA/RD-77/5, Federal Highway Administration, Washington, D.C., October, 1976.

12. Katona, M.G., Vittes, P.D., Lee, C.W., and Ho, H.T., "CANDE-1980: Box Culverts and Soil Models," Report No. FHWA/RD-80/172, Federal Highway Administration, Washington, D.C., May, 1981.
13. Kim, M.M. and Ko, H.Y., "Centrifugal Testing of Soil Slope Models," Transportation Research Record 872, pp. 7-15, 1982.
14. Kim, Y.S., Shen, C.K., and Bang, S., "Centrifuge Model Study of an Oil Storage Tank Foundation on Soft Clay," Proceedings of the 8th European Conference on Soil Mechanics and Foundation Engineering, Helsinki, Finland, May 3-26, 1983.
15. Kim, Y.S., and Davis, R.E., "Proof Testing of A Structural Plate Pipe with Varying Bedding and Backfill Parameters Section VII, Volume 3: Finite Element Analysis," Report No. FHWA/CA/SD-83/04, California Department of Transportation, Sacramento, California, August, 1983.
16. Leonards, G.A., Wu, Tzong-Hsin, and Juang, Charng-Hsein, "Predicting Performance of Buried Conduits," Report No. FHWA/IN/JHRP-81/3, Indiana State Highway Commission, Indianapolis, Indiana, June 1982.
17. Moore, C.A., "Modern Electronics for Geotechnical Engineers, 1. Introduction to Integrated Circuits," Proceedings of the ASTM Geotechnical Testing Journal, Volume 3, Number 2, June, 1980.
18. Moore, C.A., "Modern Electronics for Geotechnical Engineers, 4. Waveform Generators," Proceedings of the ASTM, Geotechnical Testing Journal, Volume 3, Number 2, June, 1980.
19. Moore, C.A., "Modern Electronics for Geotechnical Engineers, 5. Digital Logic Circuits," Proceedings of the ASTM, Geotechnical Testing Journal, Volume 3, Number 3, September, 1980.
20. Moore, C.A., "Modern Electronics for Geotechnical Engineers, 6. Process Control Applications," Proceedings of the ASTM Geotechnical Testing Journal, Volume 3, Number 4, December 1980.
21. Moore, C.A., "Modern Electronics for Geotechnical Engineers, 7. Introduction to Microprocessors," Proceedings of the ASTM Geotechnical Testing Journal, Volume 4, Number 1, March, 1981.

22. Moore, C.A., "Modern Electronics for Geotechnical Engineers 8. Microprocessor Applications," Proceedings of the ASTM, Geotechnical Testing Journal, Volume 4, Number 2, June 1981.
23. Pokrovsky, G.I., and Ryodorov, I.S., "Centrifugal Model Testing in the Mining Industry," Nedra Publishing House, Moscow, 1969.
24. Pokrovsky, G.I., and Ryodorov, I.S., "Centrifugal Model Testing in the Construction Industry," Translation Prepared by Building Establishment Library Translation Service, England, August, 1976.
25. Research Engineers, Personnel Communication, Facility Systems and Analysis Branch, and Operations Support Branch, Air Force Engineering Services Center, Tyndall AFB, Florida, May-August 1986.
26. Roden, M.S., Analog and Digital Communication, Prentice-Hall Englewood Cliffs, NJ, 1979.
27. Rohani, B., "Effectiveness of Rock-Rubble/Boulder Screens for Degrading the Penetration Capability of Kinetic Energy (KE) Projectiles," Report to Office, Chief of Engineers, U.S. Army, Waterways Experiment Station, Vicksburg, Mississippi, December, 1982, UNCLASSIFIED.
28. Schmidt, R.M., and Holsapple, K.A., Journal of Geophysical Research, Vol. 85, No. 1, January, 1980.
29. Scott, R.F., and Morgan, N.R., "Feasibility and Desirability of Constructing a Very Large Centrifuge for Geotechnical Studies," Report 760-170 NSF, California Institute of Technology and JPL, March 1977.
30. Shen, C.K., Kim, Y.S., Bang, S. and Mitchell, J., "Centrifuge Modeling of a Lateral Earth Support," Proceedings of the ASCE, Journal of the Geotechnical Engineering Division, Vol. 108, No. GT9, September, 1982.
31. Shen, C.K., Bang, S., and Kim, Y.S., "Improvement of Oil Storage Tank Foundation on Soft Clay by Fabric-Mesh-Reinforcement," proceedings of the International Symposium on In-Situ-Soil and Rock Reinforcement, Ecole Polytechnique, Ecole Nationale des Ponts et Chaussees, Paris, France, October 9-11, 1984.

32. Shen, C.K., Li, X.S., and Kim, Y.S., "Microcomputer Based Data Acquisition Systems for Centrifuge Modeling," Proceedings of the ASTM, Geotechnical Testing Journal, Volume 7, Number 4, December, 1984.
33. Wong, K.S. and Duncan, J.M., "Hyperbolic Stress-Strain Parameters for Nonlinear Finite Element Analysis of Stresses and Movements in Soil Masses," Report No. TE-74-3, University of California, Berkeley, July, 1974.

FINAL REPORT NUMBER 23  
REPORT NOT AVAILABLE AT THIS TIME  
Dr. William Schulz  
760-7MG-079

**1987-1988 RESEARCH INITIATION PROGRAM**

**Sponsored by the  
AIR FORCE OFFICE OF SCIENTIFIC RESEARCH**

**Conducted by the  
UNIVERSAL ENERGY SYSTEMS, INC.**

**FINAL REPORT**

**STRESS WAVE PROPAGATION IN  
LAYERED MEDIA**

<b>Prepared by:</b>	<b>Joseph W. Tedesco</b>
<b>Academic Rank:</b>	<b>Associate Professor</b>
<b>Department and University:</b>	<b>Department of Civil Engineering Auburn University</b>
<b>Date:</b>	<b>August 1988</b>
<b>Contract No.:</b>	<b>F49620-85-C-0013/SB5851-0360</b>
<b>Subcontract No.:</b>	<b>S-760-7MG-034</b>

(The reverse of this page is blank.)

## ABSTRACT

Protective military structures are typically constructed of massive, monolithic concrete slabs. This practice is considered necessary in order to protect personnel and/or vital equipment within the structure from the harmful blast effects of conventional weaponry. A high intensity compressive longitudinal blast wave incident upon a protective shelter propagates through the monolithic concrete shelter wall, and reflects as a tensile wave at the interior face of the wall. The reflected tensile wave can cause extensive spalling of the interior face of the shelter walls, thus posing a potentially dangerous threat to personnel and equipment in the shelter.

A comprehensive numerical analysis is conducted to evaluate the effectiveness of various "layered structures" for enhanced protection against blast effects from conventional weaponry. Of primary concern is the capability of layered systems to mitigate stress wave propagation, and the subsequent elimination of interior spalling.

The finite element method (FEM) is employed to investigate the wave propagation characteristics of three layered systems: 1) concrete-polystyrene-concrete (CPC), 2) sand-polystyrene-concrete (SPC), and 3) sand-polystyrene-concrete-polystyrene-concrete (SPCPC). Both linear and nonlinear material behavior are considered. Stress transmission ratios are determined for each layered system.

The results of the investigation indicate that layered media significantly reduce stress transmission, and that the application of layered media to protective shelters can eliminate interior spalling.

#### ACKNOWLEDGEMENTS

This research was sponsored by a research grant from the Air Force Office of Scientific Research. Special appreciation is extended to Dr. Allen Ross, Research Fellow, Engineering Research Division, Engineering and Services Laboratory, Tyndall Air Force Base, for his assistance and productive discussions.

## I. INTRODUCTION

### Motivation

Protective military shelters are typically constructed of massive, monolithic concrete slabs. This practice, which has not changed significantly since the end of the Second World War, is necessary in order to protect personnel and/or vital equipment within the structure from the harmful effects of conventional weaponry. The drastic devaluation of the dollar in the NATO nations during the past several years has made construction costs for these types of structures prohibitive. This fact dramatically underscores the urgency for the development of alternative, cost-effective protective structure designs.

When a typical monolithic concrete protective shelter is subject to an impulse loading (blast wave) from conventional weaponry, a high-intensity stress wave propagates through the shelter wall. The stress wave reflects from the interior face of the shelter wall as a tension wave and can cause extensive spalling of the interior face of the wall. The spalled concrete fragments are hurled away from the wall at high velocities, posing a

potentially dangerous threat to personnel and equipment within the shelter.

Recent experimental studies (5,26) and analytical investigations conducted by Tedesco (20,21), Tedesco et al (23,24), and Landis (14) have indicated that "layered structures" may provide a viable alternative to conventionally hardened structures. The intent of this investigation is to evaluate the effectiveness of various "layered structures" for enhanced protection against impulse loading from conventional weaponry.

#### Previous Research

Extensive information is available concerning the propagation of stress waves in elastic, isotropic media. Information is also available concerning the propagation of stress waves in inelastic media. The majority of the information, however, deals with stress wave propagation in homogeneous metal wires and bars of uniform cross-section.

Little information is available on the propagation of stress waves through layered media. Even less information exists on the use of layered media in protective shelters to resist high-intensity blast loadings. Recent research, however, indicates that layered structures may provide a viable alternative to conventionally hardened structures.

Analytical investigations conducted by Tedesco (20,21) indicate that layered systems may be utilized to

alter the stress wave propagation characteristics of a protective shelter. The investigations revealed that certain combinations of materials, constructed in layers, significantly reduce the stress transmitted through the shelter walls. It was determined that the combination of materials required to substantially reduce the transmitted stress consists of a low-density, low-strength center layer sandwiched between two high-density, high-strength layers.

Subsequent analytical investigations conducted by Tedesco et al (23,24) examined three layered systems, each consisting of a center absorption layer surrounded by two layers of concrete. The absorption layers examined included air, polystyrene, and soil. The results from these preliminary studies revealed that each layered system significantly reduced the stress transmitted to the interior of the structure.

Analytical investigations conducted by Landis (14) examined layered systems consisting of an absorption layer of polystyrene or soil, sandwiched between two layers of concrete. Both layered systems significantly reduced the stress transmitted through the structure. The polystyrene, however, proved to be a much more effective absorption layer than the soil.

The research conducted in the aforementioned studies investigated only the linear-elastic behavior of the

layered systems. The effect of nonlinear behavior upon stress wave propagation in layered media has not yet been examined.

### Objective

The primary objective of this study is to evaluate the effectiveness of layered systems to mitigate stress wave propagation via a comprehensive numerical analysis. The numerical analyses are conducted on several different types of layered systems subject to impulse loading in order to ascertain the characteristics of wave propagation through the various material layers comprising the systems. From the results of the numerical analyses, recommendations for layered systems as an alternative to conventionally hardened protective structures are presented.

### Scope of Study

The finite element method (FEM) is utilized in the numerical analyses to investigate the wave propagation characteristics of several layered systems. The layered systems investigated include a concrete-polystyrene-concrete system, a sand-polystyrene-concrete system, and a sand-polystyrene-concrete-polystyrene-concrete system. The dimensions of the concrete and sand layers are constant for each layered system. Polystyrene layers of varying thickness are examined in order to properly assess

the effect of absorption layer thickness upon wave propagation. Both linear and nonlinear material behavior are considered in the wave propagation analysis. The ratio of transmitted stress to incident stress (transmission ratio) is determined for each system investigated.

## II. STRESS WAVE PROPAGATION IN SOLIDS

In static analyses, it is assumed that a structure is gradually loaded over an interval of time such that inertial properties have no effect on the response of the structure. The structure is in a state of static equilibrium and time is not a variable in the solution. Dynamic problems, however, occur when loading conditions vary significantly in time to produce inertial forces in the structure. The structure is in a state of dynamic equilibrium, and the response of the structure is time dependent. In general, if the period of the forcing function is less than three times the fundamental period of the structure, then the problem becomes dynamic, and inertial forces must be considered in the structural response (8).

When an elastic body is subjected to dynamic loading, stresses and strains propagate throughout the structure at a finite velocity. In most structural dynamic problems, the rate of application of the load is small in comparison with the velocity of stress/strain propagation. Therefore, the entire structure responds to the loading condition immediately, and wave propagation is not a consideration in the solution. In instances where the

load is applied at a high rate (as in the case of an impact or explosion), however, the propagation of stress/strain waves must be considered in the problem solution.

### Basic Stress Wave Theory

A stress wave is defined as a moving part of a medium in a state of stress. Since any stress has associated with it a corresponding strain, stress waves and strain waves are identical. When a force is initially applied to a body, a stress wave is generated at the point of contact. The stress wave propagates away from the point of contact at approximately the seismic velocity of that body. Any point in the body remains unstressed and unaffected by the disturbance until reached by the stress wave. The stress wave propagates through the body, reflects from the boundaries of the body, and interacts with other stress waves to create very complicated stress distributions in the body.

Stress waves are classified as normal or tangential. Normal waves are analogous to the normal component of stress. Mass particles under the influence of a normal wave move parallel to the direction of propagation of the wave. A body subjected to a purely normal wave undergoes a volumetric change due to lengthening or shortening, but does not undergo any rotation. For this reason, normal waves are referred to as longitudinal waves or dilational

waves. Tangential waves are similiar to the shear component of stress. Mass particles under the influence of a tangential wave move perpendicular to the direction of wave propagation. A body subjected to a purely tangential wave undergoes a rotational displacement but does not experience a change in volume. For this reason, tangential waves are referred to as shear waves, rotational waves, or distortional waves.

The general equations governing the propagation of stress waves can be derived by analyzing a differencial volume  $\delta x \delta y \delta z$ , as shown in Figure 2.1. The residual force  $F$  in each direction can be found by summing forces in each direction. Summing forces in the  $x$  direction yields

$$F_x = \left( \sigma_x + \frac{\partial \sigma_x}{\partial x} \delta x \right) \delta y \delta z - \sigma_x \delta y \delta z + \left( \tau_{xy} + \frac{\partial \tau_{xy}}{\partial y} \delta y \right) \delta x \delta z - \tau_{xy} \delta x \delta z + \\ + \left( \tau_{xz} + \frac{\partial \tau_{xz}}{\partial z} \delta z \right) \delta x \delta y - \tau_{xz} \delta x \delta y$$

which simplifies to

$$F_x = \left( \frac{\partial \sigma_x}{\partial x} + \frac{\partial \tau_{xy}}{\partial y} + \frac{\partial \tau_{xz}}{\partial z} \right) \delta x \delta y \delta z \quad (2.1)$$

Similiarly,

$$F_y = \left( \frac{\partial \tau_{xy}}{\partial x} + \frac{\partial \sigma_y}{\partial y} + \frac{\partial \tau_{yz}}{\partial z} \right) \delta x \delta y \delta z$$

$$F_z = \left( \frac{\partial \tau_{xz}}{\partial x} + \frac{\partial \tau_{yz}}{\partial y} + \frac{\partial \sigma_z}{\partial z} \right) \delta x \delta y \delta z$$

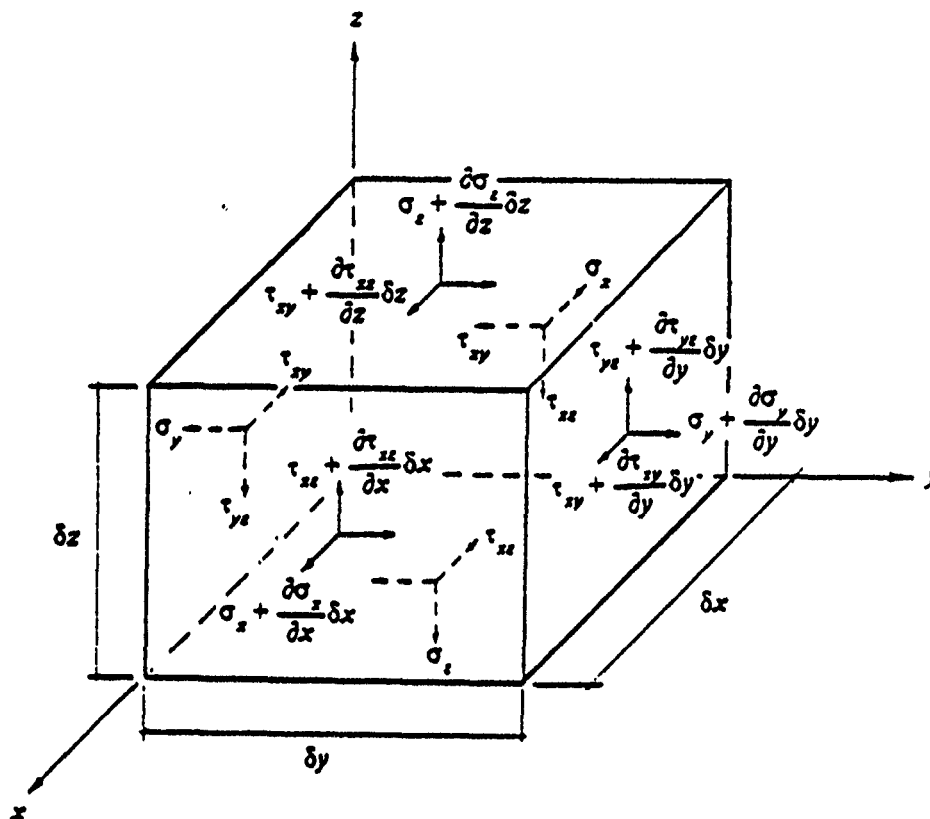


Figure 2.1. Stress Components Acting on a Differential Volume

Applying Newton's 2nd law of motion,  $F = ma$ , yields

$$F_x = \rho \delta x \delta y \delta z \frac{\partial^2 u}{\partial t^2} \quad (2.2)$$

$$F_y = \rho \delta x \delta y \delta z \frac{\partial^2 v}{\partial t^2}$$

$$F_z = \rho \delta x \delta y \delta z \frac{\partial^2 w}{\partial t^2}$$

Equating equations (2.1) and (2.2) and simplifying yields

$$\rho \frac{\partial^2 u}{\partial t^2} = \frac{\partial \sigma_x}{\partial x} + \frac{\partial \tau_{xy}}{\partial y} + \frac{\partial \tau_{xz}}{\partial z} \quad (2.3)$$

$$\rho \frac{\partial^2 v}{\partial t^2} = \frac{\partial \tau_{xy}}{\partial x} + \frac{\partial \sigma_y}{\partial y} + \frac{\partial \tau_{yz}}{\partial z}$$

$$\rho \frac{\partial^2 w}{\partial t^2} = \frac{\partial \tau_{xx}}{\partial x} + \frac{\partial \tau_{yz}}{\partial y} + \frac{\partial \sigma_z}{\partial z}$$

Equation (2.3) is the governing equation for stress wave propagation in any media, and is valid for any stress-strain relationship. Therefore, the stress wave propagation in any medium is determined by the substitution of the appropriate stress-strain relations into equation (2.3), and the concurrent application of the appropriate boundary conditions.

It has been proven (12,19) that equation (2.3) describes the dilatational and distortional stress wave components. It has also been shown (12,19) that, in any isotropic elastic medium, a stress wave must propagate at a velocity dependent upon the mechanical properties of the medium. A dilatational (longitudinal) wave must travel at a velocity of

$$c_1 = \left[ \frac{E(1-\nu)}{(1+\nu)(1-2\nu)\rho} \right]^{\frac{1}{2}} \quad (2.4)$$

and a distortional (rotational) wave must travel at a velocity of

$$c_2 = \sqrt{\frac{G}{\rho}} \quad (2.5)$$

where  $E$  is Young's modulus,  $\nu$  is Poisson's ratio,  $\rho$  is the material mass density, and  $G$  is the shear modulus (6). Moreover, for an elastic isotropic material, equation

(2.3) can be further simplified to

$$\frac{\partial^2 u}{\partial t^2} = c^2 \nabla^2 u \quad (2.6)$$

$$\frac{\partial^2 v}{\partial t^2} = c^2 \nabla^2 v$$

$$\frac{\partial^2 w}{\partial t^2} = c^2 \nabla^2 w$$

where  $\nabla^2$  represents the operation

$$\nabla^2 = \left( \frac{\partial^2}{\partial x^2} + \frac{\partial^2}{\partial y^2} + \frac{\partial^2}{\partial z^2} \right)$$

### Plane Stress Wave Propagation

Stress waves are propagated in all directions in a media from the point of a disturbance. At a great enough distance from the disturbance, however, the stress waves are, for all practical purposes, plane waves. In the case of a plane wave, it can be assumed that all mass particles under the influence of the wave are moving either parallel to the direction of wave propagation (dilatational waves) or perpendicular to the direction of wave propagation (distortional waves) (25).

For propagation in the  $x$  direction only (refer to Figure 2.2), the deformation becomes a function of  $x$  only. Equation (2.6) therefore reduces to

$$\frac{\partial^2 u}{\partial t^2} = c_1^2 \frac{\partial^2 u}{\partial x^2} \quad (2.7)$$

The general solution to this equation is

$$u(x,t) = f_1(x+c_1t) + f_2(x-c_1t) \quad (2.8)$$

where  $f_1$  and  $f_2$  are arbitrary functions depending upon initial conditions and describe the shape of the stress wave. The function  $f_1$  represents a stress wave traveling in the negative  $x$  direction with constant velocity  $c_1$ . The function  $f_2$  represents a stress wave traveling in the positive  $x$  direction with constant velocity  $c_1$ .

A segment of a plane dilatational wave is illustrated in Figure 2.2. The medium at section A-A in Figure 2.2(a) experiences a normal stress  $\sigma_x$ . After a time interval  $\delta t$ , the segment of the wave initially corresponding to section A-A has traveled a distance  $\delta x$  to section B-B (Figure 2.2(b)). The stress wave has imposed an impulse  $\sigma_x \delta t$  on the medium between sections A-A and B-B. Equating this impulse to the change in momentum yields

$$\sigma_x \delta t = \rho V \delta x = \rho V_x c_1 \delta t$$

which reduces to

$$\sigma_x = \rho c_1 V_x \quad \text{or} \quad V_x = \frac{\sigma_x}{\rho c_1} \quad (2.9)$$

where  $V_x$  is the particle velocity parallel to the direction of wave propagation. Similarly, for a distortional wave,

$$\tau_{yz} = \rho c_2 V_y \quad \text{or} \quad V_y = \frac{\tau_{yz}}{\rho c_2} \quad (2.10)$$

where  $V_p$  is the particle velocity perpendicular to the direction of wave propagation. Equations (2.9) and (2.10) indicate that stress and particle velocity are linearly related by the material impedance (acoustic resistance),  $\rho c$ .

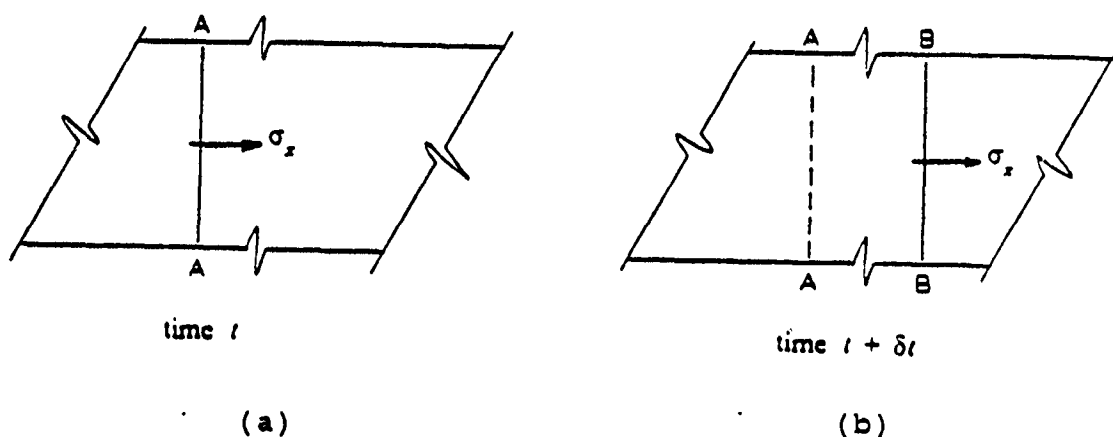


Figure 2.2. Section of Medium Subject to a Transient Stress Wave

The stress wave velocity and the particle velocities must not be construed as the same. The stress wave velocity is the velocity at which the stress wave propagates from one point to another in the medium. For an elastic isotropic medium, this velocity remains constant with both time and position in the medium. The particle velocity is the velocity of the mass particles at some point in the medium. Since the wave propagates through the medium, stressing separate sections of the medium at different times, the particle velocity is not

constant throughout the medium. It should also be noted that the particle velocities for tension and compression waves are opposite in sense. Mass particles subjected to a compressive wave travel in the direction of wave propagation. Mass particles subjected to a tensile wave, however, travel in the direction opposite that of wave propagation.

### Stress Wave Propagation in a Uniform Bar

Equation (2.3) describes the motion of a stress wave propagating through an isotropic medium. Theoretically, equation (2.3) can be used to describe the propagation of stress waves in any isotropic solid by solving for the appropriate boundary conditions. However, except for a few simple cases, the solution becomes very complex. Therefore, the propagation of stress waves in a bar of uniform cross section is investigated in order to illustrate the phenomenon.

A differential element of the bar,  $\delta x$ , is shown in Figure 2.3. Assuming plane sections remain plane and the stress is uniformly distributed over the cross section, it follows that

$$\sigma_x = E \frac{\partial u}{\partial x} \quad (2.11)$$

Summing forces in the  $x$  direction to obtain the residual

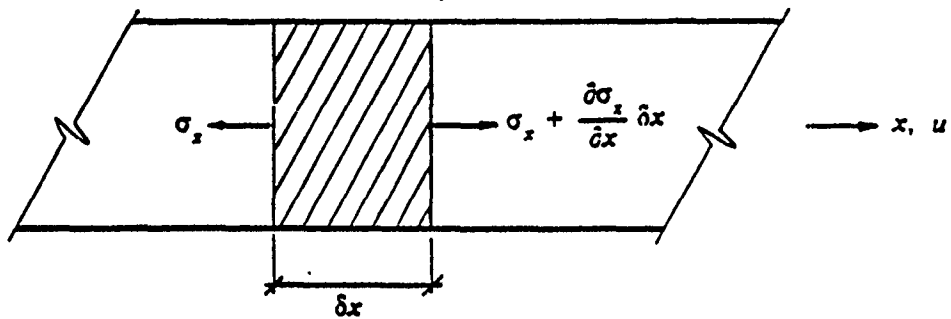


Figure 2.3. Stress Components Acting on a Differential Bar Element

force and applying Newton's second law of motion,  $F = ma$ , yields

$$A \frac{\partial \sigma_x}{\partial x} \delta x = \rho A \delta x \frac{\partial^2 u}{\partial t^2}$$

Substituting equation (2.11) for  $\sigma_x$  and simplifying yields

$$\frac{\partial^2 u}{\partial t^2} = \frac{E}{\rho} \frac{\partial^2 u}{\partial x^2}$$

or

$$\frac{\partial^2 u}{\partial t^2} = c^2 \frac{\partial^2 u}{\partial x^2} \quad (2.12)$$

where  $c$  is the velocity of propagation of longitudinal waves in the bar defined by

$$c = \sqrt{\frac{E}{\rho}} \quad (2.13)$$

Equation (2.12) is identical with equation (2.7), derived for the propagation of a one-dimensional plane wave in a linear isotropic solid. Therefore, the propagation of a plane longitudinal stress wave in a three-dimensional elastic isotropic medium is identical to the propagation of the same stress wave in a bar of uniform cross section. Equation (2.12) is applicable to any elastic isotropic bar of uniform cross section. The relationship between  $c_l/c$  and Poisson's ratio  $\nu$  is illustrated in Figure 2.4. It should be noted that for small Poisson's ratios, the velocity  $c_l$  in equation (2.4) approaches the velocity  $c$  in equation (2.13). Therefore, the velocity of longitudinal stress wave propagation in a linear isotropic solid of small Poisson ratio is approximately equal to the velocity of propagation in a bar of uniform cross section. In consideration of the above similarities, stress wave propagation in a bar of uniform cross section can be used to model the plane longitudinal stress wave propagation in a linear isotropic medium.

The general solution to equation (2.12) is

$$u(x,t) = f_1(x+ct) + f_2(x-ct) \quad (2.14)$$

where the function  $f_1$  describes a backward moving wave, and the function  $f_2$  describes a forward moving wave. Equating impulse to the change in momentum yields

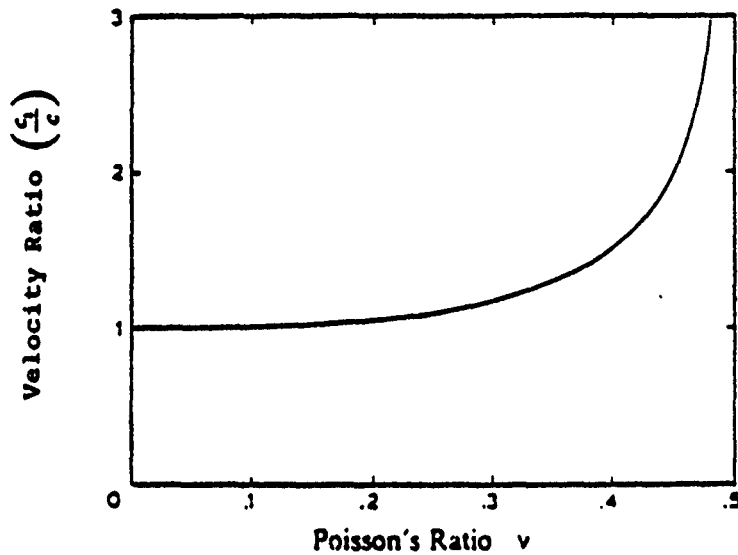


Figure 2.4. Relationship Between Velocity Ratio and Poisson's Ratio

$$\sigma_x = \rho c V \quad \text{or} \quad V = \frac{\sigma_x}{\rho c} \quad (2.15)$$

This is consistent with equation (2.9), and indicates that the particle velocity of the bar is linearly proportional to the stress by the material impedance  $\rho c$ .

For a forward moving stress wave propagating in the  $x$  direction, equation (2.14) reduces to

$$u(x,t) = f_2(x - ct). \quad (2.16)$$

If the stress wave is elastic and plane, then every segment of the stress wave is propagated with the same velocity, and the shape of the stress wave does not change. The solution given by equation (2.16) is depicted graphically in Figure 2.5. Figure 2.5(a) illustrates a forward moving stress wave  $ab$  of arbitrary shape at time  $t_1$ .

propagating in the  $x$  direction at constant velocity  $c$ . At time  $t_1 + \delta t$  (Figure 2.5(b)), the stress wave has traveled a distance  $\delta x = c \delta t$  from position  $ab$  to position  $a'b'$ . The shape and amplitude of the stress wave remain unchanged.

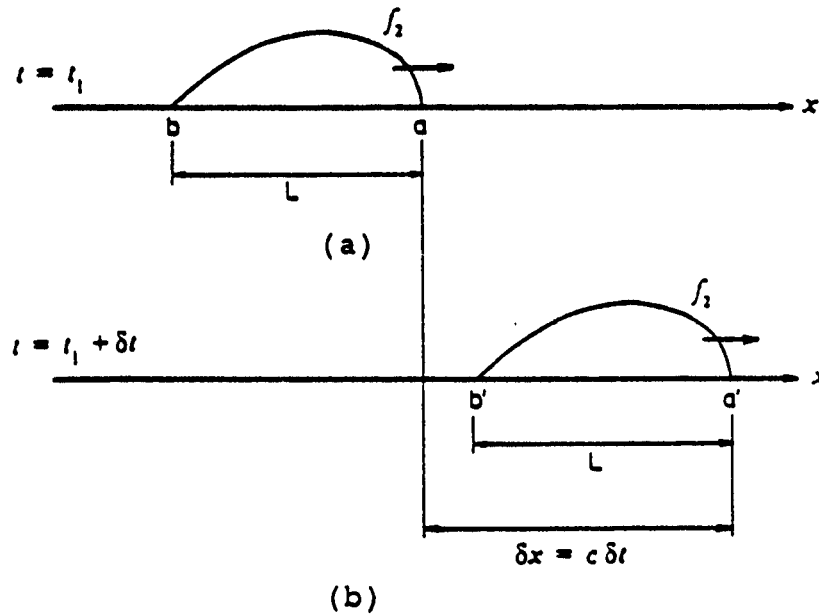


Figure 2.5. Forward Moving Stress Wave Propagating With Velocity  $c$ .

Figure 2.5 represents a single stress wave propagating through a uniform bar in the positive  $x$  direction. If this stress wave encounters a second stress wave traveling in the negative  $x$  direction, the two waves will interfere with one another. The stresses and particle velocities of the two stress waves can be superimposed to obtain the resultant stresses and particle

velocities. The interference of two compression waves traveling in opposite directions is shown in Figure 2.6. The compression waves have the same stress level  $\sigma_c$ , but have particle velocities  $V_c$  in opposite directions, as shown in Figure 2.6(a). Figure 2.6(b) reveals the superposition of a portion of the two waves. The stress level is additive in this case, and the compressive stress intensity doubles to  $2\sigma_c$ . The particle velocities, equal in magnitude but opposite in direction, cancel and become zero.

The interference of a compressive wave and a tensile wave traveling in opposite directions is shown in Figure 2.7. The waves are of equal stress level,  $\sigma_c$ , but of opposite sign. The particle velocities are identical in both magnitude and direction, as shown in Figure 2.7(a). The superposition of the two stress waves is depicted in Figure 2.7(b). In this case, the stresses cancel each other out and the particle velocity doubles to  $2V_c$ .

#### Boundary Effects on Stress Wave Propagation

A stress wave will continue to propagate through a linear, isotropic material with no change in shape, intensity, or direction until it encounters a boundary. In general, when an incident longitudinal stress wave reaches a boundary, it is reflected as two separate waves:

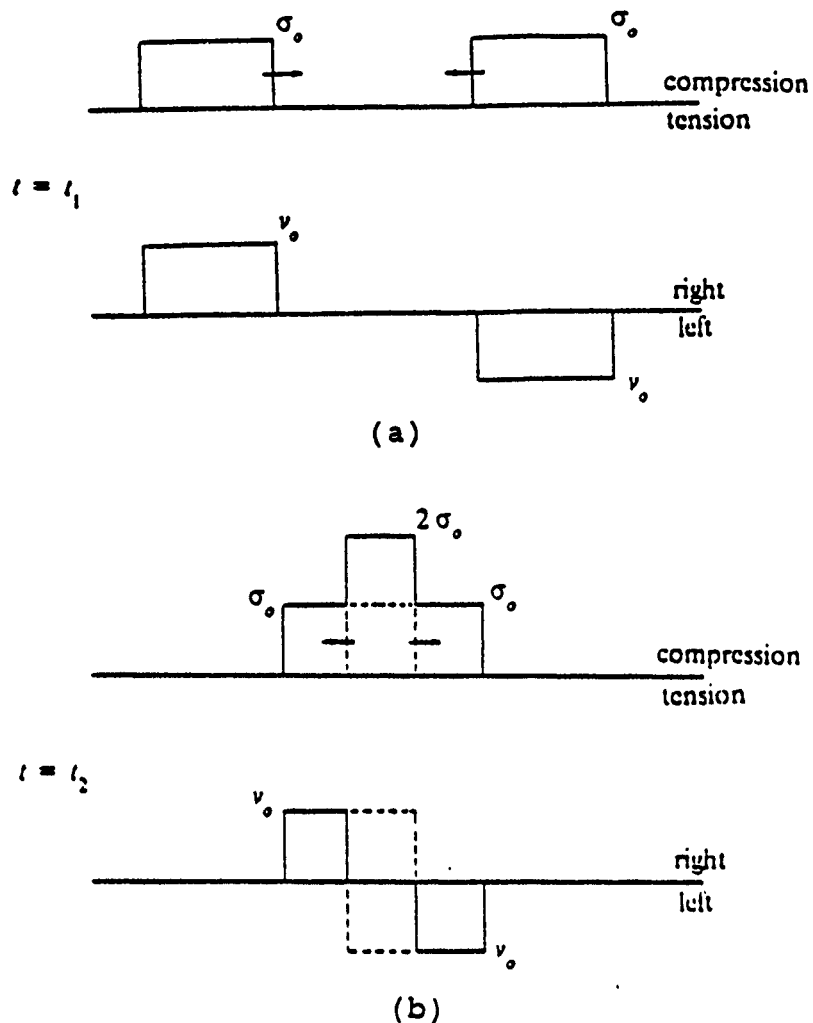
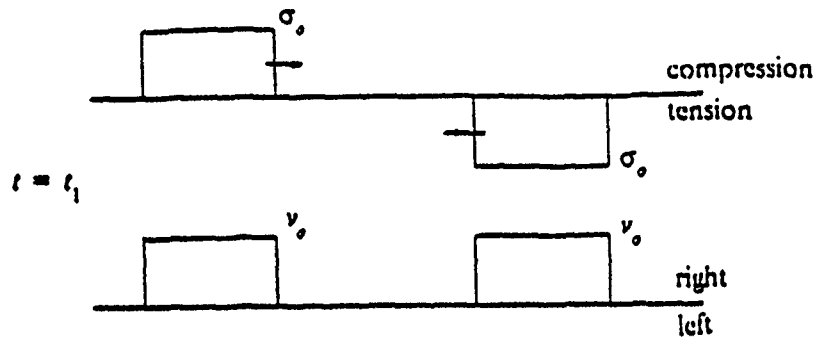


Figure 2.6. Interference and Superposition of Two Compressive Stress Waves.

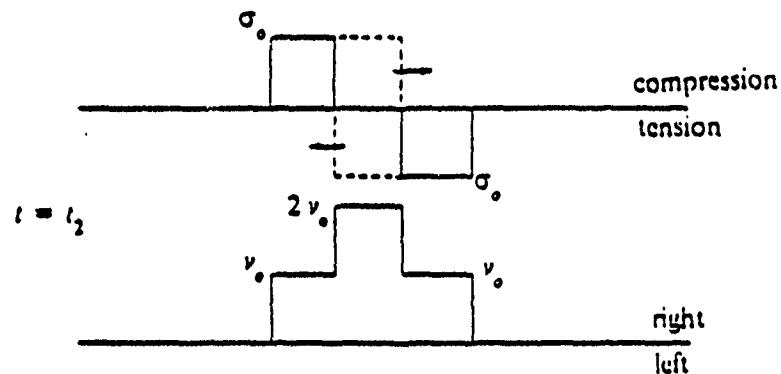
1) a longitudinal wave, and 2) a distortional wave. However, when the incident longitudinal wave is normal to the boundary, the longitudinal wave is reflected as a single longitudinal wave.

#### Reflection from a Free Surface

A longitudinal wave at normal incidence to a free boundary will be reflected as a longitudinal wave with a



(a)



(b)

Figure 2.7. Interference and Superposition of Compression and Tension Stress Waves.

change in phase. The three boundary conditions governing the reflection from a free surface are: 1) zero stress, 2) nonzero displacement, and 3) nonzero particle velocity at the free surface. An incident longitudinal compression wave will be reflected at full stress level as a longitudinal tension wave. Superposition of the incident and reflected stress waves yields zero stress but a doubling of the particle velocity at the free surface.

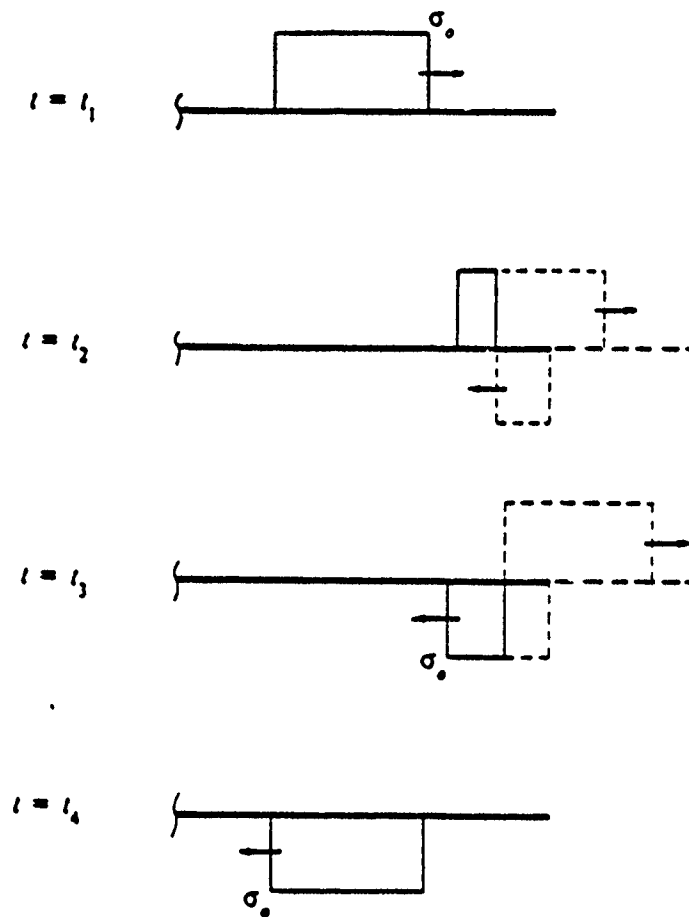


Figure 2.8. Reflection of a Rectangular Wave at a Free Surface.

The reflection of a longitudinal stress wave at normal incidence to a free surface is illustrated in Figures 2.8 and 2.9 for four intervals of time. A rectangular compressive stress wave reflecting from the free end of a bar is shown in Figure 2.8, and a triangular compressive stress wave reflecting from the free end is shown in Figure 2.9. The compression wave is reflected at full intensity as a tensile wave when it reaches the free

surface. It is noted that, upon reflection of the rectangular wave, a segment of the bar adjacent to the free surface remains unstressed. However, upon reflection of the triangular wave, only the free surface remains unstressed. In either case, the maximum stress due to superposition is equal to the maximum incident stress.

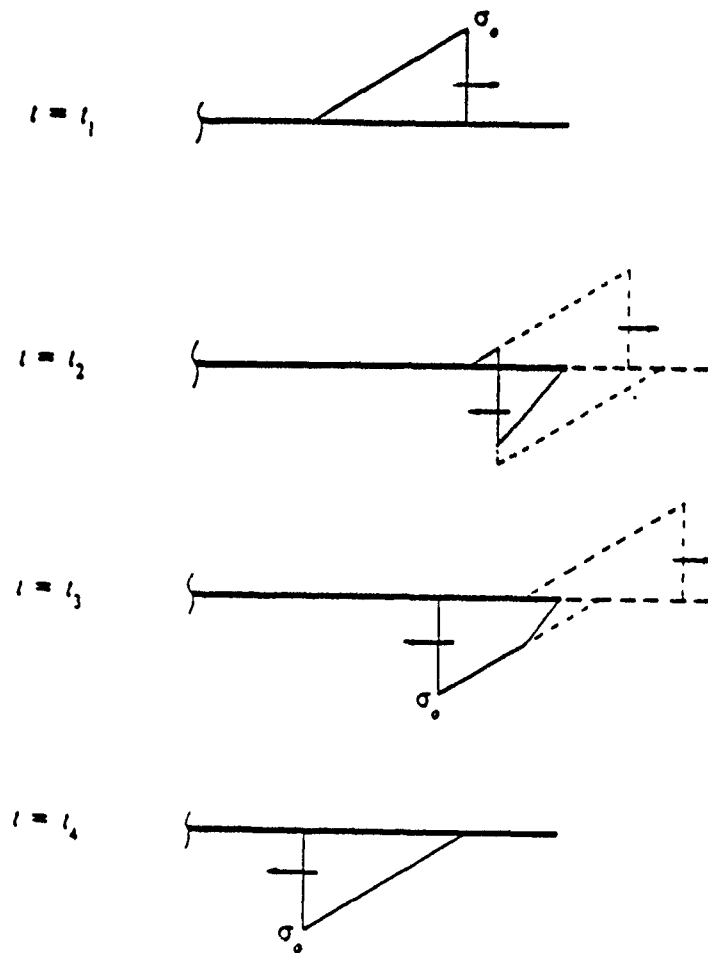


Figure 2.9. Reflection of a Triangular Wave at a Free Surface.

### Reflection From a Fixed Boundary

A longitudinal wave at normal incidence to a fixed boundary will be reflected as a longitudinal wave with no change in phase. The three boundary conditions governing the reflection from a fixed surface are: 1) zero displacement, 2) zero particle velocity, and 3) nonzero stress at the fixed surface. An incident longitudinal compression wave will be reflected at full stress level as a compression wave. Superposition of the incident and reflected stress waves yields zero particle velocity, but a doubling of the stress intensity at the fixed surface.

The reflection of a longitudinal stress wave at normal incidence to a fixed surface is illustrated in Figures 2.10 and 2.11 for four intervals of time. A rectangular compressive stress wave reflecting from the fixed end of a bar is shown in Figure 2.10, and a triangular compressive stress wave reflecting from the fixed end is shown in Figure 2.11. The compression wave is reflected at full intensity without a change of phase when it reaches the fixed surface. It is noted that, in the case of an incident triangular wave, a rectangular wave of varying length and intensity is formed as the incident and reflected waves are superimposed. In either case, however, the maximum stress due to superposition is twice that of the maximum stress of the incident wave.

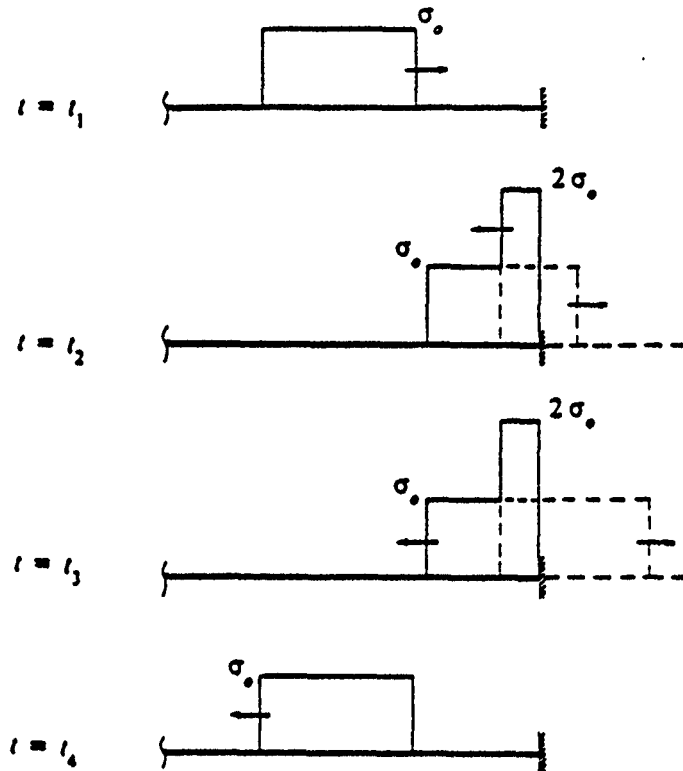


Figure 2.10. Reflection of a Rectangular Wave at a Fixed Surface.

### Stress Wave Propagation in Layered Media

The relative strength and density of two dissimilar materials forming a boundary affects stress wave propagation in the media. In general, when an incident longitudinal stress wave reaches a boundary between two dissimilar materials, the wave is reflected and refracted (transmitted) as four separate waves: 1) a reflected longitudinal wave, 2) a reflected distortional wave, 3) a transmitted longitudinal wave, and 4) a transmitted distortional wave. When the incident longitudinal wave is

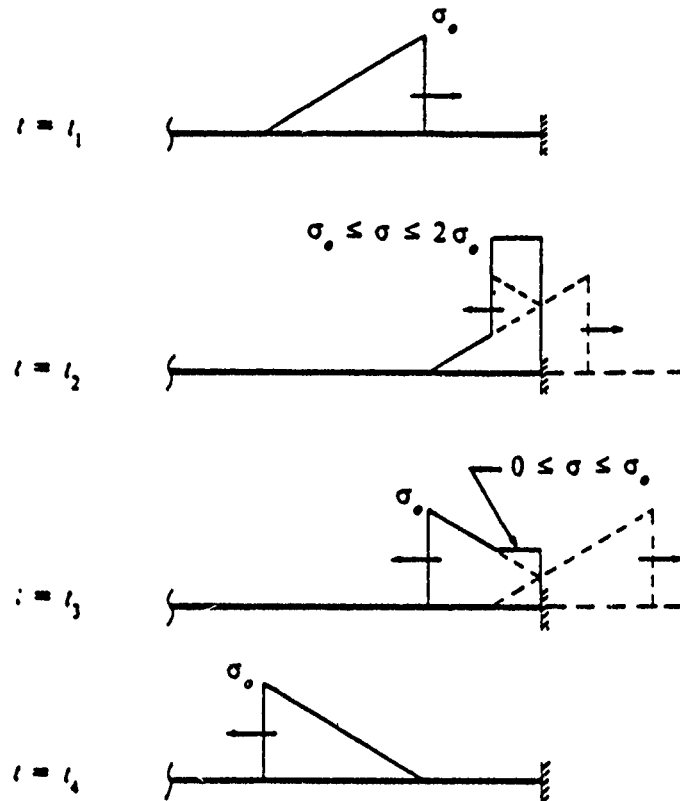


Figure 2.11. Reflection of a Triangular Wave at a Fixed Surface.

normal to the boundary, however, the incident longitudinal wave is reflected and transmitted as a longitudinal wave.

The boundary conditions governing the reflection and refraction at the boundary between two dissimilar materials are defined as the equality of stress and particle velocities in each material at the boundary. (assuming the materials remain in constant contact).

These conditions are described by the expressions

$$\sigma_I(x,t) + \sigma_R(x,t) = \sigma_T(x,t) \quad (2.17)$$

and

$$V_I(x,t) + V_R(x,t) = V_T(x,t) \quad (2.18)$$

where  $\sigma_I$ ,  $\sigma_R$ ,  $\sigma_T$  are the incident, reflected, and transmitted stresses, respectively;  $V_I$ ,  $V_R$ ,  $V_T$  are the respective incident, reflected, and transmitted particle velocities, where

$$V_I = \frac{\sigma_I}{\rho_1 c_1} \quad V_R = -\frac{\sigma_R}{\rho_1 c_1} \quad V_T = \frac{\sigma_T}{\rho_2 c_2}$$

as given by equation (2.15). The subscripts 1 and 2 refer to the first and second materials, respectively.

Substituting equation (2.15) for  $V$  in equation (2.18) yields

$$\frac{\sigma_I}{\rho_1 c_1} - \frac{\sigma_R}{\rho_1 c_1} = \frac{\sigma_T}{\rho_2 c_2} \quad (2.19)$$

Solving equations (2.17) and (2.19) simultaneously yields

$$\sigma_T = \frac{2 \rho_2 c_2}{\rho_1 c_1 + \rho_2 c_2} \sigma_I \quad (2.20)$$

$$\sigma_R = \frac{\rho_2 c_2 - \rho_1 c_1}{\rho_1 c_1 + \rho_2 c_2} \sigma_I \quad (2.21)$$

Rearranging equations (2.20) and (2.21) yields

$$\frac{\sigma_T}{\sigma_I} = \frac{2 \rho_2 c_2}{\rho_1 c_1 + \rho_2 c_2} \quad (2.22)$$

$$\frac{\sigma_R}{\sigma_I} = \frac{\rho_2 c_2 - \rho_1 c_1}{\rho_1 c_1 + \rho_2 c_2} \quad (2.23)$$

and dividing equation (2.22) by equation (2.23) results in

$$\frac{\sigma_T}{\sigma_R} = \frac{2 \rho_2 c_2}{\rho_2 c_2 - \rho_1 c_1} \quad (2.24)$$

Equations (2.20) through (2.24) also describe the fixed and free boundary conditions previously investigated. When  $\rho_2 c_2 = 0$ , i.e., a free boundary condition, then  $\sigma_r = 0$  and  $\frac{\sigma_R}{\sigma_I} = -1$ , denoting that an incident compression wave will be reflected at full stress level as a tension wave. When  $\rho_2 c_2 = \infty$ , describing a fixed boundary condition,  $\frac{\sigma_r}{\sigma_I} = 2$  and  $\frac{\sigma_R}{\sigma_I} = 1$ , indicating that a compression wave reflects at full intensity without a change in phase, and the boundary will experience a stress equal to twice that of the incident stress.

The transmission ratio  $\left(\frac{\sigma_T}{\sigma_I}\right)$  and the reflection ratio  $\left(\frac{\sigma_R}{\sigma_I}\right)$  are plotted in Figure 2.12 for a stress wave at normal incidence. When  $\rho_1 c_1 = \rho_2 c_2$ , as in a continuous media, there will be no reflection and the stress wave will be transmitted at full intensity. When  $\rho_1 c_1 < \rho_2 c_2$ , the reflection ratio is positive, and an incident stress wave will be reflected with no change in phase. When  $\rho_1 c_1 > \rho_2 c_2$ , the reflection ratio is negative, and an incident stress wave will be reflected with a change in phase. It should be noted, however, that if the boundary between the materials cannot support tension, then an incident tensile

wave will be reflected as if at a free boundary. The lower and upper limits of the transmission ratio are 0 and 2, respectively, representing the extreme cases of free and fixed boundaries. The upper and lower limits of the reflection ratio are -1 and 1, representing the limiting cases of free and fixed boundaries, respectively.

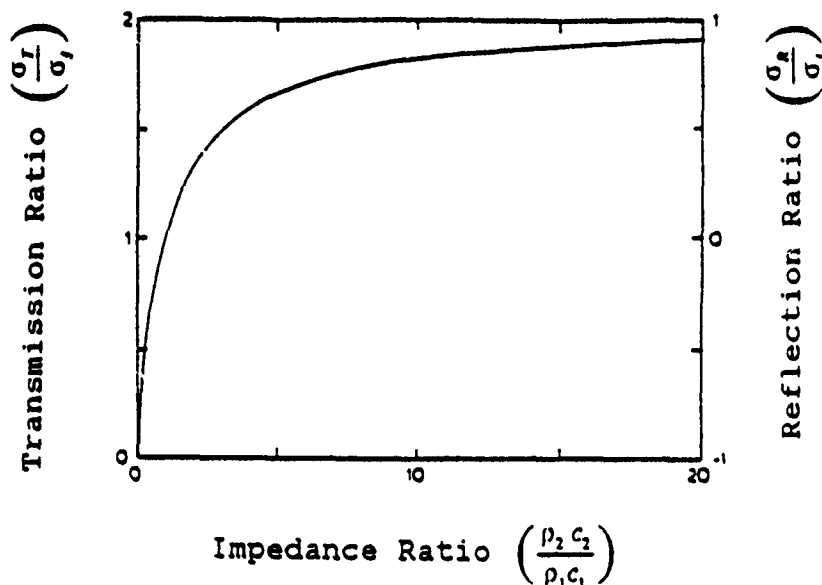


Figure 2.12. Transmission and Reflection Ratios at Normal Incidence vs. the Ratio Between Material Impedances.

The reflection and transmission of a triangular stress wave is illustrated in Figure 2.13 for  $\rho_1 c_1 < \rho_2 c_2$ . The stress wave is reflected at less than full intensity with no change in phase, and is transmitted at an increased stress level. The length of the stress wave increases in the second material due to the increased wave velocity  $c_2$  of the second material.

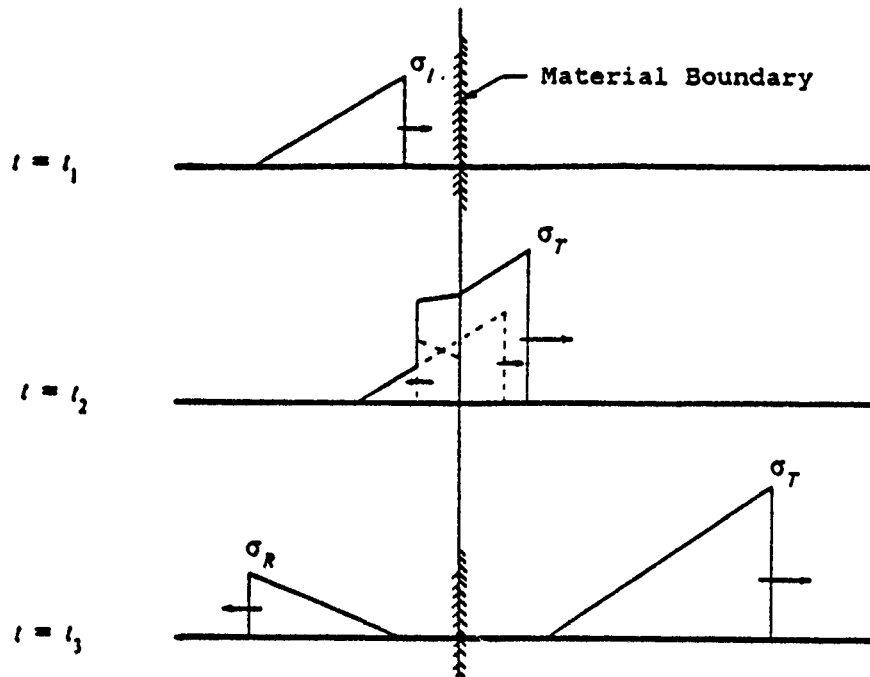


Figure 2.13. Transmission and reflection of a stress wave for  $p_1 c_1 < p_2 c_2$ .

The reflection and transmission of a triangular stress wave is illustrated in Figure 2.14 for  $p_1 c_1 > p_2 c_2$ . The stress wave is reflected at less than full intensity with a change in phase, and is transmitted at a reduced stress level. The length of the stress wave decreases in the second material due to the reduced wave velocity  $c_2$  of the second material.

#### Plastic Stress Wave Propagation

The propagation of stress waves in a nonlinear material is a very complex phenomenon. This study will

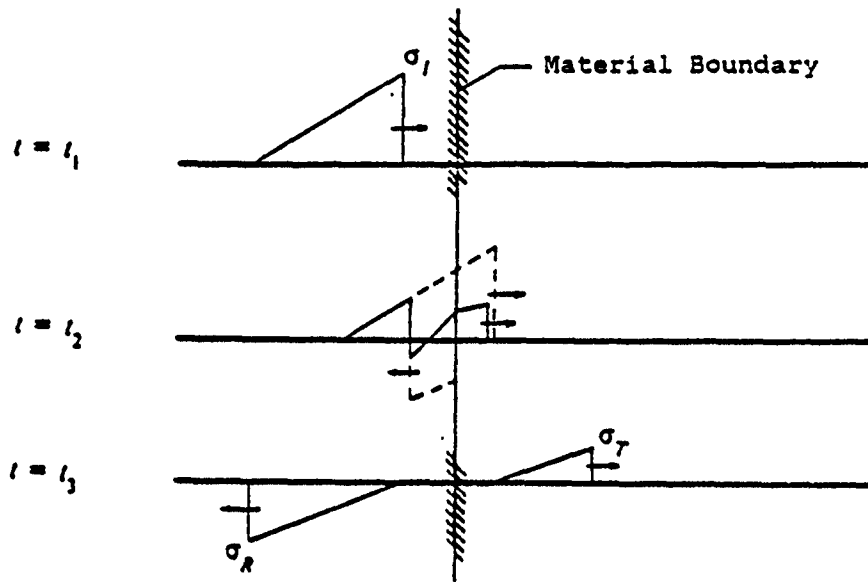


Figure 2.14. Transmission and reflection of a stress wave for  $\rho_1 c_1 > \rho_2 c_2$ .

address the basic concepts of the subject. For a more detailed investigation, the reader is referred to (10), (12), (17), and (27).

The velocity of stress wave propagation in an elastic medium has been previously defined by equation (2.13) as

$$c = \sqrt{\frac{E}{\rho}}$$

The velocity of a plastic stress wave is a function of the slope of the stress-strain curve and is defined (6) by

$$c_p = \left[ \frac{\left( \frac{\partial \sigma}{\partial \epsilon} \right)}{\rho} \right]^{\frac{1}{2}} \quad (2.25)$$

If the material is stressed in the elastic region only,

equation (2.25) simplifies to equation (2.13) by substituting  $E$  for  $\frac{\partial \sigma}{\partial \epsilon}$  in equation (2.25). A stress-strain curve for a typical elasto-plastic material is shown in Figure 2.15 along with the corresponding stress wave velocity obtained from equation (2.25). It is indicated in Figure 2.15 that, for a typical elasto-plastic material, the plastic stress wave travels at a much lower velocity than the elastic portion of the stress wave. The plastic wave front will therefore lag behind the elastic wave front.

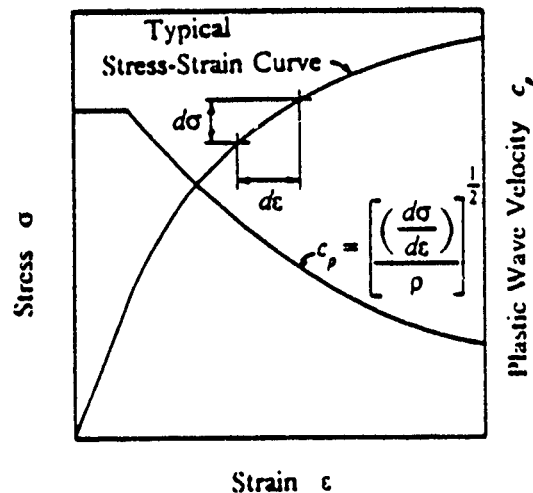


Figure 2.15. Stress-Strain Curve for a Typical Elasto-Plastic Material and Corresponding Wave Velocity.

A representation of a typical stress-strain curve for an elasto-plastic material in compression is shown in

Figure 2.16. If a high intensity shock wave, such as that shown in Figure 2.17, is applied to a material having a constitutive relation similar to that shown in Figure 2.16, the stress wave will propagate through the medium as illustrated in Figure 2.18 (10). The plastic portion of the wave propagates at a velocity less than that of the elastic portion and lags behind the elastic wave front. The wave can be separated into an unstable shock wave, a plastic wave, and an elastic wave. After the wave has traveled a sufficient distance, the unstable shock wave is reduced to a plastic wave. The plastic wave continues to lag behind the elastic wave front until it has been completely reduced to an elastic wave.

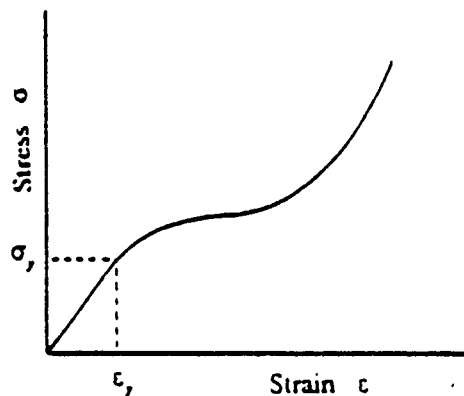


Figure 2.16. Stress-Strain Curve for an Elasto-Plastic Material in Compression.

In general, any high intensity elasto-plastic stress wave will continually change shape until it has been

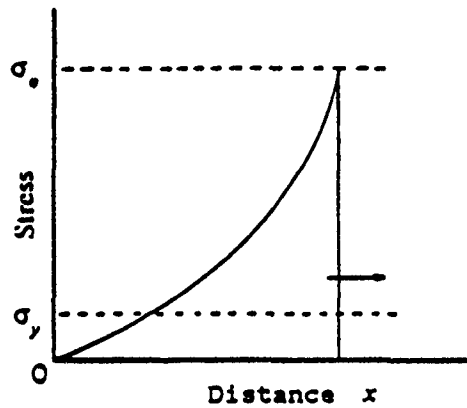


Figure 2.17. Applied High Intensity Shock Wave.

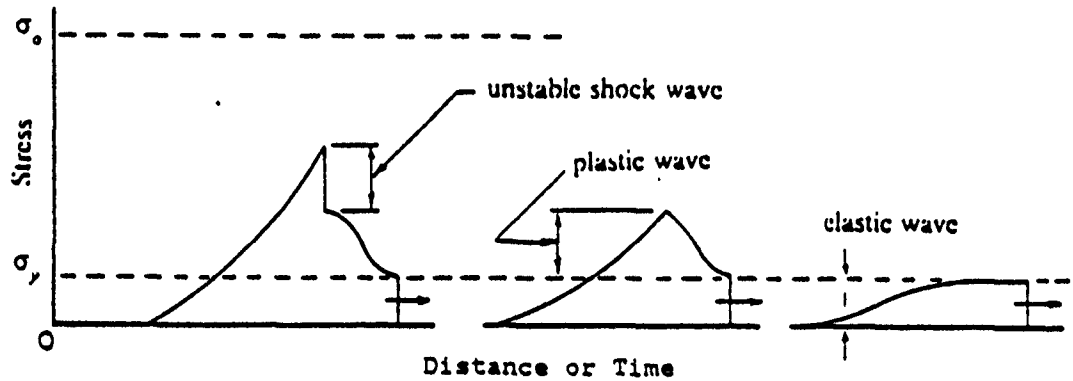


Figure 2.18. Propagation of a High Intensity Stress Wave in an Elasto-Plastic Medium.

completely reduced to an elastic wave. The stress wave is not only reduced in intensity, but is also lengthened, due to the reduced velocity of the plastic portion of the wave.

### Stress Wave Propagation and Spalling

Spalling is defined as fracturing caused when a high intensity transient stress wave reflects from a free surface (19). Spalling is a result of the interference of an incident compression wave with its reflected tensile wave at a free surface. The incident triangular compression wave shown in Figure 2.19(a) is reflected as a tensile wave from the free surface as shown in Figure 2.19(b). The superposition of the incident and reflected stress waves results in a net tensile stress near the free surface. The tensile stress increases from zero at the free surface to a maximum value of  $\sigma$ , some distance from the free surface. The distance from the free surface at which the net tensile stress reaches the maximum value  $\sigma$ , is a function of the wavelength of the incident stress wave. The maximum possible value of tensile stress due to the superposition of the incident and reflected triangular waves is shown in Figure 2.20. The maximum tensile stress  $\sigma$ , is reached at a distance of one half the wave length from the free surface.

For a rectangular incident compression wave, as shown in Figure 2.21(a), the reflection from a free surface is illustrated in Figure 2.21(b). The superposition of the incident and reflected stress waves results in an unstressed section of the medium adjacent to the free surface. However, a tensile stress of intensity  $\sigma$ ,

instantaneously develops at some distance from the free surface. The distance from the free surface at which the net tensile stress forms is a function of the wavelength of the incident stress wave. The maximum possible value of tensile stress due to the superposition of the incident and reflected rectangular waves is shown in Figure 2.22. The maximum tensile stress  $\sigma_c$  is attained at a distance of one half the wave length from the free surface. For both the rectangular and triangular wave shapes, the stress at the free surface is always zero.

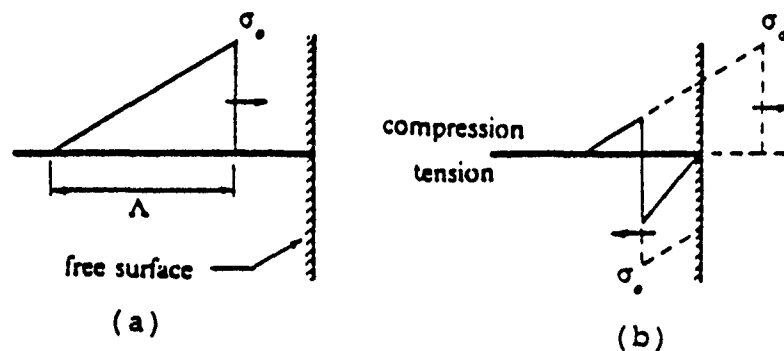


Figure 2.19. Superposition of Stresses During the Reflection of a Triangular Wave from a Free Surface.

For a medium capable of supporting the tensile stress inflicted by wave reflection, the reflected tensile wave will continue to propagate with no change in shape or intensity, and no spalling will occur. If, however, the

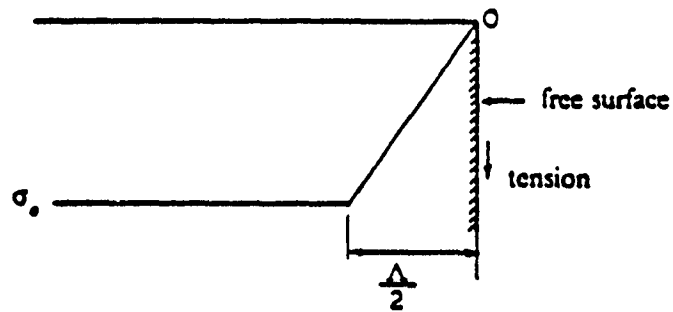


Figure 2.20. Maximum Attainable Tensile Stress During the Reflection of a Triangular Wave from a Free Surface.

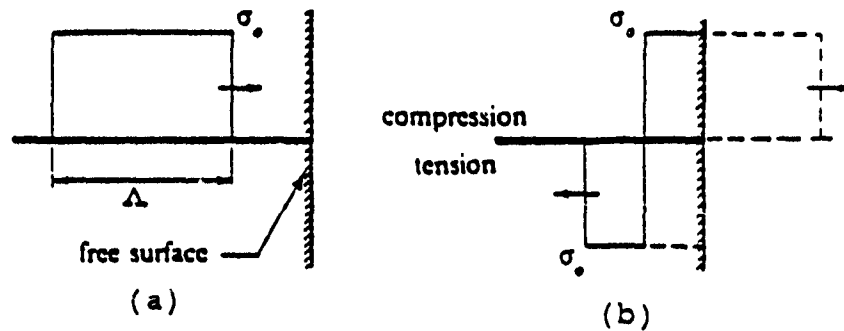


Figure 2.21. Superposition of Stresses During the Reflection of a Rectangular Wave from a Free Surface.

medium is unable to support the tensile stress, spalling will occur and propagation of the reflected stress wave will be altered. The occurrence of spalling and the location of the fractures are dependent upon three factors: 1) the resistance of the material to fracture;

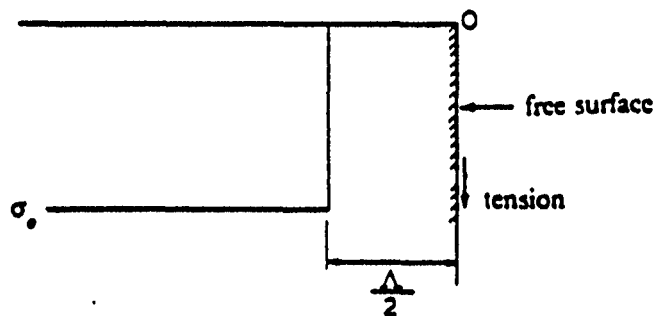


Figure 2.22. Maximum Attainable Tensile Stress During the Reflection of a Rectangular Wave from a Free Surface.

2) the intensity of the tensile stress; and 3) the shape of the stress wave (19).

The stress level at which fracturing occurs in a material is called the critical normal fracture strength. In general, the critical normal fracture strength is considerably higher than the static tensile strength of the material. However, it is difficult to experimentally determine the exact state of stress at the instant of fracture because of the instantaneous stress reversal at the point of fracture (19).

Spalling occurs when the critical normal fracture strength of the material is reached. Multiple spalling is the occurrence of spall in layers parallel to the free surface. Multiple spalling occurs when the stress level is greater than twice the critical normal fracture

strength. The occurrence of a multiple spall caused by an incident compression wave is shown in Figure 2.23. The tensile stress resulting from the superposition of the incident and reflected waves increases until the fracture strength is attained. Once the fracture strength is exceeded, the material spalls, creating a second free surface. If the remaining portion of the incident wave is greater than the fracture strength of the material, then a second spall will occur due to the reflection from the newly created free surface. This process continues until the stress wave no longer exceeds the critical normal fracture strength of the material.

The thickness of the spalled layer is affected by the stress wave profile, as indicated in Figure 2.23. A rectangular stress wave causes thicker spall than a triangular stress wave. This is a result of the shape of the maximum net tensile stress distribution formed by the superposition of the incident and reflected stress waves (refer to Figures 2.20 and 2.22). The net tensile stress resulting from a triangular stress wave builds immediately, thus restricting spall close to the vicinity of the free surface. However, the net tensile stress resulting from a rectangular stress wave remains zero for a distance equal to one half the length of the incident wave before reaching its maximum value, thus causing thicker spall.

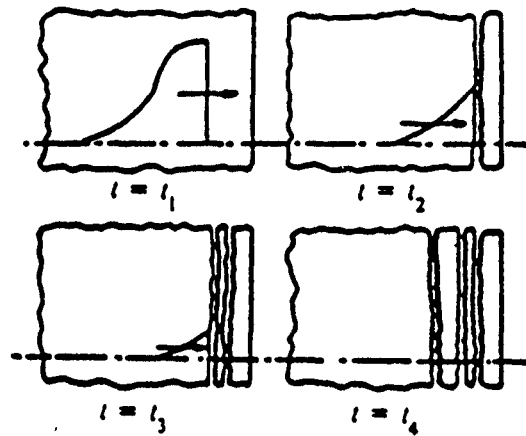


Figure 2.23. Multiple Spalling Caused by a Single Incident Compression Wave.

The particle velocity is linearly related to stress by equation (2.15). Also, the superposition of particle velocities for compression and tension waves traveling in opposite directions is additive. Therefore, the greater the stress level of the incident wave, the greater the velocity at which the spall is propagated away from the free surface. In multiple spalls, caused by a stress wave such as that shown in Figure 2.23, the first spall will have the greatest velocity, and each subsequent spall will have a decreased velocity due to the reduced intensity of the incident stress wave.

### III. LAYERED MEDIA FOR PROTECTIVE MILITARY SHELTERS

Protective military shelters are designed to house personnel, vital functions, and equipment of value. As a result, the survivability of the structure is critical and takes precedence over its appearance. The structures are invariably massive, constructed primarily of concrete and soil. Damage to protective shelters from conventional (non-nuclear) weapons occurs as a result of one or more of the following effects: penetration, fragmentation, ground shock, and blast (9). Penetration is a consideration only in the case of a direct hit. Ground shock is a consideration only in the case of a near miss. Fragmentation and blast are considerations in both cases. This study considers only the effects of the blast.

#### Typical Military Protective Shelters

Typical aboveground and underground protective shelters, designed to survive a near miss of a conventional weapon, are shown in Figures 3.1 and 3.2, respectively. The protective shelter is typically constructed of thick, monolithic concrete walls and roof. This practice is considered necessary in order to resist

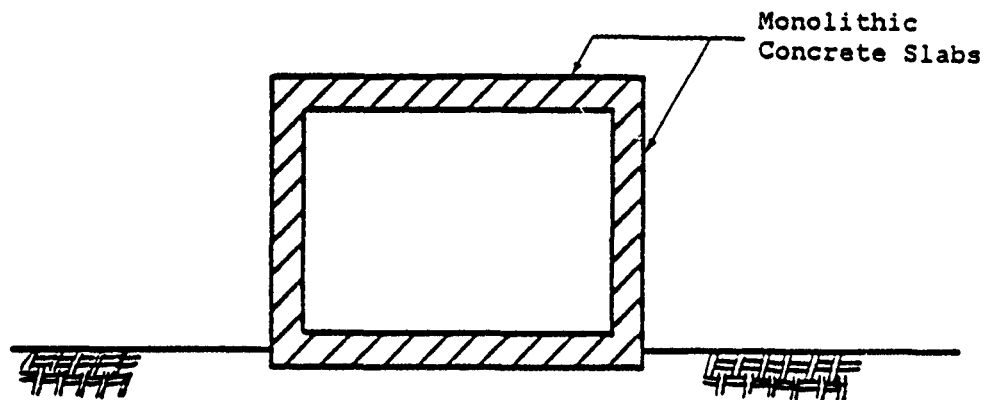


Figure 3.1. Typical Aboveground Protective Shelter.

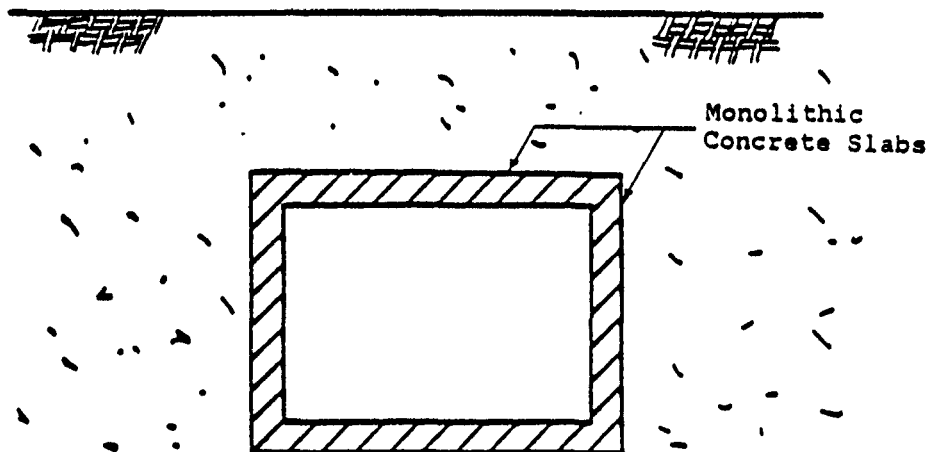


Figure 3.2. Typical Underground Protective Shelter.

the blast pressure and prevent interior spalling of the concrete walls.

A cross section of a typical protective shelter wall is shown in Figure 3.3. When the shelter wall is subject to a blast, the compressive longitudinal blast wave

contacts the exterior surface of the wall and propagates through the monolithic wall with little or no change in shape or intensity. When the compressive stress wave reaches the interior face of the wall, it is reflected at full stress level as a tension wave. The concrete will spall at the interior face of the wall if the intensity of the reflected tension wave is greater than the critical normal fracture strength of the concrete. When the stress wave is intense, the spalled concrete fragments are hurled away from the wall at high velocities, posing a potentially dangerous threat to personnel and equipment within the shelter.

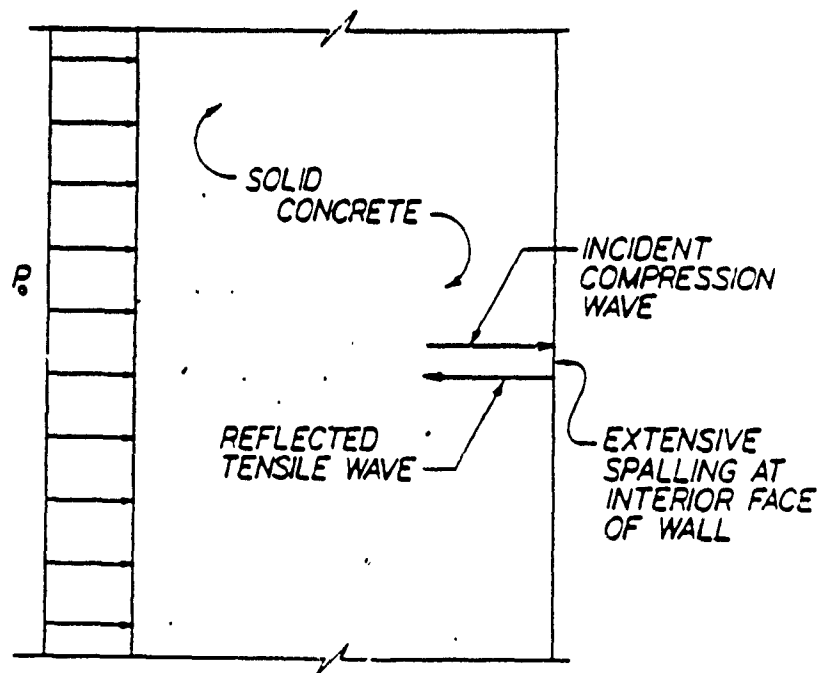


Figure 3.3. Blast Wave Propagation in Monolithic Wall of a Typical Protective Shelter.

Current procedures to reduce or eliminate spall in protective shelters include the construction of earth berms against the exterior face of the shelter walls (Figure 3.4(a)), the installation of steel spall plates on the interior face of the shelter walls (Figure 3.4(b)), and the use of thicker concrete walls (Figure 3.4(c)) (7). Of these methods, earth berms have proven to be the most successful, while the use of thicker walls has been the least successful.

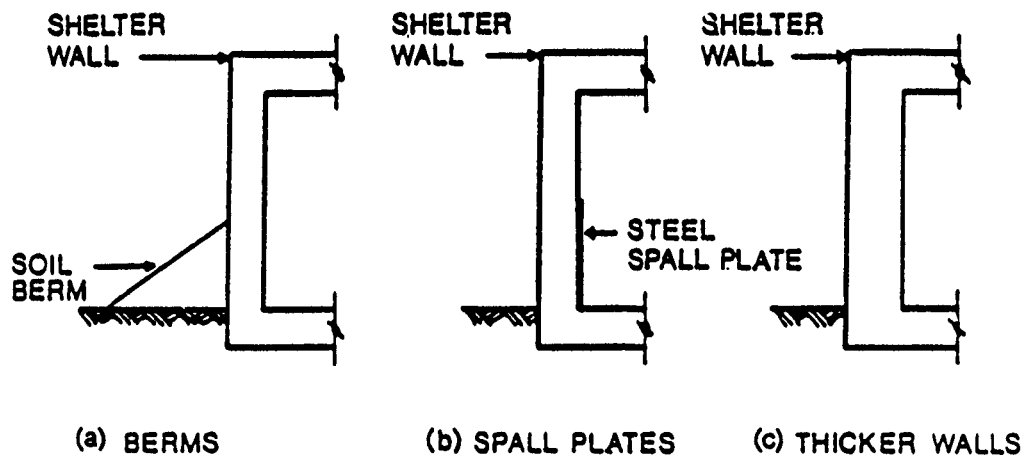


Figure 3.4. Current Procedures to Reduce Spall in Protective Shelters.

#### Layered Media Applied to Protective Military Shelters

It was shown in Chapter II that the propagation of stress waves in solid media is altered at the boundaries between dissimilar materials. Therefore, it is logical

to assume that layered media can be utilized to alter the stress wave propagation in the walls of a protective structure. The use of layered media to mitigate the incident blast wave, and therefore eliminate spall, in protective shelters is investigated in this study. The layered systems considered consist of an exterior layer of concrete or sand, an absorption layer, and an interior layer of concrete.

The transmission ratio of a three-layered system is determined by two consecutive applications of equation (2.22). Equation (2.22) is first applied to determine the stress wave transmitted from the first layer to the second layer. The stress transmitted to the second layer is the incident stress for the third layer. Equation (2.22) is applied a second time to obtain the stress transmitted to the third layer. Two consecutive applications of equation (2.22) yields

$$\frac{\sigma_T}{\sigma_I} = \left[ \frac{2 \rho_2 c_2}{\rho_1 c_1 + \rho_2 c_2} \right] \left[ \frac{2 \rho_3 c_3}{\rho_2 c_2 + \rho_3 c_3} \right] \quad (3.1)$$

where the subscripts 1, 2, and 3 refer to the first, second, and third layers, respectively. For a layered system in which the first and third layers consist of the same material (concrete) and the second layer is an absorption layer, equation (3.1) becomes

$$\frac{\sigma_T}{\sigma_I} = \frac{4 (\rho_c c_c) (\rho_a c_a)}{[(\rho_c c_c) + (\rho_a c_a)]^2} \quad (3.2)$$

where the subscripts  $c$  and  $a$  represent the concrete and absorption layers, respectively. A BASIC computer program was developed to calculate the transmission ratio for layered systems. The program listing and sample output is presented in Appendix A.

Equation (3.2) is depicted graphically in Figure 3.5. The transmission ratio for the system,  $\frac{\sigma_r}{\sigma_i}$ , is plotted against the ratio of impedances of the concrete and absorption layers,  $\frac{\rho_a c_a}{\rho_c c_c}$ . If the absorption layer has the same impedance as the concrete layer, then the transmission ratio is equal to one, and no reflection occurs at the boundary between layers. As the impedance ratio diverges from one in either direction, the transmission ratio of the system decreases. An impedance ratio less than one is necessary if the blast wave is to be significantly reduced, as is illustrated in Figure 3.5.

The blast wave propagation through a layered system with an impedance ratio less than one is illustrated in Figure 3.6. The incident compressive longitudinal blast wave propagates through the exterior layer of concrete until the first material boundary is encountered. Upon reaching the boundary between the exterior concrete and the absorption layer, a portion of the blast wave is transmitted to the absorption layer. The remainder of the blast wave is reflected back through the exterior layer of

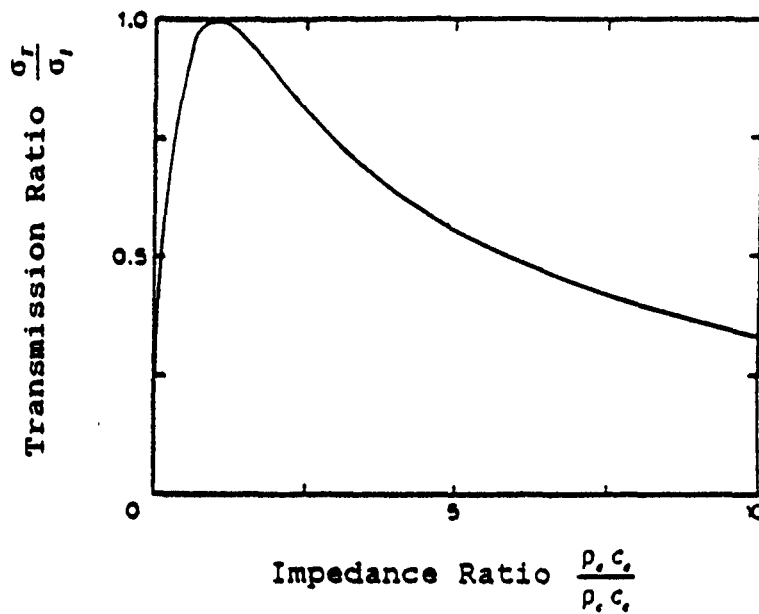


Figure 3.5. Transmission Ratio vs. the Impedance Ratio for the Three Layered System.

concrete as a tensile wave. The transmitted compression wave propagates through the absorption layer until it encounters the interior layer of concrete. At the boundary between the absorption layer and the interior layer of concrete, the compression wave is reflected back through the absorption layer as a compression wave of diminished intensity. Because the compression wave is reflected with no change in phase, the stress wave transmitted to the interior layer of concrete is greater than the reflected wave in the absorption layer. However, the stress wave transmitted to the interior layer of concrete is significantly less than the initial incident blast wave which impinged upon the exterior layer of the

system. If the stress wave transmitted to the interior layer of concrete is less than the critical normal fracture strength of the concrete, then no spalling occurs.

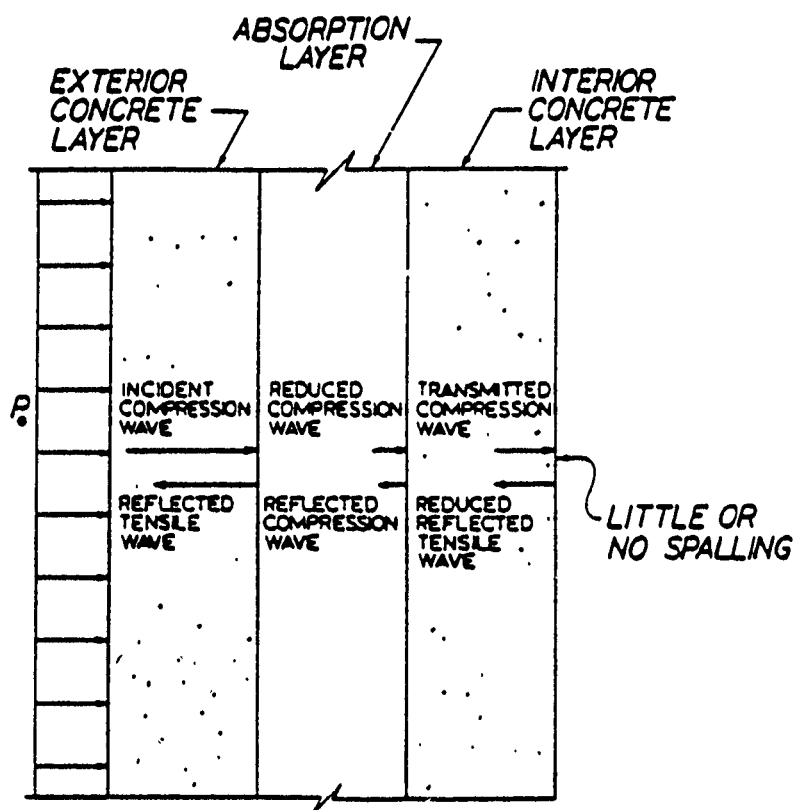


Figure 3.6. Blast Wave Propagation in a Layered System Consisting of an Exterior Concrete Layer, an Absorption Layer, and an Interior Concrete Layer for  $(p, c) < (p, c)$ .

Previous research (14,23,24) has shown polystyrene to be extremely effective as an absorption layer. It exhibits very low impedance characteristics and is available in large sheets which afford expedient

construction. For these reasons, polystyrene was selected for the absorption layer in this study.

The layered systems investigated include a concrete-polystyrene-concrete (CPC) system, a sand-polystyrene-concrete (SPC) system, and a sand-polystyrene-concrete-polystyrene-concrete (SPCPC) system. The static, linear properties of the materials are given in Table 3.1. The elastic wave speeds and material impedances for these same materials are listed in Table 3.2.

Table 3.1. Static Linear Material Properties.

	Strength $E$ (psi)	Mass Density $\rho$ ( $10^{-6}$ ) $\frac{lb \cdot sec^2}{in^4}$	Poisson's Ratio $\nu$
4000 psi Concrete	3605000	217.164	.18
110 pcf Sand	80000	164.745	.25
5.744 pcf Polystyrene	2100	8.604	.15

The intensity of the blast wave is capable of stressing the shelter into the inelastic range. This nonlinearity is addressed to some extent. It is assumed that the concrete behaves linearly at all times. Although this is not the case in the actual structure, the assumption of linearity does not significantly affect the

Table 3.2. Elastic Wave Speeds and Impedances.

	Elastic Wave Speed $c$ in/sec	Impedance $\rho c$ $\frac{\text{lb-sec}}{\text{in}^2}$
4000 psi Concrete	128842.4	28.0
110 pcf Sand	22036.3	3.63
5.744 pcf Polystyrene	15622.8	.134

overall behavior of the layered system. Both linear and nonlinear material models are employed for the sand and polystyrene. A linear elastic-perfectly plastic constitutive law, similar to that shown in Figure 3.7, is used to model the nonlinear behavior of the sand and polystyrene. The parameters for the nonlinear sand and polystyrene models are presented in Table 3.3.

The material properties given in Tables 3.1 and 3.3 represent the material behavior under static loading conditions. A protective shelter subjected to a blast loading experiences a high intensity, short duration load at a very rapid rate of application. Materials are often able to tolerate increased stress levels when loaded at a high rate. Laboratory tests performed on concrete specimens under high rates of loading have demonstrated that the dynamic secant modulus, ultimate strength, and tensile strength greatly exceed the corresponding

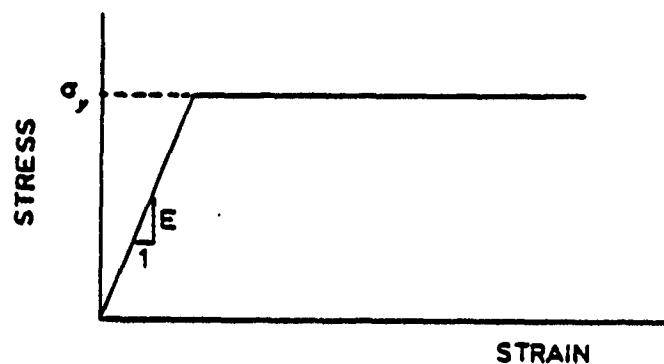


Figure 3.7. Linear Elastic-Perfectly Plastic Constitutive Law Used to Model Nonlinear Behavior.

Table 3.3. Static Nonlinear Material Properties.

	Strength $E$ (psi)	Yield Stress $\sigma_y$ (psi)	Mass Density $\rho$ ( $10^6$ ) $\frac{\text{lb-sec}^2}{\text{in}^4}$	Poisson's Ratio $\nu$
Unconfined Sand	80000	20	164.745	.25
5.744 pcf Polystyrene	2100	55	8.604	.15

strengths determined from static tests (9,15,16,18). Under dynamic loading, the compressive strength of concrete can increase by as much as a factor of 1.8, and the tensile strength can increase by as much as a factor of 2.2.

Tests on polystyrene at high rates of loading have indicated that the dynamic ultimate strength of polystyrene is much greater than the static strength.

Polystyrene subjected to a dynamic loading can withstand a stress as much as 1.6 times that of the static ultimate strength (11). Soils also exhibit a tendency to withstand higher loads under dynamic loading conditions. The increase in strength is a function of moisture content, porosity, and pre-existing static stress. However, due to the uncertainties involved in accurately assessing the high strain rate effects on material strength, the use of the dynamic material properties in this study is limited.

#### Concrete-Polystyrene-Concrete System

The concrete-polystyrene-concrete (CPC) system is intended to be used for an aboveground protective shelter. A typical cross section of the CPC system is shown in Figure 3.8. The exterior concrete layer is intended to partially withstand blast effects and to stop any incident fragments. The polystyrene absorption layer causes a significant portion of the blast wave to be reflected back through the exterior concrete layer. The polystyrene layer also traps any concrete fragments spalled from the exterior layer. The interior layer of concrete resists that portion of the stress wave which propagates through the polystyrene layer.

The aboveground CPC system may be constructed by forming the concrete walls against sheets of polystyrene. A possible construction procedure consists of casting the interior concrete wall against polystyrene sheets backed

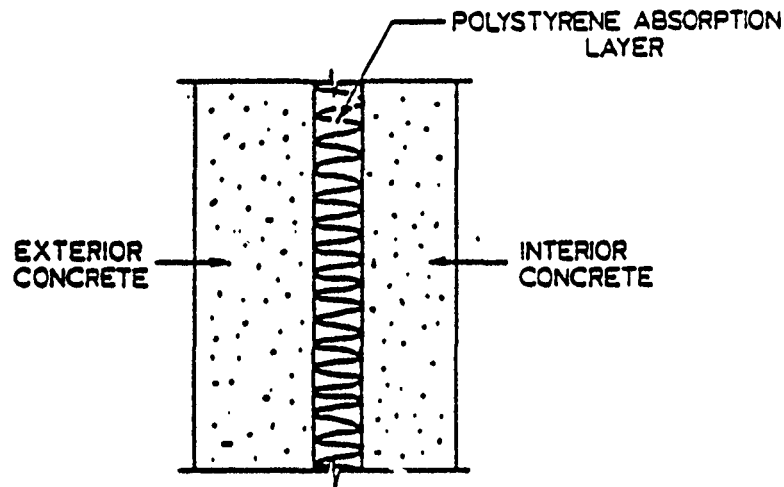


Figure 3.8. Cross Section of the Concrete-Polystyrene-Concrete (CPC) Layered System.

by plywood or metal forms. After the forms are removed, the outside surface of the exterior wall is formed, and the exterior layer of concrete is placed.

#### Sand-Polystyrene-Concrete System

The sand-polystyrene-concrete (SPC) system is intended to be used for both aboveground and underground protective shelters. A typical cross section of the SPC system is shown in Figure 3.9. The layer of sand is intended to partially withstand the blast effects and to stop any incident fragments. The polystyrene absorption layer reflects a portion of the blast wave back through the sand and reduces the intensity of the blast which wave reaches the interior layer of concrete. The interior layer of concrete resists the remaining portion of the blast.

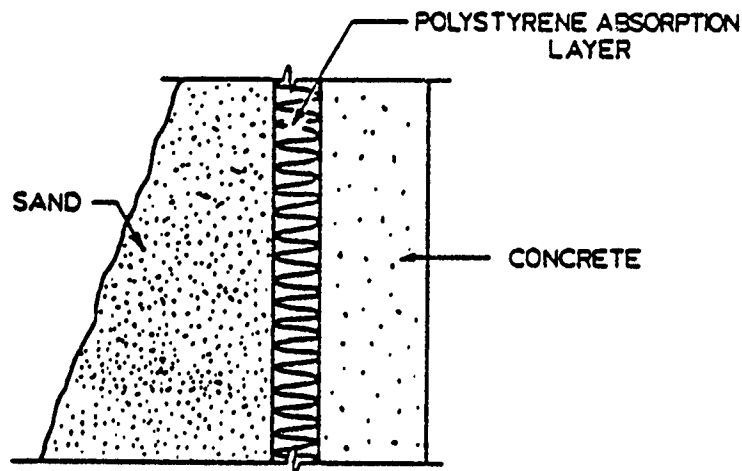


Figure 3.9. Cross Section of the Sand-Polystyrene-Concrete (SPC) Layered System.

Construction of the aboveground SPC system consists of placing sheets of polystyrene against the walls of an existing monolithic concrete shelter. A sand berm is then constructed against the polystyrene sheets to complete the layered system. A typical aboveground SPC system is depicted in Figure 3.10.

Construction of the underground SPC system consists of placing sheets of polystyrene against the walls and roof of a monolithic concrete shelter. The layered system is completed by backfilling against the polystyrene sheets with sand. A typical underground SPC system is illustrated in Figure 3.11.

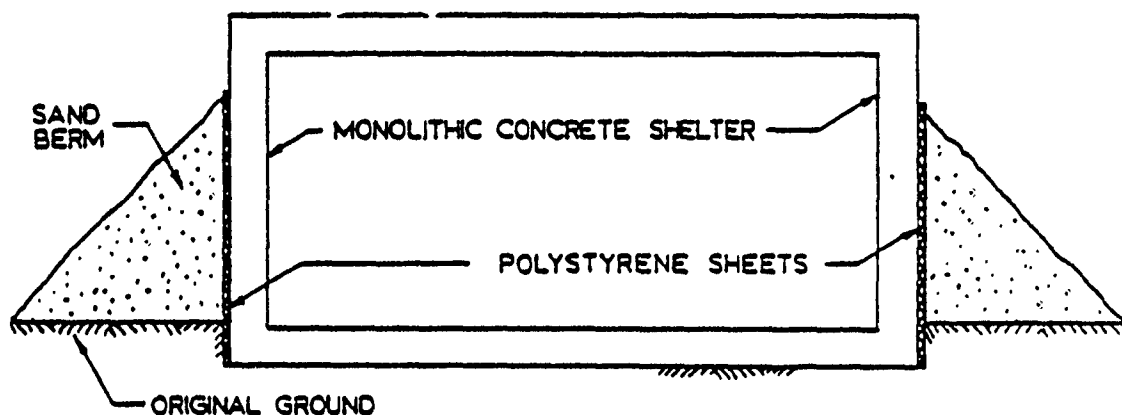


Figure 3.10. Typical Aboveground SPC Layered System.

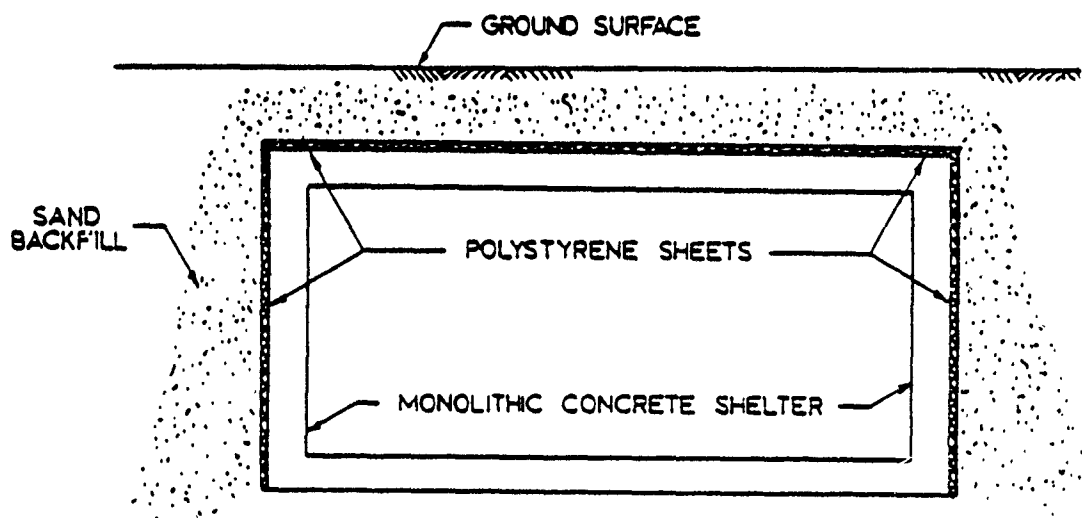


Figure 3.11. Typical Underground SPC Layered System.

#### Sand-Polystyrene-Concrete-Polystyrene-Concrete System

The sand-polystyrene-concrete-polystyrene-concrete (SPCPC) layered system is intended for use as an aboveground shelter when very high intensity blasts are expected.

A typical cross section of the SPCPC system is shown in Figure 3.12. The sand layer partially withstands the effects of the blast wave and stops any incident fragments. The first polystyrene layer reflects a portion of the blast wave back through the sand, and reduces the blast wave which reaches the exterior layer of concrete. The remaining concrete-polystyrene-concrete layers resist the transmitted blast wave as described in the section on the CPC layered system.

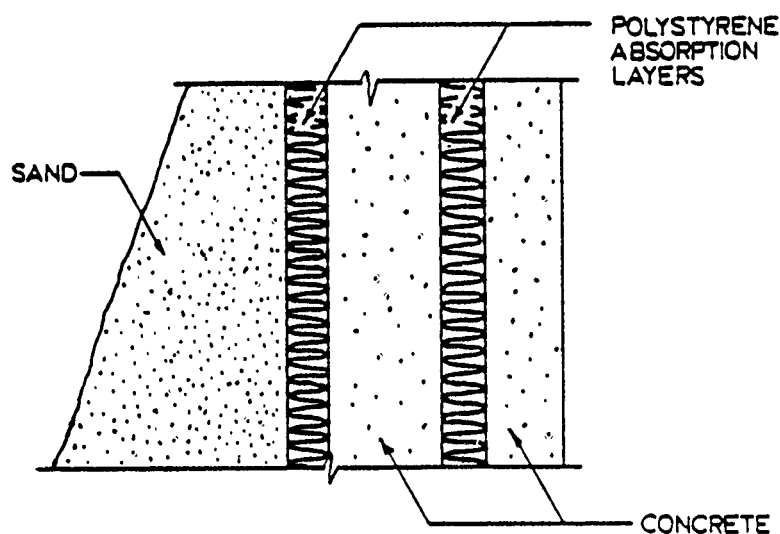


Figure 3.12. Cross Section of the SPCPC Layered System.

Construction of the aboveground SPCPC system consists of adding the exterior polystyrene and soil layers to a CPC system. After the CPC system has been constructed and the exterior forms removed, sheets of polystyrene are placed against the exterior concrete walls. A soil berm

is then constructed against the polystyrene sheets, completing the layered system.

#### Protective Shelter Loading Condition

An explosion is a violent release of energy from within a confined space. The explosion causes a sudden pressure increase in the surrounding medium, resulting in the formation of a blast wave. The blast wave travels away from the point of detonation at a velocity in excess of the sonic velocity of the surrounding medium. The velocity diminishes with distance, but remains in excess of the sonic velocity. The variation in velocity leads to the rapid formation of a shock front, as illustrated in Figure 3.13 (9). The shock front decays with distance from the point of detonation, as illustrated in Figure 3.14, and eventually drops below atmospheric pressure and becomes negative (9).

The free-field time history of the blast wave at a specified distance from the point of detonation is depicted in Figure 3.15. The shock front arrives at time  $t_1$  with a peak pressure of  $P_m$ . The pressure then decays to the ambient pressure at time  $t_2$ , thus ending the positive phase of the blast. The pressure then becomes negative, beginning the negative phase of the blast. The negative phase lasts longer than the positive phase, but its

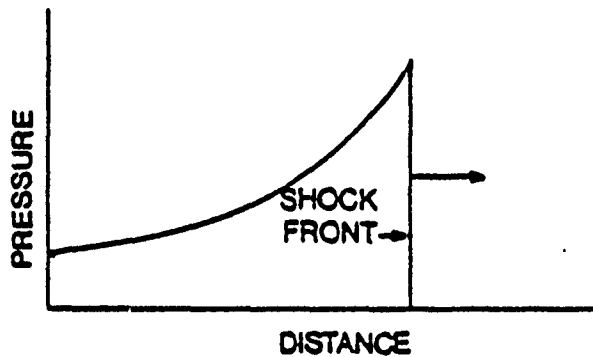


Figure 3.13. Formation of a shock front (c).

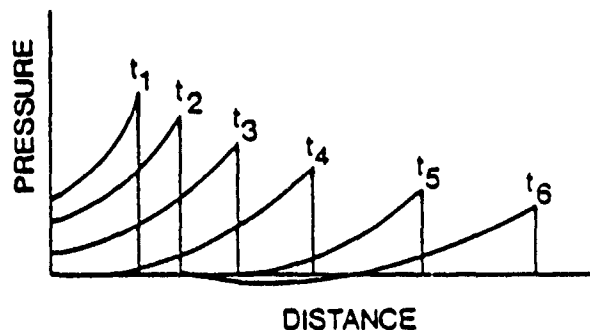


Figure 3.14. Variation of a shock wave with distance at selected times (13).

intensity is small in comparison with the positive phase and is usually neglected.

When the blast wave comes in contact with a rigid surface, such as the wall of a protective shelter, a reflected pressure in excess of the incident pressure is immediately formed. A typical reflected pressure-time

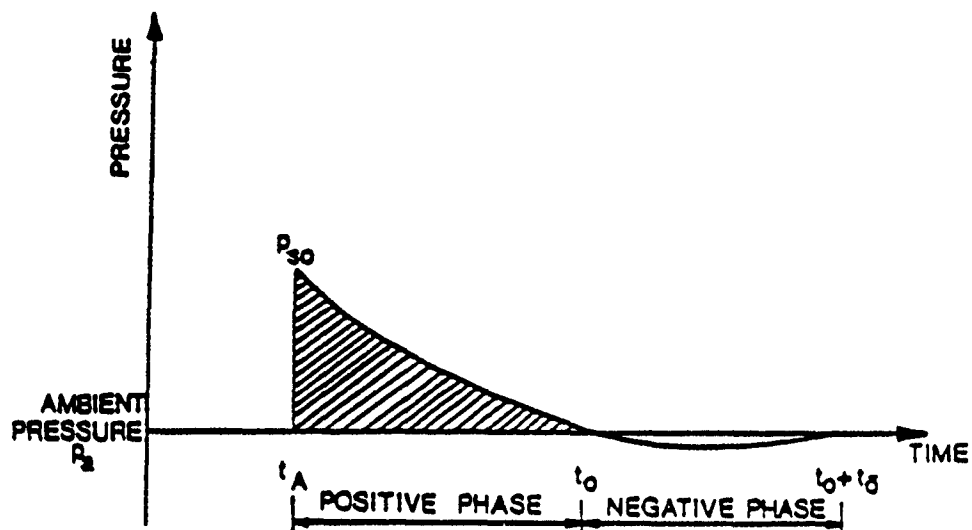


Figure 3.15. Free-field pressure-time history of a given distance from the point of detonation (9).

history is shown in Figure 3.16. The incident pressure  $P_i$  causes the reflected pressure  $P_r$  to develop. The magnitude of the reflected pressure is a function of the incident pressure and the angle formed between the wave front and the rigid surface.

The magnitude and distribution of the blast pressure on a structure are dependent on the type of explosive, the weight of the explosive, the location of the explosion with respect to the structure, the interaction of the shock front with the ground and surrounding obstructions, and the interaction of the shock front with the structure itself (9). A typical reflected blast pressure-time history measured in half-scale field tests (7) is shown in Figure 3.17. The pressure-time history can be represented by the simple triangular pulse shown in Figure 3.18, thus

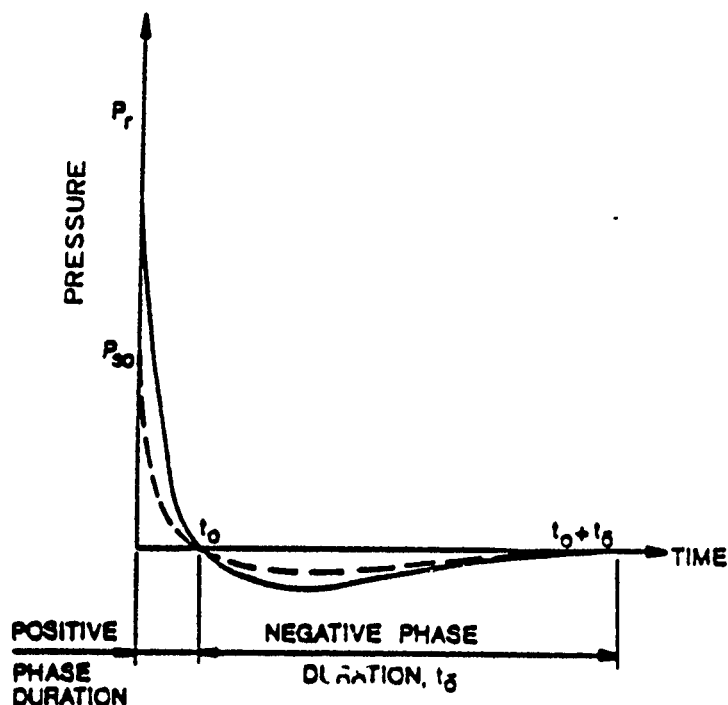


Figure 3.16. Typical reflected pressure-time history (9).

neglecting the short rise time and the negative phase of the blast. The pressure time histories used in this investigation are illustrated in Figures 3.18 through 3.20. A triangular pulse of duration  $t_d = 50 \mu \text{ sec}$  is depicted in Figure 3.18 and is used to investigate the response of the layered systems to a short duration blast wave. A rectangular pulse of the same duration, shown in Figure 3.19, is used to model the blast condition in order that the results can be more readily interpreted. A longer triangular pulse of  $t_d = 850 \mu \text{ sec}$ , illustrated in Figure 3.20, is used to approximate the actual blast durations measured in reference (7).

The magnitude of the blast loading is varied. A peak pressure of 1,000 psi is used in the linear models in

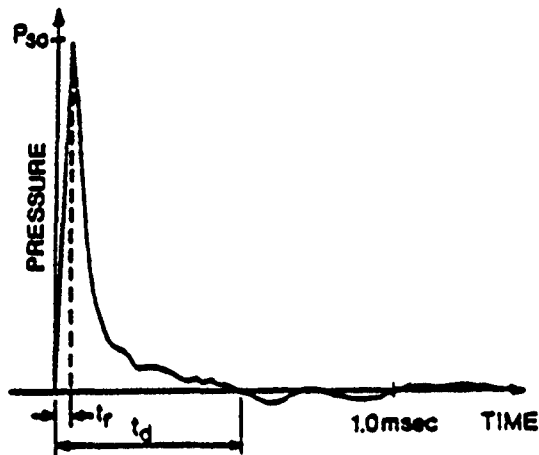


Figure 3.17. Typical reflected pressure-time history measured in tests in reference (7).

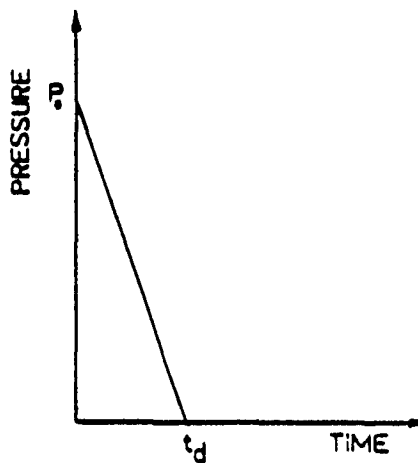


Figure 3.18. Simplified triangular pressure-time history used in the present analysis.

order to facilitate interpretation of the results. In the linear analyses, the resultant stresses can be scaled to any blast load intensity. A peak pressure of 10,000 psi is used in the nonlinear analysis of the layered systems. The 10,000 psi pressure is representative of that induced by currently employed conventional weaponry.

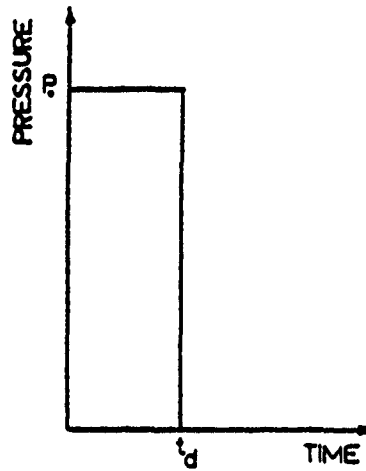


Figure 3.19. Rectangular pressure-time history used in the present analysis.

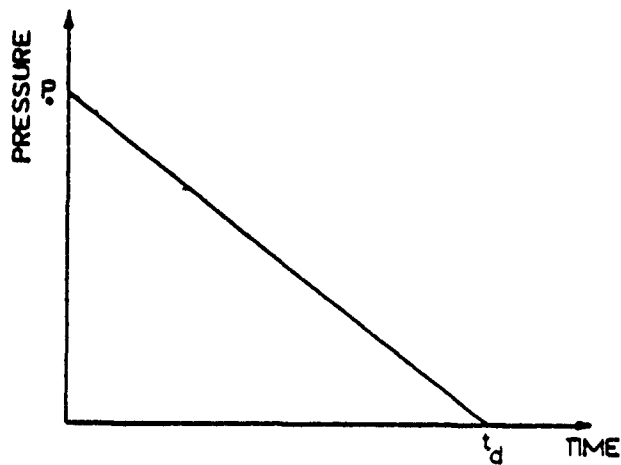


Figure 3.20. Approximation to measured pressure-time history used in the present analysis.

#### IV. ANALYSIS OF STRESS WAVE PROPAGATION BY THE FINITE ELEMENT METHOD

A comprehensive finite element method (FEM) investigation of stress wave propagation in the layered systems described in Section III was conducted. The FEM study was performed through implementation of the ADINA (1,2,3,4) computer programs. The computer analyses were executed on the Auburn University IBM 3083 academic mainframe and the Alabama Supercomputer Network Cray X-MP/24.

##### General Description of the Finite Element Models

Any FEM model used in a wave propagation study must consist of a very fine mesh in order to produce accurate results. For this reason, only a very small cross section of each layered system is analyzed. Each FEM model consists of a single column of two-dimensional, nine-node isoparametric finite elements. A typical mesh is illustrated in Figure 4.1(a) and a typical nine-node isoparametric finite element is depicted in Figure 4.1(b).

The major difference between a wave propagation problem and a structural dynamics problem is the number of

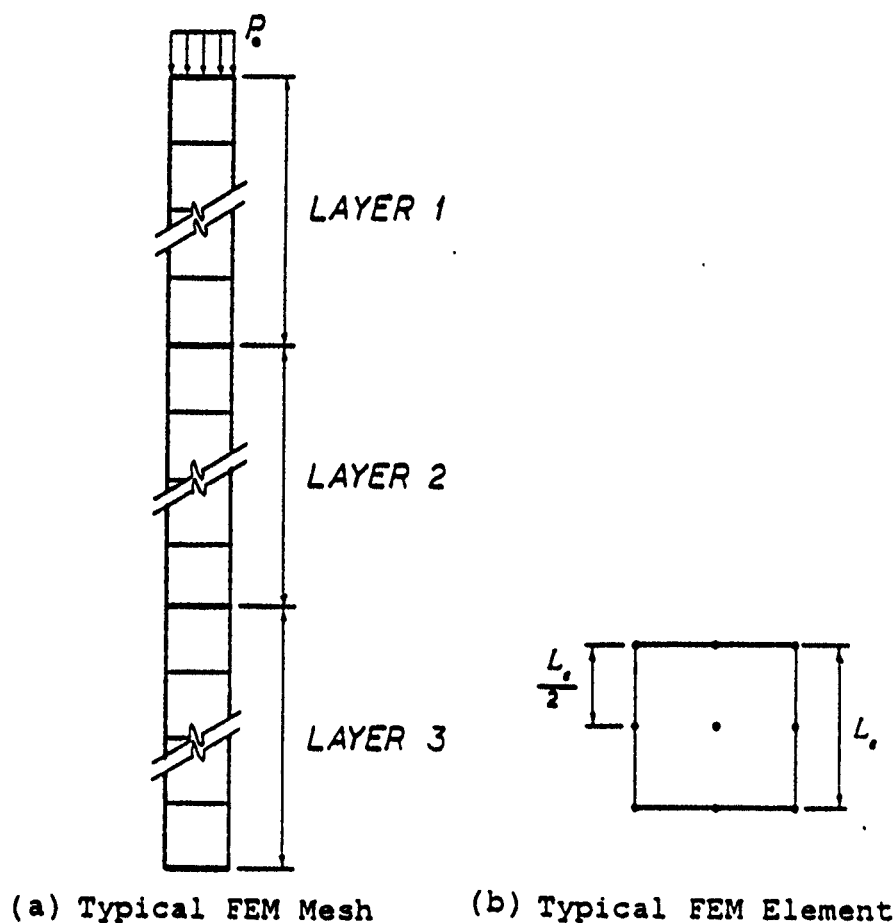


Figure 4.1. Typical Finite Element Mesh Consisting of Nine-Node Isoparametric Elements.

modes that significantly contribute to the response of the structure. In most structural dynamics problems, only a few lower frequencies are excited. Therefore, only these lower modes contribute significantly to the response of the system. In a wave propagation problem, a large number of frequencies are excited. Therefore, a large number of modes significantly contributes to the structural response. For this reason, modal analyses generally do not yield cost effective, accurate results, and a direct

numerical integration procedure must be utilized in the wave propagation analysis.

In the present study, the Newmark method of implicit time integration and a consistent mass matrix formulation are employed. The nonlinear equations are solved with the BFGS matrix update equilibrium iteration method with line searches. A modified Newton equilibrium iteration method is used in several instances to corroborate the results obtained with BFGS method.

The time step selected for temporal integration in a wave propagation problem is critical to the accuracy and stability of the solution. Since the Newmark method is unconditionally stable, selection of the time step can be based entirely upon accuracy considerations. In a wave propagation problem, the maximum time step is related to wave speed in the material and element size. The maximum time step is selected so that the stress wave propagates the distance between element integration points within that time increment. For the nine-noded element depicted in Figure 4.1(b), the maximum time step is defined by

$$(\Delta t)_{\max} = \frac{L_e/2}{c} \quad (4.1)$$

where  $L_e$  is the length of an element in the direction of wave propagation, and  $c$  is the velocity of wave propagation. It has been determined from previous experience (24) that a time step of

$$\Delta t \leq \frac{1}{3}(\Delta t)_{\max} \quad (4.2)$$

yields accurate results.

The investigation of stress wave propagation in a nonlinear material by the finite element method requires a very fine discretization. Due to the prohibitive computational cost required for the analysis of a completely nonlinear layered system, models consisting only of a single nonlinear material layer are investigated. However, the results of the nonlinear single layer models are used to predict the transmission ratios for the completely nonlinear layered systems, as described in Chapter V.

#### Linear Concrete Model

A single layer concrete model is investigated to determine the discretization necessary to produce accurate results. The discretization is considered adequate when the incident wave shape is retained as the stress wave propagates through the FEM model. This model is also used as a control to verify that the FEM analysis correctly predicts the stress wave propagation and reflection characteristics of an elastic medium. A typical mesh for the single layer concrete model is illustrated in Figure 4.2. The material properties for the concrete were previously presented in Table 3.1.

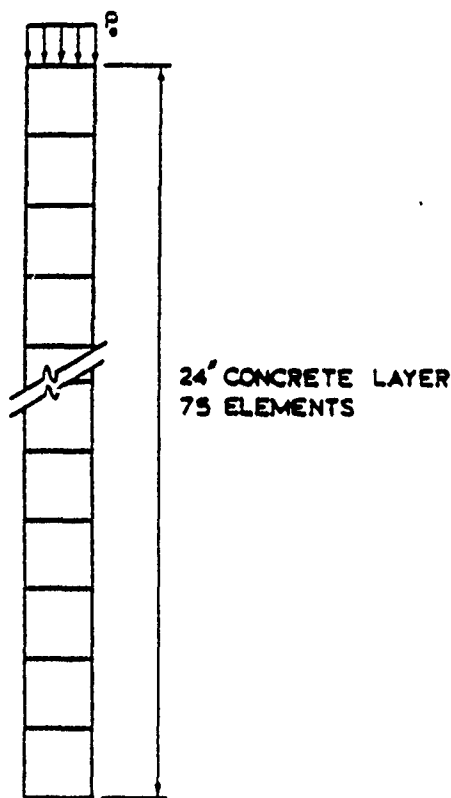


Figure 4.2. Typical Finite Element Mesh for the Linear Concrete Model.

#### Nonlinear Concrete Model

A nonlinear, single layer concrete FEM model is analyzed to verify that the wave propagation properties of the layered systems are not significantly altered by the assumption of linear behavior of the concrete. A linearly elastic-perfectly plastic constitutive law, such as that illustrated in Figure 3.7, is used to approximate the nonlinearity. The nonlinear model is investigated using both the static and dynamic material properties of concrete. The dynamic strength is taken as 1.6 times the static strength (15,16,18). The static and dynamic nonlinear concrete parameters are presented in Table 4.1.

Table 4.1. Nonlinear Concrete Parameters.

	Strength $E$ (psi)	Yield Stress $\sigma_y$ (psi)	Mass Density $\rho$ ( $10^{-4}$ ) $\frac{\text{lb-sec}^2}{\text{in}^4}$	Poisson's Ratio $\nu$
4000 psi Concrete (static)	3605000	4000	217.164	.18
4000 psi Concrete (dynamic)	4560000	6400	217.164	.18

The FEM model considered is a 16" long column comprised of 200 elements (Figure 4.3). Several different wave types are examined in order to ascertain the effects of the nonlinearity upon wave shape and wave duration. The propagation of a 50  $\mu$  sec short duration triangular stress wave, an 850  $\mu$  sec long duration triangular stress wave, and a 50  $\mu$  sec rectangular stress wave are investigated. Stress wave intensities of 7,500 and 10,000 psi are considered.

#### Nonlinear Polystyrene Model

A nonlinear polystyrene model is investigated in order to examine the effects of the nonlinear absorption layer upon wave propagation. A linearly elastic-perfectly plastic constitutive law, such as that illustrated in Figure 3.7, is used to approximate the nonlinearity. The nonlinear polystyrene parameters were previously presented in Table 3.3.

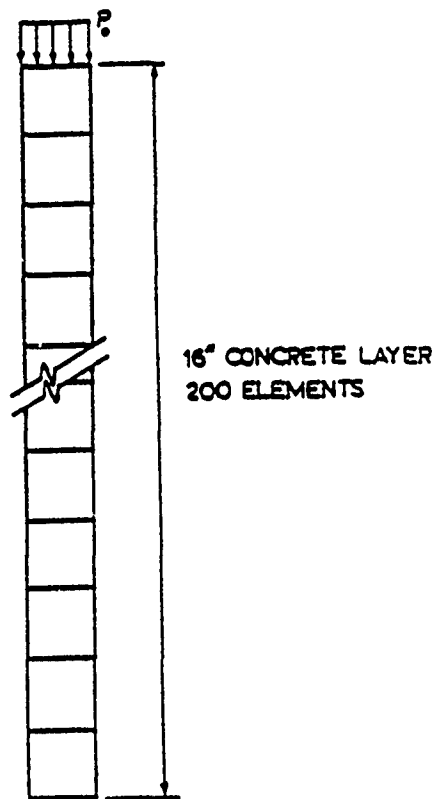


Figure 4.3. Typical Finite Element Mesh for the Nonlinear Concrete Model.

The FEM model considered is a 16" long column comprised of 200 elements (Figure 4.4). Several different wave types are investigated in order to determine the effects of the nonlinearity upon wave shape and wave duration. The propagation of a 50  $\mu$  sec short duration triangular stress wave, an 850  $\mu$  sec long duration triangular stress wave, and a 50  $\mu$  sec rectangular stress wave are investigated. Stress wave intensities of 500 and 1,000 psi are considered.

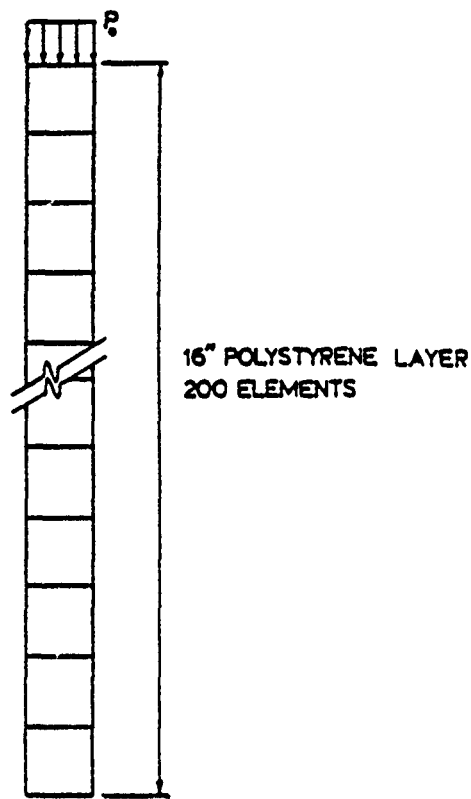


Figure 4.4. Typical Finite Element Mesh for the Nonlinear Polystyrene Model.

#### Nonlinear Sand Model

A nonlinear FEM sand model is analyzed in order to examine the effect of nonlinearity in the exterior sand layer upon wave propagation. A linearly elastic-perfectly plastic constitutive law, such as that illustrated in Figure 3.7, is used to approximate the nonlinearity. This constitutive law is a very crude representation for the nonlinear response of sand, but does provide some insight to assessing the effects of the nonlinearity upon wave propagation. The nonlinear sand parameters were previously presented in Table 3.3.

The FEM model considered is a 16" long column comprised of 200 elements (Figure 4.5). Several different wave types are investigated in order to determine the effects of nonlinearity upon wave shape and wave duration. The propagation of a 50  $\mu$  sec short duration triangular stress wave, an 850  $\mu$  sec long duration triangular stress wave, and a 50  $\mu$  sec rectangular stress wave are investigated. Stress wave intensities of 5,000 and 10,000 psi are considered.

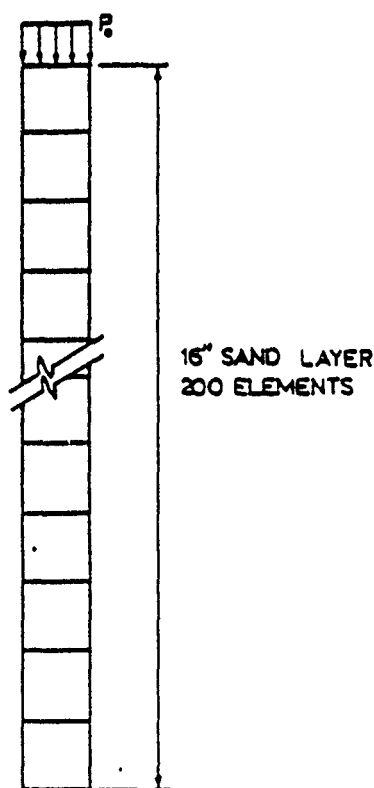


Figure 4.5. Typical Finite Element Mesh for the Nonlinear Sand Model.

### Concrete - Polystyrene - Concrete System

Three concrete-polystyrene-concrete (CPC) layered systems are investigated. The length of the polystyrene absorption layer is varied from 2" to 8". The length of the exterior layer of concrete is 10", and the length of the interior layer of concrete is 8". A typical mesh for the CPC system is illustrated in Figure 4.6. The length of the polystyrene layer and the number of elements in each model are given in Table 4.2. Typical ADINA-IN and ADINA-PLOT data files for the CPC-4 FEM models are presented in Appendix B.

The CPC systems are investigated using both linear and nonlinear constitutive laws for the polystyrene absorption layer. The properties for the linear and nonlinear materials were previously presented in Tables 3.1 and 3.3, respectively. An incident stress wave having an intensity of 1,000 psi is applied to the linear systems. A 10,000 psi incident stress wave is applied to the CPC layered systems with the nonlinear polystyrene absorption layer.

Additionally, the nonlinear, single layer analyses of the concrete and polystyrene are utilized to estimate the transmission ratios of the completely nonlinear CPC layered systems. An incident stress wave of 10,000 psi is used in the nonlinear single layer analyses.

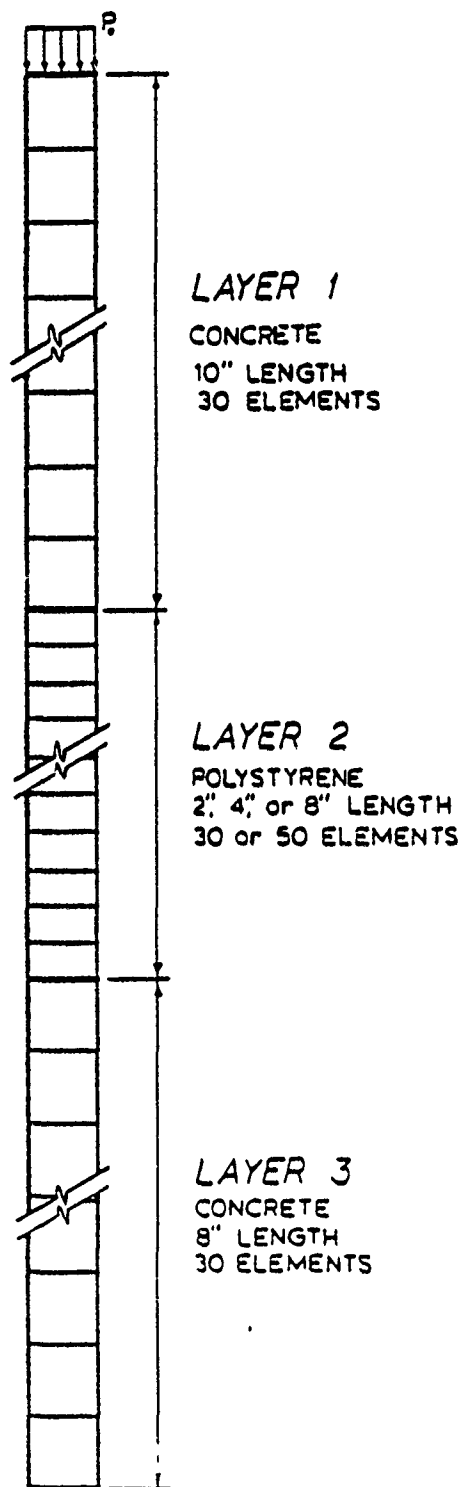


Figure 4.6. Typical Finite Element Mesh for the CPC Layered Systems.

Table 4.2. CPC Model Dimensions and Number of Elements.

Model	Total Length and No. Elements		Exterior Concrete Layer		Polystyrene Absorption Layer		Interior Concrete Layer	
	$L$	no. el.	$L_1$	no. el.	$L_2$	no. el.	$L_3$	no. el.
CPC-2	20"	90	10"	30	2"	30	8"	30
CPC-4	22"	90	10"	30	4"	30	8"	30
CPC-8	26"	110	10"	30	8"	50	8"	30

#### Sand - Polystyrene - Concrete System

Three sand-polystyrene-concrete (SPC) layered systems are investigated. The length of the polystyrene absorption layer is varied from 2" to 8". The length of the sand layer is 10", and the length of the concrete layer is 12". A typical mesh for the SPC system is illustrated in Figure 4.7. The length of the polystyrene layer and the number of elements in each model are given in Table 4.3.

The finite element method is utilized only in the investigation of the linear SPC systems. The properties for the linear material models were previously presented in Table 3.1. An incident stress wave of 1,000 psi intensity is used in the linear investigation.

The transmission ratios for the nonlinear SPC systems are estimated using the results of the nonlinear single

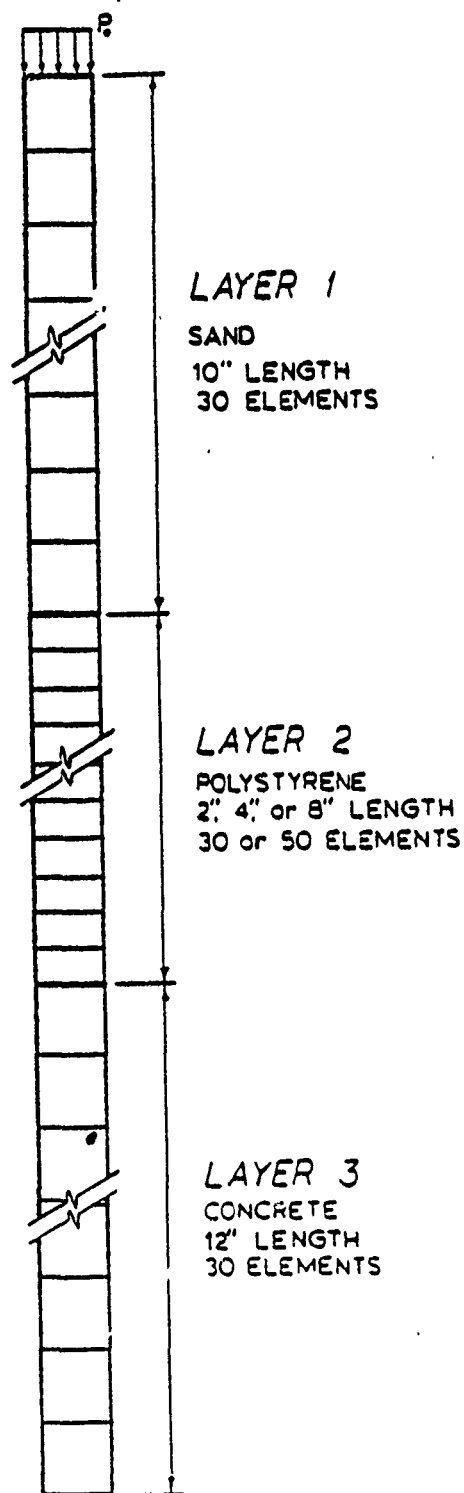


Figure 4.7. Typical Finite Element Mesh for the SPC Layered Systems.

Table 4.3. SPC Model Dimensions and Number of Elements.

Model	Total Length and No. Elements		Exterior Sand Layer		Polystyrene Absorption Layer		Interior Concrete Layer	
	$L$	no. el.	$L_1$	no. el.	$L_2$	no. el.	$L_3$	no. el.
SPC-2	24"	90	10"	30	2"	30	12"	30
SPC-4	26"	90	10"	30	4"	30	12"	30
SPC-8	30"	110	10"	30	8"	50	12"	30

layer analyses. An incident stress wave of 10,000 psi intensity is used in the nonlinear single layer investigation.

Sand-Polystyrene-Concrete-Polystyrene-Concrete System

Three sand-polystyrene-concrete-polystyrene-concrete (SPCPC) layered systems are investigated. However, an FEM analysis is not conducted for this model due to the prohibitive computational costs. The length of the polystyrene absorption layer is varied from 2" to 8". The length of the sand layer is 10", and the length of each concrete layer is 12". A typical SPCPC system is illustrated in Figure 4.8. The length of the layers for each of the SPCPC models is given in Table 4.4. The properties for the linear and nonlinear materials were previously presented in Tables 3.1 and 3.3.

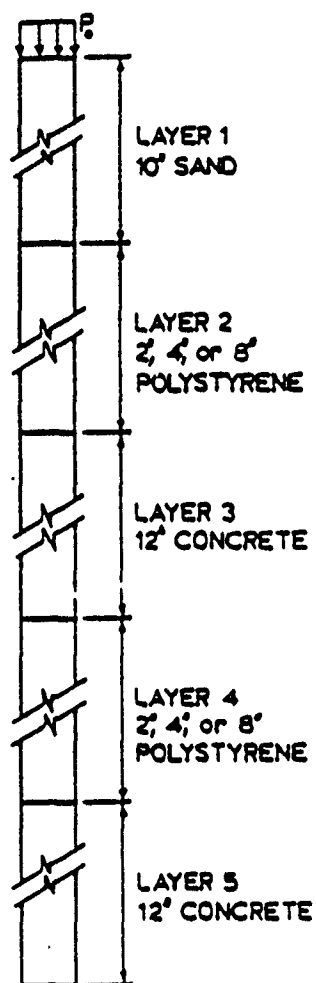


Figure 4.8. Typical SPCPC Layered System.

The transmission ratios of the linear systems is determined by the successive application of equation (2.24). The transmission ratios of the completely nonlinear SPCPC layered systems is estimated from the nonlinear single layer analyses. A 10,000 psi intensity incident stress wave is assumed for the nonlinear investigation.

Table 4.4. SPCPC Layered System Dimensions.

Model	Total Length $L$	Ext. Sand Layer $L_1$	Poly. Abs. Layer $L_2$	Ext. Conc. Layer $L_3$	Poly. Abs. Layer $L_4$	Int. Conc. Layer $L_5$
SPCPC-2	34"	10"	2"	12"	2"	8"
SPCPC-4	38"	10"	4"	12"	4"	8"
SPCPC-8	46"	10"	8"	12"	8"	8"

## V. RESULTS OF ANALYSIS

### Linear Concrete Model.

A typical stress-time history for a point in the linear concrete model, described in Chapter IV, is illustrated in Figure 5.1. The figure depicts an incident rectangular compressive stress wave of intensity 1,000 psi and the corresponding tension wave reflected from the free end. The stress wave is reflected at full intensity. The high frequency oscillations defining the shape of the stress wave are caused by the excitation of high frequency modes in the structure. The theoretical wave propagation and reflection are also shown in Figure 5.1 as a dashed line.

A typical stress trace from wave propagation tests conducted on the Split Hopkinson Pressure Bar (SHPB) (22) is depicted in Figure 5.2. The bar is loaded axially with a high intensity, short duration pressure wave at one end. Each end of the bar is a free surface. An incident compressive wave and two reflected waves are depicted in the figure. The first reflection is caused by the compressive wave reflecting from the unloaded end of the bar as a tension wave. The second reflection is caused when the tensile wave propagates back to the loaded end of

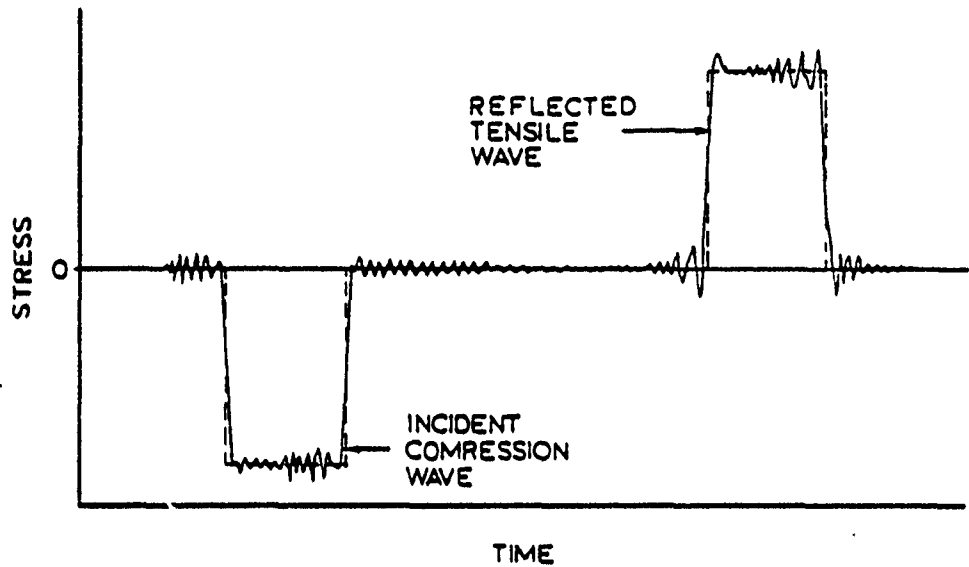


Figure 5.1. Typical Stress-Time History for a Point in the Linear Concrete Model.

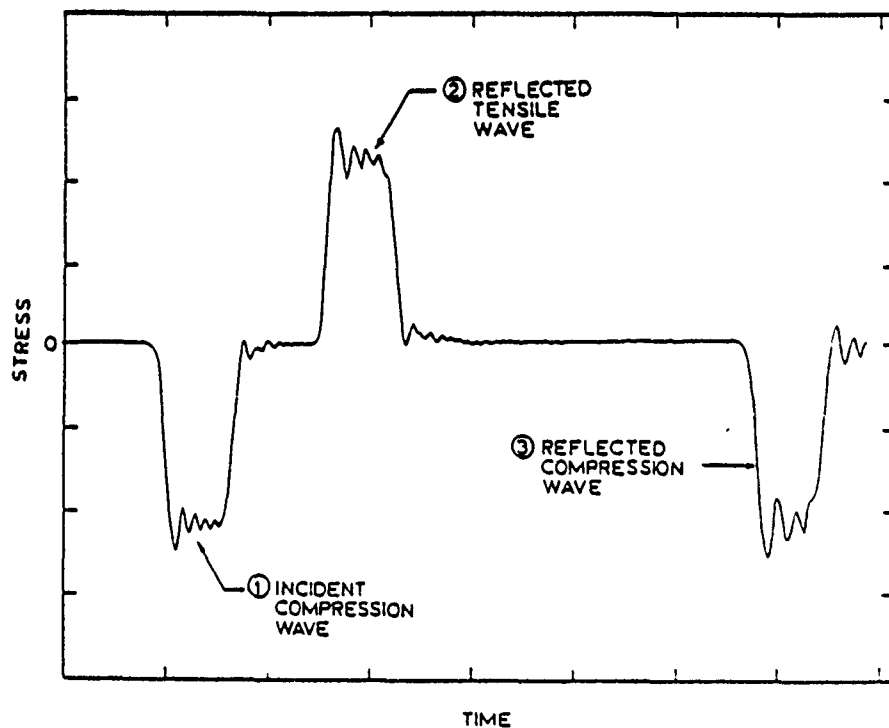


Figure 5.2. Typical Stress-Time History for a Point in the SHPB.

the bar and is reflected as a compression wave. The stress wave is reflected from each free surface at full intensity. It is noted that the stress trace obtained from the SHPB contains the same high frequency oscillations exhibited by the FEM analysis.

#### Nonlinear Concrete Model

The mitigation of stress waves in the nonlinear concrete model, described in Chapter IV, is illustrated in Figure 5.3. The maximum stress resulting from three types of incident stress waves ( 1. a short duration triangular wave, 2. a short duration rectangular wave, and 3. a long duration triangular wave) is shown. It is noted that the rate at which the stress wave degenerates is a function of the shape and duration of the incident stress wave. The short duration triangular wave decays very rapidly. However, both the short duration rectangular wave and the long duration triangular wave decay very gradually.

It is observed that the inelastic behavior of the concrete (as modeled by the bilinear constitutive law illustrated in Figure 3.7) does not significantly affect the propagation of either the rectangular or the long duration triangular stress waves. The intensity of the short duration triangular stress wave, however, is drastically reduced in a short distance.

The attenuation of stress waves in the nonlinear concrete model, considering the dynamic strength

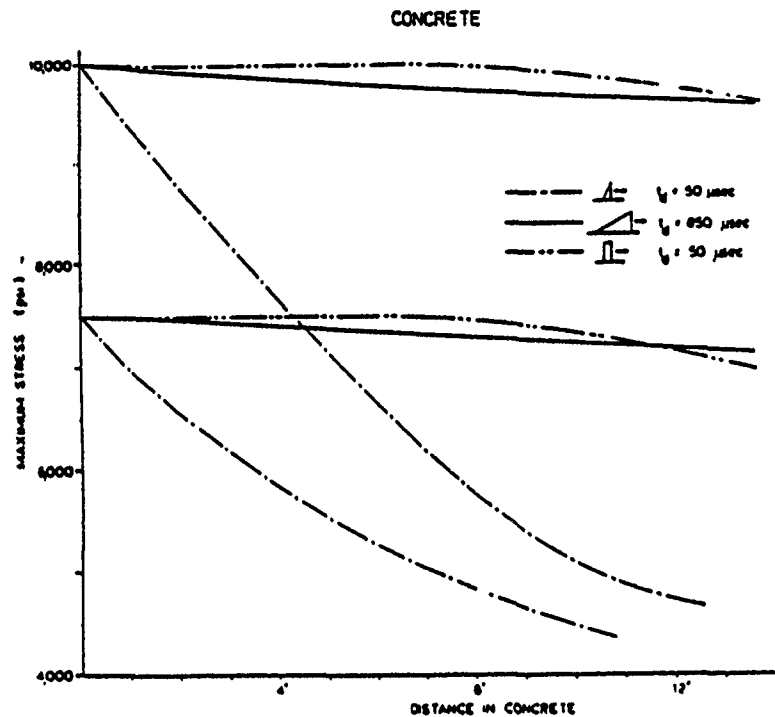


Figure 5.3. Maximum Stress Wave Intensity Versus Distance in Nonlinear Concrete.

characteristics specified in Table 4.1, is represented in Figure 5.4. The nonlinearity of the concrete has a significant effect on the propagation of the short duration triangular wave. However, the rate of decay of the stress wave is lessened. The intensities of the rectangular and long duration triangular waves are not significantly affected.

#### Nonlinear Polystyrene Model

The propagation of a plastic stress wave in a nonlinear polystyrene medium is illustrated in Figures 5.5 through 5.7. The results are very similar to the theoretical predictions of plastic wave propagation

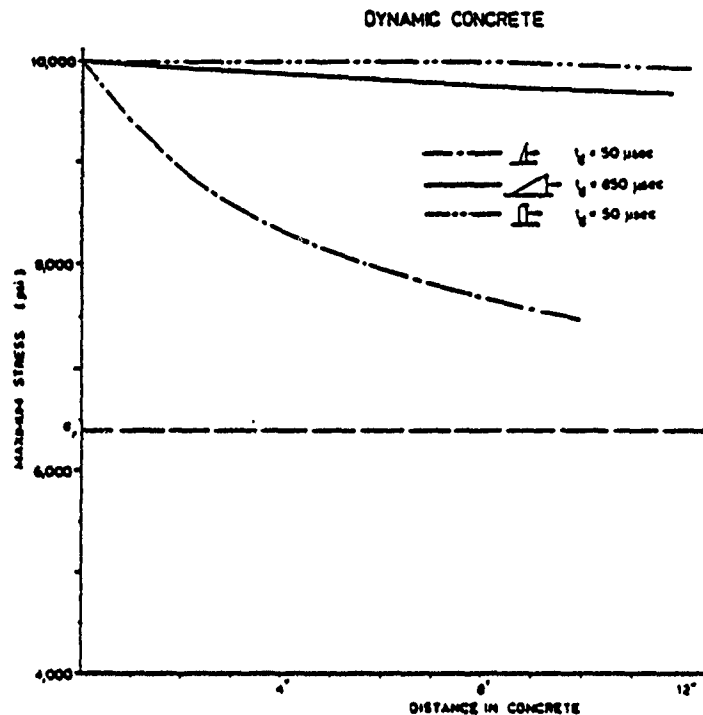


Figure 5.4. Maximum Stress Wave Intensity Versus Distance in Nonlinear Concrete When Dynamic Strength is Considered.

presented in Figure 2.18. In Figure 5.5, the propagation of a short duration triangular stress wave is represented. The plastic portion of the wave propagates at a lower velocity than the elastic portion and lags behind it. As the stress wave propagates through the medium, the wave length increases and the intensity decreases. The entire stress wave becomes elastic after the wave has propagated a sufficient distance.

The propagation of an incident short duration rectangular stress wave is depicted in Figure 5.6. The rectangular stress wave disperses and attenuates with distance. The incident rectangular stress wave becomes

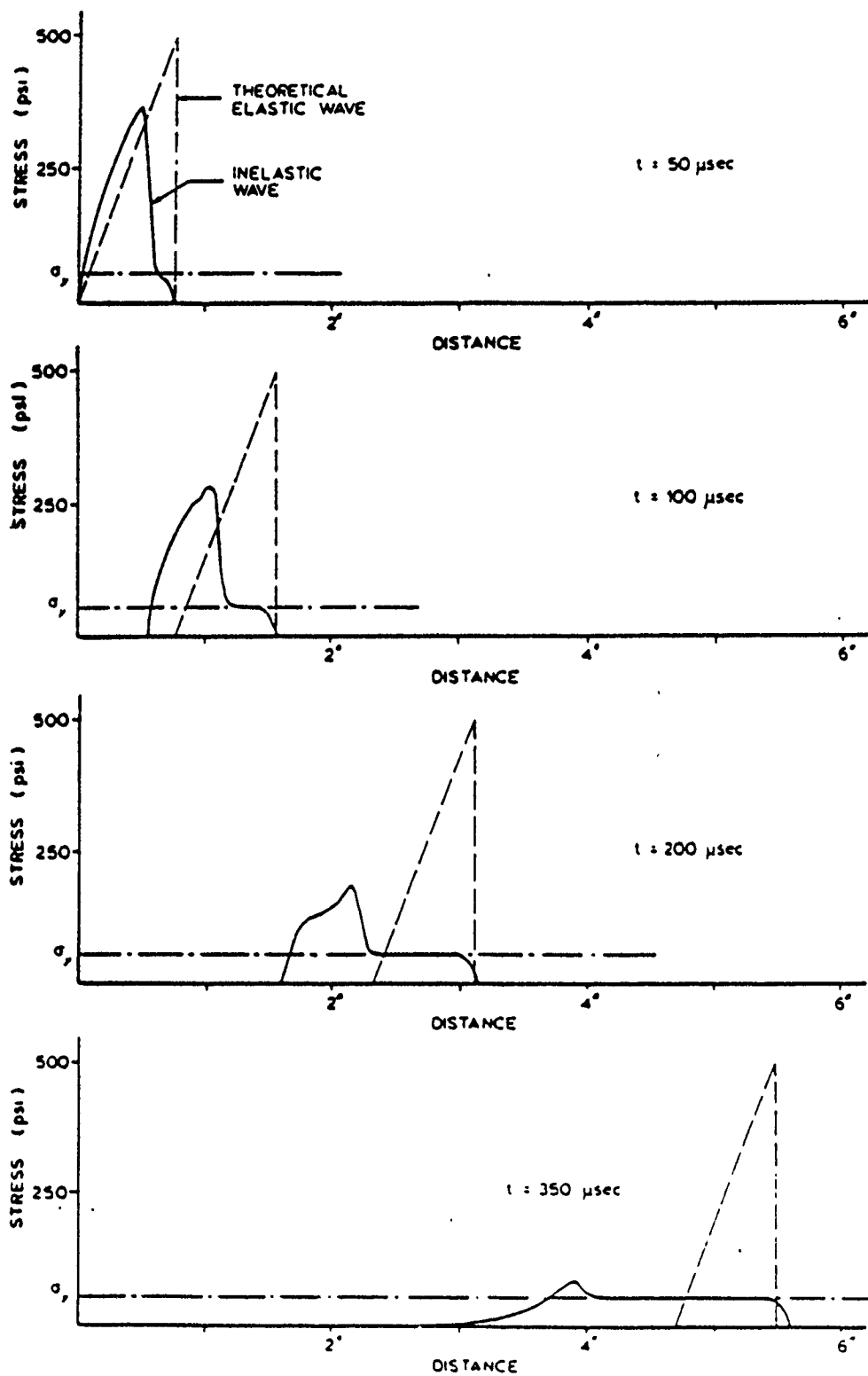


Figure 5.5. Propagation of a Plastic Short Duration Triangular Stress Wave in Polystyrene.

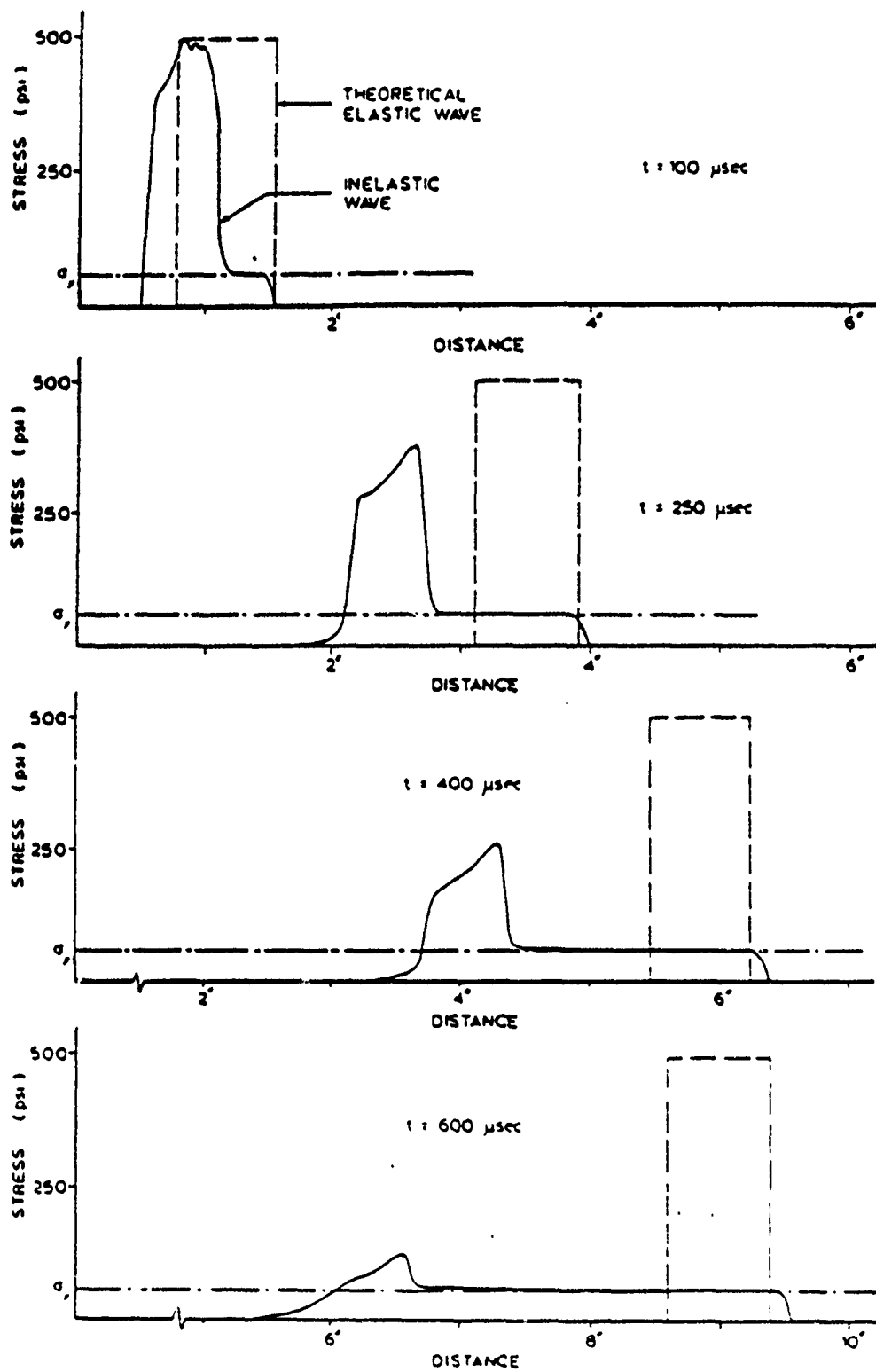


Figure 5.6. Propagation of a Plastic Short Duration Rectangular Stress Wave in Polystyrene.

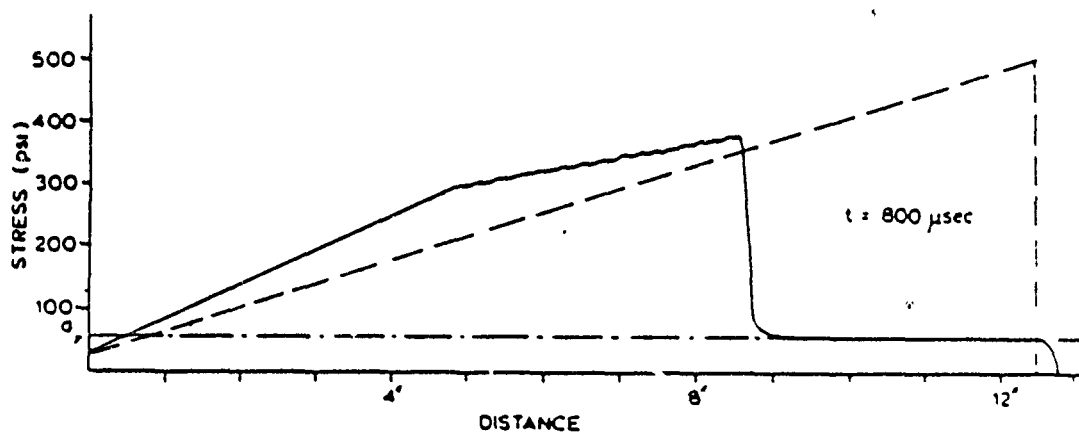
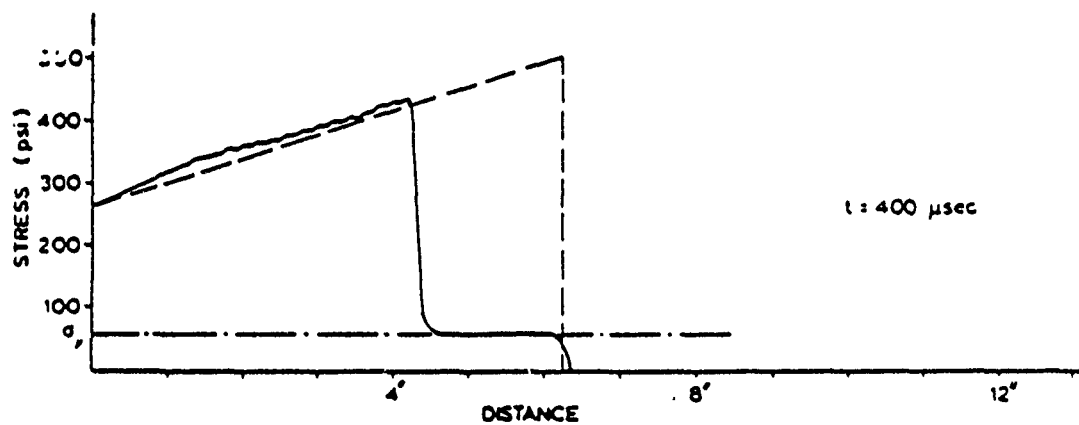
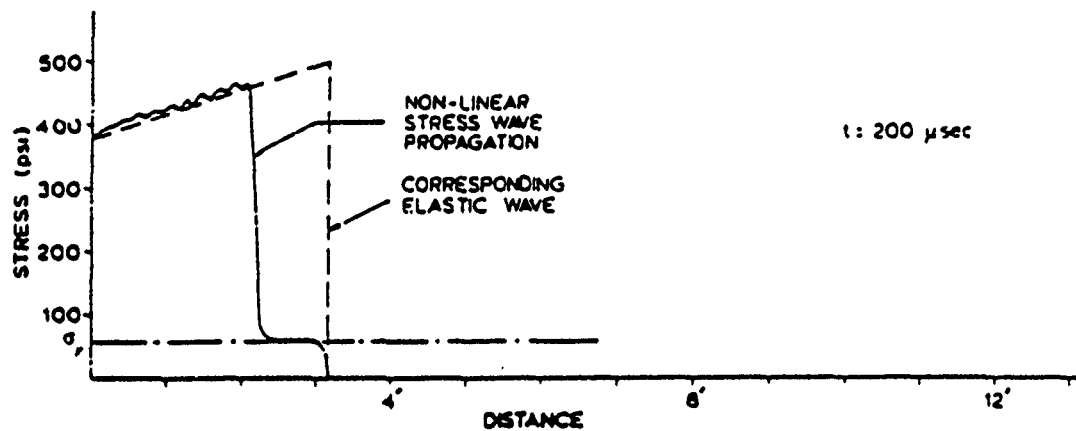


Figure 5.7. Propagation of a Plastic Long Duration Triangular Stress Wave in Polystyrene.

entirely elastic in a greater distance than required for the short duration triangular wave.

The propagation of a long duration triangular stress wave is illustrated in Figure 5.7. The plastic portion of the wave lags behind the elastic portion but exhibits little dispersion. The long duration triangular wave must travel a great distance through the medium before it is fully mitigated to an elastic wave.

The attenuation of several plastic stress waves in nonlinear polystyrene is illustrated in Figure 5.8. It is evident from Figure 5.8 that the degree of attenuation of a plastic stress wave, as it propagates through the polystyrene, is a function of the incident wave shape and initial intensity.

The short duration triangular wave exhibits a high attenuation rate as it propagates through the polystyrene. After a short distance, the intensity of the short duration triangular stress wave is reduced to the yield stress. The rate of attenuation exhibited by the long duration triangular wave, however, is significantly less. A much greater distance is required for the intensity of the long duration triangular stress wave to be reduced to the yield stress of the polystyrene. The attenuation rate of the short duration rectangular wave is less than that of the short duration triangular wave, but is much greater than that of the long duration triangular wave.

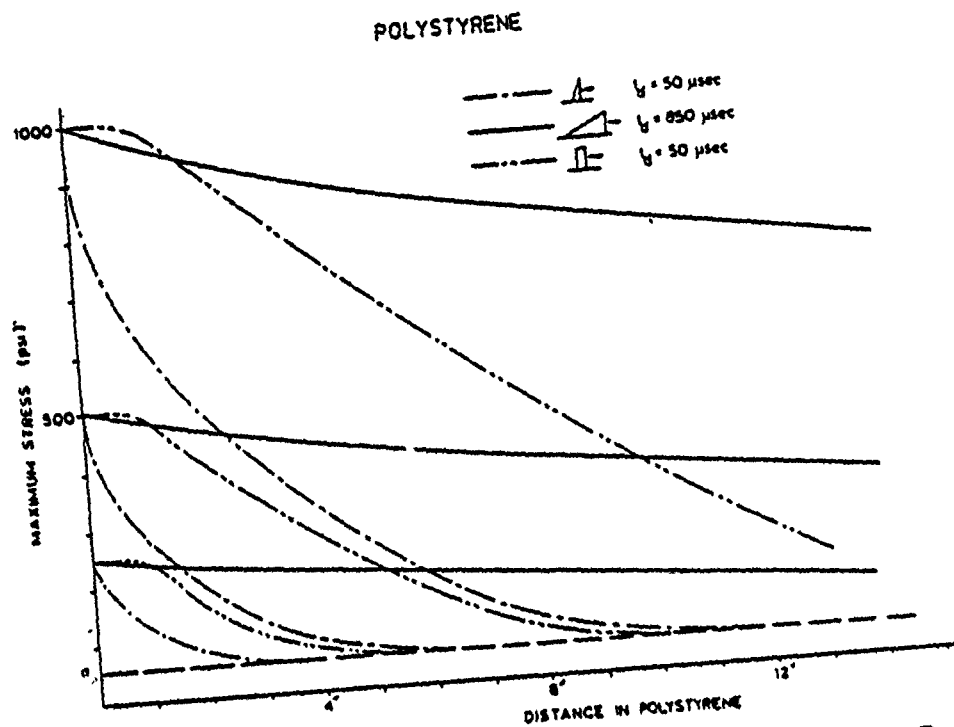


Figure 5.8. Maximum Stress Wave Intensity Versus Position in Polystyrene.

#### Nonlinear Sand Model

The attenuation of several plastic stress waves in the nonlinear sand model is illustrated in Figure 5.9. Incident stress waves of 500 psi and 1,000 psi intensity are examined. It is evident from Figure 5.9 that the attenuation rate of a plastic stress wave, as it propagates through the sand, is a function of the incident wave shape and initial intensity. The short duration triangular wave exhibits a high rate of attenuation in the nonlinear sand. However, the attenuation rates for the rectangular wave and long duration triangular wave are not as significant.

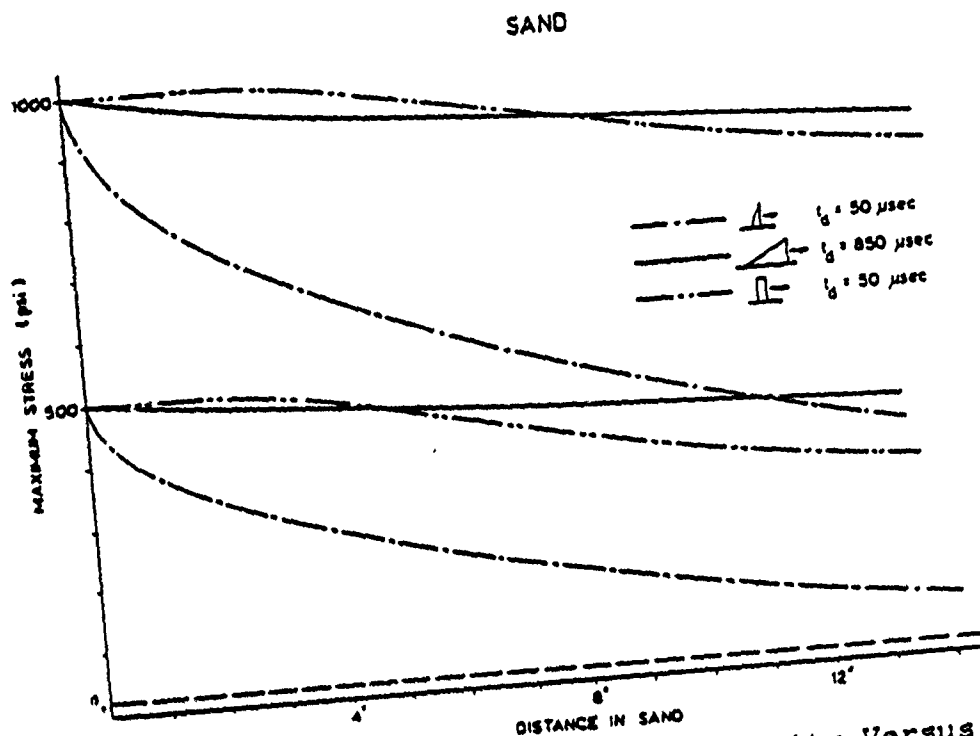


Figure 5.9. Maximum Stress Wave Intensity Versus Position in Sand.

The attenuation of high intensity plastic stress waves in the nonlinear sand is illustrated in Figure 5.10. Incident stress wave intensities ranging from 2,500 psi to 10,000 psi are considered. The attenuation of the short duration triangular wave is significantly affected by the nonlinearity, but the attenuation of the short duration rectangular wave and the long duration triangular wave is not significant.

The influence of Young's modulus,  $E$ , and the yield stress,  $\sigma_y$ , upon the attenuation of a short duration triangular wave is illustrated in Figure 5.11. Young's moduli of 20,000 psi and 80,000 psi, and yield stresses of

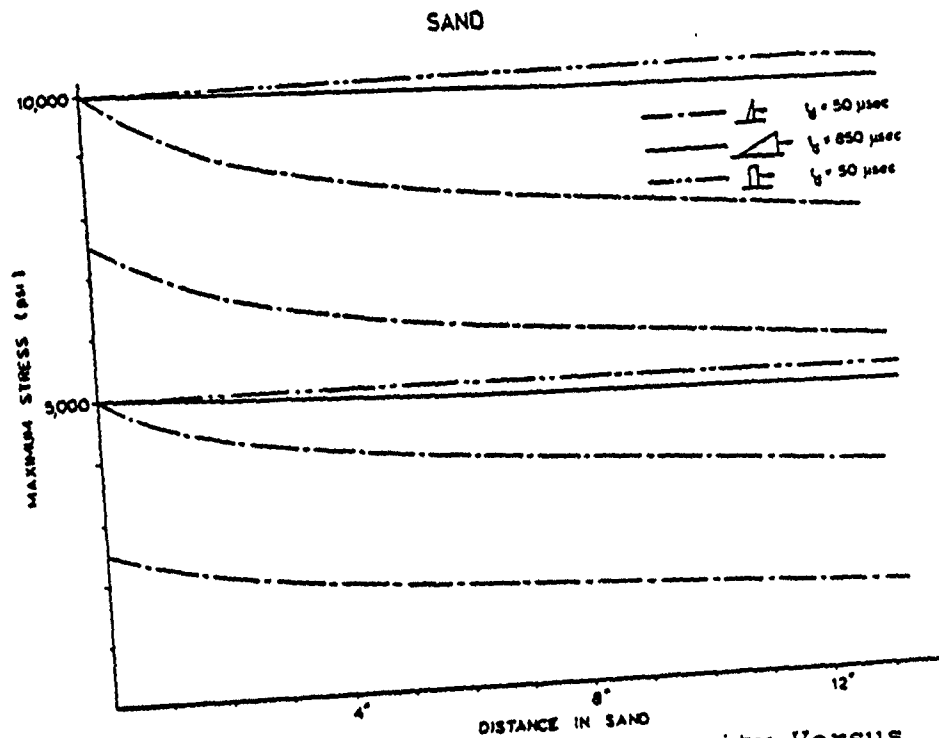


Figure 5.10. Maximum Stress Wave Intensity Versus Position in Sand for Several High-Intensity Incident Stress Waves.

20 psi and 40 psi, are considered. It is noted that as  $E$  decreases and/or  $\sigma$ , increases, the rate of attenuation increases.

#### Concrete - Polystyrene - Concrete System

Typical stress profiles for the CPC system are shown in Figures 5.12 through 5.14. Stress versus position in the model is plotted at selected times. The stress scale is reduced for the polystyrene and interior concrete layers so that observation of the attenuated stress wave can be facilitated. The stress axis for the exterior concrete layer ranges from -10,000 to 10,000 psi. The

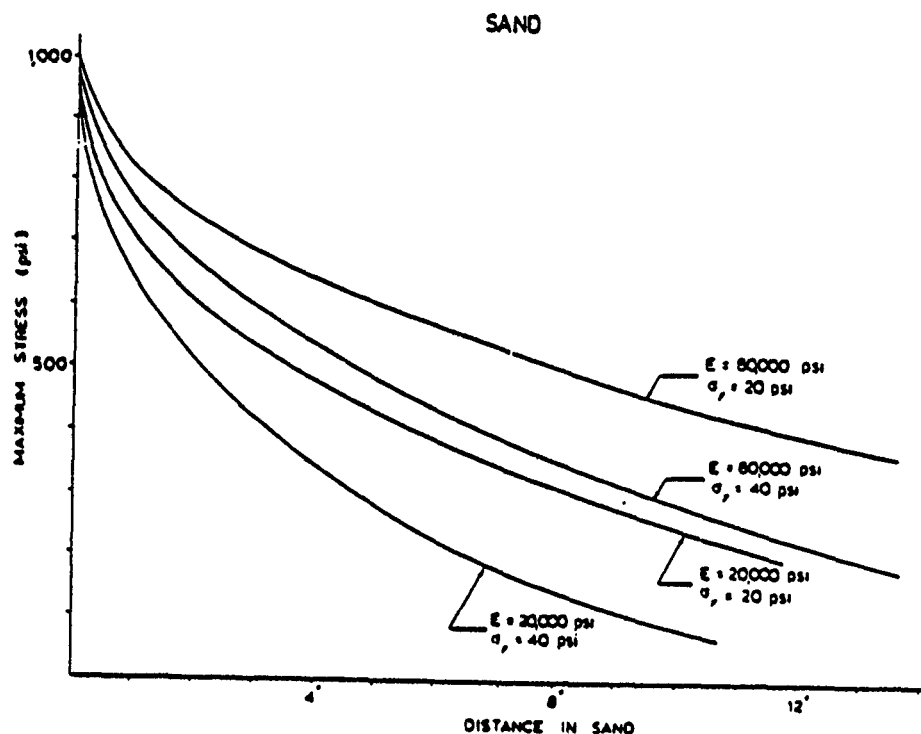


Figure 5.11. Effect of Strength and Yield Stress on Maximum Stress Wave Intensity in Sand.

stress axis for the polystyrene absorption layer and the interior concrete layer ranges from -45 to 45 psi.

The propagation of a short duration rectangular stress wave is illustrated in Figures 5.12 through 5.14. The stress wave profile at a time before the wave encounters the boundary between the exterior concrete layer and the polystyrene absorption layer is depicted in Figure 5.12. The stress profile at a time after the wave encounters the boundary between the exterior concrete layer and the polystyrene absorption layer is presented in Figure 5.13. It is observed that a very small percentage (0.96%) of the stress wave is transmitted to the polystyrene absorption layer, and that the major portion

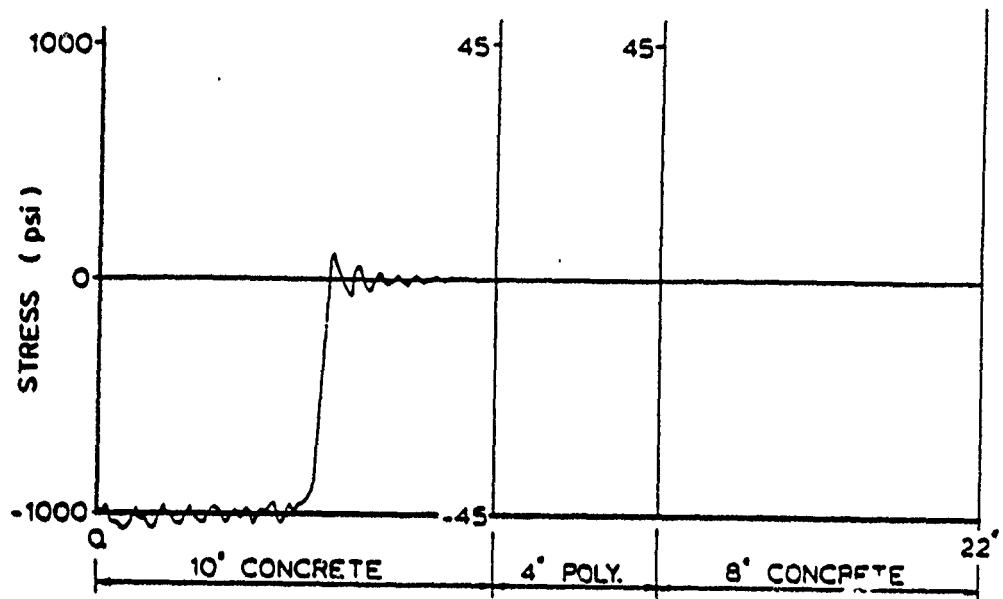


Figure 5.12. Stress Profile of the CPC-4 Layered System Subject to a 1000 psi Short Duration Rectangular Stress Wave. Time = 40.E-6 sec.

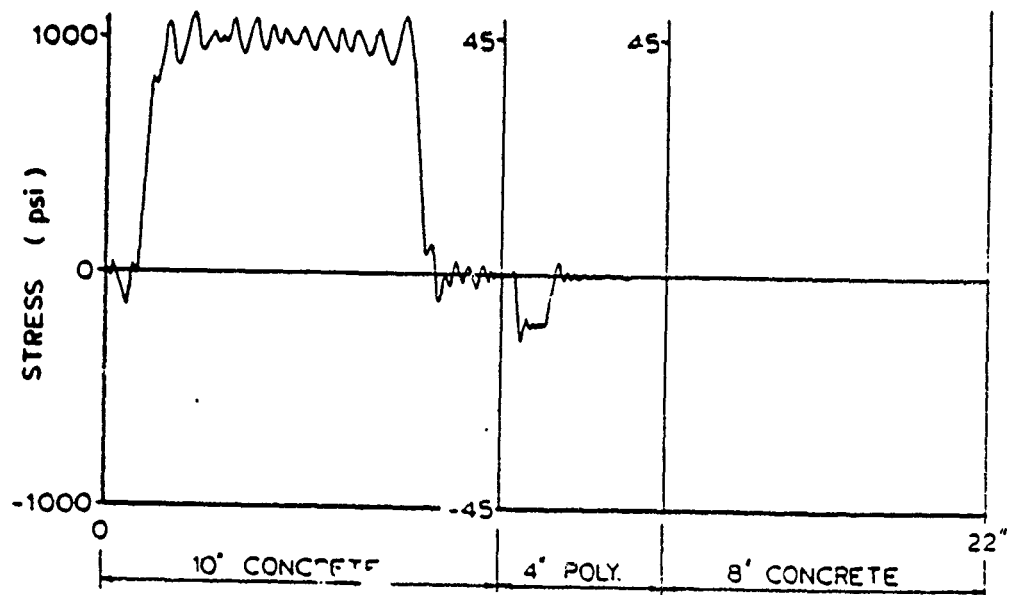


Figure 5.13. Stress Profile of the CPC-4 Layered System Subject to a 1000 psi Short Duration Rectangular Stress Wave. Time = 140.E-6 sec.

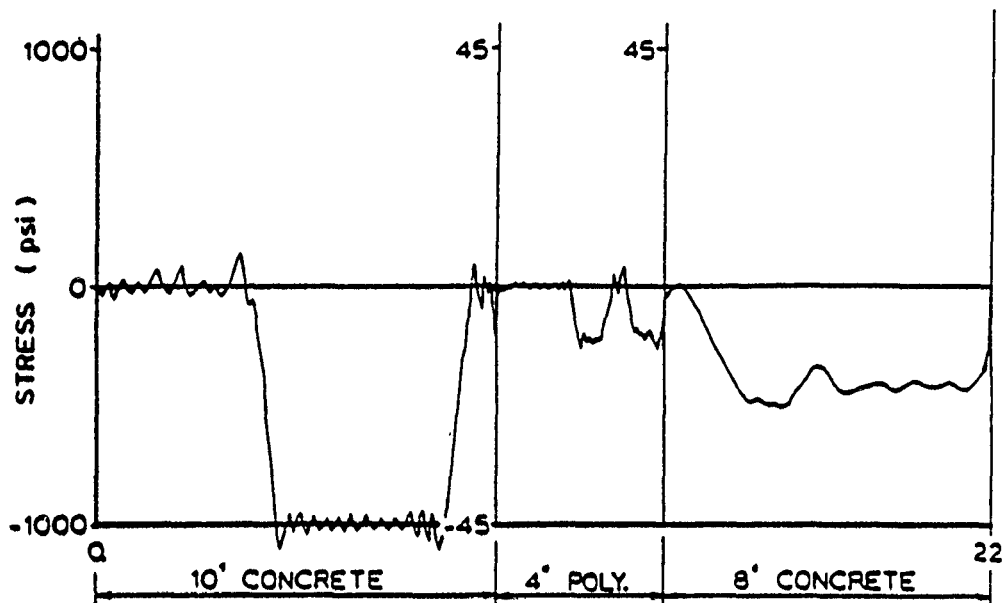


Figure 5.14. Stress Profile of the CPC-4 Layered System Subject to a 1000 psi Short Duration Rectangular Stress Wave. Time = 380.E-6 sec.

of the wave is reflected back through the exterior concrete layer as a tensile wave.

The stress condition in the model at a time after the wave encounters the interior layer of concrete is illustrated in Figure 5.14. The stress wave is transmitted from the polystyrene layer to the interior layer of concrete at an increased intensity. The wave length in the polystyrene is much shorter than in the concrete layers because the wave speed,  $c_p$ , in the polystyrene is much less than the wave speed,  $c_c$ , in the concrete.

A second stress wave propagating in the polystyrene layer is also shown in Figure 5.14. This wave is caused

by reflections generated in the exterior layer of concrete. These reflections will not occur in the actual structure because the concrete will not withstand the reflected tensile stress. The exterior layer of concrete will spall, thereby diminishing the stress wave until the intensity no longer exceeds the spall threshold of the concrete. Additional stress profiles for the CPC layered systems are presented in Appendix D.

The transmission ratios for the CPC layered system obtained using linear wave transmission and reflection theory are presented in Table 5.1. The theoretical transmission ratios were obtained using the BASIC computer program WAVEPROP.BAS (Appendix A). The program results for the CPC layered system are given in Appendix C. The transmission ratios obtained from the linear FEM analysis are also listed in Table 5.1. The results of the linear FEM analysis exhibit excellent correlation with the predictions of linear stress wave propagation theory.

Transmission ratios for the CPC layered systems, based upon the single layer nonlinear FEM analyses, are given in Table 5.2 for a short duration rectangular incident stress wave. Plastic wave attenuation in each layer is determined directly from the single layer nonlinear analyses described in Chapter IV. The stress transmitted across material boundaries is estimated from linear wave propagation theory.

**Table 5.1. Linear Transmission Ratios for the CPC Layered Systems.**

Model	Transmission Ratio	
	Linear Theory	Linear FEM Analysis
CPC-2	0.019	0.018
CPC-4	0.019	0.020
CPC-8	0.019	0.019

**Table 5.2. Estimated Nonlinear Transmission Ratios for the CPC Layered Systems Subject to a Short Duration Rectangular Incident Stress Wave.**

	CPC-2	CPC-4	CPC-8
Incident Upon Ext. Concrete	10,000	10,000	10,000
Intensity at Boundary	9,900	9,900	9,900
Transmitted to Polystyrene	95	95	95
Intensity at Boundary	55	55	55
Transmitted to Int. Concrete	110	110	110
Nonlinear Transmission Ratio	.0110	.0110	.0110

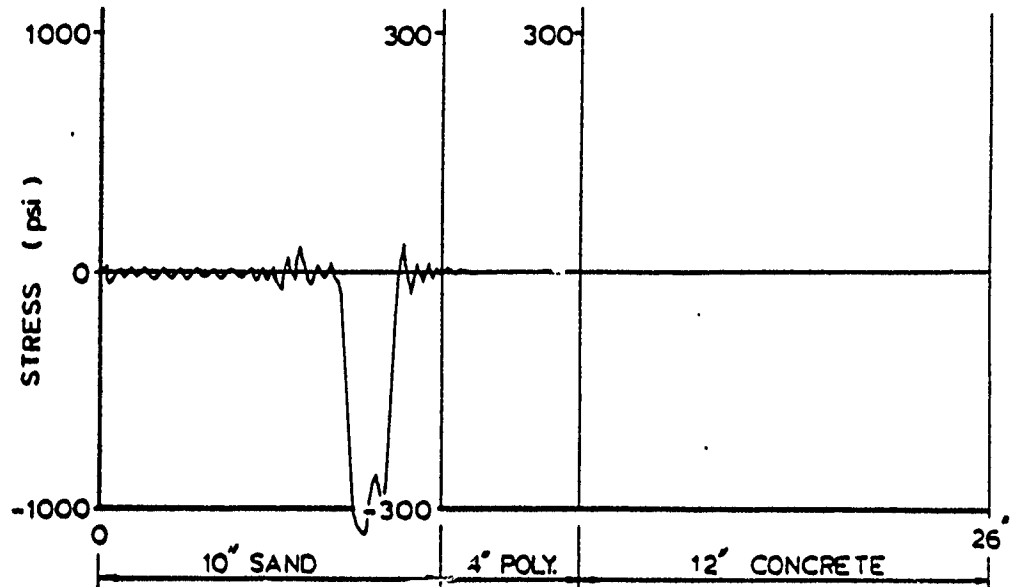


Figure 5.15. Stress Profile of the SPC-4 Layered System Subject to a 1000 psi Short Duration Rectangular Stress Wave. Time = 350.E-6 sec.

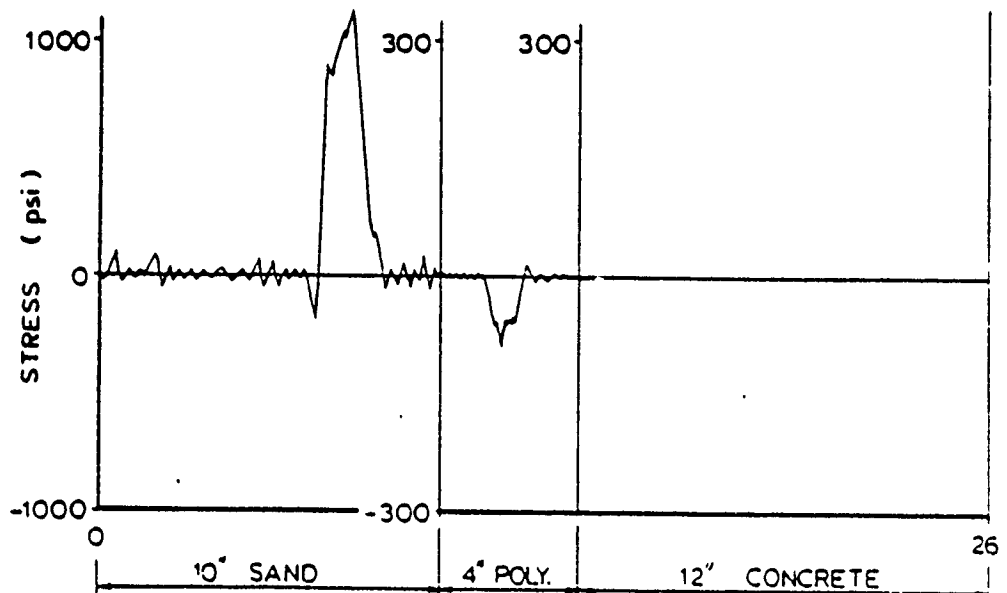


Figure 5.16. Stress Profile of the SPC-4 Layered System Subject to a 1000 psi Short Duration Rectangular Stress Wave. Time = 550.E-6 sec.

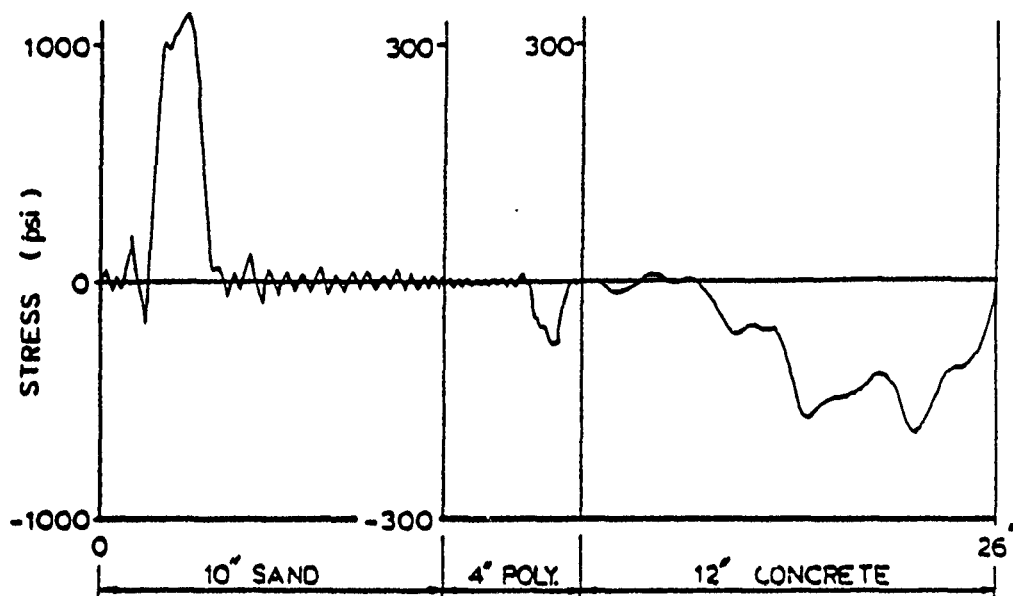


Figure 5.17. Stress Profile of the SPC-4 Layered System Subject to a 1000 psi Short Duration Rectangular Stress Wave. Time = 750.E-6 sec.

The propagation of a short duration rectangular stress wave is illustrated in Figures 5.15 through 5.17. The stress wave profile at a time before it encounters the boundary between the sand and polystyrene layers is depicted in Figure 5.15. The stress profile at a time after the boundary between the exterior sand layer and the polystyrene absorption layer is encountered is represented in Figure 5.16. It is observed that a small percentage (7.14%) of the stress wave is transmitted to the polystyrene absorption layer, and that the major portion of the wave is reflected back through the exterior sand layer as a tensile wave.

The stress condition in the model at a time after the wave encounters the interior layer of concrete is illustrated in Figure 5.17. The stress wave is transmitted from the polystyrene layer to the interior layer of concrete at an increased intensity. Additional stress profiles for the SPC layered systems are presented in Appendix E.

The transmission ratios for the SPC layered systems obtained using linear wave transmission and reflection theory are listed in Table 5.5. The theoretical transmission ratios were obtained using the BASIC computer program WAVEPROP.BAS (Appendix A). The program results for the SPC layered system are given in Appendix C. The transmission ratios obtained from the linear FEM analysis are also listed in Table 5.5. The results of the linear FEM analysis exhibit excellent correlation with the predictions of linear wave propagation theory.

Transmission ratios for the SPC layered systems, based upon the single layer nonlinear FEM analyses, are given in Table 5.6 for a short duration triangular stress wave. Plastic wave attenuation in each layer is determined directly from the single layer nonlinear analyses described in Chapter IV. The stress transmitted across material boundaries is estimated from linear wave propagation theory.

**Table 5.5. Linear Transmission Ratios for the SPC Layered Systems.**

Model	Transmission Ratio	
	Linear Theory	Linear FEM Analysis
SPC-2	0.142	0.130
SPC-4	0.142	0.150
SPC-8	0.142	0.150

**Table 5.6. Estimated Nonlinear Transmission Ratios for the SPC Layered Systems Subject to a Short Duration Triangular Incident Stress Wave.**

	SPC-2	SPC-4	SPC-8
Incident Upon Exterior Sand	10,000	10,000	10,000
Intensity at Boundary	8,900	8,900	8,900
Transmitted to Polystyrene	635	635	635
Intensity at Boundary	274	152	55
Transmitted to Int. Concrete	545	303	110
Nonlinear Transmission Ratio	.0545	.0303	.0110

The transmission ratios estimated from the single layer nonlinear FEM analyses are summarized in Table 5.7. The transmission ratio decreases as the thickness of the polystyrene layer is increased. A plot of transmission ratio versus the thickness of the polystyrene absorption layer, for both the linear and nonlinear materials, is shown in Figure 5.18. It is indicated that a thicker polystyrene absorption layer increases the capacity of the layered system to mitigate an incident stress wave, thereby increasing the structures resistance to interior spalling.

Table 5.7. Estimated Nonlinear Transmission Ratios for the SPC Layered Systems Subject to a 10,000 psi Incident Stress Wave.

	Estimated Nonlinear Transmission Ratio		
	SPC-2	SPC-4	SPC-8
Short Duration Triangular Stress Wave	.0545	.0303	.0110
Short Duration Rectangular Stress Wave	.1260	.0967	.0496
Long Duration Triangular Stress Wave	.1304	.1226	.1107

### SPC LAYERED SYSTEM

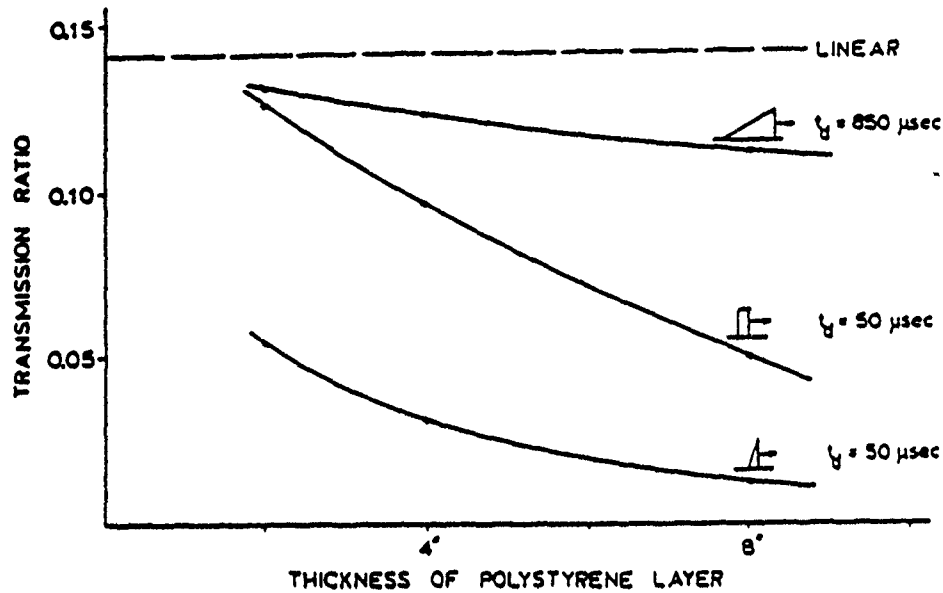


Figure 5.18. Transmission Ratio Versus the Thickness of the Polystyrene Absorption Layer of the SPC Layered System.

### Sand-Polystyrene-Concrete-Polystyrene-Concrete System

The transmission ratios for the SPCPC layered systems, based upon the single layer nonlinear FEM analyses, are given in Table 5.8 for a long duration triangular incident stress wave. Plastic wave attenuation in each layer is determined directly from the single layer nonlinear analyses described in Chapter IV. The stress transmitted across material boundaries is estimated from linear wave propagation theory.

The transmission ratios estimated from the single layer nonlinear FEM analyses are summarized in Table 5.9. It is noted that the transmission ratio decreases as the

Table 5.8. Estimated Nonlinear Transmission Ratios for the SPCPC Layered Systems Subject to a 10,000 psi Long Duration Triangular Incident Stress Wave.

	SPCPC-2	SPCPC-4	SPCPC-8
Incident Upon Exterior Sand	10,000	10,000	10,000
Intensity at Boundary	9,900	9,900	9,900
Transmitted to Polystyrene	707	707	707
Intensity at Boundary	655	616	556
Transmitted to Ext. Concrete	1304	1226	1107
Transmitted to Polystyrene	13	12	11
Transmitted to Int. Concrete	26	24	22
Nonlinear Transmission Ratio	.0026	.0024	.0022

thickness of the polystyrene layer is increased. A plot of transmission ratio versus the thickness of the polystyrene absorption layer is shown in Figure 5.19. It is indicated that a thicker polystyrene absorption layer increases the capacity of the layered system to mitigate an incident stress wave, thereby increasing the structures resistance to interior spalling.

Table 5.9. Estimated Nonlinear Transmission Ratios for the SPCPC Layered Systems Subject to a 10,000 psi Incident Stress Wave.

	Estimated Nonlinear Transmission Ratio		
	SPCPC-2	SPCPC-4	SPCPC-8
Short Duration Triangular Stress Wave	.0010	.0006	.0002
Short Duration Rectangular Stress Wave	.0024	.0018	.0010
Long Duration Triangular Stress Wave	.0026	.0024	.0022

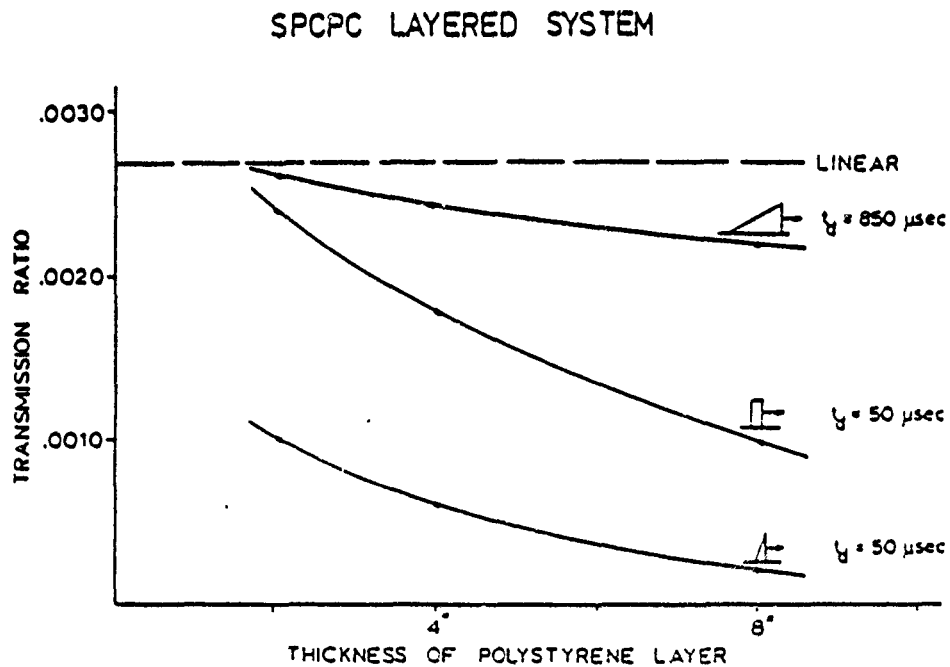


Figure 5.19. Transmission Ratio Versus the Thickness of the Polystyrene Absorption Layer of the SPCPC Layered System.

The thickness of the polystyrene absorption layer has no effect on the transmission ratio of the linear system (see Figure 5.19). The linear transmission ratio for the SPCPC layered systems, obtained from the BASIC computer program WAVEPROP.BAS (Appendix A), is 0.0027. The program results for the SPCPC layered system are given in Appendix C.

## VI. CONCLUSIONS AND RECOMMENDATIONS

### Conclusions

The finite element method (FEM) has been successfully employed to predict the propagation, reflection, and transmission of stress waves in both homogeneous and layered media. However, very fine discretizations and small integration time steps are required in order for the FEM analyses to yield accurate results. This has resulted in significant computational costs, even for simple FEM models.

It has been shown that layered media significantly alter stress wave propagation characteristics. The proper combination of high impedance and low impedance materials has demonstrated substantial enhancement of stress wave attenuation. This finding suggests that the implementation of layered media in the construction of protective shelters can eliminate blast induced spalling at the interior surface of the shelter walls.

The concrete-polystyrene-concrete (CPC), sand-polystyrene-concrete (SPC), and sand-polystyrene-concrete-polystyrene-concrete (SPCPC) layered systems have been shown to be extremely effective in mitigating an incident stress wave as it propagates through the system. The

transmission ratios for these layered systems, calculated on the assumption of linear material behavior, indicate that their deployment in the construction of protective shelters will eliminate blast induced spalling. The transmission ratios for these systems, calculated on the assumption of inelastic behavior of the media, indicate an even higher degree of attenuation for propagating stress waves, thus lending additional credibility to the layered system concept.

The SPCPC layered system exhibits the highest degree of stress wave attenuation. The linear transmission ratio for this system is calculated to be 0.0027. The nonlinear transmission ratio of the SPCPC-8 layered system is estimated to be as low as 0.0002 for a short duration triangular stress wave, and 0.0022 for a long duration triangular stress wave.

The CPC layered system also exhibits a significant degree of stress wave attenuation. The linear transmission ratio for the CPC systems is 0.019. The nonlinear transmission ratio of the CPC layered system is estimated to be as low as 0.0098 for a short duration triangular stress wave, and 0.0110 for a long duration triangular stress wave.

The SPC layered system is the least effective in terms of stress wave mitigation. The linear transmission ratio for the SPC layered system is 0.142. The nonlinear

transmission ratio of the SPC-8 system is estimated to be 0.011 for a short duration triangular stress wave and 0.1107 for a long duration stress wave. The SPC systems considered were comprised of a 10" thick layer of sand. A structure surrounded by a sand bed, or a buried structure, would be tantamount to a sand layer much thicker than 10". Therefore, the actual nonlinear transmission ratios for the SPC systems would be much less than those determined for the SPC models investigated in this study.

In all the layered systems examined, the thickness of the absorption layer significantly effects the nonlinear transmission ratio. A thicker polystyrene absorption layer results in a reduced nonlinear transmission ratio.

#### Recommendations

The FEM analyses conducted in this study indicate that the CPC, SPC, and SPCPC layered systems are highly effective in reducing transmitted stresses. However, the transmission ratios were obtained without consideration of the dynamic properties of the concrete, sand, and polystyrene. Also, the nonlinear soil and concrete approximations of linear elastic-perfectly plastic constitutive relations are very crude.

The present study has examined only the wave propagation and attenuation characteristics of the CPC, SPC, and SPCPC layered systems. It is recommended that

additional numerical studies be conducted to investigate the overall structural response of protective shelters employing the layered system concept.

It is recommended that field tests of the CPC, SPC, and SPCPC layered systems be conducted to determine their effectiveness in reducing spall. It is recommended that layered systems consisting of polystyrene layers of 4", 8", and 12" thicknesses be tested.

The SPC layered system is the most cost-effective alternative for retrofitting existing protective shelters. It is recommended that extensive field testing be conducted on the SPC layered systems to determine the optimum thickness of the polystyrene absorption layer.

## BIBLIOGRAPHY

1. ADINA - A Finite Element Program For Automatic Dynamic Incremental Nonlinear Analysis, Report AE 84-1, ADINA Engineering, Inc., Watertown, MA, 1984.
2. ADINA-IN - A Program for Generation of Input Data to ADINA, Report AE 84-6, ADINA Engineering, Inc., Watertown, MA, 1984.
3. ADINA-PLOT - A Program for Display and Post-Processing of ADINA Results, Report AE 84-3, ADINA Engineering, Inc., Watertown, MA, 1984.
4. ADINA System Verification Manual, Report AE 84-5, ADINA Engineering, Inc., Watertown, MA, 1984.
5. Balags, P. and Vretblad, B., "Model Tests on Composite Slabs of Light Gauge Metal and Concrete Subjected to Blast Loading," Proceedings of the Second Symposium on the Interaction of Nonnuclear Munitions with Structures, Panama City Beach, FL, 15-18 April, 1985, pp. 143-148.
6. Blake, A., Practical Stress Analysis in Engineering Design, Marcel Dekker, New York, 1982.
7. Colthorp, D.R., Kiger, S.A., Vitayaudom, K.P., and Hilferty, T.J., "Blast Response Tests of Reinforced Concrete Box Structures," Proceedings of the Second Symposium on the Interaction of Nonnuclear Munitions with Structures, Panama City Beach, FL, 15-18 April, 1985, pp. 95-100.
8. Cook, R.D., Concepts and Applications of Finite Element Analysis, 2nd Edition, John Wiley and Sons, New York, 1981.
9. Fundamentals of Protective Design for Conventional Weapons, Department of the Army Waterways Experiment Station, Corps of Engineers, Vicksburg, MS, 1984.
10. Henrych, J., The Dynamics of Explosion and Its Use, Elsevier Scientific Publishing, New York, 1979.

11. Hodge, K.G., and Wasley, R.J., "Dynamic Compressive Behavior of Various Foam Materials," Applied Polymer Symposia, No. 12, pp. 97-109, 1969.
12. Kolsky, H., Stress Waves in Solids, Dover Publications, New York, 1963.
13. Kornhauser, M., Structural Effects of Impact, Spartan Books, Baltimore, MD, 1964.
14. Landis, D.W., Wave Propagation in Layered Structures, Final Report, submitted to AFOSR, Washington, D.C., September, 1987.
15. Malvern, L.E., Jenkins, D.A., Tang, T., and Ross, C.A., "Dynamic Compressive Testing of Concrete," Proceedings of the Second Symposium on the Interaction of Nonnuclear Munitions with Structures, Panama City Beach, FL, 15-18 April, 1985, pp. 194-199.
16. Malvern, L.E., and Ross, C.A., Dynamic Response of Concrete and Concrete Structures, Final Report, submitted to AFOSR, Washington, D.C., May, 1986.
17. Nowacki, W.K., Stress Waves in Non-Elastic Solids, Pergamon Press, New York, 1978.
18. Raphael, J.M., "Tensile Strength of Concrete," ACI Journal, March-April 1984, pp. 158-165.
19. Rhinehart, J.S., Stress Transients in Solids, Hyper Dynamics, Santa Fe, NM, 1975.
20. Tedesco, J.W., Analysis of Layered Structures to Resist Blast Effects of Conventional Weapons, Final Report, submitted to AFOSR, Washington, D.C., April 1987.
21. Tedesco, J.W., Dynamic Stress Analysis of Layered Structures, Final Report, submitted to AFOSR, Washington, D.C., September, 1985.
22. Tedesco, J.W., Pressure Waves in Foam and Foam-Sand Samples, Final Report, submitted to AFOSR, Washington, D.C., September, 1987.

23. Tedesco, J.W., Hayes, J.R., and Landis, D.W., "Dynamic Analysis of Layered Structures," International Symposium on the Interaction of Coventional Munitions with Protective Shelters, Mannheim, West Germany, March 9-13, 1987, Vol. I, pp. 34-43.
24. Tedesco, J.W., Hayes, J.R., and Landis, D.W., "Dynamic Response of Layered Structures Subject to Blast Effects of Nonnuclear Weaponry," Journal of Computers and Structures, Vol. 26, No. 1 of 2, 1987, pp. 79-86.
25. Timoshenko, S.P. and J.N. Goodier, Theory of Elasticity, 3rd Edition, McGraw-Hill Book Company, New York, 1979.
26. Vretblad, B. and Balags, P., "Composite Structures Exposed to Blast Loads," Proceedings of the Third Symposium on the Interaction of Nonnuclear Munitions with Structures, Mannheim, West Germany, March 9-13, 1987, Vol. II, p. 736.
27. Wasley, R.J., Stress Wave Propagation in Solids, Marcel Dekker, New York, 1973.

Appendices can be obtained from  
Universal Energy Systems, Inc.

FINAL REPORT NUMBER 25  
REPORT NOT AVAILABLE AT THIS TIME  
Dr. Dennis Truax  
760-7MG-105